Viscoelastic properties and dynamical stress correlations in polymer and colloidal glass-forming model systems

Liudmyla Klochko

Université de Strasbourg

UNIVERSITÉ DE STRASBOURG

École doctorale Physique, chimie-physique ED 182 Université de Strasbourg

ÉCOLE DOCTORALE de Physique et Chimie-Physique (ED 182)

Institut Charles Sadron

THÈSE présentée par :

Liudmyla Klochko

soutenue le : **21 January 2021**

pour obtenir le grade de : **Docteur de l'université de Strasbourg**

Discipline/ Spécialité : Physique

Viscoelastic properties and dynamical stress correlations in polymer and colloidal glass-forming model systems

THÈSE dirigée par :

Dr. Alexander Semenov Directeur de recherche, ICS, Université de Strasbourg

Codirecteur de THÈSE :

Pr. Jörg Baschnagel Professeur, ICS, Université de Strasbourg

RAPPORTEURS :

Pr. Liesbeth Janssen Professeur, Eindhoven University, The Netherlands

Pr. Matthias Fuchs Professeur, University of Konstanz, Germany

---

AUTRES MEMBRES DU JURY :

Pr. Eckhard Bartsch Professeur, University of Freiburg, Germany

Pr. Jean Farago Professeur, ICS, Université de Strasbourg

Dr. Joachim Wittmer Directeur de recherche, ICS, Université de Strasbourg

Dr. Fabrice Thalmann Maître de conférences, ICS, Université de Strasbourg

To my beloved twin sister Tetiana.

Aknowledgements

> "What we know is not much. What we don't know is enormous."
>
> *Pierre-Simon de Laplace*

This work would never have been done without the support of many amazing people, especially my scientific advisers Dr. Alexander Semenov and Prof. Jörg Baschnagel. Moreover, without their help during writing, this manuscript would never be finished.

Foremost, I would like to express my deep appreciation and gratitude to my thesis supervisor Dr. Alexander Semenov. I am fortunate that three years ago we began to work together on this project. His motivation, hints, and tasks helped me a lot in understanding the crucial problems of the glass transition phenomena during my thesis. Alexander's enthusiasm, various training, and scientific guidance helped me to develop my professional skills on a new level.

I would like to pay my special thanks to my co-supervisor Prof. Jörg Baschnagel for his supervision and support during my thesis. I am glad that I had the opportunity to meet and work with such a delightful person as he is. His patience, orator skills, and knowledge in different scientific fields have been inspiring for me to work harder.

From the bottom of my heart, I would like to acknowledge the "IRTG" organization and its directors, Prof. Jörg Baschangel and Prof. Günter Reiter, for all the possibilities that I had during being part of this collaboration. It was a great time during which I met wonderful people, visited conferences, and different picturesque places. Many thanks to the coordinators of the "IRTG" Dr. Jana Husse and Birgitta Zovko who were always open to help. I wish to acknowledge my colleagues from the "TSP" group for their helpful advice and discussions.

I am extremely grateful to Dr. Olivier Benzerara, who was instrumental in my un-

derstanding of the technical aspects of my work. His support and explanation of the simulation aspects helped me succeed in programming and various modifications of the software.

With many thanks to my office-mates and friends Lisa Berezovska, Dmytro Kushnir, Dr. Geevarghese George, Dr. Victoriia Untilova, Kateryna Ryndia, Maryna Hrytsaienko, Dr. Céline Ruscher, Iryna Makarchuk, Dr. Anatolii Makhort, Fedir Demidiuk, Raisa Kociurzynski for productive discussions and creating together the warm memories about the wonderful time that we have spent.

Finally, I would like to thank my family for their understanding, love, and support which they have been giving to me. Their faith in me helped me not to give up and move on.

Résume

Motivation

Le verre est l'un des matériaux les plus anciens connus de l'homme. Par exemple, à l'âge de pierre, l'obsidienne (le verre naturel, formé par la solidification rapide de la lave sans cristallisation) était utilisée pour fabriquer les premières armes et traiter les outils de coupe. Une autre réalisation étonnante a été la découverte de vitraux colorés en ajoutant des sels métalliques, des oxydes et des nanoparticules métalliques.

Quand le liquide vitrifiable est refroidi et forme un verre, il devient dur et fragile, comme un cristal solide. Une compréhension approfondie des processus se produisant lors de la vitrification, est nécessaire afin d'affiner les propriétés des matériaux vitreux pour les besoins pratiques. La présente étude des corrélations dynamiques et statiques dans des liquides vitrifiables est motivée par cet objectif.

Objectifs

Lorsqu'un liquide visqueux est refroidi suffisamment rapidement pour éviter la cristallisation, le système peut atteindre un état métastable appelé liquide surfondu. Aux températures élevées, le temps de relaxation à l'équilibre est d'environ $\tau \approx 10^{-13} - 10^{-9}$ s et la viscosité est $\eta \approx 10^{-3} - 10^{2}$ Poise. Dès que l'état vitreux est atteint, le temps de relaxation et la viscosité augmentent considérablement $\tau \approx 10^{2} - 10^{3}$ s and $\eta \approx 10^{12} - 10^{13}$ Poise [1,2]. La température à laquelle ces valeurs sont observables s'appelle – la température de transition vitreuse T_g. L'une des propriétés principales des liquides surfondus est leur comportement viscoélastique, comme par exemple la réponse en fonction du temps du matériau à une contrainte de dilatation ou de déformation.

Ça peut être illustré à l'aide de différents modèles mécaniques tels que le modèle Maxwell. Une caractéristique rhéologique importante est le module de relaxation des

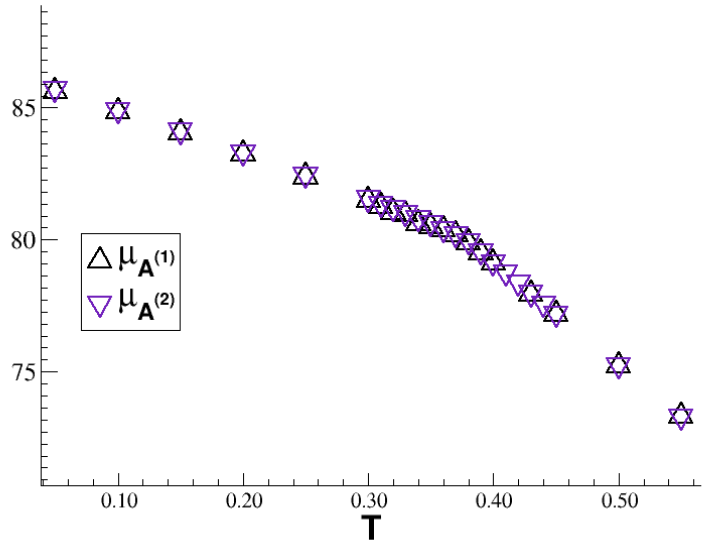

Figure 1: Dépendance de la température de module de cisaillement affine μ_A pour le système $M = 768$ et $N = 4$.

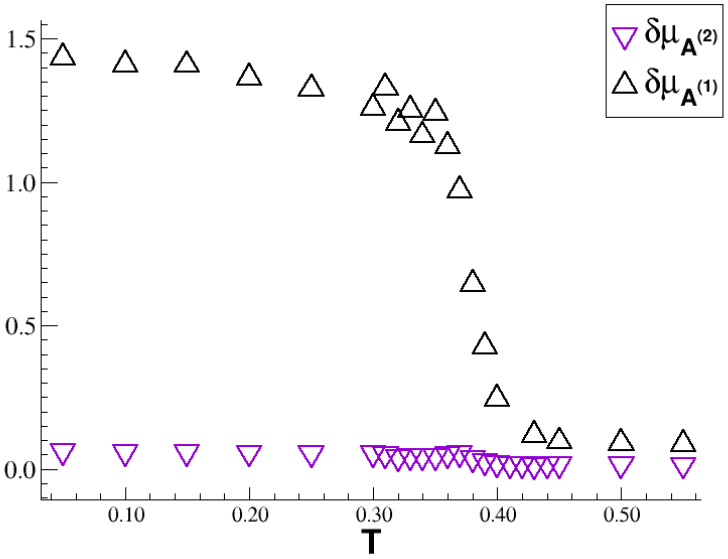

Figure 2: Dépendance de la température de l'écart-type du module de cisaillement affine $\delta\mu_A$ pour le système $M = 768$ et $N = 4$. Toutes les données sont présentées en unités de LJ.

contraintes de cisaillement ou la fonction de réponse $G(t)$ qui définit la contrainte de cisaillement au temps t après une petite marche de déformation de cisaillement. La réponse instantanée du système s'appelle module de cisaillement affine μ_A : $G(t = 0) = \mu_A$.

En revanche, le module de cisaillement statique μ définit la réponse de contrainte à long terme. Sa dépendance en T est une caractéristique dynamique de la transition vitreuse [3–6]. Dans le cadre de mon projet de doctorat, la dépendance du module de cisaillement de la température a été étudiée et simulée en utilisant la méthode de la Dynamique Moléculaire (MD). De nombreuses propriétés mécaniques (viscoélastiques, rhéologiques) des liquides vitrifiables peuvent être obtenues en analysant les fluctuations des contraintes.

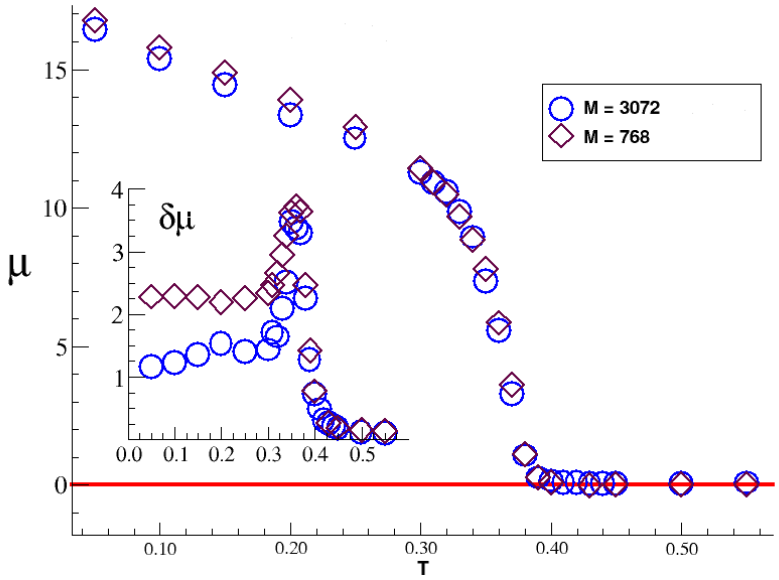

Figure 3: Module de cisaillement statique μ et son écart-type $\delta\mu$ en fonction de la température pour deux systèmes différents : nouveau système (diamants marrons) ($M = 768$, $N = 4$) et système plus grand similaire ($M = 3072$, $N = 4$) (cercles bleus) [7]. La ligne rouge correspond à $\mu = 0$. On peut voir que pour les deux systèmes $\delta\mu$ montre un pic près de la région de la transition vitreuse, $T_g \approx 0.38$.

En particulier, la fonction de corrélation temporelle de la contrainte de cisaillement $C(t)$ est étroitement liée au module de relaxation de cisaillement $G(t)$. Il a été montré récemment que de telles relations dans différents ensembles statistiques peuvent être utilisées dans la modélisation moléculaire pour une détermination précise du module de cisaillement près de la transition vitreuse [8].

Cependant, une caractérisation beaucoup plus précise de la rhéologie et de la micro-rhéologie des systèmes vitrifiables peut être obtenue en étudiant la dépendance en longueur d'onde de leurs corrélations des contraintes [10]. La fonction complète de la corrélation

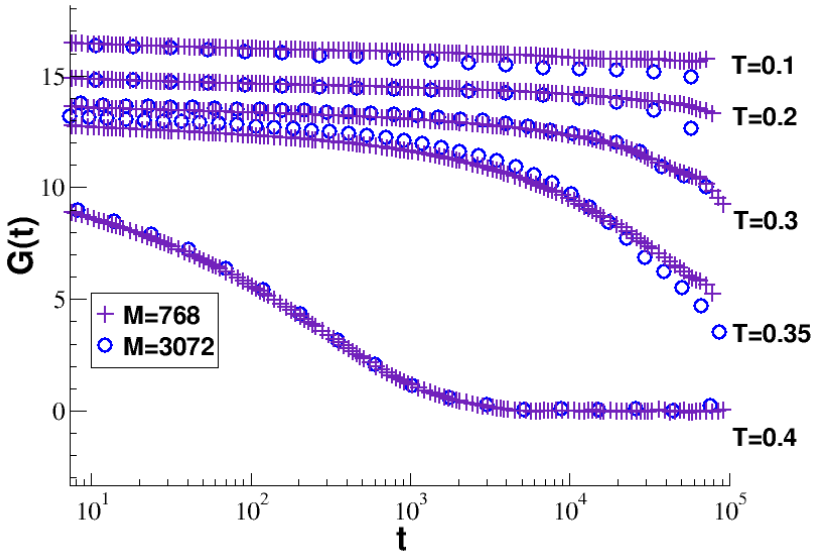

Figure 4: Le module de cisaillement $G(t)$ en fonction de T pour les deux systèmes. Toutes les données sont présentées en unités de LJ.

des contraintes de cisaillement est définie comme :

$$C_{\alpha\beta\gamma\delta}(\boldsymbol{q},t) = \frac{1}{V}\left\langle \sigma_{\alpha\beta}(\boldsymbol{q},t)\,\sigma^{\star}_{\gamma\delta}(\boldsymbol{q},0)\right\rangle, \tag{1}$$

où $\sigma_{\alpha\beta}$ est le tenseur des contraintes. Cette fonction ne dépend pas seulement du module (q) mais également de l'orientation du vecteur d'onde $\boldsymbol{q}$. Donc, $C_{\alpha\beta\gamma\delta}(\boldsymbol{q},t)$ est présentée comme un outil idéal pour étudier la viscoélasticité anisotrope des systèmes vitrifiables. Cependant, la dépendance anisotrope du vecteur d'onde de $C_{\alpha\beta\gamma\delta}(\boldsymbol{q},t)$ n'a pas été étudiée jusqu'à présent, et cette lacune suggère clairement une telle étude.

Description du projet

Dans ce projet, nous avons étudié et analysé comment les propriétés viscoélastiques et des fonctions de corrélations structurales et dynamiques des oligomères tridimensionnels et des liquides simples bidimensionnels évoluent lorsque la température T est diminue en utilisant les simulations de MD.

Au cours de la première partie du projet, le système d'oligomères, similaire à celui étudié dans les travaux précédents [7], a été étudié. Il s'agit d'un système tridimensionnel qui se compose de $M = 768$ chaînes d'oligomères avec 4 billes reliées par des liaisons harmoniques. Les particules ont la même masse et les mêmes propriétés. Les billes qui ne sont

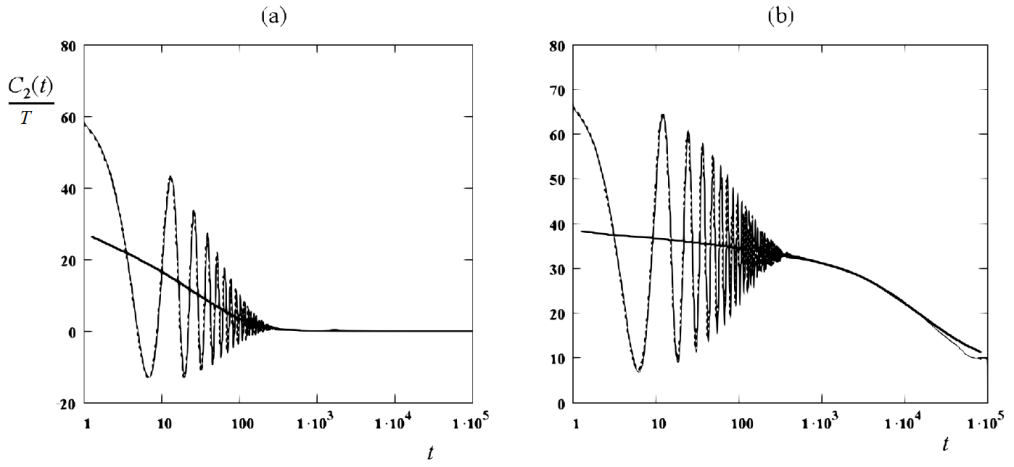

Figure 5: Dépendance temporelle de la fonction de corrélation des contraintes $C_2(t)/T$ pour le système polydisperse bidimensionnel à $q = 2\pi/L$ à: (a) $T = 0.24$ (en dessous de T_g); (b) $T = 0.30$ (au-dessus de T_g). La courbe pleine mince correspond aux données de la MD et la courbe en pointillés épaisse correspond aux prédictions théoriques [9]. La courbe solide épaisse est la fonction de corrélation lissée $C_{2\sim}(t)/T$ sans oscillations. Toutes les données sont présentées en unités de LJ.

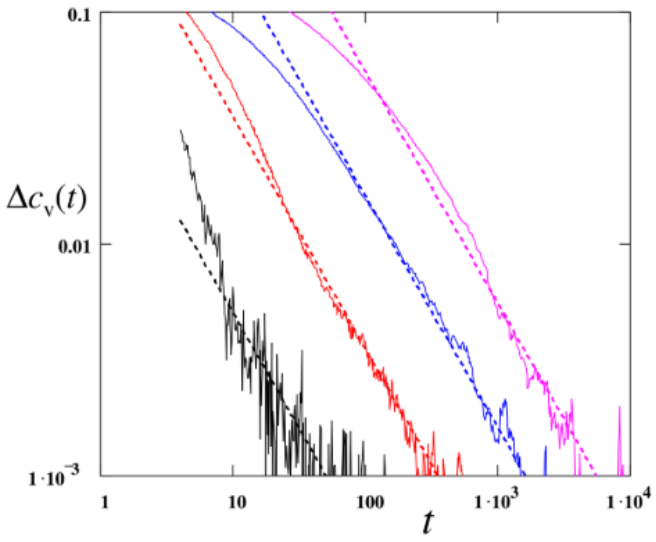

Figure 6: Incrément de la chaleur spécifique $\Delta c_v(t) = c_v(\infty) - c_v(t)$ en fonction du temps t dans les unités de LJ à différentes T. Lignes pointillées : ajustement avec la dépendance théorique $1/t$, car $c_v(\infty) - c_v(t) \propto t^{-d/2}$ avec $d = 2$.

pas reliées par des liaisons interagissent avec un potentiel de Lennard-Jones (LJ), $u_{\mathrm{LJ}}(r)$. Les particules reliées par des liaisons interagissent par le potentiel quadratique, $u_{\mathrm{b}}(r)$. Nous avons étudié la dépendance de la température et les effets de la taille du système

pour le module de cisaillement statique μ, le module de cisaillement affine μ_A, le module de relaxation de cisaillement $G(t)$, le module de fluctuation μ_F et leurs fluctuations, $\delta\mu_F$, etc.

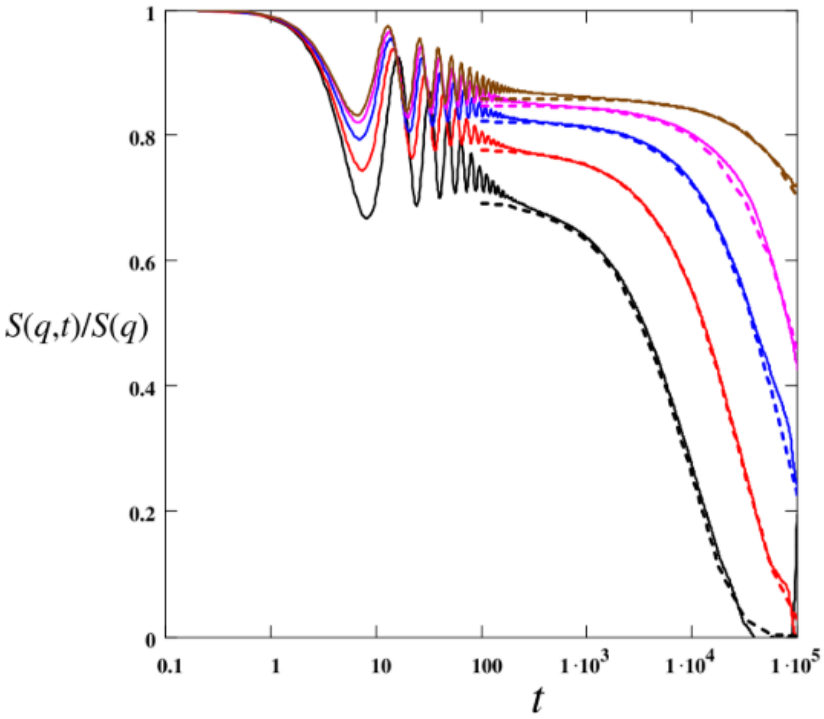

Figure 7: Fonction de diffusion intermédiaire cohérente pour le système bidimensionnel polydisperse $\phi_q(t) = S(q,t)/S(q,0)$ à $q = q_{\min} = 2\pi/L$. Les lignes pointillées montrent la prédiction théorique (cf. l'article soumis) pour la relaxation finale de $\phi_q(t)$. Pour les courbes du bas en haut les températures sont $T = 0.5, 0.4, 0.35, 0.325$.

Au cours de la deuxième partie du projet, le système bidimensionnel de particules sphériques polydisperses (de type LJ) a été étudié par des simulations de dynamique moléculaire. Le système contient $N = 10^4$ particules différentes au total. Nous avons étudié le comportement en température du facteur de structure dynamique $S(q,t)$ et de la capacité calorique dynamique $C_V(t)$. Pour analyser la corrélation des contraintes locales dans des liquides complexes et surfondus en nous concentrant sur les dépendances temporelles et spatiales de la fonction-tenseur de corrélation des contraintes $C(\boldsymbol{r},t)$ nous avons développé une théorie [9], qui prévoit que les corrélations des contraintes de cisaillement sont à longue portée au voisinage de la transition vitreuse.

L'étude du comportement de $C(\boldsymbol{q},t)$ est un objectif important car cette fonction montre si les corrélations ont un caractère à longue ou à courte portée. Notre théorie

est en accord avec le travail de simulation effectué par Lemaître [11] pour le calcul de la fonction de corrélation des contraintes de cisaillement dans les structures inhérentes uniquement, et avec la théorie de Fuchs et al. [12, 13].

Résultats et perspectives:

1. **Système d'oligomères tridimensionnel**

   (i) Il a été constaté que le module de cisaillement μ est presque indépendant de la taille du système [6] mais son écart-type montre une dépendance considérable de la taille du système en dessous de T_g. Pour le régime liquide ($T \gg T_g$) le module de cisaillement s'annulle, $\mu = 0$ (Fig. 3). Lorsque la température est abaissée vers T_g, le module de cisaillement augmente fortement. La comparaison entre notre nouveau système ($M = 768$ et la longueur de chaîne $N = 4$) et un système plus grand similaire obtenu lors des travaux antérieurs [7] ($M = 3072$, $N = 4$) est présentée sur la Fig. 3.

   Sur la Fig. 4 on peut voir que des quantités telles que $G(t)$ présentent un comportement similaire par rapport aux travaux antérieurs [7]. La principale différence entre les deux systèmes est que le système $M = 768$ montre un temps de relaxation structurale un peu plus long dans le régime de basse température, $T \ll T_g$ [6].

   (ii) Nous avons développé une technique [6] qui permet de diminuer les fluctuations de μ_A en faisant la moyenne sur toutes les orientations possibles (en supposant que notre système est isotrope, nous pouvons faire la moyenne sur les rotations du système des coordonnées). L'effet de la pré-moyenne complète a une signification simple : les fluctuations de μ_A sont principalement dues à des variations d'orientation des liaisons. De plus, nous avons constaté que l'écart-type de μ_A, $\delta\mu_A$, est presque indépendant de la température. Les résultats obtenus sont présentés sur les Fig. 1 et Fig. 2 (où la nouvelle façon de calcul est notée avec un exposant "(2)" et l'ancienne avec un exposant "(1)").

   (iii) Nous avons développé une théorie quantitative [6] prédisant $\delta\mu_F$ en termes du module de relaxation $G(t)$ qui est en excellent accord avec les résultats de simulation en régime liquide. L'approche théorique est basée sur l'approximation Gaussienne des fluctuations de la contrainte, qui est asymptotiquement exacte pour les grands systèmes, $V \to \infty$.

De plus, il a été montré que le plateau de $\delta\mu_F$, observé à basse température, diminue fortement à mesure que le système s'agrandit. Cet effet est attribué à une structure amorphe très hétérogène des liquides vitreux surfondus conduisant à une variance nettement non-Gaussienne des modules de cisaillement, $\mathrm{var}\,(\mu_F)_{\mathrm{nG}} \approx \mathrm{var}\,(\mu)_{\mathrm{nG}}$, qui diminue avec la taille de système comme $1/V^{\alpha}$ où $\alpha < 1\,(\alpha \approx 0.7 \pm 0.1)$.

2. **Système de liquides simples bidimensionnels**

   (i) Nous avons fait une comparaison entre les résultats déjà existants, obtenus en utilisant la méthode de Monte Carlo (MC), et avons effectué une analyse des données des nouvelles simulations MD en utilisant des configurations équilibrées par MC (obtenues par le Dr. Wittmer dans notre équipe). Les modules μ, μ_A, leurs fluctuations $\delta\mu$, $\delta\mu_A$, et la fonction de réponse $G\,(t)$ ont été obtenus, analysés et résumés. Il a été montré qu'ils présentent un comportement assez similaire à celui du système d'oligomères étudié auparavant.

   (ii) Bien au-dessus de T_g nous avons constaté que la relation entre la compressibilité et le facteur de structure statique $S\,(q)$ est fortement violée et que la chaleur spécificque dépendante du temps, $c_v\,(t) = C_V(t)/N$, présente une queue en loi de puissance pour des temps longs, ce qui est montré sur la Fig. 4.7. En outre, dans le régime liquide, le facteur de structure dynamique $S\,(q,t)$ montre une relaxation en deux étapes à faibles vecteurs d'onde, comme le montre la Fig. 7.

   (iii) Pour étudier plus directement la relaxation des contraintes de cisaillement, nous avons analysé $C_{\alpha\beta\gamma\delta}\,(\boldsymbol{q},t)$ à différents vecteurs d'onde $\boldsymbol{q}$. Les données numériques de la MD montrent un excellent accord quantitatif avec les résultats théoriques obtenus avant [9] à la fois au-dessus et en dessous de la T_g.

   Les résultats pour $C_2\,(t) = C_{2222}\,(\boldsymbol{q},t)$ (de l'équation 1) pour $q = 2\pi/L$ (où $L \approx 100$ est la dimension linéaire de la boîte de simulation) sont présentés sur la Fig. 5: ils se superposent presque exactement dans les deux régimes de température. Nos nouvelles données indiquent également que la corrélation des contraintes décroît en $1/r^2$ avec la distance r en accord avec les résultats de simulation précédents [11] et les prédictions théoriques [9].

Contents

List of Symbols

N	total number of particles in a system
c	number density of a system
V	volume of a system
v	specific volume of a system
W	statistical weight
S	entropy
ΔS	excess entropy
Γ	speed of cooling or cooling rate
$G(t)$	shear relaxation modulus
G_∞	infinite frequency shear modulus
$C(t)$	time correlation function of shear stress
T_g	glass-transition temperature
T_m	melting temperature
T_0	Vogel-Fulcher temperature
T_K	Kauzmann temperature
η	viscosity
μ	shear modulus
μ_A	affine shear modulus
μ_F	fluctuation modulus
$\mu_F^{(\mathrm{G})}$	Gaussian contribution to the fluctuation modulus
$\mu_F^{(\mathrm{nG})}$	non-Gaussian contribution to the fluctuation modulus
μ_0	ensemble- and time-averaged squared shear stress
μ_1	square of the ensemble- and time-averaged shear stress
C_p	heat capacity at constant pressure p
c_p	specific heat at constant pressure p
τ_α	structural relaxation time

τ_β	beta relaxation time
Δt	simulation time
τ_∞	asymptotic relaxation time at high T
σ	stress of a system
γ	strain of a system
E_a	activation energy
m	fragility parameter
ξ_s	static correlation length
$\boldsymbol{q}$	wave vector
$S(\boldsymbol{q})$	static structure factor
$g(r)$	radial distribution function
$S(\boldsymbol{q}, t)$	dynamical structure factor
$C_{\alpha\beta\gamma\delta}(\boldsymbol{q}, t)$	full stress correlation function
$u_{\mathrm{LJ}}(r)$	Lennard-Jones potential
$u_{\mathrm{b}}(r)$	harmonic or bond potential
Q	thermal inertial coeficient
s	additional degree of freedom for the heat bath
p_s	conjugate momentum of s
ξ	friction coefficient
ζ	expansion rate
$K_b(t)$	time-dependent bulk compression modulus
$K(t)$	longitudinal modulus
$M(t)$	mixed modulus
η_A	affine dilatational elasticity
η_F	total pressure variance
$C_b(t)$	total pressure autocorrelation function
ν	Poisson's ratio
K^*	long-time limit of the time-dependent longitudinal modulus
M^*	long-time limit of the time-dependent mixed modulus
$\sigma_{\alpha\beta}^{\mathrm{micro}}(\boldsymbol{r})$	space-resolved microscopic stress tensor at point $\boldsymbol{r}$
$\hat{\sigma}_{\alpha\beta}^{\mathrm{micro}}(\boldsymbol{q})$	microscopic stress tensor at wave vector $\boldsymbol{q}$
C_T	component C_{1212} of the full stress correlation function
C_2	component C_{2222} of the full stress correlation function

$C_{\parallel}$	component C_{1111} of the full stress correlation function
$C_{\perp}$	component C_{2211} of the full stress correlation function
δ_P	polydispersity index of particle sizes (PDI)
n_q	maximum magnitude of $\boldsymbol{q}$
c_T	transverse (shear) sound velocity
c_L	longitudinal (shear) sound velocity

Chapter 1

Introduction

Glass is one of the most ancient materials known to human. For example, in Stone Age, obsidian (natural glass, formed by the rapid solidification of lava without crystallization) was used for making first weapons and processing cutting tools.

The history of first glassy objects made by mankind dates back to ancient time. The earliest known glass objects, of the mid third millennium B.C., were found in Egypt (green beads, well known as Egyptian faience) and Easter Mesopotamia (Mesopotamian cylindrical glass seal). Glass had been produced by melting sand, sea shells and natron from dry saline lake beds [14].

Since that period, glassy products became more and more expensive during time. Another amazing achievement was the discovery of stained glass which is colored by adding metallic salts, oxides and metal nanoparticles. In the XV century A.D. Venice became one of the monopolists in glass production, and the whole world became familiar with Venetian glass [14, 15].

Now it is hard to imagine our lives without glassy products. We use glass to make screens for such devices as smartphones or tablets, people buy perfumes in glassy bottles and drink from glassy cups.

But not only price and rarity were among the main reasons of taking an interest in glass-forming studies. From physical point of view, glass has also very interesting dynamical and mechanical properties. One of the popular examples is "Prince Rupert's drops" [16, 17].

Let us briefly describe the main idea of this phenomenon. After a drop of a molten glass falls into a cold water, it solidifies into a tadpole with a thin tail. If someone tries to smash the head of such construction with a hammer, the glass does not break. But if

the point of the impact is shifted to the tail then the tadpole will break into small pieces. That happens because the outer layer of the tadpole is cooled so fast that it hardens immediately and forms some kind of a shell with hot glass inside (where the head or the core of the tadpole is located). As the inner part is still cooling, the core is exposed to the tensile stress on its inner surface unlike the outer layer where compressive residual stress is acting. After a crack enters the interior tension zone, it multiplies, all stresses are released and the tadpole explodes. This example shows that preparation techniques can have an important influence on the behavior of the resulting glassy material. Modern technology exploits this avenue, for instance for glasses with extraordinary scratch resistance ("Gorilla glasses") used for smartphones.

Looking at the structure of glass we can see that it is disordered as a liquid, in spite of having a very high viscosity like a solid. When a glass-forming liquid is cooled down it becomes hard and brittle, like a solid crystal.

A deep understanding of the processes occurring when a liquid is cooled down into a glass is required in order to fine-tune the properties of glassy materials for practical needs. The present study of dynamical and static correlations in liquids on approach to the glassy state and of their other properties is related to this goal. This attracts our interest to work on this topic.

1.1 Review of important physical properties of glasses

1.1.1 What is a glass and its distinctions from liquids and solids

When a viscous liquid is cooled fast enough so that crystallization is avoided, the system can reach a metastable state known as supercooled liquid. At high temperatures the equilibrium relaxation time is roughly $\tau \approx 10^{-13} - 10^{-9}$s and a viscosity is $\eta \approx 10^{-3} - 10^{2}$Poise. As soon as the glassy state is reached the relaxation time and the viscosity drastically increase $\tau \approx 10^{2} - 10^{3}$s and $\eta \approx 10^{12} - 10^{13}$Poise [1,2,18]. The temperature at which such values are observable is called the glass transition temperature T_g. As T_g is not a precisely defined quantity it can be empirically determined in different ways based on the methods which will be discussed in subsection 1.1.2.

In the metastable phase the supercooled liquid is structurally disordered and a number of the slow structural relaxation processes can be observed. Such processes are related to the dynamic glass transition and are not observed as precursors of the first-order phase

transition to the crystal. As the time needed for a glassy system to reach the equilibrium is higher than the experimental time scale for $T < T_g$, glasses are often considered as non-equilibrium systems. Based on that, observable properties will change very slowly and depend on the time that passed from the moment when the system was cooled below T_g. This process is known as aging [2, 18].

One of the ways to avoid crystallization in a glass-forming liquid is continuous and fast enough cooling. For this reason it is necessary to define a parameter which represents the speed of cooling. Such quantity is known as the cooling rate Γ [19–21] and has the dimension [Temperature/time]. Let us define it more precisely. Supposing that an experiment starts at the initial temperature T_i, which is well above T_g, we continuously cool the liquid with some speed $T(t) = T_i - \Gamma t$ to a final temperature T_f at time $t = t_f$, which is below T_g:

$$\Gamma = \frac{T_i - T_f}{t_f} \tag{1.1}$$

Temperatures T_i and T_f should be sufficiently close to each other so that such quantities as volume V at constant pressure p and number of particles N for liquid vary essentially linear with temperature in the chosen interval [21].

Single component systems where crystallization can be avoided and thus a glassy state achieved are polymer or oligomer systems on cooling [6, 7, 18], hard-sphere (HS) colloidal systems on pressure increase, polydisperse HS systems on cooling or pressure rise.

Glass can be formed from different elements and chemical compounds [22]: oxides like SiO_2, metallic alloys like $Au_{75}Si_{25}$ [23] and from the polymeric organic compounds like polypropylene (PP) $(C_3H_6)_n$ or polyvinyl chloride (PVC) $(C_2H_3Cl)_n$. Various physical properties for a few glass-forming materials are shown in Table 1.1.

Table 1.1: Comparison of the density ρ, the glass transition temperature T_g and Young's modulus E_Y in SiO_2 and rigid PVC.

	ρ, g/cm^3	T_g, K	E_Y, GPa
SiO_2 [24, 25]	2.18-2.27	1450-1475	60.1-63.5
Unplasticized (Rigid) PVC	1.35-1.5	333.15-373.15	2.4-4

To understand the nature of the glass transition it is common to use a concept of potential energy landscape which will be discussed in more detail in subsection 1.2.2. According to the energy landscape theory, at high temperatures a system is able to explore

all possible configurations. In other words it means that at high temperatures the system is ergodic. When the system is cooled towards T_g, experimental time scales become smaller than a time which system needs for exploring phase space. That leads to the fact that the system is confined to a group of local energy minima in the phase space, i.e. the system becomes non-ergodic since it cannot explore the whole phase space [2]. The potential energy landscape includes a set of energy minima which are called "basins". Within this framework two relaxation processes occur - fast or β relaxation and slow or α relaxation processes. The first corresponds to local transitions between neighboring minima and the second one to the cooperative transitions between distant minima providing structural relaxation. A schematic representation of the relaxation processes is shown in Fig. 1.8.

One of the main keys for investigating the properties of the supercooled liquid is understanding its viscoelastic behavior. Constraints which are commonly used in such studies are small strains γ and stresses σ. Viscoelastic behavior is represented as a time-dependent response of a material to a stress or a strain. It can be illustrated using various mechanical models. One of the commonly used representations is one spring and one dashpot arranged in series known as the Maxwell model. In this model a spring represents Hookean or elastic behavior and a dashpot represents viscous or Newtonian behavior.

An important rheological characteristic is the shear stress relaxation modulus or response function $G(t)$ which defines the relaxation of shear stress at time t after a small step of shear strain and it can be measured for liquids, solids and glasses. A schematic representation of the behavior of $G(t)$ for glass, liquid and glass transition region is represented in Fig. 1.1. From the Maxwell model it is known that $G(t) = G_\infty \exp\left(-\frac{t}{\tau_\alpha}\right)$ where G_∞ is the zero time shear modulus and τ_α is the structural relaxation time. This equation and its derivation will be discussed in subsection 1.2. At high temperatures an exponential decay is expected as it is shown in Fig. 1.1 (for simple liquids and times longer than the regime of microscopic dynamics). With lowering temperature the relaxation time τ_α rapidly increases, the decay of $G(t)$ gets slower and becomes non-Maxwellian.

From Fig. 1.1 it can be seen that in the glass transition region (middle curve) the relaxation modulus $G(t)$ shows a shoulder which gets longer and gradually transforms into a plateau as temperature T decreases towards T_g. In the glass $G(t)$ does not decay on experimental time scales (top curve). So the (long-time) decay of the relaxation modulus becomes entirely non-exponential [2] in the regime of the supercooled liquid.

Investigation of the behavior of the shear relaxation function $G(t)$ for different tem-

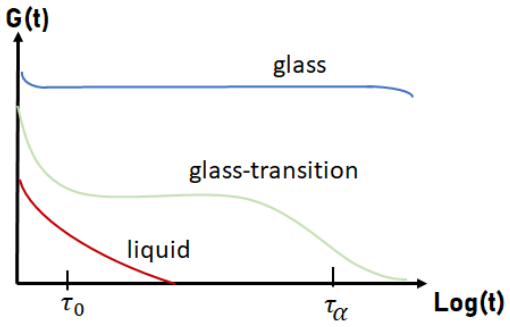

Figure 1.1: The schematic presentation of $G(t)$ as a function of measurement time in $\log(t)$: the glass region $T \ll T_g$ (top curve), the region of the glass-liquid transition (middle curve) and in the liquid state $T \gg T_g$ (bottom curve).

peratures is one of the main goals of the current thesis. More detailed explanation of such dependence for different systems will be given in Chapters 3 and 4.

The values of the relaxation time and viscoelastic properties are not the only differences between glass and liquid or solid (crystalline) phases. It is also important to analyze the difference of the states based on their structure.

A schematic representation of a system for 3 states — crystalline solid, liquid and glass — is shown in Fig. 1.2. There T_m is the melting temperature, at which the first-order phase transition between liquid and crystal occurs, and T_g is the dynamic glass transition temperature, at which the relaxation time exceeds the experimental time of 10^3s [2]. The quantity t_0 is the time which a particle needs to move across its own size. It is hard to distinguish between a liquid and a glass because of a disordering in the structure of both phases. On the other hand in the case of a crystal the particles show ordering and the difference is obvious.

Before starting to discover how the relaxation occurs in all 3 cases, let us define basic mechanical properties of each system. For solids the elastic shear modulus μ is defined as the ratio of the shear stress σ_{xy} to the shear strain γ. As for a liquid $\mu = 0$ the ratio of shear stress σ_{xy} to shear strain rate $\dot{\gamma}$, $\gamma \to 0$, is its viscosity η_l. For an ideal crystal a steady shearing is impossible, $\dot{\gamma} = 0$ and that gives an infinite value for the viscosity.

If an observation time t is long enough, $t \gg t_0$, the structure of the three states will show significant differences. In the solid phase atoms still show ordering and vibrate around their regular equilibrium positions while in the liquid state the structure does not show any ordering anymore. On the other hand in glasses atoms exhibit similar behavior to that one of the solid state (they vibrate around their equilibrium position) despite

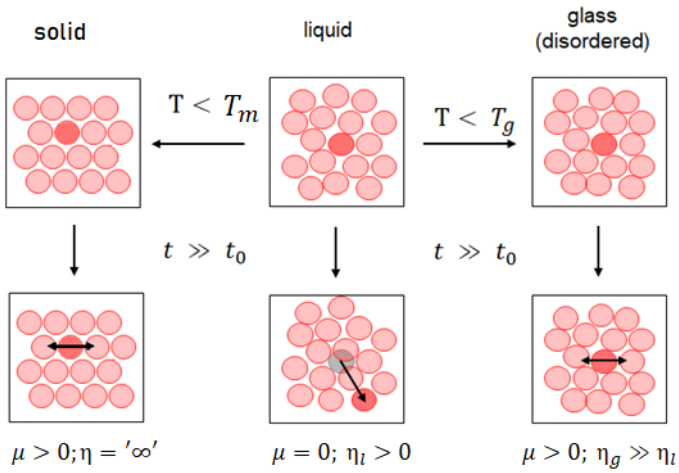

Figure 1.2: Schematic representation of a system in the 3 states: crystalline solid, liquid and glassy phase. Here T_m is the melting point and T_g is the dynamic glass transition temperature. Viscosity for the solid, liquid and glass is noted as η, η_l and η_g respectively and the elastic shear modulus is μ for all cases. t_0 is the time which a particle needs to move across its own size. When a liquid is cooled towards T_g, the values for the shear modulus μ and the viscosity η_g start to increase and the liquid-glass transition occurs. For the glass η_g is not infinite as it is for an ideal crystal but it is still much larger than in the case of the liquid, $\eta_g \gg \eta_l$. Let us wait long enough so that the measurement time t is much larger than the time t_0, and look at the structure of each state again. For crystals one can see that atoms show ordering and vibrate around their regular equilibrium positions. In liquids atoms are able to move far. However, for glasses despite the similar disordered structure atoms are not able to move far.

having the same disordered structure as liquids.

When a liquid is cooled towards T_g, its viscosity η_l strongly increases and an intermediate time windows open where $G(t)$ is close to a plateau and thus shows solid-like ("elastic") features. Therefore, viscoelasticity emerges upon cooling towards the glass transition. On the other hand, for a glass η_g is not infinite as it is for a crystalline solid but much larger than in the case of the liquid, $\eta_g \gg \eta_l$. This combination of such different features is what makes glasses an interesting and important object to explore. Here a key question is whether $G(t)$ and μ can be related and what their respective T dependence is [3–6]. Within the PhD thesis framework the temperature dependence of the shear modulus was studied, simulated by using Molecular Dynamics (MD) method and analyzed as will be discussed in more detail in Chapters 3 and 4.

1.1.2 Determination of the glass transition temperature

As was mentioned in the previous subsection, T_g is the temperature at which system reaches state when its viscosity is $\eta \sim 10^{13}$Poise or where the structural relaxation time drastically increases to $\tau_\alpha \sim 10^3$s [1, 18].

First of all it is necessary to mention that the dynamical glass transition temperature T_g does not correspond to a thermodynamic phase transition. The T_g is not a precise point and can be defined in different ways.

The temperature of glass transition T_g also depends on how fast the system is being cooled down. In further subsection 1.2 it is shown in detail that T_g has a weak logarithmic dependence on the cooling rate and slower cooling produces a lower value for T_g.

One way for the empirical definition of T_g is to record values of the volume during cooling and plot the obtained data versus temperature [6, 7, 26]. Let us start from the schematic representation of the dependence of the specific volume $v = \frac{V}{N}$ on temperature for the liquid-crystal transition which is shown in Fig. 1.3. One can see a sharp change of volume at the melting temperature T_m. Such "jump" occurs due to the first-order phase transition, when a discontinuity appears in a first derivative of the Gibbs energy G: $\left(\frac{\partial G}{\partial p}\right)|_T = V$. Because of the similarity of structure of the glassy system to that of the liquid, the volume V changes continuously during cooling and such sharp change does not occur. The glass transition temperature can be defined from the intersection of the tangent lines on the plot of specific volume v vs. temperature T. As glass 1 was formed due to the faster cooling than glass 2 and according to the statements from subsection 1.2.1, the intersection of the tangent lines (blue lines) on Fig. 1.3 defines two glass transition temperatures T_{g1} and T_{g2}.

Another way to empirically define T_g is to determine it from a specific heat c_p measurement [26, 28]. The specific heat is the heat capacity per unit mass $c_p = \frac{C_p}{m}$. The heat capacity is related to the entropy as $C_p = T\left(\frac{\partial S}{\partial T}\right)|_p$. Let us describe such observation in more detail based on the schematic representation of $c_p(T)$ dependencies which is shown in Fig. 1.4.

Based on the statements above the glass is a non-equilibrium and non-ergodic system. That means that experimental time is smaller than the time which a glassy system actually needs for exploring the phase space. The system becomes confined to the local energy minima in the phase space with a reduced number of degrees of freedom as compared to those which are accessible to the system at equilibrium and provide a contribution to

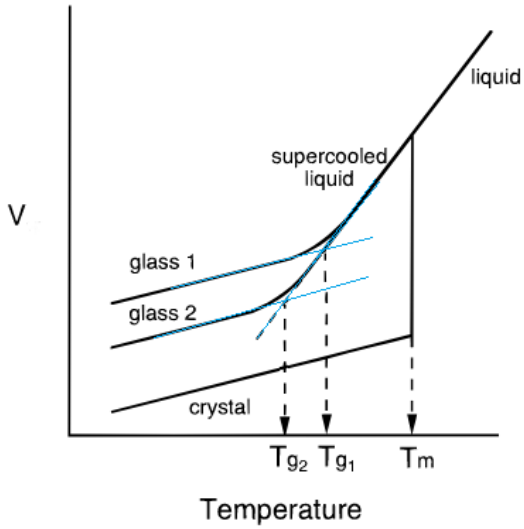

Figure 1.3: The schematic representation of the temperature dependence of the specific volume v (volume per particle $v = \frac{V}{N}$) at constant pressure. Glass 1 was formed due to the faster cooling than glass 2. As will be discussed in subsection 1.2.1, the glass transition temperature T_g depends on the cooling rate Γ, so for glass 1 and glass 2 two different temperatures T_{g1} and T_{g2} are obtained. The intersection point of the tangent lines (blue lines) of the glassy state back to the supercooled liquid line defines the temperature of glass transition. This plot was copied from ref. [26].

the specific heat. This explains why c_p is drastically decreasing on cooling near T_g (and reaches approximately the same value as it has in the crystal phase). So a sharp drop is observed in the glass transition region. Thus T_g can be defined as the temperature, at which the specific heat c_p has accomplished the sharp drop. The schematic representation of the behavior of $c_p(T)$ for 2 glasses is shown in Fig. 1.4. The difference between the two samples is only in the speed of cooling. As glass 1 was formed due to the faster cooling than glass 2, the temperature T_{g1} at which the system starts to exhibit the glass transition (dashed curve) is higher than T_{g2} for the second glass. One more feature which can be seen from the Fig. 1.4 and from the statement above is that due to the structure properties at low temperatures the specific heat for glass is very close to that of the crystal [2, 27]. It is also important to note, that $c_p(T)$ at the melting temperature T_m shows a discontinuous behavior due to the fact that at T_m the system exhibits the first-order phase transition and by analogy with volume the entropy shows a sharp change.

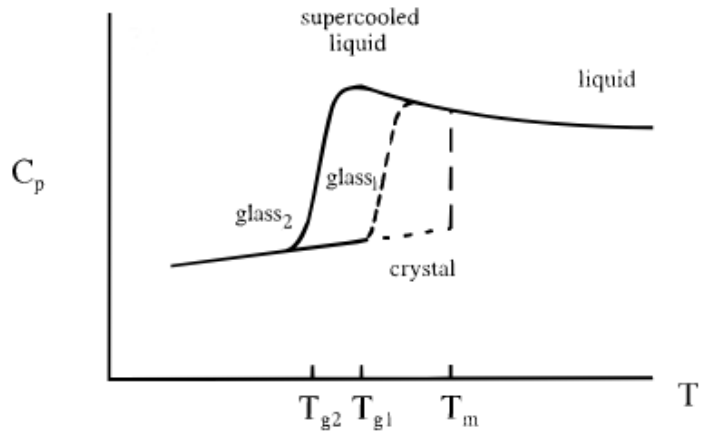

Figure 1.4: Temperature dependence of the specific heat c_p at a given pressure p. Glass 1 was formed due to the faster cooling than glass 2. Such difference in the speed of cooling shows up when the specific heat drops at the T_{g1} for the first sample and at T_{g2} for the second one. When the liquid is cooled towards T_g, the specific heat c_p for the glass shows a sharp drop in a region near T_g. It happens because below T_g the system is not ergodic anymore, which means that the system does not have enough time to explore the phase space and the configurational degrees of freedom which gave a significant contribution to the specific heat in the liquid regime are not accessible anymore [2, 27]. The temperature of the glass transition T_g is defined as the temperature, at which specific heat has the sharp drop. This plot was copied from ref. [26].

1.1.3 Colloidal glasses

Colloidal dispersions are indispensable for many technologically important applications [29, 30]. However, the main problem is that the colloidal particles tend to aggregate due to van-der-Waals attraction, hence stabilization is required. It is known [29] that a certain amount of free polymer added to a colloidal system may enhance its stability (so-called "depletion stabilization"). This effect is opposite to the well understood depletion attraction which was intensively studied in the context of arrest scenarios (attractive glass versus gel transitions) [31]. Recent theoretical studies [32–35] show that the depletion stabilization effect could open new ways to control colloid stability.

Numerous applications of colloidal systems (as paints, gels, glues, etc.) hinge on their dynamical properties, in particular, their rheological behavior [36, 37]. The most important and fundamental dynamical effect is related to the ability of colloidal dispersions to vitrify rather than crystallize at high enough volume concentration (or on cooling below the glass transition temperature T_g). In the concentration or temperature regime preced-

ing the glass transition, these systems exhibit a dramatic increase of the shear viscosity and relaxation times, unusually slow and strongly nonlinear viscoelastic response (for shear rates faster than the relaxation time), and other remarkable rheological properties in the glassy phase (including aging and prehistory-dependent structure and relaxation dynamics). All of this behavior is also typical of supercooled liquids. Much progress had been done recently in quantitative description of nonlinear rheology of certain colloidal systems [38–41].

One of the important parameters for investigation of colloidal glass transition is the mean-square displacement (MSD) and diffusion coefficient D. The colloidal particles execute Brownian motion due to random and frequent collisions with solvent molecules. Because collisions are random in orientation and magnitude the average particle displacement in a given direction is zero [42]. But the motion during time t is well described by the mean-square displacement:

$$\mathrm{MSD}\,(t) = \frac{1}{N}\sum_{i=1}^{N}\left\langle \left(\boldsymbol{r}_i\,(t+t_0) - \boldsymbol{r}_i\,(t_0)\right)^2\right\rangle, \tag{1.2}$$

where $\boldsymbol{r}$ is the position of a colloidal particle, N is the number of colloidal particles, t_0 is an initial time, and brackets $\langle ... \rangle$ correspond to an average over the initial time t_0. For times t longer compared to the relaxation time, MSD increases linearly with time for a liquid. In this case the slope of MSD is proportional to the diffusion coefficient D such as:

$$\mathrm{MSD}\,(t) = 2dDt, \tag{1.3}$$

where d is the dimension of the system.

For a spherical particle the diffusion coefficient is given by the Stokes-Einstein relation:

$$D = \frac{k_B T}{3\pi\eta_s\sigma}, \tag{1.4}$$

where η_s is the viscosity of the solvent, σ is a diameter of the particle. Eq. 1.3 and 1.4 are applicable only for a diffusing sphere much larger than the molecules comprising the fluid [2]. The time which particle needs to diffuse over a distance comparable to its own radius is:

$$\tau_d = \frac{3\pi\eta_s\sigma^3}{2k_B T} \tag{1.5}$$

The volume fraction ϕ can be found from relation $\phi = \frac{N}{V}\frac{\pi\sigma^3}{6}$, where V is the volume of a system. Volume fraction is a dimensionless analogue of a particle number density [42]. Below $\phi = 0.494$ [42, 43] the sample is in a liquid phase. Colloidal samples with low polydispersity can crystallize for $\phi < \phi_g$, where $\phi_g \sim 0.58$ [42–44] is the glass transition volume fraction. For colloids the long time self diffusion coefficient $D = \lim_{t\to\infty} \frac{\text{MSD}}{2dt}$ goes to 0 when $\phi \to \phi_g$ and such behavior can be used as the way to define the glass transition. A lot of progress has been made in the studying of the glass transition phenomena of colloids based on the comparison between experimental, theoretical and simulation works [33, 43, 45–48]. For example, by using the confocal or video microscopy it became possible to directly visualize the dynamics of the colloidal particles. All these results are very important for further investigations.

1.2 Basic phenomenological laws and some theoretical concepts in glass dynamics

1.2.1 Strong and fragile glasses

It is known that not only macromolecular systems and biological objects such as muscles, blood vessels, human skin combine viscous and elastic properties but so do glass-forming and supercooled liquids. Viscoelasticity theory is the key to understanding the mechanical and viscous properties of a molecular system. These properties can be modeled by the Maxwell model, a schematic representation of which is shown in Fig. 1.5. It is a series of connected elastic and viscous elements: Hookean spring with a strain γ_e and a stress σ_e and Newtonian dashpot with a strain γ_v and a stress σ_v.

Figure 1.5: The schematic representation of a serial connection of a Hookean spring and a Newtonian dashpot.

For the Maxwell model the total strain of the system is additive $\gamma = \gamma_e + \gamma_v$ and the total stress of the system is uniform $\sigma = \sigma_e = \sigma_v$. Also in this model stresses can be expressed via the viscosity and shear modulus with such equations: $\sigma_e = G_\infty\gamma_e$ and $\sigma_v = \eta\dot{\gamma}_v$. After rearranging those expressions and using the idea that Maxwell model is

subjected to a constant strain γ_0 at time $t = 0$, for which the initial value of $\sigma = \sigma_0$ and the shear modulus G_∞ (at time $t = 0$) is G_∞, the stress response can be obtained by:

$$\begin{aligned} &\dot{\gamma} = \dot{\sigma}/G + \sigma/\eta = 0, \\ &\sigma(t) = \sigma_0 \exp\left(-\frac{G_\infty}{\eta} t\right), \\ &G(t) = \sigma(t)/\gamma_0 \end{aligned} \tag{1.6}$$

From eq. 1.6 for Maxwell liquids, we can define an intimate relation between viscosity and (local but collective) α relaxation time τ_α:

$$\tau_\alpha = \frac{\eta}{G_\infty} \tag{1.7}$$

For the glassy system, upon cooling towards T_g, the structural relaxation time shows a drastic increase over 14 orders of magnitude [18]. The relaxation time τ_α can be determined by dielectric spectroscopy, monitoring the reorientational dynamics of electrical dipoles associated to the particles, or by the dynamical structure factor $S(\boldsymbol{q}, t)$ at the first peak of $S(\boldsymbol{q})$ related to the local packing in the system.

For the characterization of the glass transition phenomenon it is important to know how the viscosity η, which is proportional to the the structural relaxation time, changes with temperature T.

Let us introduce the temperature dependence (scaled over T_g) of the viscosity η for glass-former liquids such as SiO_2, glycerol and *o*-Terphenyl which is represented in Fig. 1.6. One can gather from Fig. 1.6 that some liquids like SiO_2 show approximate linear dependence or Arrhenius behavior, which can be expressed by:

$$\tau_\alpha(T) = \tau_\infty \exp\left(\frac{E_a}{k_\mathrm{B} T}\right), \tag{1.8}$$

where E_a is an activation energy, τ_∞ is the pre-exponential relaxation time, which depends on the material and is roughly temperature independent, and k_B is the Boltzmann constant.

The similar expression can be applied for the determination of a viscosity:

$$\eta(T) = \eta_\infty \exp\left(\frac{E_a}{k_\mathrm{B} T}\right), \tag{1.9}$$

where $\eta(T)$ is the viscosity and η_∞ is a roughly temperature independent constant.

From Fig. 1.6 it can be seen that some liquids (glycerol and *o*-Terphenyl) exhibit super-Arrhenius behavior, which is not linear at all. In this case the T-dependence of the

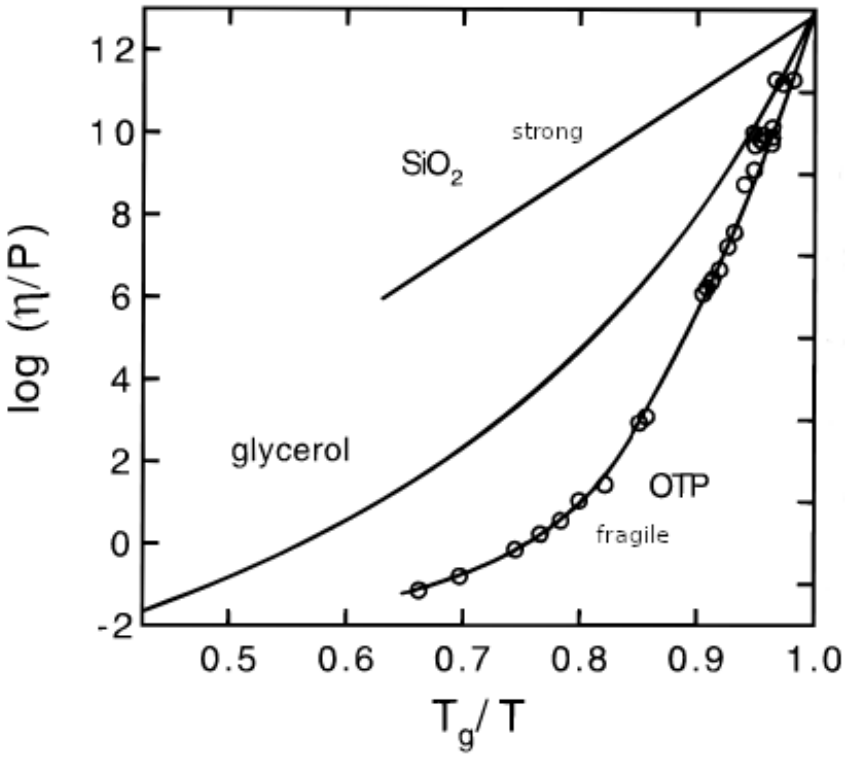

Figure 1.6: Temperature dependence (scaled by T_g) of the logarithm of viscosity for SiO_2, glycerol and *o*-Terphenyl above T_g. Strong liquids like SiO_2 show approximate linear dependence (or Arrhenius behavior) and fragile liquids (glycerol and *o*-Terphenyl) exhibit super-Arrhenius behavior, which is not linear at all. The plot for viscosity (in Poise or P) was copied from ref. [26].

relaxation time can be fitted by the Vogel-Fulcher-Tammann (VFT) equation:

$$\tau_\alpha(T) = \tau_\infty \exp\left(\frac{B}{T - T_0}\right), \tag{1.10}$$

where τ_∞ is the asymptotic relaxation time at high T, B is the material characteristic temperature scale, T_0 is the "Vogel-Fulcher" temperature at which the relaxation time appears to diverge [2, 49, 50].

Moreover, eq. 1.10 can be re-expressed in terms of viscosity [1]:

$$\eta(T) = \eta_\infty \exp\left(\frac{B}{T - T_0}\right), \tag{1.11}$$

To distinguish between these cases Angell [51, 52] proposed to label liquids with Arrhenius behavior as ***strong***, and those with super-Arrhenius behavior as ***fragile***.

A fragility parameter m characterizes the slope of the viscosity (or a structural relaxation time [53], τ_α) vs. temperature above T_g. It can be used to classify glass-forming

liquids and is expressed as:

$$m = \frac{d \ln(\eta)}{d\left(\frac{T_g}{T}\right)}|_{T=T_g} \tag{1.12}$$

The fragility parameter m is large for most liquids, but it takes the highest values for fragile liquids. For example, the typical values for the fragility parameter m [53] are $m_{\text{o-Terphenyl}} = 76$ (fragile liquid), $m_{\text{glycerol}} = 53$ (moderately fragile liquid) and $m_{SiO_2} = 20$ (strong liquid). Moreover, the "moderately fragile liquids" are commonly referred to as "intermediate liquids".

Such names as ***strong*** *and* ***fragile*** do not have anything in common with mechanical properties of the material. For example, fragility has no direct relationship with the brittleness of a material.

After rewriting eq. 1.10 for $T = T_g$ and using the criterion $\tau_\alpha(T_g) \approx t^*$, where $t^\star$ is the time of cooling through the region around T_g where τ_α increases by a factor of 2, $t^\star \approx \hat{C}\Gamma^{-1}$ [18, 21, 54–56], where $\hat{C}$ is an empirical constant which has the dimension of temperature and is related to the E_a ($B = E_a/k_B$), k_B and T_g. From equations $\hat{C} = \Gamma\tau_\alpha$ and $\frac{d\tau_\alpha}{dT} = -\frac{1}{\Gamma}$ one can see that $\hat{C}$ is proportional to B [57]. The equation which gives the dependence of temperature of T_g on cooling rate Γ will be [18, 54]:

$$T_g = T_0 + \frac{B}{\ln\left(\frac{\hat{C}}{\Gamma\tau_\infty}\right)}, \tag{1.13}$$

where T_0 is the "Vogel-Fulcher" temperature. As eq. 1.13 shows, T_g has a weak logarithmic dependence on cooling rate and slower cooling produces a lower value for T_g.

By varying the parameter T_0 in eq. 1.10, we can describe the typical behaviors of liquids: from strong ($T_0 \approx 0$) to a more fragile-like with higher T_0 [2].

1.2.2 Thermodynamic aspects

To understand the complex dynamics of a supercooled liquid it is important to consider the influence of the system's energy landscape on the relaxation processes it displays [58].

Let us consider a system of N structureless particles, without internal orientational and vibrational degrees of freedom. A potential energy of the system as a function of particle coordinates is called the energy landscape and it is a $(3N + 1)$-dimensional object. The topographical view of the energy landscape is represented in Fig. 1.7.

The innumerous potential minima are called "basins". From the energy landscape, quantities of interest are the number of inherent structures (or potential minima) of a given depth and the nature of the saddle points separating neighbouring minima [1,2,59].

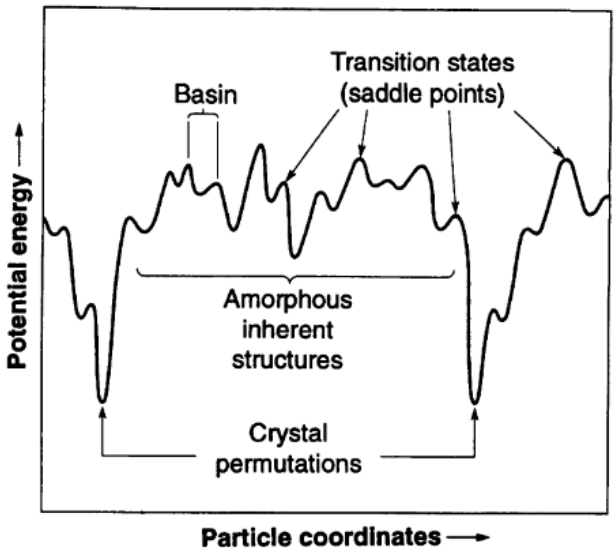

Figure 1.7: Schematic representation of an energy landscape as a function of all coordinates. This plot was copied from ref. [59].

The potential energy landscape involves a set of minima and in order to visit different minima in the attempt of being ergodic the system has to cross the barriers separating these minima [2]. For high temperatures T, an access to most basins is possible due to kinetic energy. But, for low T, the sampling shifts to lower energies and transitions among basins become subject to considerable activation [58].

According to the potential energy landscape scenario that was briefly discussed in section. 1.1 and defined in ref. [59], we can say that the processes which occur due to the elementary relaxation between neighboring minima (or basins) are called β relaxation processes and the processes due to transitions from one profound basin (or "metabasin") to another are α relaxation processes. The schematic representation of such processes near T_g is shown in Fig. 1.8.

1.2.2.1 Entropy crisis

Let us remind the general formula to define the entropy

$$S = -k_B \langle \ln (p(x)) \rangle , \tag{1.14}$$

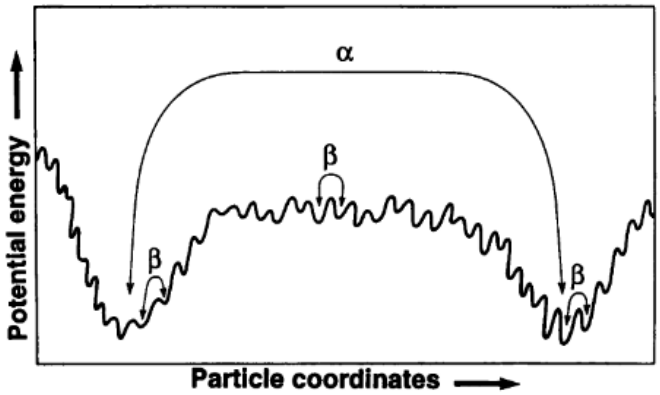

Figure 1.8: Schematic representation of an energy landscape as a function of all coordinates near T_g. The elementary transitions between neighboring minima correspond to the β relaxation process and the transitions between deep minima correspond to α relaxation process. This plot was copied from ref. [59].

where $p(x)$ is the probability (density) to find the microstate x and $\langle ... \rangle$ is the thermal average pertaining to the ensemble. According to the interpretation from the microcanonical ensemble, the entropy S is interpreted as the logarithm of the number of microstates W [60] compatible with the external constraints, e.g. $N = T = p = \text{constant}$. As $W > 1$, the entropy cannot be negative.

The entropy of a liquid decreases much more rapidly on cooling than that of a crystal. This feature is related to the fact that the heat capacity (for a given pressure p) for a liquid $c_p^l(T)$ is larger than $c_p^c(T)$ for a crystal and can be seen in Fig. 1.4 as well. Such difference occurs due to the reason that in the liquid regime configurational and vibrational degrees of freedom are active compared to the solid state where basically only vibrational contributions are significant [2]. For example for normal pressure, for water at $T = 300K$ $c_p^l(T) = 4.18\frac{kJ}{kgK}$ and for ice at $T = 273K$ $c_p^c(T) = 2.11\frac{kJ}{kgK}$ [27].

The rate of change of entropy with T at constant pressure is:

$$\left(\frac{\partial S}{\partial T}\right)|_p = \frac{c_p(T)}{T} \tag{1.15}$$

The excess entropy is the difference between the entropy of liquid S_l and crystal S_c:

$$\Delta S(T) = S_l(T) - S_c(T) \tag{1.16}$$

$\Delta S(T)$ is decreasing when the temperature T decreases. The dependence $\Delta S(T)$ vs. T for some samples normalized by their melting point T_m with a low-T extrapolation is shown in Fig. 1.9 (Kauzmann plot [27]).

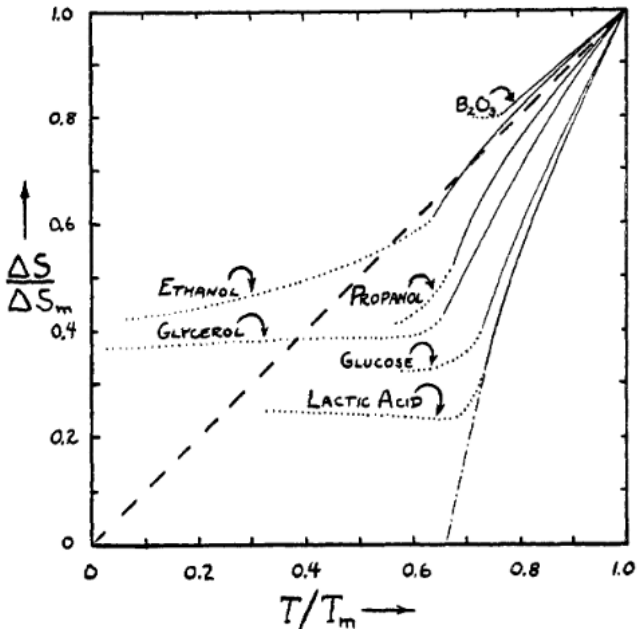

Figure 1.9: The low-T extrapolation of the excess entropy ΔS for various materials normalized by their value at melting point $\frac{\Delta S}{\Delta S_m}$ vs. $\frac{T}{T_m}$ proposed by Kauzmann. This plot was copied from ref. [27].

Kauzmann also showed that for some materials the extrapolated excess entropy could vanish at finite temperature [2,27].This temperature is called Kauzmann temperature T_K:

$$\Delta S\left(T_K\right) = 0 \tag{1.17}$$

For $T < T_K$, the entropy of the supercooled liquid $S_l\left(T\right)$ could become lower than the entropy of the crystal $S_c\left(T\right)$. This phenomenon is called the entropy crisis or Kauzmann's paradox because it hints at a negative entropy $S_l\left(0\right)$.

The entropy crisis does not violate the second law of thermodynamics due to the positive difference in chemical potentials $\Delta\mu$ between the supercooled liquid and the stable crystal at T_K [1]. It also does not violate the third law. This statement is described in more detail below.

1.2.2.2 Third law and configurational entropy

The third law was postulated by Walther Nernst and states that entropy of the system at absolute zero is a constant, which can be taken as zero.

Based on that, it is hard to say right away that Kauzmann's paradox really does not violate the third law, because the statement above does not allow for possibility of

negative value for excess entropy ΔS at $T = 0$.

Kauzmann introduced a way to eliminate the problems related to T_K. He postulated that each extrapolated equilibrium curve of the supercooled liquid is always interrupted by a kinetic spinodal at a temperature $T_{sp} > T_K$ [2,27]. Below T_{sp} the supercooled liquid is equilibrated into a crystalline phase and the extrapolated entropy of the liquid becomes irrelevant. Based on that, T_K must be a good estimation for how far a liquid can be supercooled before the glass transition occurs.

Within the framework of the potential energy landscape, the entropy S_l can be split into two terms [2]:

- S_v - vibrational contribution due to the short-time vibrational dynamics in the minima. It shows the amount of configurations within each minima. The vibration component of the amorphous minima is quite similar (but not identical) to the entropy of the crystal S_c, $S_v \approx S_c$;
- $S_{\text{conf}} = \frac{1}{N} \ln(n)$ - configurational contribution per particle [61], which is related to the number of different configurations (spatial arrangements of the particles). Here n is the number of amorphous minima visited by the system at equilibrium.

Eq. 1.16 can be rewritten in new terms:

$$\begin{aligned} S_l &= S_v + S_{\text{conf}} \approx S_c + S_{\text{conf}}, \\ \Delta S(T) &= S_l(T) - S_c(T) \approx S_{\text{conf}} \end{aligned} \tag{1.18}$$

The excess entropy ΔS is roughly equal to the configurational entropy S_{conf}. Based on the eq. 1.17, T_K is the temperature, at which the configurational entropy becomes negligible. One of the ways to avoid the Kauzmann's paradox is to assume a thermodynamic phase transition from the supercooled liquid to a new amorphous phase at T_K [2]. This new amorphous phase is called "ideal glass" [61,62]. As the glass transition occurs earlier than the system reaches the Kauzmann's temperature $T_g > T_K$, the entropy crisis is avoided [63,64] so that there is no contradiction with the third law of thermodynamics.

1.2.3 Link between kinetics and thermodynamics of glasses

Let us consider a system that is finite and has N particles with short-range interactions. In order for the system to get relaxed, a finite number of particles w have to locally rearrange in the space. This number of particles is temperature dependent $w = w(T)$

and with decreasing temperature the number of such rearranging particles increases and the value for the energy barrier increases as well. In addition, the size of the region being rearranged becomes larger. This size can be associated with the static correlation length ξ_s [2].

Adam and Gibbs provided a concept of cooperative rearranging regions (CRR) [65]. CRR is the smallest region of the correlated particles, which can be rearranged independently from its surrounding. At low temperatures T, the relaxation process proceeds because of the rearrangement of the cooperative rearranging regions [2].

Each CRR has a typical number of particles w which are connected with its linear size ξ_s by a power law $w \sim \xi_s^d$, where d is the space dimension. The total number of CRR can be found from ref. [2, 65]:

$$M_{\mathrm{CRR}} = \frac{N}{w} \tag{1.19}$$

According to the Adam-Gibbs theory, a typical CRR can be found in a number of locally stable states Ξ, where $\Xi \geq 2$. The number of global states n is connected with Ξ via a relation $n = \Xi^{M_{\mathrm{CRR}}}$ and the configurational entropy per particle then can be expressed as [2]:

$$S_{\mathrm{conf}}(T) = \frac{\ln(\Xi)}{w(T)} \tag{1.20}$$

From eq. 1.20 it can be seen that with decreasing temperature $w(T)$ increases since the configurational entropy $S_{\mathrm{conf}}(T)$ decreases. A formula from Adam and Gibbs provides connection between relaxation time and configurational entropy using Arrhenius eq. from ref. [65]:

$$\tau_\alpha = \tau_\infty \exp\left(\frac{\tilde{C}}{T S_{\mathrm{conf}}}\right), \tag{1.21}$$

where $\tilde{C}$ is some constant [1, 2, 65].

For finding a relation between the configurational entropy and the difference of the specific heat Δc_p between liquid and crystal let us rewrite the eq. 1.18 and 1.15 and integrate them from T_K to T [2]:

$$\begin{aligned} \frac{dS_{\mathrm{conf}}(T)}{dT} &= \frac{\Delta c_p}{T} \\ S_{\mathrm{conf}}(T) - S_{\mathrm{conf}}(T_K) &= \int_{T_K}^{T} \frac{\Delta c_p}{T'} dT', \end{aligned} \tag{1.22}$$

where T_K is the Kauzmann temperature. The Adam-Gibbs theory implies that the Δc_p is weakly dependent on temperature and $S_{\mathrm{conf}}(T_K) = 0$, then the equation above takes

form:

$$S_{\text{conf}}(T) = \Delta c_p \ln\left(\frac{T}{T_K}\right) \tag{1.23}$$

Applying a Taylor expansion up to the first order, the eq. 1.23 will take form:

$$S_{\text{conf}}(T) \approx \Delta c_p \frac{T - T_K}{T_K} \tag{1.24}$$

By combining eq. 1.24 and 1.21, the relaxation time can be obtained as:

$$\tau_\alpha = \tau_\infty \exp\left(\frac{T_K}{\Delta c_p T(T - T_K)}\right), \tag{1.25}$$

or

$$\tau_\alpha = \tau_\infty \exp\left(\frac{\tilde{A}}{T - T_K}\right), \tag{1.26}$$

where $\tilde{A} = \frac{T_K}{\Delta c_p T}$.

Comparing eq. 1.10 and 1.26, the approximate value for T_K is T_0. This correspondence gives us a quantitative relation between dynamic and thermodynamic glass transition parameters [2].

1.2.4 Correlation properties of glasses

The nature of the structural glass transitions remains a mystery in spite of enormous and long-lasting efforts for its theoretical elucidation [2].

Some theories consider vitrification of liquids as a purely dynamical phenomenon associated with rapidly increasing structural relaxation time and viscosity on approaching T_g. Other approaches invoke the idea of an equilibrium phase transition underlying the vitrification. Indeed, it was shown that glass transition is normally accompanied by an abrupt change in measured thermodynamic quantities like specific heat, thermal expansion coefficient or isothermal compressibility [27, 51], pointing to a second-order phase transition. On the other hand, a first-order transition is hinted at by the discontinuous behavior of the shear elastic modulus near T_g. All experimental data seem to show that glassy systems are characterized by a disordered molecular arrangement [2]. Yet, the very idea that vitrification in liquids is accompanied by a qualitative structural change (reflected in static, equilibrium properties) proved to be very appealing theoretically [2, 27]. However, currently there is no definitive evidence, either experimental, or theoretical, or coming from computer simulations, on the existence of such a transition. There are, however,

indications that as a liquid approaches its glass transition, it shows a growth of some dynamical [2,66] or structural [2,67,68] length-scales. The origin of the glass transition thus remains a challenging problem and a subject of an active debate in soft-matter physics.

Vitrification in colloidal and supercooled-liquid systems can be viewed as a transition from liquid to amorphous solid state. Many mechanical (viscoelastic, rheological) properties of vitrifying liquids can be obtained by analyzing stress fluctuations in these systems. In particular, the time-correlation function of shear stress $C(t)$ is closely related to the shear relaxation modulus $G(t)$. It was shown recently that such relations in different statistical ensembles can be employed by computer simulations for an accurate determination of shear modulus near the glass transition [8]. However, much more precise characterization of the rheology and micro-rheology of vitrifying systems can be obtained by studying the wave-length dependence of their stress correlations [10]. In addition, the full stress correlation function $C_{\alpha\beta\gamma\delta}(\boldsymbol{q},t) = \frac{1}{V}\left\langle \sigma_{\alpha\beta}(\boldsymbol{q},t)\,\sigma^{\star}_{\gamma\delta}(\boldsymbol{q},0)\right\rangle$, where $\sigma_{\alpha\beta}$ is the stress tensor. This function depends not only on the wave-length but also on the orientation of the wave-vector $\boldsymbol{q}$. The full stress correlation function appears therefore an ideal tool to study anisotropic viscoelasticity of vitrifying systems and has therefore attracted a lot of attention recently [11–13].

It is important that stress fluctuations show qualitatively different length-scale dependencies in the liquid and solid states: correlations are long-range in crystals but short-range in liquids. A similar difference is expected between a liquid and an amorphous solid on the two sides of the glass transition. In particular, it is anticipated that a vitrified liquid at $T = 0$ may show stress correlations of infinite range. The emergence of such long-range correlation effects in glass-forming systems have been indicated in several theoretical works on 4-point structure factor [69, 70]; this concept is also supported by analytical calculations [68] and the Gardner transition theory [71–73] pointing to an amorphous phase exhibiting long-range correlations of elastic properties. The last point also supports our idea that the local tensor of the frozen residual stress is the appropriate variable to probe long-range structural effects. Therefore, an investigation of the stress correlation effects may prove to become a step forward towards a universal description of structural glasses.

To analyze the local stress correlation in complex and supercooled liquids focusing on the time and distance dependencies of the shear stress correlation function $C(\boldsymbol{r},t)$ we developed a theory [9], which shows that the stress correlations are long-range in viscoelastic and glass-forming fluids. The theory is based on the general relationship

between the stress correlation function and the memory function from the fluctuation-dissipation theorem (FDT) and will be discussed in more detail below. The results based on our theory are applicable to simulation studies which concern finite box systems (with box-size L) with periodic boundary conditions (PBC).

For the 2-dimensional (2d) case the shear stress correlation function $C(\boldsymbol{r}, t)$ connects with wave-vector and time dependent correlation function $C(\boldsymbol{q}, t)$ as:

$$C(\boldsymbol{r}, t) = \frac{1}{L^2} \sum_{\boldsymbol{q}} C(\boldsymbol{q}, t) \exp(\mathrm{i}\boldsymbol{q}\boldsymbol{r}), \tag{1.27}$$

where $\boldsymbol{q} = \frac{2\pi}{L}\boldsymbol{n}$ and $\boldsymbol{n}$ is the vector which components take independently all integer values.

Studying the behavior of $C(\boldsymbol{q}, t)$ is an important goal because this function shows if the correlations have long- or short-range character. This function is easier to obtain from the simulation than experimentally. Our theory agrees with the simulation work performed by Lemaître [11] for calculation of the correlation function for the inherent stress only, and with the theory by Fuchs et al. [12, 13].

1.3 Outline of the manuscript

Description of the project. Within the framework of this thesis we studied and analyzed how the viscoelastic properties and the range of structural and dynamical correlations in glass-forming 3-dimensional oligomer and 2-dimensional simple liquid systems are changing as they vitrify with decreasing T using Molecular Dynamics (MD) simulations. The quantities which we studied and all the theoretical approaches which we have developed will be discussed in more detail below. Lennard-Jones (LJ) units are used throughout the manuscript.

During the first part of the thesis the glass-forming oligomer system which is similar to that studied in the earlier work [7, 74] was studied. This is a 3-dimensional system which consists of $M = 768$ oligomer chains with 4 beads connected by bonds. The particles have the same mass and properties. The beads that are not connected by bonds interact with a Lennard-Jones potential $u_{\mathrm{LJ}}(r)$. The particles which are connected by bonds interact via quadratic potential $u_{\mathrm{b}}(r)$. We studied the temperature dependence and the system size effects for the static shear modulus μ, the affine shear modulus μ_A, the shear relaxation modulus $G(t)$, the fluctuation modulus μ_F and their fluctuations. Detailed description of the protocols, simulation aspects, results, conclusions are provided in Chapter 3.

During the second part of the PhD thesis a 2-dimensional system of polydisperse (pLJ) spherical particles was studied. The system was equilibrated by the swap Monte-Carlo method by Dr. Joachim Wittmer and Molecular Dynamics simulations were performed afterwards. The system contains $N = 10^4$ different particles in total. Each pair of atoms is interacting with a Lennard-Jones potential energy which was normalized by their half sum of diameters. In the same way as for the glass-forming oligomer system the temperature dependencies of such moduli as μ, μ_A, $G(t)$ and their fluctuations were studied. We also investigated temperature behavior of the dynamical structure factor $S(\boldsymbol{q}, t)$, the dynamical heat capacity at constant volume $C_V(t)$ and the total stress correlation function $C_{\alpha\beta\gamma\delta}(\boldsymbol{q}, t)$. Detailed description of the protocols, simulation aspects, results, conclusions is provided in Chapter 4.

The manuscript is organized as follows:

- In Chapter 2 we have provided a brief introduction to the basic simulation and theoretical aspects invoked during our thesis. We have provided briefly introduction to the Molecular Dynamics (MD) method, explained why and which thermostats we applied to our system and how they work. In section 2.2 the theoretical aspects for our analysis are displayed;

- In Chapter 3 we have presented the glass-forming 3-dimensional oligomer model. Our thesis has started from studying this system. We have presented all possible results and comparisons with data obtained by a former PhD student [7] from our group, including new ways and approaches for analysis of well known quantities [6] such as μ, μ_A, $G(t)$. It was found that μ_A and μ are roughly independent of the system size but their standard deviations show significant system size dependence below T_g. I describe a new method which allows to decrease fluctuations in μ_A by averaging over all possible orientations (assuming that our system is isotropic we can do averaging over rotations of the system coordinates) proposed in ref. [9]. It was shown that such quantities as the shear modulus μ or the response function $G(t)$ exhibit similar behavior with respect to the earlier works [7];

- In Chapter 4 we have presented new results on the glass-forming 2-dimensional simple liquid system. In this chapter we have also done a comparison between already existing results, obtained using Monte Carlo (MC) method and have performed an analysis of the data from new MD simulations using swap equilibrated configurations from Dr. Joachim Wittmer;

- In Chapter 5 we have provided main conclusions, discussions and summaries for both systems:

  1. **For the glass-forming 3-dimensional oligomer model** a new way to describe the fluctuations of the shear modulus μ [6] is discussed. The nature and range of stress correlations in this system are inferred on this basis. The temperature and system size dependencies of μ, μ_A and $G(t)$ are summarized. We developed a quantitative theory predicting the fluctuations $\delta\mu_F$ of μ_F in terms of the relaxation modulus $G(t)$ which is in excellent agreement with the simulation results in the liquid regime. The theoretical approach is based on the Gaussian approximation for stress fluctuations, which is asymptotically exact for large systems, $V \to \infty$. Moreover, it is shown that the low T plateau of $\delta\mu_F$ strongly decreases as the system gets larger. This effect is attributed to a highly heterogeneous amorphous structure of the supercooled glassy liquids leading to markedly non-Gaussian part of the variance of shear moduli, $\mathrm{var}(\mu_F)_{\mathrm{nG}} \approx \mathrm{var}(\mu)_{\mathrm{nG}}$, which decreases with the system size as $\frac{1}{V^\alpha}$ with $\alpha < 1\,(\alpha \approx 0.7 \pm 0.1)$.

  2. **For the glass-forming 2-dimensional polydisperse liquid system** a number of interesting features for the glassy state are discovered. For the liquid regime (well above T_g) we found that the relation between the compressibility and the static structure factor $S(\boldsymbol{q})$ is strongly violated and the time-dependent heat capacity $c_v(t)$ involves a long-time power-law tail. Furthermore, at low wave-vectors $\boldsymbol{q}$ the dynamical structure factor $S(\boldsymbol{q}, t)$ shows a two-step relaxation well above the vitrification temperature.

     To study the spatial range of stress correlations for that system more directly we analyzed the correlation function $C_{\alpha\beta\gamma\delta}(\boldsymbol{q}, t)$ of the stress tensor at different wave-vectors $\boldsymbol{q}$ using Molecular Dynamics (MD) simulations. It is important to note that the MD simulations data show excellent quantitative agreement with the theoretical results derived before [9] both above and below T_g. Our new data also indicate that the stress correlation decays as $\frac{1}{r^2}$ with distance r in agreement with the previous simulation results [11] and theoretical predictions [9]. In addition, the temperature dependencies of the moduli μ, μ_A, μ_F, their fluctuations and the dynamical quantities such as $G(t)$, $C(t)$ were studied as well. It was shown that they exhibit a rather similar behavior as for

the 3-dimensional glass-forming olygomer system.

During my PhD thesis we have published and submitted several papers, which were mostly represented in Chapter 3 and Chapter 4.

Published papers:

- L. Klochko, J. Baschnagel, J. P. Wittmer, and A. N. Semenov, "Long-range stress correlations in viscoelastic and glass-forming fluids," Soft Matter, vol. 14, pp. 6835–6848, 2018.
- L. Klochko, J. Baschnagel, J. P. Wittmer, and A. N. Semenov, "Relaxation dynamics in supercooled oligomer liquids: From shear-stress fluctuations to shear modulus and structural correlations," The Journal of Chemical Physics, vol. 151, no. 5, p. 054504, 2019.
- L. Klochko, J. Baschnagel, J. P. Wittmer, O.Benzerara, C. Ruscher, A. N. Semenov, "Composition fluctuations in polydisperse liquids: Glass-like effects well above the glass transition", Phys. Rev. E, vol. 102, p. 042611, 2020.

Submitted papers:

- G. George, L. Klochko, A. N. Semenov J. Baschnagel, and J. P. Wittmer, "Ensemble fluctuations matter for variances of macroscopic variables", European Physical Journal E.

Papers in preparation:

- G. George, L. Klochko, A. N. Semenov J. Baschnagel, and J. P. Wittmer, "Variances of non-ergodic stochastic processes".

Chapter 2

Computer simulation techniques and fluctuation relations for glass-forming systems

At present time it is hard to imagine life without computers. Any field in science nowadays, starting from the natural sciences, such as chemistry and physics, and to human sciences, such as psychology and sociology, is subject to rapid modernization of research methods. For example, computer simulation methods became usual routine for such areas as physics, mathematical modeling, biology and chemistry. Theoretical models combined with computer science can be used to discover new predictions about studied system or to estimate the behavior of that system under the extreme conditions which cannot be or hard to achieve in real life experiments.

For condensed matter physics computer simulations play an important role and have a significant impact on both theory and experimental work. We use the Molecular Dynamics (MD) technique for reaching our goals. Basically the main idea of MD is to integrate the classical Newton's equations of motion for a many-body system. Thereby it allows us to determine thermodynamic, structural and dynamic properties of a given system [75]. Concluding the above information it is obvious that computer simulations are an important tool in modern research. In this thesis an optimized code, the LAMMPS (Large-scale Atomic/Molecular Massively Parallel Simulator) code [76], was used to access static and transport features of the studied systems, which will be discussed later.

2.1 Classical molecular dynamics (MD) simulation

Consider a classical system in the microcanonical ensemble, which consists of N particles, has some fixed volume V and total energy E. Each particle $i, (i = 1..N)$, has a velocity $\boldsymbol{v}_i$ and a position $\boldsymbol{r}_i$. For simplicity we assume that all particles have equal mass m ($m_1 = m_2 = ... = m_N = m$). Based on the positions $(\boldsymbol{r}_1(t), ..., \boldsymbol{r}_N(t))$ and the velocities $(\boldsymbol{v}_1(t), ..., \boldsymbol{v}_N(t))$ of all particles at a certain time t, the evolution of the microscopic configuration of the system can be determined. For this we have to integrate Newton's second law of motion for all particles:

$$\begin{cases} \frac{d^2\boldsymbol{r}_1(t)}{dt^2} = \frac{1}{m}\boldsymbol{F}_1(t) \\ \frac{d^2\boldsymbol{r}_2(t)}{dt^2} = \frac{1}{m}\boldsymbol{F}_2(t) \\ ... \\ \frac{d^2\boldsymbol{r}_N(t)}{dt^2} = \frac{1}{m}\boldsymbol{F}_N(t), \end{cases} \tag{2.1}$$

where $\boldsymbol{F}_i(t)$ is the total force on particle i, which can be defined as:

$$\boldsymbol{F}_i(t) = -\frac{\partial u_N(\boldsymbol{r}_1(t), ..., \boldsymbol{r}_N(t))}{\partial \boldsymbol{r}_i(t)}, \tag{2.2}$$

where $u_N(\boldsymbol{r}_1(t), ..., \boldsymbol{r}_N(t)) = u\left(\boldsymbol{r}^{\boldsymbol{N}}\right)$ is the potential energy.

Periodic boundary conditions (PBC). It is common in computer simulations to apply periodic boundary conditions to minimize surface effects. PBC represent a system as periodically replicated in the all spatial directions (creating images of all particles confined in the box). A representation of the PBC is shown in Fig. 2.1.

To calculate the distance between particles in the system and to distinguish which atoms are placed within the interaction radius r_{cut} with PBCs, the minimum image convention (MIC) is used [77]. The idea of MIC is to find the minimum distance between two particles or their images in the neighboring replicas. If the distance between particles i and j, $r_{ij} = |r_i - r_j|$, is larger than the cutoff distance of the interaction potential (which is smaller than half of the box size, $L/2$), the interaction between particles i and j vanishes. However, the interaction between a particle i and the nearest image of the particle j, j', must be considered (cf. Fig. 2.1) [77, 78].

Integration of the equations of motion. Consider time increment δt, which corresponds to the "time-step" in MD simulations. The force on each particle $\boldsymbol{F}_i(t)$ can be calculated using the information about its position $\boldsymbol{r}_i(t)$ at time t. Next, using Taylor

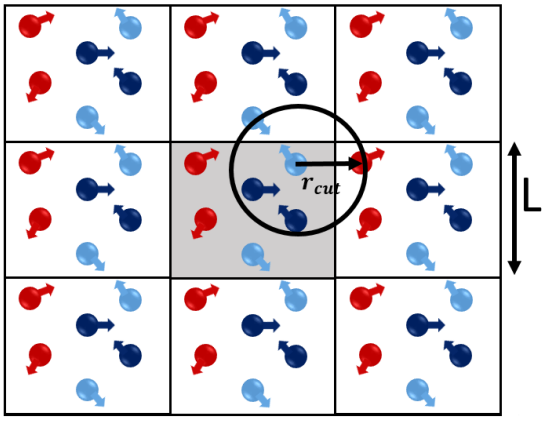

Figure 2.1: Illustration of the periodic boundary conditions. The unit cell (marked by gray color filling) is our simulation box and spheres with different colors represent particles in our system, L is the box size of the unit cell, and r_{cut} is the maximum interaction distance, which should not exceed $L/2$.

expansion, one can get an estimation of the new position and velocity at time $t+\delta t$ [18]:

$$\boldsymbol{r}_i\left(t+\delta t\right) \approx \boldsymbol{r}_i\left(t\right) + \boldsymbol{v}_i\left(t\right)\delta t + \frac{\boldsymbol{F}_i\left(t\right)}{2m}\delta t^2 \tag{2.3}$$

and

$$\boldsymbol{v}_i\left(t+\delta t\right) \approx \boldsymbol{v}_i\left(t\right) + \frac{\boldsymbol{F}_i\left(t\right)}{m}\delta t + \frac{\dot{\boldsymbol{F}}_i\left(t\right)}{2m}\delta t^2, \tag{2.4}$$

where $\dot{\boldsymbol{F}}_i\left(t\right) = \frac{d}{dt}\boldsymbol{F}_i\left(t\right)$, and $i = 1..N$.

Iteration of this procedure therefore leads to a discretized trajectory of the system, $\boldsymbol{x}\left(t_k = k\delta t\right)$, with $k = 0, 1, 2, .., N_{\max}$, starting from the initial configuration $(k = 0)$ up to the final configuration for the maximum number $N_{\max}$ of time steps simulated.

The problem that arises when using eqs. 2.3 – 2.4 is that the equations are not time-reversible while the initial eq. 2.1 is. Time-reversibility defines the symmetry in time, $t \to -t$. As the eqs. 2.3 – 2.4 are not time-reversible, they are generally not satisfied for the reverse motion, $t \to -t$. To fix this issue, an improved and most commonly used algorithm for integration — the "velocity-Verlet" algorithm — is used [78, 79]:

$$\boldsymbol{r}_i\left(t+\delta t\right) \approx \boldsymbol{r}_i\left(t\right) + \boldsymbol{v}_i\left(t\right)\delta t + \frac{\boldsymbol{F}_i\left(t\right)}{2m}\delta t^2, \tag{2.5}$$

$$\boldsymbol{v}_i\left(t+\delta t\right) \approx \boldsymbol{v}_i\left(t\right) + \frac{\boldsymbol{F}_i\left(t\right)}{2m}\delta t + \frac{\boldsymbol{F}_i\left(t+\delta t\right)}{2m}\delta t, \tag{2.6}$$

where $\boldsymbol{F}_i\left(t+\delta t\right)$ is calculated for $r_i = r_i\left(t+\delta t\right)$, $i = 1..N$, defined in eq. 2.5.

One can see that the time-step parameter δt is an important quantity. The main problem which occurs while using that algorithm is its stability and accuracy. It is obvious that taking δt as large as possible would allow us to extend the longest simulation time at the fixed computational effort $N_{\max}$ as $\Delta t_{\max} = \delta t N_{\max}$ [18]. But the Taylor expansions in eqs. 2.5 and 2.6 are appropriate only for a small δt. The main advantage of using the velocity-Verlet method is that this algorithm conserves a quantity that is close to the exact Hamiltonian [80] and the volume in the phase space even over very long periods of time [62, 81]. Which value of δt should be used? To answer this question one should consider the interaction potential between particles in the system [18].

Let us begin the discussion with an introduction of the system, where particles interact via the Lennard-Jones (LJ) potential which was introduced by Lennard-Jones in 1924 [82]. This potential consists of two parts — a repulsive term and an attractive term, representing the London dispersion forces. The LJ potential is given by:

$$u_{\mathrm{LJ}}(r) = 4\epsilon_{\mathrm{LJ}}\left[\left(\frac{\sigma_{\mathrm{LJ}}}{r}\right)^{12} - \left(\frac{\sigma_{\mathrm{LJ}}}{r}\right)^{6}\right], \tag{2.7}$$

where ϵ_{LJ} is the depth of the potential minimum, σ_{LJ} is the particle diameter or distance, at which the intermolecular potential between the two particles is zero (these 2 constants set a scale for the energy and the length), and r is the distance between the centers of interacting particles [18].

The LJ potential also leads to a scale for the time in the simulation, the "Lennard-Jones time":

$$\tau_{\mathrm{LJ}} = \sqrt{\frac{m\sigma_{\mathrm{LJ}}^2}{\epsilon_{\mathrm{LJ}}}} \tag{2.8}$$

In this thesis $\delta t = 0.005\tau_{\mathrm{LJ}}$ was chosen [18]. After introducing dimensionless quantities such as $u^*_{\mathrm{LJ}} = u_{\mathrm{LJ}}/\epsilon_{\mathrm{LJ}}$ and $r^* = r/\sigma_{\mathrm{LJ}}$ one can show that the Taylor expansion in eqs. 2.5 – 2.6 will be a good approximation to the exact classical trajectory, if $\omega_{\mathrm{int}}\delta t \ll 1$, where ω_{int} is the highest frequency of physical oscillations in the system, leading to $\delta t/\tau_{\mathrm{LJ}} \ll 0.1$ [83]. The previous equations describe the classical MD technique, which can be used only for the NVE ensemble. To perform simulations using different ensembles such as NPT or NVT, the original MD method has to be extended [78,84]. Such methods will be discussed in sections 2.1.1 and 2.1.2.

2.1.1 Simulation in the NVT ensemble

To make simulations in the canonical ensemble the temperature of the system has to be fixed at a prescribed level and controlled. In the NVE ensemble temperature can be calculated but cannot be controlled. To fix this issue a thermostat is introduced. Nowadays, several ways to control temperature applying different algorithms for thermostats exist [18, 83]:

- Nosé-Hoover thermostat;
- Berendsen thermostat;
- Anderson thermostat;
- Langevin thermostat.

As in this thesis the Nosé-Hoover thermostat was chosen, it is important to discuss its properties in more detail. The idea of the Nosé-Hoover algorithm is to include the additional degree of freedom for the heat bath, s, in the system's Hamiltonian. This method is called the extended system method (ES). The original idea of fixing temperature or pressure during simulation comes from H. Andersen in ref. [85] and was then improved by Nosé and Hoover in ref. [86, 87].

The major difference between the ES and the real dynamics is that in the ES a very small system is considered as an external system instead of a macroscopic reservoir [88]. The total energy of the physical system is allowed to fluctuate because of a thermal contact with a heat bath. As a result one expects that there exist real variables such as particle momenta $\boldsymbol{p}'_i$, coordinates $\boldsymbol{q}'_i$ (corresponding to realistic motions) and virtual variables $\boldsymbol{p}_i$, $\boldsymbol{q}_i$ (introduced to control the temperature). The relation between the real and virtual variables comes from the noncanonical transformation [88]:

$$\begin{aligned} \boldsymbol{q}'_i &= \boldsymbol{q}_i, \\ \boldsymbol{p}'_i &= \boldsymbol{p}_i/s, \\ dt' &= \frac{dt}{s}, \\ \dot{\boldsymbol{q}}'_i &= s\dot{\boldsymbol{q}}_i \end{aligned} \tag{2.9}$$

where t' is a real time, t is a virtual time.

The Hamiltonian of the ES of the particles and the variable s in terms of the virtual variables postulated by Nosé reads:

$$H_{\text{Nosé}} = \sum_i \frac{\boldsymbol{p}_i^2}{2m_i s^2} + u\left(\boldsymbol{q}^{\boldsymbol{N}}\right) + p_s^2/2Q + gk_{\text{B}}T\ln(s)\,, \tag{2.10}$$

where m_i is the mass of particle i, p_s is the conjugate momentum of s, Q is the thermal inertia coefficient, which behaves as a mass for the motion of s, $u\left(\boldsymbol{q}^{\boldsymbol{N}}\right)$ is the potential energy of the system, and g is the number of degrees of freedom of the physical system, $g = dN$ [86], where d is the space dimension. A term for a potential energy for s, $gk_{\text{B}}T\ln(s)$ is chosen in such a way that the canonical ensemble is reproduced [88].

Let us take a look at the equations of motion for the virtual variables proposed by Nosé [86]:

$$\begin{aligned}
\dot{\boldsymbol{q}}_i &= \frac{\partial H_{\text{Nosé}}}{\partial \boldsymbol{p}_i} = \frac{\boldsymbol{p}_i}{m_i s^2},\\
\dot{\boldsymbol{p}}_i &= -\frac{\partial H_{\text{Nosé}}}{\partial \boldsymbol{q}_i} = -\frac{\partial u\left(\boldsymbol{q}^{\boldsymbol{N}}\right)}{\partial \boldsymbol{q}_i},\\
\dot{s} &= \frac{\partial H_{\text{Nosé}}}{\partial p_s} = \frac{p_s}{Q},\\
\dot{p}_s &= -\frac{\partial H_{\text{Nosé}}}{\partial s} = \sum_i \frac{\boldsymbol{p}_i^2}{m_i s^3} - \frac{gk_{\text{B}}T}{s},
\end{aligned} \tag{2.11}$$

where $\dot{\boldsymbol{q}}_i$ and $\dot{\boldsymbol{p}}_i$ correspond to the first derivative with respect to time t of the virtual coordinate and momentum of a particle i.

For applications in simulation it is important to transform eqs. 2.11 to eqs. with real variables using relations from eq. 2.9 [88]:

$$\begin{aligned}
\dot{\boldsymbol{q}}'_i &= \frac{\boldsymbol{p}'_i}{m_i},\\
\dot{\boldsymbol{p}}'_i &= -\frac{\partial u\left(\boldsymbol{q}'^{\boldsymbol{N}}\right)}{\partial \boldsymbol{q}'_i} - \frac{1}{s}\frac{ds}{dt'}\boldsymbol{p}'_i,\\
\frac{ds}{dt'} &= s^2 p'_s/Q,\\
\dot{p}'_s &= \left(\sum_i \frac{p_i'^2}{m_i} - gk_{\text{B}}T\right)\Big/ s - \frac{1}{s}\frac{ds}{dt'}p'_s,
\end{aligned} \tag{2.12}$$

where $p'_s = p_s/s$, $\dot{\boldsymbol{q}}'_i$, $\dot{\boldsymbol{p}}'_i$, and $\dot{p}'_s$ are the first derivatives over real time.

It is important to note that eqs. 2.12 are no longer canonical since the quantities $\dot{\boldsymbol{p}}'_i$ and $\dot{p}'_s$ have additional force terms. The Nosé Hamiltonian in terms of real variables

reads [86] (cf. page 513, eq. 2.23):

$$H'_{\text{Nosé}} = \sum_i \frac{p_i'^2}{2m_i} + u\left(\boldsymbol{q}'^{\boldsymbol{N}}\right) + s^2 p_s'^2/2Q + gk_{\text{B}}T\ln(s) \tag{2.13}$$

Note that eq. 2.13 is not a proper Hamiltonian anymore, but it is still conserved, $\dot{H}'_{\text{Nosé}} = 0$ [86].

Hoover proposed an improvement and simplification [87] to the above algorithm by choosing a new variable, the thermodynamic friction coefficient ξ, which can be defined as $\xi = \frac{1}{s}\frac{ds}{dt'} = sp'_s/Q = p_s/Q$ [88]. Now, eq. 2.12 becomes:

$$\begin{aligned}
\dot{\boldsymbol{q}}'_i &= \frac{\boldsymbol{p}'_i}{m_i}, \\
\dot{\boldsymbol{p}}'_i &= -\frac{\partial u\left(\boldsymbol{q}'^{\boldsymbol{N}}\right)}{\partial \boldsymbol{q}'_i} - \xi \boldsymbol{p}'_i, \\
\dot{s}' &= s^2 \frac{p'_s}{Q}, \\
\dot{p}'_s &= \left(\sum_i \frac{p_i'^2}{m_i} - gk_{\text{B}}T\right) \Big/ s - \xi p'_s
\end{aligned} \tag{2.14}$$

The first derivative of the thermodynamic friction coefficient, $\dot{\xi}$, can be found based on the eq. 2.11 [88]:

$$\begin{aligned}
\xi &= s\frac{p'_s}{Q}, \\
\frac{\mathrm{d}\xi}{\mathrm{d}t'} &= \frac{1}{Q}\frac{d\left(sp'_s\right)}{dt'} = \frac{s}{Q}\dot{p}_s, \\
\dot{p}_s &= \sum_i \frac{p_i^2}{m_i s^3} - \frac{gk_{\text{B}}T}{s} = \left(\sum_i \frac{p_i'^2}{m_i} - gk_{\text{B}}T\right) \Big/ s, \\
\frac{\mathrm{d}\xi}{\mathrm{d}t'} &= \frac{1}{Q}\left[\sum_i \frac{p_i'^2}{m_i} - gk_{\text{B}}T\right],
\end{aligned} \tag{2.15}$$

where $g = dN$. Combining eqs. 2.12, 2.14 and 2.15 one can get the equations of the Nosé-Hoover thermostat for controlling temperature in the system [88]:

$$\begin{aligned}
\dot{\boldsymbol{q}}'_i &= \frac{\boldsymbol{p}'_i}{m_i}, \\
\dot{\boldsymbol{p}}'_i &= -\frac{\partial u\left(\boldsymbol{q}'^{\boldsymbol{N}}\right)}{\partial \boldsymbol{q}'_i} - \xi \boldsymbol{p}'_i, \\
\frac{\mathrm{d}\xi}{\mathrm{d}t'} &= \frac{1}{Q}\left[\sum_i \frac{p_i'^2}{m_i} - gk_{\text{B}}T\right]
\end{aligned} \tag{2.16}$$

The choice of the mass parameter Q is very important. Setting a very large value for $Q \to \infty$ corresponds to the microcanonical ensemble. Moreover, choosing the large value of Q will be inefficient due to the very slow energy exchange with the heat bath [83,88]. On the other hand, very small value of Q leads to a sequence of problems, for example the heat bath variable s will be an isolated mode and will continue an oscillation independently. In such a system the distribution of the total kinetic energy driven by this oscillation deviates significantly from the Gaussian distribution, and during the simulation this system will not reach the equilibrium state [88]. The statements above lead to the conclusion that the choice of the mass parameter Q is a crucial task. An assessment of the Q-effect can be done in two ways. The first one is to take the second derivative of ξ using eqs. 2.16 as in ref. [83]:

$$\begin{aligned} \frac{\mathrm{d}^2\xi}{\mathrm{d}t'^2} &= \frac{1}{Q}\sum_i \frac{\mathrm{d}}{\mathrm{d}t'}\left(\frac{\left(\boldsymbol{p}_i'\right)^2}{m_i}\right) = \frac{1}{Q}\sum_i \frac{2\boldsymbol{p}_i'\dot{\boldsymbol{p}}_i'}{m_i} = \frac{2}{Q}\sum_i \frac{\boldsymbol{p}_i'}{m_i}\left[-\frac{\partial u\left(\boldsymbol{q}'^{\boldsymbol{N}}\right)}{\partial \boldsymbol{q}_i'} - \xi \boldsymbol{p}_i'\right] \\ &\approx -\frac{2}{Q}\xi\sum_i \frac{p_i'^2}{m_i} \approx -\left(\frac{2gk_\mathrm{B}T}{Q}\right)\xi \end{aligned} \tag{2.17}$$

Due to the fact that positions $\boldsymbol{q}_i$ and momenta $\boldsymbol{p}_i$ of particles are uncorrelated at the thermal equilibrium, the average value of the product $\boldsymbol{p}_i'\frac{\partial u\left(\boldsymbol{q}'^{\boldsymbol{N}}\right)}{\partial \boldsymbol{q}_i'}$ must vanish and it is possible to neglect this term in eq. 2.17. The kinetic contribution $\sum_i \frac{p_i'^2}{m_i}$ is almost constant and can be approximately replaced with $gk_\mathrm{B}T$ (cf. Fig. 4.1 from ref. [83]). It can be seen that eq. 2.17 is equivalent to the harmonic oscillator equation with frequency [83, 88]:

$$\omega_T = \left(\frac{2gk_\mathrm{B}T}{Q}\right)^{\frac{1}{2}} \tag{2.18}$$

The second way to obtain the proper value of the mass parameter Q is to use the criteria introduced by Nosé [88]. As was mentioned at the beginning of this section, Nosé proposed the idea of the virtual variables in order to control the temperature in the system. So, let us switch again to the virtual variables by applying the time-transformation $\boldsymbol{p}_i' = \boldsymbol{p}_i/s$ in the last eq. 2.16 in order to follow his steps. The fluctuation δs of the variable s around its average value $\langle s\rangle$ can be defined as $\delta s = s\left(t\right) - \langle s\rangle$. In the small-$Q$ limit the fluctuations of s are much faster than those of the original system and the constant temperature is maintained by s, $\sum_i \frac{p_i^2}{m_i\langle s\rangle^2} = gk_\mathrm{B}T$ [88]. Linearization can be done as

follows:

$$
\begin{aligned}
& s\frac{\mathrm{d}^2 s}{\mathrm{d}t^2} = \frac{1}{Q}\left(\sum_i \frac{p_i^2}{m_i s^2} - g k_\mathrm{B} T\right),\ \delta s = s\left(t\right) - \langle s \rangle \\
& \Rightarrow \sum_i \frac{p_i^2}{m_i \left(\langle s \rangle + \delta s\right)^2} = \sum_i \frac{p_i^2}{m_i \langle s \rangle^2 \left(1 + \frac{\delta s}{\langle s \rangle}\right)^2} = \\
& = \sum_i \frac{p_i^2}{m_i \langle s \rangle^2}\left(1 + \frac{\delta s}{\langle s \rangle}\right)^{-2} = \sum_i \frac{p_i^2}{m_i \langle s \rangle^2}\left(1 - 2\frac{\delta s}{\langle s \rangle}\right) \\
& \langle s \rangle Q \frac{\mathrm{d}^2\left(\delta s\right)}{\mathrm{d}t^2} = \sum_i \frac{p_i^2}{m_i \langle s \rangle^2}\left(1 - 2\frac{\delta s}{\langle s \rangle}\right) - g k_\mathrm{B} T = -2\frac{g k_\mathrm{B} T}{\langle s \rangle}\left(\delta s\right) \\
& \frac{\langle s \rangle^2 \mathrm{d}^2\left(\delta s\right)}{\mathrm{d}t^2} \simeq \frac{\mathrm{d}^2\left(\delta s\right)}{\mathrm{d}t'^2} \\
& \frac{\mathrm{d}^2\left(\delta s\right)}{\mathrm{d}t'^2} = -2\frac{g k_\mathrm{B} T}{Q}\left(\delta s\right)
\end{aligned}
\tag{2.19}
$$

The above relation is similar to a harmonic oscillator equation [83,88] with frequency (in real time) which is equivalent to eq. 2.18:

$$
\omega_s = \left(\frac{2 g k_\mathrm{B} T}{Q}\right)^{\frac{1}{2}} \tag{2.20}
$$

In eq. 2.16 the variable ξ is not constant and can be either positive or negative. If the kinetic energy of the system is larger than $(g/2)k_\mathrm{B}T$, the time derivative of ξ, $\dot{\xi}$, is positive, and then ξ increases and will become positive. That means that in a case of positive friction coefficient ξ the equations become similar to those for the system with a friction force. The kinetic energy decreases due to the fact that the velocity of particle is decreasing by the friction. On the contrary, in a situation of kinetic energy lower than $(g/2)k_\mathrm{B}T$, ξ decreases, and in the negative ξ region, the system is heated up [88]. Obviously the kinetic energy is fluctuating around its average value $(g/2)k_\mathrm{B}T$, which leads to vanishing time average of the time derivative variable. This also guarantees that the average of kinetic energy coincides with the results of the equipartition theorem [88,89]:

$$
\left\langle x_i \frac{\partial H}{\partial x_j} \right\rangle = \delta_{ij} k_\mathrm{B} T, \tag{2.21}
$$

where H is the Hamiltonian of a system, δ_{ij} is the Kronecker symbol, $x_{i,j}$ are the generalized coordinates, and $\langle ... \rangle$ is the canonical ensemble average.

Due to the non-canonical nature of equations 2.16, they do not conserve the volume in phase space $(\boldsymbol{p}, \boldsymbol{q}, \xi)$ where the density function $f_\mathrm{NVT}\left(\boldsymbol{p^N}, \boldsymbol{q^N}, \xi\right)$ is defined. The

Liouville's theorem, $\dot{f} = 0$, is not applicable in this case [87, 88]. However, the volume fluctuations are very small for large systems, typically $\sim 1/\sqrt{g}$. It was also shown that the density function has a canonical distribution and is expressed as [86]:

$$f_{\mathrm{NVT}}\left(\boldsymbol{q}^{\boldsymbol{N}}, \boldsymbol{p}^{\boldsymbol{N}}, \xi\right) = C \exp\left[-H_T\left(\boldsymbol{p}^{\boldsymbol{N}}, \boldsymbol{q}^{\boldsymbol{N}}, \xi\right)/k_{\mathrm{B}}T\right] \tag{2.22}$$

where $H_T = \sum_i {p^2}_i/2m_i + u\left(\boldsymbol{q}^{\boldsymbol{N}}\right) + Q\xi^2/2$ [88], and $\boldsymbol{p}$, $\boldsymbol{q}$ are now real momenta and coordinates.

2.1.2 Simulation in the NPT ensemble

A year after deriving eq. 2.16, Hoover extended those equations to the NPT case [90]. In this section the procedure of applying Nosé-Hoover algorithm for the simulations in isobaric-isothermal ensemble, known as the NPT ensemble will be briefly discussed.

To extend the idea from previous section to the isobaric-isothermal ensemble reduced coordinates from eqs. 2.9 by a length of a simulation unit cell are introduced [88]:

$$\begin{aligned} \boldsymbol{q}_i' &= V^{1/d}\boldsymbol{q}_i, \\ \boldsymbol{p}_i' &= V^{-1/d}\boldsymbol{p}_i, \\ \dot{\boldsymbol{q}}_i' &= V^{1/d}\dot{\boldsymbol{q}}_i \end{aligned} \tag{2.23}$$

where $\dot{\boldsymbol{q}}_i'$ is the velocity of particle i, V is the volume of the simulation unit cell, d is the dimension of the system. As in the previous section, the variables with a prime are the real variables corresponding to the real physical system and the scaled variables are represented without the prime [88].

To describe the change of the volume V with the time, $\dot{V}$, the expansion rate $\zeta = \frac{\dot{V}}{dV}$ is introduced [90], where d is the space dimension. The equations of motion for scaled variables [90]:

$$\begin{aligned} \dot{\boldsymbol{q}}_i &= \frac{\boldsymbol{p}_i}{m_i} + \zeta\boldsymbol{q}_i, \\ \dot{\boldsymbol{p}}_i &= -\frac{\partial u\left(\boldsymbol{q}^{\boldsymbol{N}}\right)}{\partial \boldsymbol{q}_i} - \left(\xi + \zeta\right)\boldsymbol{p}_i, \\ \dot{\xi} &= \frac{1}{Q}\left[\sum_i \frac{p_i^2}{m_i} - gk_{\mathrm{B}}T\right], \\ \zeta &= \frac{\dot{V}}{dV}, \\ \dot{\zeta} &= \frac{V}{W}\left(P\left(t\right) - P\right), \end{aligned} \tag{2.24}$$

where P is a fixed "external pressure" (which is imposed), $\dot{\zeta}$ is the first derivative over time of the expansion rate, W is the mass parameter for the volume changes, which determines frequency of the volume fluctuations, and $P(t)$ is an instantaneous (or internal) pressure of the system, defined as:

$$P(t) = \frac{1}{dV}\left[\sum_i \frac{p_i^2}{m_i} + \sum_{i<j} \boldsymbol{r}_{ij} \cdot \boldsymbol{F}_{ij}\right], \tag{2.25}$$

where $\boldsymbol{r}_{ij} = \boldsymbol{r}_j - \boldsymbol{r}_i$ is the distance vector, and $\boldsymbol{F}_{ij}$ is the force of particle i on particle j. The balance between an internal $P(t)$ and an external pressure P governs the change of the volume [88], $\dot{V} = \zeta V d$.

It was shown in ref. [83,88,90] that eq. 2.24 is compatible with the equilibrium solution for the density function

$$f_{\mathrm{NPT}}\left(\boldsymbol{p}^{\boldsymbol{N}}, \boldsymbol{q}^{\boldsymbol{N}}, \xi, \zeta\right) = \mathrm{const} \cdot \exp\left[-H^*\left(\boldsymbol{p}^{\boldsymbol{N}}, \boldsymbol{q}^{\boldsymbol{N}}, \xi, \zeta\right) \Big/ k_{\mathrm{B}}T\right], \tag{2.26}$$

where $H^* = \sum_i {p^2}_i/2m_i + u\left(\boldsymbol{q}^{\boldsymbol{N}}\right) + Q\xi^2/2 + d\zeta^2 W/2 + PV$, and N is the total number of particles in the system, $i = 1..N$.

To perform the simulations in LAMMPS [76] one can adjust the parameters P_{damp} and T_{damp}. Those parameters determine how rapidly the temperature or pressure is relaxed and have dimension of time. They are related to the mass parameter for the volume changes W and the thermal inertia coefficient Q which were implemented in LAMMPS as [76]:

$$\begin{aligned} W &= dNk_{\mathrm{B}}T \times P_{\mathrm{damp}}^2, \\ Q &= dNk_{\mathrm{B}}T \times T_{\mathrm{damp}}^2 \end{aligned} \tag{2.27}$$

The parameter T_{damp} is related to the frequency ω_T defined in eq. 2.18 as [83]:

$$T_{\mathrm{damp}} = \frac{\sqrt{2}}{\omega_T} \tag{2.28}$$

The parameter P_{damp} is related to the frequency ω_v obtained below (cf. eq. 2.31) as [76]:

$$P_{\mathrm{damp}} = \frac{1}{\omega_v}\sqrt{\frac{K_b}{cT}}, \tag{2.29}$$

where $c = N/V$ is the density of the system, and K_b is the bulk compression modulus. To define ω_v let us investigate the time-evolution of the volume fluctuations $\delta V(t) = V(t) - \langle V \rangle$ and the instantaneous pressure $\delta P(t) = P(t) - \langle P \rangle$, where $\langle ... \rangle$ corresponds

to the ensemble averaging. One can see from eq. 2.24, $\delta\dot{V} = \dot{V} = \zeta dV$ [83]. The second derivative of the latter above takes form:

$$\begin{aligned}\ddot{V} &= \dot{\zeta} dV + \zeta d\dot{V} = \\ &= \frac{V}{W} dV \delta P + (\zeta d)^2 V = \frac{dV^2}{W}\frac{\delta P}{\delta V}\delta V + \left(\frac{\delta\dot{V}}{V}\right)^2 V = \\ &= -\frac{dV^2}{W}\frac{K_b}{V}\delta V + \left(\frac{\delta\dot{V}}{V}\right)^2 V = -\frac{dV}{W}K_b\delta V\end{aligned} \tag{2.30}$$

It is possible to neglect the term "$\left(\frac{\delta\dot{V}}{V}\right)^2 V$" in eq. 2.30 taking into account that δV and $\delta\dot{V}$ are the same order of magnitude, and $\delta V/V \ll 1$. From eq. 2.30 one can introduce the frequency ω_v which is connected with W via [83]:

$$\omega_v = \left(\frac{dV}{W}K_b\right)^{1/2}, \tag{2.31}$$

where K_b is the bulk compression modulus and V is the volume of the system.

2.2 Fluctuation-dissipation theorem

2.2.1 Shear stress

As was discussed in Chapter 1, the shear-stress relaxation modulus $G(t)$ can be obtained in a simple-shear experiment recording a shear-stress increment $\delta\sigma(t)$ generated by a small prescribed steplike shear deformation $\gamma \ll 1$ at $t = 0$:

$$G(t) = \lim_{\gamma \longrightarrow 0} \langle \delta\sigma(t) \rangle / \gamma \tag{2.32}$$

Based on the fluctuation-dissipation theorem (FDT) [60,62], which is exact for equilibrium systems, $G(t)$ is closely related to the shear stress correlation function $C(t)$ via the stress-fluctuation equation [6,8,9] (relating the relaxation modulus in the linear response regime to fluctuations of the shear stress):

$$C(t) = \langle \sigma(t + t')\, \sigma(t') \rangle \tag{2.33}$$

where $\sigma(t) = \sigma_{xy}(t)$ is the instant shear stress, averaged over the system volume V, and $\langle ... \rangle$ means the ensemble-averaging.

The FDT relation is:

$$G(t) = \frac{V}{T} C(t) + \mathbf{CONST}, \tag{2.34}$$

The constant term **CONST** from eq. 2.34 depends on the boundary conditions applied to obtain $C(t)$. For example, **CONST=0** with free boundary (in this case, eq. 2.34 is exact only for $V \to \infty$) or when the boundary is coupled to a highly damping external medium [91]. The effect of such overdamped force was implemented in computations with PBC using a hybrid MD-Monte Carlo (MC) scheme [91] involving canonical-affine shear deformations as MC moves. This scheme (the shear barostat) implies that the PBC are generally nonrectangular thus allowing for shearing of the simulation cell. The nonphysical MC steps are chosen to be very small in order to sufficiently slowdown a backflow (shear reversal) after an imposed shear strain. However, the constant **CONST** from eq. 2.34 is generally nonzero in standard simulations with fixed PBC in the canonical ensemble.

While eq. 2.34 is strictly valid for equilibrium systems (in particular, in the liquid state), it is also valid for glassy (supercooled) systems as argued below: In this latter case, the system stays virtually trapped for a long time in a particular metabasin, MB (is a group of inherent structures, IS, of the potential energy landscape in the configurational space [92]), so it becomes equilibrated within each MB. Hence, the FDT can be applied individually to each MB provided that transfer rates $f \sim 1/\tau_\alpha$ between the glassy states (MBs) are very low, and therefore, it must also be valid on the average (for ensemble-averaged quantities) with any (generally, non-equilibrium) probability distribution between the glassy states (the MBs). The general condition for the FDT relation 2.34 to be valid is that the system must be equilibrated (prior to the measurements) during a long time strongly exceeding the time shift t in $C(t)$. Let us define a "sampling time" Δt as a time, which takes to simulate one configuration. For $t \sim \Delta t$ the latter condition ensures that aging is negligible within the relevant time window Δt, as was verified in ref. [7].

The constant term **CONST** can be represented for 2 regimes — liquid and glass — below:

$$\mathbf{CONST} = \begin{cases} 0, & \text{liquid} \\ G(0) - \frac{V}{T} C(0), & \text{glass} \end{cases} \tag{2.35}$$

On using both eq. 2.34 and eq. 2.35, the final formula connecting $G(t)$ and $C(t)$ becomes:

$$G(t) = \frac{V}{T} C(t) + \begin{cases} 0, & \text{liquid} \\ G(0) - \frac{V}{T} C(0), & \text{glass} \end{cases} \tag{2.36}$$

Considering that Δt is our laboratory time-scale (the longest accessible time for experiment or simulation) one can define the long-time shear modulus as $\mu \approx G(\Delta t)$. The instantaneous response is given by $G(0) = \mu_A$. More detailed discussion about μ_A is provided in subsection 2.2.2. Furthermore, the function $C(t)$ can be obtained using the FDT relation, eq. 2.36, which takes the form:

$$G(t) = \frac{V}{T} C(t) + G(0) - \mu_0, \tag{2.37}$$

with μ_0 measuring the ensemble- and time-averaged square of the shear stress:

$$\mu_0 = \frac{V}{T} C(0) = \frac{V}{T} \left\langle \overline{\sigma^2} \right\rangle, \tag{2.38}$$

where

$$\overline{\sigma^2} = \frac{1}{\Delta t} \int_0^{\Delta t} \sigma(t)^2 \, dt \tag{2.39}$$

The time-averaged stress is defined for each system of the ensemble as

$$\overline{\sigma} = \frac{1}{\Delta t} \int_0^{\Delta t} \sigma(t) \, dt \tag{2.40}$$

As follows directly from the definition of $C(t)$, eq. 2.33,

$$\left\langle \overline{\sigma}^2 \right\rangle = \frac{1}{\Delta t^2} \int_0^{\Delta t} C(t - t') \, dt dt' \tag{2.41}$$

Eq. 2.41 can be considered as an average of $C(t)$ over the time scale Δt. A similar average of $G(t)$ reads:

$$\mu = \frac{1}{\Delta t^2} \int_0^{\Delta t} G(|t - t'|) \, dt dt' \tag{2.42}$$

Eqs. 2.36 and 2.37 now can be represented as follow:

$$G(t) = \frac{V}{T} C(t) + \begin{cases} 0, & \text{liquid} \\ \mu_A - \frac{V}{T} C(0), & \text{glass} \end{cases} \tag{2.43}$$

and

$$G(t) = \frac{V}{T} C(t) + \mu_A - \mu_0 \tag{2.44}$$

Using eqs. 2.41, 2.42, and 2.44, μ can be rewritten in terms of μ_A and time-averaged shear-stress fluctuations μ_F:

$$\mu = \mu_A - \mu_F, \tag{2.45}$$

where

$$\mu_F = \mu_0 - \mu_1,\ \mu_1 = \frac{V}{T}\left\langle \overline{\sigma}^2 \right\rangle. \tag{2.46}$$

The fluctuation modulus μ_F measures the mean-square fluctuation of σ over the sampling time Δt:

$$\mu_F = \frac{V}{T}\left\langle \overline{(\sigma - \overline{\sigma})^2} \right\rangle \tag{2.47}$$

Also, μ_F can be considered as an effective drop of $G(t)$ during the time Δt:

$$\mu_F(\Delta t) = G(0) - \mu(\Delta t) \tag{2.48}$$

and can be treated as the average for individual moduli $\tilde{\mu}_F$ defined for each independent dynamical trajectory of a system from the ensemble:

$$\mu_F = \langle \tilde{\mu}_F \rangle, \tag{2.49}$$

with

$$\tilde{\mu}_F = \frac{V}{T}\left(\overline{\sigma^2} - \overline{\sigma}^2\right) \equiv \tilde{\mu}_0 - \tilde{\mu}_1 \tag{2.50}$$

Apart from the factor V/T, $\tilde{\mu}_0$ is the mean-squared shear stress of the trajectory and $\tilde{\mu}_1$ is the square of the mean stress $\tilde{\sigma}$. The latter equation can be rewritten as:

$$\tilde{\mu}_F = \frac{V}{2T}(\Delta t)^{-2}\int_0^{\Delta t}\left[\sigma(t_1) - \sigma(t_2)\right]^2 dt_1 dt_2 \tag{2.51}$$

Eq. 2.51 directly shows that any constant (quenched) stress does not affect μ_F. Using eqs. 2.49 and 2.51 one can get:

$$\mu_F = \frac{2}{\Delta t^2}\int_0^{\Delta t}(\Delta t - t)\, h(t)\, dt, \tag{2.52}$$

where

$$h(t) = \frac{V}{2T}\left\langle \left[\sigma(t+t') - \sigma(t')\right]^2 \right\rangle = \frac{V}{T}\left[C(0) - C(t)\right] = G(0) - G(t) \tag{2.53}$$

is proportional to the mean-square shear stress increment. Thus, the functions $\mu_F(\Delta t)$, $h(t)$ and $G(t)$ are closely related defining each other with eq. 2.52 or with the inverse equation:

$$h(t) = \frac{1}{2}\frac{d^2}{dt^2}\left[t^2 \mu_F(t)\right]. \tag{2.54}$$

2.2.2 Impulsive correction

Let us consider an infinitesimal canonical affine transformation of positions and velocities of all particles. The affine shear modulus μ_A is defined by the stress response on such transformation. For example, if we consider shear in the xy plane, then such transformation can be expressed as:

$$x \to x + \gamma y,\ v_y \to v_y - \gamma v_x, \tag{2.55}$$

where x, y are coordinates and v_x, v_y are velocity components of a particle. Then eq. 2.32 at $t = 0$ can be rewritten in terms of μ_A:

$$\langle \delta\sigma \rangle \cong \gamma \mu_A \tag{2.56}$$

As was shown in refs. [8, 93], the modulus μ_A can be also defined by the following general expression:

$$\tilde{\mu}_A = \frac{1}{V}\sum_{i=1}^{N} m_i v_{i,x}^2 + \frac{1}{V}\sum_{l} n_y^2 \left[r^2 u_l''(r)\, n_x^2 + r u_l'(r) \left(1 - n_x^2\right) \right], \tag{2.57}$$

where $\mu_A = \langle \tilde{\mu}_A \rangle$, "tilde" indicates that the modulus is calculated for an instantaneous micro-state of the system, m_i,$v_{i,x}$ correspond to the mass and the velocity component along x direction of the ith particle, N is the total number of particles in the system. The first sum runs over all particles in the system and the second sum runs over all different pairs of the interacting particles, where index l labels the interaction between the particles i and j with $i < j$. The term $u_l(r)$ is the interaction potential for the l-pair, $u_l'(r)$ and $u_l''(r)$ are its first and second derivatives with respect to $r = |\boldsymbol{r}|$, respectively, where $\boldsymbol{r} = \boldsymbol{r}_l$ is the distance vector and $\boldsymbol{n} = \boldsymbol{r}_l / r_l$ is the normalized distance vector between interacting particles i and j.

The first term in eq. 2.57 is the kinetic (ideal-gas) contribution, while the second (excess) term is due to particle interactions. In practice, the kinetic term can always be ensemble-averaged giving just cT, where $c = N/V$ is the particle concentration and T is the temperature in energy units ($T = k_{\mathrm{B}} T_{\mathrm{abs}}$, with T_{abs} being the absolute temperature).

Potential truncation at r_{cut}, with r being the distance between two particles i and j, allows to reduce the number of interactions computed for an energy and a force. The shifting of the potential leading to $u(r_{\mathrm{cut}}) = 0$ allows to avoid its discontinuous behavior at $r = r_{\mathrm{cut}}$. After those procedures the interaction energy goes smoothly to zero at $r = r_{\mathrm{cut}}$,

without any numerical instability in the equations of motion and without problems in energy conversation.

While the chosen LJ potential is continuous:

$$u_{\mathrm{LJ}}(r) = \begin{cases} 4\epsilon_{\mathrm{LJ}}\left[\left(\frac{\sigma_{\mathrm{LJ}}}{r}\right)^{12} - \left(\frac{\sigma_{\mathrm{LJ}}}{r}\right)^{6}\right] - 4\epsilon_{\mathrm{LJ}}\left[\left(\frac{\sigma_{\mathrm{LJ}}}{r_{\mathrm{cut}}}\right)^{12} - \left(\frac{\sigma_{\mathrm{LJ}}}{r_{\mathrm{cut}}}\right)^{6}\right], & \text{if } r < r_{\mathrm{cut}} \\ 0, & \text{otherwise} \end{cases} \tag{2.58}$$

its derivative is not, giving rise to a singular contribution to μ_A known as an impulsive correction $\Delta\mu_A$ [94].

One can obtain the impulsive correction $\Delta\mu_A$ for monodisperse systems using equation 2.59 which is shown in ref. [6]. Our glass-forming 3-dimensional oligomer model is the good example of such a monodisperse system. Detailed explanations about this model and the resulting $\Delta\mu_A$ are provided in Chapter 3, section 3.4. Based on the equations from ref. [94] and section 3.4 the impulsive correction for monodisperse systems can be defined as:

$$\Delta\mu_A = -\frac{2\pi}{15}c^2 u'_{LJ}(r_{\mathrm{cut}})\, r_{\mathrm{cut}}^4 g_{nb}(r_{\mathrm{cut}}), \tag{2.59}$$

where c is the monomer concentration $c = N_m/V$, N_m is the total number of monomers in the system, and g_{nb} is the radial distribution function (RDF) for nonbonded monomer pairs. Here by nonbonded monomers we mean monomers that are not connected by permanent bonds: only those monomer pairs are interacting with the LJ potential according to the model of Chapter 3. Eq. 2.59 was derived in ref. [94] taking into account the Born term $C_{\mathrm{B}}^{\alpha\beta\gamma\delta}$:

$$C_{\mathrm{B}}^{\alpha\beta\gamma\delta} = \frac{1}{V}\sum_l \left\langle (s_l^2 u''_s(s_l) - s_l u'_s(s_l)) n_l^\alpha n_l^\beta n_l^\gamma n_l^\delta \right\rangle, \tag{2.60}$$

where $s_l = r_l/\sigma_{\mathrm{LJ}}$ is the reduced dimensionless distance between interacting particles i and j, n_l^α is the corresponding component of the normalized distance vector [94], and $u_s(s_l) = u_{\mathrm{LJ}}(r_l)$ is the truncated and shifted potential. Now setting for $C_{\mathrm{B}}^{\alpha\beta\gamma\delta}$ $\alpha = \gamma = 1$ and $\beta = \delta = 2$, the impulsive correction $\Delta\mu_A$ is simply obtained using ref. [94]:

$$\Delta\mu_A = -\lim_{s\to s_{\mathrm{cut}}} \frac{1}{d(d+2)V}\sum_l \left\langle s_l^2 u'_s(s_l)\,\delta(s_l - s)\right\rangle, \tag{2.61}$$

where $s_{\mathrm{cut}} = r_{\mathrm{cut}}/\sigma_{\mathrm{LJ}}$ is the reduced dimensionless cutoff distance.

However, it is not possible to calculate the impulsive correction for the polydisperse system (Chapter 4) using eq. 2.59: eq. 2.59 is not correct for such systems. In this case

the radial distribution function should be obtained by linear superposition of eq. 2.59 for different sizes of particles i and j [94]. Following ref. [93, 95], the pair potential $u_{\mathrm{LJ}}(r)$ scales as $u_{\mathrm{LJ}}(r) \equiv u_s(r/\sigma_{ij})$, where σ_i and σ_j are diameters of interacting particles, $\sigma_{ij} = (\sigma_i + \sigma_j)/2$ is their half-sum. To simplify notations, r/σ_{ij} can be replaced by a reduced dimensionless distance s, such as $s = r/\sigma_{ij}$. Now, eq. 2.58 can be written in the following way:

$$u_{\mathrm{LJ}}(s) = \begin{cases} 4\epsilon_{\mathrm{LJ}}\left[(s)^{-12} - (s)^{-6}\right] - 4\epsilon_{\mathrm{LJ}}\left[(s_{\mathrm{cut}})^{-12} - (s_{\mathrm{cut}})^{-6}\right], & \text{if } s < s_{\mathrm{cut}} \\ 0, & \text{otherwise} \end{cases} \tag{2.62}$$

where s_{cut} is the reduced cutoff radius and is the same for all interaction pairs, $s_{\mathrm{cut}} = r_{\mathrm{cut}}/\sigma_{ij} = 2^{7/6}$.

We developed a method which allows us to calculate μ_A without an additional calculation of the impulsive correction $\Delta\mu_A$. Focusing on the virial contribution to the μ_A, eq. 2.57, we have modified the second derivative of the potential energy, $u''_{\mathrm{LJ}}(s)$, by adding the additional contribution:

$$\tilde{u}''_{\mathrm{LJ}}(s) = u''_{\mathrm{LJ}}(s) + \mathrm{C} \cdot F(s), \tag{2.63}$$

where the constant $C = -\frac{1}{\Delta} \cdot u'_{\mathrm{LJ}}(s_{\mathrm{cut}})$ and the function $F(s)$ can be expressed as:

$$F(s) = \begin{cases} 4 - 6(s_{\mathrm{cut}} - s)/\Delta, & \text{if } 0 < (s_{\mathrm{cut}} - s) < \Delta \\ 0, & \text{otherwise} \end{cases} \tag{2.64}$$

where $\Delta \ll s_{\mathrm{cut}}$. As was shown in ref. [94], the second derivative of truncated and shifted potential is $u''_s(s) = u''(s)\,H(s_{\mathrm{cut}} - s) - u'(s)\delta(s_{\mathrm{cut}} - s)$, where $H(s_{\mathrm{cut}} - s)$ is the Heaviside step function. One can observe that the latter expression contains the delta-function term. As the delta-function $\delta(s - s_{\mathrm{cut}})$ shows the singularity at $s = s_{\mathrm{cut}}$, its smooth approximation given by the new function $F(s)$ is applied for our case. Therefore we can avoid a singular behavior because the new function $F(s)$ is finite.

Moreover, we successfully implemented directly in the LAMMPS the eqs. 2.63 and 2.64. This modification of the LAMMPS package allows us to reduce time of the calculation of μ_A. We choose $\Delta = 0.025$ which is about 1% of s_{cut}.

2.2.3 Pressure correlations

Let us start with explaining the further notations. We assume that at each temperature T we kept the data for m independent configurations obtained by the NPT tempering (the protocol of the equilibration is discussed in Chapters 3 and 4). This set of independent configurations $k = 1, 2, ..., m$ is called ensemble.

In the same way as in eq. 2.33, the total pressure autocorrelation function, $C_b(t)$, can be defined as:

$$C_b(t) = \langle \delta P(t + t') \, \delta P(t') \rangle \tag{2.65}$$

where $P(t) = -(\sigma_{xx}(t) + \sigma_{yy}(t))/2$, and $\delta P(t) = P(t) - P_k(t)$, $P(t)$ is the instantaneous total pressure of the k^{th} configuration from the ensemble, $P_k = \overline{P(t)}$ is the time-averaged value of the instantaneous total pressure $P(t)$ of the k^{th} configuration (the overbar $\overline{...}$ stands for the time-averaging, and $\langle ... \rangle$ for the ensemble-averaging).

Let us introduce a quantity which characterizes the elastic response with respect to a volumetric (dilatational) strain [93] and is called "bulk compression modulus" K_b. It has a similar physical meaning as the static compression modulus η (which is analogous to μ but concerns the total pressure rather than shear stress):

$$\eta = -V \frac{\partial P}{\partial V}\Big|_V = \rho \frac{\partial P}{\partial \rho}\Big|_V \tag{2.66}$$

and K_b also could be time dependent in analogy with $G(t)$. An expression derived by Rowlinson [96] allows us to compute $K_b^* = K_b(t \to \infty) = \eta$ as [93]:

$$K_b^* \equiv \eta_A - \eta_F, \tag{2.67}$$

where η_A is the "affine dilatational elasticity" (corresponding to μ_A) and η_F (corresponding to μ_F) [93] is the total pressure fluctuation modulus. The first term can be defined as $\eta_A \equiv K_b(0)$.

Introducing C_b from eq. 2.65 allows us to find the time-dependent bulk compression modulus $K_b(t)$ using the same FDT approach [6, 9, 93] leading to eq. 2.36:

$$K_b(t) = K_b(0) + \Big[C_b(t) - C_b(0) \Big] \frac{V}{T} \tag{2.68}$$

or

$$K_b(t) = \eta_A + \Big[C_b(t) - C_b(0) \Big] \frac{V}{T} \tag{2.69}$$

To calculate the fluctuation modulus η_F the same procedure as that resulted in eq. 2.50, by analogy with the fluctuation modulus μ_F, was used. One can split η_F into two parts η_0 and η_1 (analogous to μ_0 and μ_1):

$$\eta_F = \eta_0 - \eta_1 \tag{2.70}$$

with:

$$\eta_0 = (V/T) \left\langle \overline{(\delta P(t))^2} \right\rangle, \tag{2.71}$$

Using $\delta P(t) = P(t) - P_k$ instead of $P(t)$ allows us to reduce the numerical error for calculation of η_F, note that:

$$\eta_1 = (V/T) \left\langle \overline{\delta P(t)}^2 \right\rangle = 0 \tag{2.72}$$

The longitudinal modulus $K(t)$ is the coefficient between the stress increment σ_{xx} due to a small uniaxial extension along x-axis (the strain ϵ_{xx}) with no transverse strain (see eqs. 2.118 and 2.119) [9]. The time-dependent compression modulus K_b provides a connection with the longitudinal modulus $K(t)$ [97, 98]:

$$K(t) = K_b(t) + 2\frac{d-1}{d} G(t) \tag{2.73}$$

Let us now consider solid glassy systems which we consider to be equilibrated in the sense discussed before eq. 2.35. The free energy of such systems must change due to an imposed small pure shear strain γ in, for example, xy-plane in the $NV\gamma T$ ensemble (with fixed number of particles N, volume V and temperature T). For a plain shear strain with fixed volume V the excess part of the free energy contribution [93] is defined as:

$$F_{\text{ex}}(T, \gamma) = -k_{\text{B}} T \ln\left(Z_{\text{ex}}(\gamma)\right), \tag{2.74}$$

where γ is an imposed extremely small pure shear strain, T is the temperature, and $Z_{\text{ex}}(\gamma)$ is the excess partition function. Based on the derivation of the compression modulus by Rowlinson [93], the function $Z_{\text{ex}}(\gamma)$ can be expressed as:

$$Z_{\text{ex}}(\gamma) = \sum_s \exp\left(-\beta U_s(\gamma)\right), \tag{2.75}$$

where the sum is done over all the microstates s of the undeformed system, $U_s(\gamma) = \sum_{i<j} u\left(r_{ij}(\gamma)\right)$ is the total interaction energy, $r(\gamma) = \left((x+\gamma y)^2 + y^2\right)^{1/2}$, and $\beta = \frac{1}{k_{\text{B}}T}$.

Thus, $\sum_s$ in eq. 2.75 is equivalent to the integral over all coordinates $(x, y, ...)$ of all particles before the deformation. The excess partition function $Z_{\text{ex}}(\gamma)$ of the unperturbed solid system at $\gamma = 0$, $Z_{\text{ex}}(0)$, is the Boltzmann-weighted sum over all states s of the system which are accessible within the measurement time t (note that $Z_{\text{ex}}(\gamma)$ does not depend on t). For ideal gas $Z_{\text{ex}}(0) = \int_V \mathrm{d}^{3N} r \exp(-\beta U_s(0))$, where $U_s(0) = 0$, because there is no interaction between particles of ideal gas. This leads to $Z_{\text{ex}}(0) = \int_V \mathrm{d}^{3N} r = V^N$, where V is the volume of the system.

It was shown [93] that the derivatives of the excess partition function:

$$\frac{\partial \ln(Z_{\text{ex}}(\gamma))}{\partial \gamma} = \frac{Z'_{\text{ex}}(\gamma)}{Z_{\text{ex}}(\gamma)} \tag{2.76}$$

$$\frac{\partial^2 \ln(Z_{\text{ex}}(\gamma))}{\partial \gamma^2} = \frac{Z''_{\text{ex}}(\gamma)}{Z_{\text{ex}}(\gamma)} - \left(\frac{Z'_{\text{ex}}(\gamma)}{Z_{\text{ex}}(\gamma)}\right)^2 \tag{2.77}$$

where

$$\begin{aligned}
Z'_{\text{ex}}(\gamma) &= \frac{\partial Z_{\text{ex}}(\gamma)}{\partial \gamma} = -\sum_s \beta U'_s(\gamma) \exp(-\beta U_s(\gamma)), \\
Z''_{\text{ex}}(\gamma) &= \frac{\partial^2 Z_{\text{ex}}(\gamma)}{\partial \gamma^2} = \sum_s (\beta U'_s(\gamma))^2 \exp(-\beta U_s(\gamma)) - \sum_s \beta U''_s(\gamma) \exp(-\beta U_s(\gamma)), \\
U'_s(\gamma) &= \frac{\partial}{\partial \gamma} \sum_{i<j} u(r_{ij}(\gamma)) = \sum_{i<j} u'(r_{ij}(\gamma)) \frac{\partial r_{ij}(\gamma)}{\partial \gamma}, \\
U''_s(\gamma) &= \sum_{i<j} u''(r_{ij}(\gamma)) \left(\frac{\partial r_{ij}(\gamma)}{\partial \gamma}\right)^2 + \sum_{i<j} u'(r_{ij}(\gamma)) \frac{\partial^2 r_{ij}(\gamma)}{\partial \gamma^2}
\end{aligned} \tag{2.78}$$

Based on the latter expressions is it possible to define the static shear modulus μ and the shear stress tensor σ_{xy} in terms of γ [94]:

$$\mu \equiv \frac{\partial \sigma_{xy}(\gamma)}{\partial \gamma}|_{\gamma=0} \tag{2.79}$$

where $\sigma_{xy}(\gamma)$ is:

$$\sigma_{xy}(\gamma) \equiv \left\langle \frac{1}{V} U'_s(\gamma)|_{\gamma=0} \right\rangle \tag{2.80}$$

where the averaging $\langle ... \rangle$ is defined as [93]:

$$\langle ... \rangle = \frac{1}{Z_{\text{ex}}(\gamma)} \sum_s ... \exp(-\beta U_s(\gamma)) \tag{2.81}$$

The above equations lead to:

$$\sigma_{xy}(\gamma) = \frac{1}{V}\frac{\partial F_{\text{ex}}(T,\gamma)}{\partial \gamma} \tag{2.82}$$

The eqs. 2.76 – 2.78 stated for γ are still valid after replacing γ by relative volume change ε:

$$\varepsilon \equiv V(\varepsilon)/V(0) - 1, \tag{2.83}$$

where $V(0)$ is the volume of the unperturbed simulation box. It was derived in ref. [93] that the excess contribution P_{ex} to the total pressure P and the excess contribution K_{ex} to the total bulk compression modulus K_b are valid for an arbitrary conservative potential. One can define the instantaneous excess pressure $\hat{P}_{\text{ex}}$ using eq. 2.78 [93]:

$$\hat{P}_{\text{ex}}(0) \equiv -\frac{1}{V(0)}\frac{\partial U_s(\varepsilon)}{\partial \varepsilon}\Big|_{\varepsilon=0}, \tag{2.84}$$

where $\frac{\partial}{\partial\varepsilon}U_s(\varepsilon) = \frac{\partial}{\partial\varepsilon}\sum_{i<j}u(r_{ij}(\varepsilon)) = \sum_{i<j}u'(r_{ij}(\varepsilon))\frac{\partial r_{ij}(\varepsilon)}{\partial\varepsilon}$, where $r(\varepsilon) = r(0)(1+\varepsilon)^{1/d}$, d is the dimension, $\frac{\partial r(\varepsilon)}{\partial\varepsilon} = \frac{r(0)(1+\varepsilon)^{1/d}}{d(1+\varepsilon)}$, $\frac{\partial^2 r(\varepsilon)}{\partial\varepsilon^2} = \frac{r(0)(1-d)(1+\varepsilon)^{(1-2d)/d}}{d^2}$. The latter equation is related to the excess pressure P_{ex} such as $P_{\text{ex}} = \left\langle \hat{P}_{\text{ex}} \right\rangle$, where P_{ex} is defined as:

$$P_{\text{ex}}(\varepsilon) = -\frac{1}{V(0)}\frac{\partial F_{\text{ex}}(\varepsilon)}{\partial\varepsilon} \tag{2.85}$$

and the averaging $\langle ... \rangle$ is analogous to that defined in eq. 2.81 with γ replaced by ε.

It is possible to obtain the excess part of the static compression bulk modulus $K^*_{b,\text{ex}} = K_{b,\text{ex}}(t\to\infty)$ by taking the $\lim \varepsilon \to 0$ in eqs. 2.77, 2.78 [93], 2.85 and taking into account the first relation from eq. 2.66:

$$K^*_{b,\text{ex}} = V\frac{\partial^2 F_{\text{ex}}(V)}{\partial V^2} = -\frac{\partial P_{\text{ex}}(\varepsilon)}{\partial\varepsilon} = \frac{1}{V(0)}\frac{\partial^2 F_{\text{ex}}(\varepsilon)}{\partial\varepsilon^2} = \langle U_s''(\varepsilon)\rangle/V - \beta V\left\langle \delta\hat{P}^2_{\text{ex}} \right\rangle, \tag{2.86}$$

where $\varepsilon\to 0$, $U_s''(\varepsilon) = \sum_{i<j}u''(r_{ij}(\varepsilon))\left(\frac{\partial r_{ij}(\varepsilon)}{\partial\varepsilon}\right)^2 + \sum_{i<j}u'(r_{ij}(\varepsilon))\frac{\partial^2 r_{ij}(\varepsilon)}{\partial\varepsilon^2}$, $\left\langle \delta\hat{P}^2_{\text{ex}} \right\rangle$ is the variance of the excess part of the total pressure (the excess part of the total pressure is defined in eq. 2.92). The first term is called the excess contribution $\eta_{A,\text{ex}} = \langle U_s''(\varepsilon=0)\rangle/V$ to the affine dilatational elasticity η_A. The second term corresponds to the excess contribution $\eta_{F,\text{ex}}$.

The total pressure variance η_F can be written as:

$$\eta_F = \eta_{F,\mathrm{id}} + \eta_{F,\mathrm{ex}}, \tag{2.87}$$

where $\eta_{F,\mathrm{id}}$ is the ideal part of pressure fluctuations, and $\eta_{F,\mathrm{ex}}$ is the excess contribution due to the interactions between the particles. The relation 2.67 now becomes $K_b^* \equiv \eta = \eta_{\mathrm{id}} + \eta_{\mathrm{ex}}$ with:

$$\begin{aligned} \eta_{\mathrm{ex}} \equiv K^*_{b,\mathrm{ex}} &= \eta_{A,\mathrm{ex}} - \eta_{F,\mathrm{ex}}, \\ \eta_{\mathrm{id}} &= \eta_{A,\mathrm{id}} - \eta_{F,\mathrm{id}} \end{aligned} \tag{2.88}$$

The affine dilatational elasticity can be also defined as [93]:

$$\eta_A = \frac{d+2}{d} cT + \eta_{A,\mathrm{ex}}, \tag{2.89}$$

where $c = N/V$ is the concentration of the system at the temperature T, d is the dimension of the system, and $\eta_{A,\mathrm{ex}}$ is the excess part of the total η_A. The first term in eq. 2.89 corresponds to $\eta_{A,\mathrm{id}}$. In a similar way we find: $\eta_{F,\mathrm{id}} = (2/d)\, cT$. This leads to the result: $\eta_{\mathrm{id}} = cT$. The last term in eq. 2.89 can be re-expressed as:

$$\eta_{A,\mathrm{ex}} = \eta_B + P_{\mathrm{ex}}, \tag{2.90}$$

where η_B [93] is:

$$\eta_B = \frac{1}{d^2 V} \left\langle \sum_l r_l^2 u''(r_l) + r_l u'(r_l) \right\rangle, \tag{2.91}$$

and P_{ex} means the excess part of the total pressure and can be written as:

$$P_{\mathrm{ex}} = -\frac{1}{dV} \left\langle \sum_l r_l u'(r_l) \right\rangle \tag{2.92}$$

For the total pressure P_{tot} one can introduce the following formula:

$$P_{\mathrm{ex}} = P_{\mathrm{tot}} - cT \tag{2.93}$$

Combining eqs. 2.91, 2.92 and 2.93, eq. 2.90 can be written as:

$$\eta_{A,\mathrm{ex}} = -\frac{1}{dV} \left\langle \sum_l r_l u'(r_l) \right\rangle + \frac{1}{d^2 V} \left\langle \sum_l r_l^2 u''(r_l) + r_l u'(r_l) \right\rangle \tag{2.94}$$

Based on that, eq. 2.89 can be expressed in a new way:

$$\eta_A = -\frac{1}{dV} \left\langle \sum_l r_l u'(r_l) \right\rangle + \frac{1}{d^2 V} \left\langle \sum_l r_l^2 u''(r_l) + r_l u'(r_l) \right\rangle + \frac{d+2}{d} cT \tag{2.95}$$

To calculate $\eta_{A,\mathrm{ex}}$ in the simulations we proceeded as follows. The affine modulus μ_A was calculated using the general eqs. 2.57 and 2.59 [7, 94]. Recalling the macroscopic isotropy of the system, we tried a different approach to obtain instant $\tilde{\mu}_A$ using pre-averaging over all possible shear planes. The resultant expression for the preaveraged instant μ_A does not involve bond orientations and can be conveniently written as:

$$\mu_A^{\mathrm{or}} = \frac{1}{d(d+2)} \frac{1}{V} \sum_l \left[r_l^2 u''(r_l) + (d+1) \cdot r_l \cdot u'(r_l) \right] + cT, \tag{2.96}$$

where d is the space dimension.

As was shown and discussed in ref. [6] the orientational-averaged formula for μ_A^{or} allows us to decrease fluctuations of μ_A. It is then possible to express η_A in terms of μ_A^{or}:

$$\eta_A = \frac{d+2}{d} cT + \left(1 + \frac{2}{d}\right) \left(\mu_A^{\mathrm{or}} + P_{\mathrm{tot}} - 2cT\right) - \frac{2}{d} \left(P_{\mathrm{tot}} - cT\right) + P_{\mathrm{tot}} - cT \tag{2.97}$$

After simplification of eq. 2.97, the new form of η_A is:

$$\eta_A = \left(1 + \frac{2}{d}\right) \mu_A^{\mathrm{or}} + 2P_{\mathrm{tot}} - 2cT \tag{2.98}$$

2.2.4 Stress correlations in q-space

Let us start with the definition of the space-resolved microscopic stress at point $\boldsymbol{r}$, $\sigma_{\alpha\beta}^{\mathrm{micro}}(\boldsymbol{r}, t)$ [80, 99]:

$$\begin{aligned} \sigma_{\alpha\beta}^{\mathrm{micro}}(\boldsymbol{r}, t) = &- \frac{1}{2} \sum_{j \neq i}^{N} \boldsymbol{F}_{ij}^{\alpha}(t) \, \boldsymbol{r}_{ij}^{\beta}(t) \int_0^1 \mathrm{d}\alpha \cdot \delta\left(\boldsymbol{r}_i - \boldsymbol{r} - \alpha \boldsymbol{r}_{ij}\right) \\ &- \sum_{j=1}^{N} m_j \boldsymbol{v}_j^{\alpha}(t) \, \boldsymbol{v}_j^{\beta}(t) \, \delta\left(\boldsymbol{r}_j - \boldsymbol{r}\right) \end{aligned} \tag{2.99}$$

where $\boldsymbol{F}_{ij}^{\alpha}$ is the interaction force applied along direction α by particle j on particle i, $\boldsymbol{r}_{ij}^{\beta}$ is the vector connecting particles i and j along β direction (a schematic representation for 2 particles is shown in Fig. 2.2), $\boldsymbol{r}$ is a point on the lattice, $\boldsymbol{v}_j^{\beta}$ and $\boldsymbol{v}_j^{\alpha}$ are velocities along the β and α direction respectively, $\boldsymbol{r}_j$ and $\boldsymbol{r}_i$ are positions of particles j and i, $\boldsymbol{r}_{ij} = \boldsymbol{r}_i - \boldsymbol{r}_j$, and $\delta\left(\boldsymbol{r}_i - \boldsymbol{r}\right)$ is the Dirac's delta-function.

Based on eq. 2.99 one can define microscopic stress tensor (in terms of particle coor-

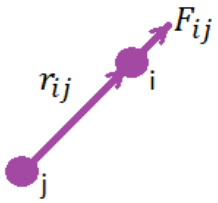

Figure 2.2: The schematic presentation of the interacting force F_{ij} applied along direction α by particle j on particle i.

dinates and interaction potentials) of the mean stress $\sigma_{\alpha\beta}(t)$ [80]:

$$\begin{aligned}
\sigma_{\alpha\beta}(t) &= \frac{1}{V}\int \mathrm{d}^{\mathrm{d}}r \cdot \sigma^{\mathrm{micro}}_{\alpha\beta}(\boldsymbol{r},t) = \\
&= \frac{1}{V}\int \mathrm{d}^{\mathrm{d}}r\Big[-\frac{1}{2}\sum_{j\neq i}^{N}\boldsymbol{F}^{\alpha}_{ij}(t)\,\boldsymbol{r}^{\beta}_{ij}(t)\int_0^1 \mathrm{d}\alpha\cdot\delta\left(\boldsymbol{r}_i-\boldsymbol{r}-\alpha\boldsymbol{r}_{ij}\right) \\
&- \sum_{j=1}^{N} m_j \boldsymbol{v}^{\alpha}_j(t)\,\boldsymbol{v}^{\beta}_j(t)\,\delta\left(\boldsymbol{r}_j-\boldsymbol{r}\right)\Big] \\
&= -\frac{1}{2}\frac{1}{V}\sum_{j\neq i}^{N}\boldsymbol{F}^{\alpha}_{ij}(t)\,\boldsymbol{r}^{\beta}_{ij}(t)\int \mathrm{d}^{\mathrm{d}}r\int_0^1 \mathrm{d}\alpha\cdot\delta\left(\boldsymbol{r}_i-\boldsymbol{r}-\alpha\boldsymbol{r}_{ij}\right) \\
&- \frac{1}{V}\sum_{j=1}^{N} m_j \boldsymbol{v}^{\alpha}_j(t)\,\boldsymbol{v}^{\beta}_j(t)\int \mathrm{d}^{\mathrm{d}}r\,\delta\left(\boldsymbol{r}_j-\boldsymbol{r}\right) \\
&= -\frac{1}{2}\frac{1}{V}\sum_{j\neq i}^{N}\boldsymbol{F}^{\alpha}_{ij}(t)\,\boldsymbol{r}^{\beta}_{ij}(t) - \frac{1}{V}\sum_{j=1}^{N} m_j \boldsymbol{v}^{\alpha}_j(t)\,\boldsymbol{v}^{\beta}_j(t)
\end{aligned} \tag{2.100}$$

The key to the spatial averaging is the weight function $\phi(\boldsymbol{r})$. To obtain the coarse-grained local stress tensor at point $\boldsymbol{r}$, one can use the Goldhirsch and Goldenberg approach [11, 100] using a smooth function ϕ instead of the delta-function:

$$\sigma_{\alpha\beta}(\boldsymbol{r},t) = -\frac{1}{2}\sum_{j\neq i}^{N}\boldsymbol{F}^{\alpha}_{ij}(t)\,\boldsymbol{r}^{\beta}_{ij}(t)\int_{s=0}^{1}\mathrm{d}s\phi\left(\boldsymbol{r}_i-\boldsymbol{r}+s\boldsymbol{r}_{ij}\right) - \sum_{j=1}^{N} m_j \boldsymbol{v}^{\alpha}_j(t)\,\boldsymbol{v}^{\beta}_j(t)\,\phi\left(\boldsymbol{r}_j-\boldsymbol{r}\right), \tag{2.101}$$

where the function $\phi > 0$ and vanishes beyond r_{c} (not to be confused with r_{cut}). It follows from the definition of the weight function that $\int \mathrm{d}^{\mathrm{d}}r\phi(\boldsymbol{r}) = 1$. It is easy to see that relation between $\sigma_{\alpha\beta}(\boldsymbol{r},t)$ and $\sigma^{\mathrm{micro}}_{\alpha\beta}(\boldsymbol{r},t)$ still holds when in replacing delta-function $\delta(\boldsymbol{r})$ from eq. 2.101 with the weight function $\phi(\boldsymbol{r})$ from eq. 2.100.

To calculate the local stress tensor in q-space, one can apply the Fourier transform [11,

62] to eqs. 2.99 and 2.101:

$$\begin{aligned}\hat{\sigma}_{\alpha\beta}^{\text{micro}}(\boldsymbol{q}) = &-\sum_{j\neq i}^{N} \boldsymbol{F}_{ij}^{\alpha}(t)\,\boldsymbol{r}_{ij}^{\beta}(t)\exp\left(-\mathrm{i}\boldsymbol{q}\cdot\overline{\boldsymbol{r}}_{ij}\right)\sin\left(\boldsymbol{q}\cdot\boldsymbol{r}_{ij}/2\right)/(\boldsymbol{q}\cdot\boldsymbol{r}_{ij}) \\ &-\sum_{j=1}^{N} m_j \boldsymbol{v}_j^{\alpha}(t)\,\boldsymbol{v}_j^{\beta}(t)\exp\left(-\mathrm{i}\boldsymbol{q}\cdot\boldsymbol{r}_j\right),\end{aligned} \tag{2.102}$$

where $\overline{\boldsymbol{r}}_{ij} = (\boldsymbol{r}_i + \boldsymbol{r}_j)/2$ is the mid point of each pair. The Fourier transform of the local stress tensor in q-space with weighted function now becomes [11, 100]:

$$\begin{aligned}\sigma_{\alpha\beta}(\boldsymbol{q}) = \hat{\phi}(\boldsymbol{q})\Big[&-\sum_{j\neq i}^{N} \boldsymbol{F}_{ij}^{\alpha}(t)\,\boldsymbol{r}_{ij}^{\beta}(t)\exp\left(-\mathrm{i}\boldsymbol{q}\cdot\overline{\boldsymbol{r}}_{ij}\right)\sin\left(\boldsymbol{q}\cdot\boldsymbol{r}_{ij}/2\right)/(\boldsymbol{q}\cdot\boldsymbol{r}_{ij}) \\ &-\sum_{j=1}^{N} m_j \boldsymbol{v}_j^{\alpha}(t)\,\boldsymbol{v}_j^{\beta}(t)\exp\left(-\mathrm{i}\boldsymbol{q}\cdot\boldsymbol{r}_j\right)\Big] = \hat{\phi}(\boldsymbol{q})\,\hat{\sigma}_{\alpha\beta}^{\text{micro}}(\boldsymbol{q})\end{aligned} \tag{2.103}$$

where $\hat{\phi}(\boldsymbol{q})$ is the Fourier transform of the weight function $\phi(\boldsymbol{r})$. To prove consistency between eqs. 2.103 and 2.100 let us find a $q \to 0$ limit:

$$\begin{aligned}\frac{1}{V}\lim_{q\to 0}\sigma_{\alpha\beta}(\boldsymbol{q}) = \frac{1}{V}\lim_{q\to 0}\hat{\phi}(\boldsymbol{q})\Big[&-\sum_{j\neq i}^{N} \boldsymbol{F}_{ij}^{\alpha}(t)\,\boldsymbol{r}_{ij}^{\beta}(t)\exp\left(-\mathrm{i}\boldsymbol{q}\cdot\overline{\boldsymbol{r}}_{ij}\right)\sin\left(\boldsymbol{q}\cdot\boldsymbol{r}_{ij}/2\right)/(\boldsymbol{q}\cdot\boldsymbol{r}_{ij}) \\ &-\sum_{j=1}^{N} m_j \boldsymbol{v}_j^{\alpha}(t)\,\boldsymbol{v}_j^{\beta}(t)\exp\left(-\mathrm{i}\boldsymbol{q}\cdot\boldsymbol{r}_j\right)\Big] \\ = -\frac{1}{2V}\sum_{j\neq i}^{N} &\boldsymbol{F}_{ij}^{\alpha}(t)\,\boldsymbol{r}_{ij}^{\beta}(t) - \frac{1}{V}\sum_{j=1}^{N} m_j \boldsymbol{v}_j^{\alpha}(t)\,\boldsymbol{v}_j^{\beta}(t) = \sigma_{\alpha\beta}(t)\end{aligned} \tag{2.104}$$

Let us turn to the space-resolved correlations of the local shear stress $\sigma_{xy}(\boldsymbol{r}, t)$:

$$C(\boldsymbol{r}, t) = \langle \sigma_{xy}(\boldsymbol{r}', t')\,\sigma_{xy}(\boldsymbol{r}' + \boldsymbol{r}, t' + t)\rangle \tag{2.105}$$

This generalized shear stress correlation function is also related to rheological characteristics of the fluid (see the sections below). The distance-dependent stress correlations have been considered in recent simulation studies [11] as well as theoretically [12]. These studies show that the stress correlation function is both nonlocal and anisotropic.

The stress correlation function is defined in the general case as a tensor:

$$C_{\alpha\beta\alpha'\beta'}(\boldsymbol{r}, t) = \langle \tilde{\sigma}_{\alpha'\beta'}(\boldsymbol{r}', t')\,\tilde{\sigma}_{\alpha\beta}(\boldsymbol{r}' + \boldsymbol{r}, t' + t)\rangle, \tag{2.106}$$

where $\langle ... \rangle$ means averaging over an equilibrium ensemble, $\tilde{\sigma}_{\alpha\beta}(\boldsymbol{r},t) = \sigma_{\alpha\beta}(\boldsymbol{r},t) - \langle \sigma_{\alpha\beta} \rangle$ is the tensor of local stress increments, $\alpha, \beta, ...$ are Cartesian components, and $\langle \sigma_{\alpha\beta} \rangle = \langle \sigma_{\alpha\beta}(\boldsymbol{r},t) \rangle$ is the stress tensor averaged over the equilibrium ensemble (the system is assumed to be translational-invariant and stationary). The function C has obvious symmetries: it is invariant with respect to exchanges $\alpha\beta \to \beta\alpha$, $\alpha'\beta' \to \beta'\alpha'$, and $C_{\alpha\beta\alpha'\beta'}(\boldsymbol{r},t) = C_{\alpha'\beta'\alpha\beta}(-\boldsymbol{r},-t)$ [9].

The time reversibility and uniformity demand that:

$$C_{\alpha\beta\alpha'\beta'}(\boldsymbol{r},t) = C_{\alpha'\beta'\alpha\beta}(-\boldsymbol{r},t) = C_{\alpha\beta\alpha'\beta'}(\boldsymbol{r},-t) \tag{2.107}$$

In addition, all even-dimensional systems and all achiral systems obey:

$$C_{\alpha\beta\alpha'\beta'}(\boldsymbol{r},t) = C_{\alpha\beta\alpha'\beta'}(-\boldsymbol{r},t) \tag{2.108}$$

hence

$$C_{\alpha\beta\alpha'\beta'}(\boldsymbol{r},t) = C_{\alpha'\beta'\alpha\beta}(\boldsymbol{r},t) \tag{2.109}$$

The general fluctuation-dissipation theorem (FDT) relates the function C with the linear response of stress to a small instant deformation of the system at $t = -0$ like:

$$\boldsymbol{r} \to \boldsymbol{r} + \underline{u}(\boldsymbol{r}), \tag{2.110}$$

where $\underline{u}(\boldsymbol{r})$ is an infinitesimal particle-displacement field (the particle momenta $\boldsymbol{p}$ are also changed to render the whole transformation canonical in the Hamiltonian phase-space of the system: $p_\alpha \to p_\alpha - u_{\beta,\alpha} p_\beta$, where $u_{\beta,\alpha} = \partial u_\beta / \partial r_\alpha$). Then, according to the FDT the mean stress increment $\langle \tilde{\sigma}_{\alpha\beta} \rangle$ induced by the infinitesimal strain field:

$$\gamma_{\alpha\beta}(\boldsymbol{r}) = u_{\beta,\alpha} + u_{\alpha,\beta} \tag{2.111}$$

can be written as:

$$\langle \sigma_{\alpha\beta}(\boldsymbol{r},t) \rangle = \frac{1}{2T} \int d^d r' C_{\alpha\beta\alpha'\beta'}(\boldsymbol{r}-\boldsymbol{r}',t)\, \gamma_{\alpha'\beta'}(\boldsymbol{r}'), \tag{2.112}$$

where d is the space dimension and the "tilde" over σ is omitted here and below, and summation over repeated indices is implied. Note that $\langle \sigma_{\alpha\beta} \rangle$ means an out-of-equilibrium

average stress increment due to an applied field here and below. Summation over α' and β' is essential in eq. 2.112. Doing Fourier transformation of the last equation we get:

$$\langle \sigma_{\alpha\beta}(\boldsymbol{q},t)\rangle = \frac{1}{2T} C_{\alpha\beta\alpha'\beta'}(\boldsymbol{q},t)\,\gamma_{\alpha'\beta'}(\boldsymbol{q}), \tag{2.113}$$

where $C_{\alpha\beta\alpha'\beta'}(\boldsymbol{q},t) = \frac{1}{V}\left\langle \sigma_{\alpha\beta}(\boldsymbol{q},t)\,\sigma^*_{\alpha'\beta'}(\boldsymbol{q},0)\right\rangle$. Note that the Fourier transforms of C and γ are indicated by the wave-vector argument $\boldsymbol{q}$, while the functions are not changed for notation simplicity. Note that eqs. 2.107 and 2.108 imply that $C_{\alpha\beta\alpha'\beta'}(\boldsymbol{q},t)$ is real and does not depend on the sign of t:

$$C_{\alpha\beta\alpha'\beta'}(\boldsymbol{q},t) = C_{\alpha\beta\alpha'\beta'}(\boldsymbol{q},-t) = C^*_{\alpha\beta\alpha'\beta'}(\boldsymbol{q},t) \tag{2.114}$$

Let us try to obtain the stress correlation function C using the FDT relation 2.113 and based on the known relaxation moduli. To this end we first find the stress response to the deformation of the system using an independent approach outlined in ref. [10]. In the linear response approximation the mean stress must be a linear function of the flow velocity field. For a Newtonian fluid the local stress is just proportional to the local rate-of-strain $\dot\gamma_{\alpha\beta}(\boldsymbol{r}) = v_{\alpha,\beta} + v_{\beta,\alpha}$ (here $v_\alpha = v_\alpha(\boldsymbol{r},t)$ is the flow velocity), while in the general case of a complex fluid with memory effects the relation is:

$$\langle \sigma_{\alpha\beta}(\boldsymbol{q},t)\rangle = \frac{1}{2}\int_{-\infty}^{t} E_{\alpha\beta\alpha'\beta'}(\boldsymbol{q},t-t')\,\dot\gamma_{\alpha'\beta'}(\boldsymbol{q},t')\,dt' \tag{2.115}$$

Note that E is symmetric with respect to α', β' permutations and eq. 2.115 can be used to predict the stress field if the flow field is known (is imposed or prescribed). Using Laplace transformation the latter equation can be written as (in what follows we assume no flow at $t<0$):

$$\langle \sigma_{\alpha\beta}(\boldsymbol{q},s)\rangle = E_{\alpha\beta\alpha'\beta'}(\boldsymbol{q},s)\,\dot\gamma_{\alpha'\beta'}(\boldsymbol{q},s)/2, \tag{2.116}$$

where $\langle \sigma_{\alpha\beta}(\boldsymbol{q},s)\rangle = \int_0^\infty \langle \sigma_{\alpha\beta}(\boldsymbol{q},t)\rangle\, e^{-st}\mathrm{d}t$, etc. (A special case of the above relation was employed before [10]). Taking into account the space isotropy and that:

$$\dot\gamma_{\alpha\beta}(\boldsymbol{q},s) = i\left(q_\alpha v_\beta(\boldsymbol{q},s) + q_\beta v_\alpha(\boldsymbol{q},s)\right), \tag{2.117}$$

the stress response to the flow can be written as:

$$\langle \sigma_{\alpha\beta}(\boldsymbol{q},s)\rangle = G(q,s)\,\dot\gamma_{\alpha\beta}(\boldsymbol{q},s) + \dot\varepsilon\left[M(q,s)\,\delta_{\alpha\beta} + (K-2G-M)\,\frac{q_\alpha q_\beta}{q^2}\right], \tag{2.118}$$

where $\dot{\varepsilon} = \dot{\varepsilon}(\boldsymbol{q}, s) = \frac{1}{2}\operatorname{Tr}\dot{\gamma}$, and $G(q,s)$, $K = K(q,s)$, $M = M(q,s)$ are Laplace transforms of the following 3 material functions (the generalized time-dependent relaxation moduli): the shear modulus $G(q,t)$, the longitudinal modulus $K(q,t)$ (not to be confused with the bulk modulus) and the mixed modulus $M(q,t)$ which all depend on magnitude $|\boldsymbol{q}|$ of the wave-vector (but do not depend on its direction). The physical meaning of these material functions is clear: $G(q,t)$ defines the shear stress response to a shear strain, while $K(q,t)$ and $M(q,t)$ define, respectively, the longitudinal and transverse stress generated by a longitudinal strain (by transverse stress we mean the normal stress in a direction perpendicular to $\boldsymbol{q}$).

More formally, these definitions can be presented using the natural coordinate frame with the first axis ($\boldsymbol{e}_1$) parallel to $\boldsymbol{q}$. The response to an instant deformation $\underline{v}(t) = \underline{u}\delta(t)$ with $\underline{u} = (u_1, u_2, 0)$ then reads (here $\delta(t)$ is the Dirac's delta):

$$\langle \sigma_{11}(\boldsymbol{q}, t)\rangle = K(q,t)\,\varepsilon,\ \langle \sigma_{22}(\boldsymbol{q}, t)\rangle = M(q,t)\,\varepsilon,\ \langle \sigma_{12}(\boldsymbol{q}, t)\rangle = G(q,t)\,\gamma, \tag{2.119}$$

where $\varepsilon = iqu_1$, and $\gamma = iqu_2$ (all other components of the induced stress, except σ_{11}, σ_{22} and $\sigma_{21} = \sigma_{12}$, are equal zero). The moduli G, K, M are related to the components of the tensor $E_{\alpha\beta\alpha'\beta'}$: $G = E_{1212}$, $K = E_{1111}$ and $M = E_{2211}$.

Eqs. 2.119 are valid if an external time-dependent force is applied to the fluid in order to keep it still (no flow, $\underline{v} = 0$) at $t > 0$. Otherwise, if no external force is applied, the fluid motion is defined by the momentum equation:

$$\frac{\partial}{\partial t} J_\alpha = \sigma_{\alpha\beta,\beta},\ t > 0 \tag{2.120}$$

where $J_\alpha = \rho v_\alpha$ is the momentum density and ρ is the fluid mass per unit volume. Within the linear approximation we can treat ρ as a constant (the mean density of the fluid) and rewrite the above equation in terms of the ensemble-averaged quantities:

$$\rho\frac{\partial}{\partial t}\langle v_\alpha\rangle = iq_\beta\langle\sigma_{\alpha\beta}\rangle,\ t > 0 \tag{2.121}$$

Solving eqs. 2.121 and 2.118 for the stress $\langle\sigma_{\alpha\beta}(\boldsymbol{q}, t)\rangle$ and comparing the results with eqs. 2.113 we get (using again a natural coordinate frame related to a given $\boldsymbol{q} \neq 0$):

$$C_T(q,s) \equiv C_{1212}(\boldsymbol{q}, s) = T\frac{\rho s G(q,s)}{\rho s + q^2 G(q,s)} \tag{2.122}$$

$$C_{||}(q,s) \equiv C_{1111}(\boldsymbol{q}, s) = T\frac{\rho s K(q,s)}{\rho s + q^2 K(q,s)} \tag{2.123}$$

$$C_{\perp}(q,s) \equiv C_{2211}(\boldsymbol{q},s) = T\frac{\rho s M(q,s)}{\rho s + q^2 K(q,s)}, \tag{2.124}$$

where $C_{\alpha\beta\alpha'\beta'}(\boldsymbol{q},s) = \int_0^\infty C_{\alpha\beta\alpha'\beta'}(\boldsymbol{q},t)\exp(-st)\,\mathrm{d}t$.

Eq. 2.122 is well-established [98, 101]; its FDT-based derivation is given in ref. [10]. The second relation of eq. 2.123 is mentioned in ref. [97].

It is worth stressing again that the above results are valid for $q \neq 0$. The situation for $q = 0$ is more subtle [93, 97]: in this case the fluctuations of mean stress averaged over the whole system are involved; their dynamics and statistics depend on the boundary conditions. If the total volume and shape of the system are not allowed to fluctuate (which is often the most convenient option for computer simulations), then $C_{\parallel}(0,t)$ and $C_T(0,t)$ may not coincide with $\lim_{q\to 0} C_{\parallel}(q,t)$ and $\lim_{q\to 0} C_T(q,t)$ [97], As a result, the FDT relations for $q = 0$ in the general case become [7, 91, 93, 97]:

$$C_{\parallel}(0,t) = T\left[K(t) - K_e\right],\ C_T(0,t) = T\left[G(t) - G_e\right] \tag{2.125}$$

where $G(t) = G(q=0,t)$, $K(t) = K(q=0,t)$, and K_e and G_e are the equilibrium longitudinal and shear moduli (for infinitesimal strain), respectively ($G_e > 0$ for cross-linked polymer systems or crystalline solids, but $G_e = 0$ for uncrosslinked systems like liquids and amorphous systems considered herein). We do not consider here non-ergodic amorphous systems below the putative ideal glass transition temperature T_K which may exhibit $G_e > 0$ [102, 103]. In our view the finite rigidity in this regime is due to some (hidden) long-range static structural correlations. To avoid fictitious problems (arriving at $G_e = 0$ even for crystalline solids [104]) we define the moduli taking first the limit of infinitesimal strain, $\gamma \to 0$, and then the thermodynamic limit, the number of particles $N \to \infty$.

As for the 3$^{\mathrm{rd}}$ correlation function $C_{\perp}(0,t)$, it is not independent for $q = 0$:

$$C_{\perp}(0,t) = C_{\parallel}(0,t) - 2C_T(0,t)\ \left(\text{since } M(0,t) = K(0,t) - 2G(0,t)\right) \tag{2.126}$$

It is important that the stress correlation function $C_{\alpha\beta\alpha'\beta'}(\boldsymbol{q},t)$ is discontinuous at $q = 0$. For example, $\lim_{q\longrightarrow 0} C_{\parallel}(q,t) \neq C_{\parallel}(q=0,t)$ in the general case [97]. Moreover, $C_{\alpha\beta\alpha'\beta'}(q=0,t)$ is also known to be notoriously ensemble-dependent [9, 78, 97]. By contrast, the correlation function $C_{\alpha\beta\alpha'\beta'}(q,t)$ for a finite q is independent of the statistical ensemble in the thermodynamic limit, $N \to \infty$. That is why in what follows we focus on the $q \neq 0$ regime for the stress correlation function.

The FDT-based relations 2.122, 2.123 and 2.124 provide 3 independent components of the stress correlation tensor $C_{\alpha\beta\alpha'\beta'}$. However, the whole tensor function C remains yet unknown as it generally involves 4 or 5 independent components in total (including C_{2222} for 2-dimensional systems, and, in addition, C_{2233} in 3 dimensions). These extra components cannot be derived from any FDT relation, nor can they be directly expressed in terms of a material function like those considered above. (Note that the number of independent material functions (= 3) is defined mathematically by the most general linear relationship (as given in eq. 2.118) between the tensor σ and the vector $\boldsymbol{v}$, compatible with the system isotropy and involving the second vector $\boldsymbol{q}$.) Fortunately, however, all the stress-correlation components can be calculated in the hydrodynamic regime as will be discussed below.

2.3 Hydrodynamic fluctuations

In what follows we focus on the dynamics at long length-scales and therefore small wave-vectors $\boldsymbol{q}$, $qa_m \ll 1$, where a_m is the molecular size. The details of the short-scale structure (at length scale $\sim a_m$) and the short-time processes (like molecular collisions with the time-scale τ_m) are disregarded (wiped-out) within the adopted hydrodynamic approach. Of course, thermal fluctuations drive the fluid motion also at large scales. Such slow motions are explicitly taken into account in the model considered below.

According to this approach the local stress field can be generally represented as a sum of 2 contributions (the treatment given here is close in spirit to the classical fluctuation theories [105]):

$$\sigma_{\alpha\beta}\left(\boldsymbol{q},t\right)=\sigma^{\mathcal{D}}_{\alpha\beta}\left(\boldsymbol{q},t\right)+\sigma^{n}_{\alpha\beta}\left(\boldsymbol{q},t\right), \tag{2.127}$$

where the first term $\sigma^{\mathcal{D}}$ is the "regular" flow-generated stress defined by the current strain and strain rate or, more generally, by the whole flow (deformation) history; $\sigma^{\mathcal{D}}$ depends on the flow in the linear-response fashion reflected in eq. 2.115. The linear response is valid since the flow is weak at long length-scales, $qa_m \ll 1$. The second term σ^n is the random stress due to structural (packing) irregularities and thermal fluctuations of particle velocities (thermal noise) which is independent of the macroscopic flow for the same reason: weak flow does not affect much the local fluid structure defining the noise σ^n.

To obtain the noise correlation function:

$$C^n_{\alpha\beta\alpha'\beta'}(\boldsymbol{q},t) = \frac{1}{V}\left\langle \sigma^n_{\alpha\beta}(\boldsymbol{q},t+t')\,\sigma^{n*}_{\alpha\beta}(\boldsymbol{q},t)\right\rangle \tag{2.128}$$

we recall that σ^n reflects thermal fluctuations of the fluid structure. Such structural correlations are always short-range in a fluid, their range ξ_s is comparable to a_m. Fragile glass-forming liquids are characterized by a super-Arrhenius increase of the relaxation time on cooling towards T_g. An actively debated question is whether the associated increase of the activation energy is caused by the growth of an underlying static glass correlation length ξ_s [2,50,106,107]. Since static pair correlations (as measured by the static structure factor) do not change much with decreasing temperature, a length scale extracted from these correlations is unlikely to be a suitable candidate for ξ_s. Recent suggestions involve point-to-set correlations which increase more strongly, but typically do not exceed a few a_m over the range of temperatures accessible to computer simulations [106]. However, even for temperatures approaching the laboratory T_g, ξ_s would not need to exceed more than $\sim 10a_m$ in order to explain the super-Arrhenius behavior of the relaxation time [106]. So, the growth of ξ_s in glass-forming liquids is expected to be rather limited [2,108,109].

Therefore, the q-dependence of C^n must be weak for $q\xi_s \ll 1$. Hence, C^n can be approximated by setting $q = 0$. Conveniently, for $q = 0$ the fixed boundary conditions also eliminate the flow (i.e., $\sigma^{\mathcal{D}} = 0$), so the random stress σ^n coincides with the total stress in this case. The correlation function C^n can then be obtained using eq. 2.125:

$$\frac{1}{T}C^n_{\alpha\beta\alpha'\beta'}(\boldsymbol{q},t) \simeq \frac{1}{T}C^n_{\alpha\beta\alpha'\beta'}(0,t) = [G(t)-G_e]\left(\delta_{\alpha\alpha'}\delta_{\beta\beta'}+\delta_{\alpha\beta'}\delta_{\alpha'\beta}\right)+[M(t)-M_e]\,\delta_{\alpha\beta}\delta_{\alpha'\beta'}, \tag{2.129}$$

where $M(t) = K(t) - 2G(t)$, $M_e = K_e - 2G_e$ and it is taken into account that at $q = 0$ the stress correlation tensor must be isotropic. For liquids therefore:

$$C^n_{\alpha\beta\alpha'\beta'}(\boldsymbol{q},t) \to 0 \text{ at } t \to \infty, \tag{2.130}$$

as is should be since the mean random stress must vanish due to its fluctuation nature in the liquid state $\left(\lim_{t_{\max}\to\infty}\frac{1}{t_{\max}}\int_0^{t_{\max}}\sigma^n(t)\,\mathrm{d}t = 0\right)$.

The correlation function C of the total stress can then be obtained by solving the general momentum eq. 2.120 with the total stress defined in eq. 2.127, where $\sigma^{\mathcal{D}}$ can be calculated using eqs. 2.115 and 2.118, while the σ^n contribution can be considered as an independent driving force whose statistics are defined in eqs. 2.128 and 2.129. The

independence of σ^n permits one to formally consider it as weak "external force" applied to the fluid particles and generating their slow motion.

It is important that the relaxation moduli involved in eq. 2.118 are analytical functions of $\boldsymbol{q}$ since the deformation-generated stress is defined by the local structure of the system (local correlations of the neighboring interacting particles). Hence the $\boldsymbol{q}$-dependence of the material function must be weak for length-scales exceeding the structural correlation length ξ_s comparable with the molecular size (and interaction length), a_m. In particular, we can neglect the $\boldsymbol{q}$-dependence of the generalized viscosity $\eta(\boldsymbol{q}) = \int_0^\infty G(q,t)\,\mathrm{d}t$. This dependence was studied in detail by simulations of a model glass-former [110] showing that while $\eta(\boldsymbol{q})$ is significantly lower than the macroscopic viscosity $\eta = \eta(0)$ for $\boldsymbol{q}\xi_\eta \gtrsim 1$, the $\boldsymbol{q}$-dependence of the generalized viscosity can be neglected for $\boldsymbol{q}\xi_\eta \ll 1$, where the characteristic viscosity-based length ξ_η grows up to $\sim$4 particle diameters ($\sim 4a_m$) in a highly supercooled state. It appears therefore that ξ_η is similar to the static correlation length ξ_s which typically increases up to $\sim$5 particle diameters near T_g [108, 109, 111]. Accordingly, the condition $\boldsymbol{q}\xi_s \ll 1$ is applied in what follows to specify the region where the material functions are nearly independent of $\boldsymbol{q}$.

It is also noteworthy that in some systems (like, polymer fluids) the molecules are large, so there is a significant range between the atomic size and a_m where the relaxation modulus $G(q,t)$ are the generalized viscosity $\eta(q)$ may significantly depend on $\boldsymbol{q}$; this dependence has been calculated in ref. [10]. In what follows, however, we consider a more universal regime of longer length-scales, $1/q \gg a_m$, ξ_s, where the material functions can be approximated by the $\boldsymbol{q} = 0$ limit, $G(t) = G(0,t)$, etc. (since the relaxation moduli are continuous at $\boldsymbol{q} = 0$):

$$G(q,t) \simeq G(t)\,,\; K(q,t) \simeq K(t)\,,\; M(q,t) \simeq K(t) - 2G(t) \tag{2.131}$$

The last equation follows merely from the fact that at $\boldsymbol{q} = 0$ the stress (in eq. 2.118) must not depend on the orientation of $\boldsymbol{q}$, so $K - 2G - M = 0$. Thus, only two functions, $G(t)$ anf $K(t)$, are involved in the regime of interest. These functions can be directly measured in rheological and acoustic experiments [62, 105, 112].

In what follows we shall restrict the consideration to achiral 2-dimensional systems which are invariant with respect to reflection of the second axis $\boldsymbol{e}_2$ (the unit vector $\boldsymbol{e}_2$ is perpendicular to the wave-vector $\boldsymbol{q}$). Therefore, for example, C_{1112} must vanish, and the only non-vanishing independent components (apart from permutations of subscripts) are C_{1212}, C_{1111}, C_{2211} and C_{2222}. The Laplace transforms of the first 3 functions calculated

as described above coincide with expressions given in eqs. 2.122 – 2.124 once the latter are simplified by replacing $G(q,s)$ with $G(s)$, $K(q,s)$ with $K(s)$, and $M(q,s)$ with $M(s) = K(s) - 2G(s)$. The last function, C_{2222}, which cannot be deduced from a FDT relation, takes the form:

$$C_{2222}(q,s) \equiv C_2(q,s) \simeq T\Big[K(s) - \frac{q^2 M(s)^2}{\rho s + q^2 K(s)}\Big],\ 0 < q \ll 1/\xi_s \tag{2.132}$$

We first obtain the Fourier transform of $C_{2222}(q,t)$ with respect to time, and then the Laplace transform on this function. It is obvious that while $C_{2222}(t)$ generally differs from $C_{1111}(t)$, they tend to the same limit ($= TK(t)$) as $\boldsymbol{q} \to 0$ at a fixed time.

Using the results at hand and the space isotropy, the correlation tensor function can be written in the following general form (valid for any coordinate frame):

$$\begin{aligned} C_{\alpha\beta\alpha'\beta'}(\boldsymbol{q},s) = (C_2 - 2C_T)\,\delta_{\alpha\beta}\delta_{\alpha'\beta'} + (C_\perp - C_2 + 2C_T)\,(q_\alpha q_\beta \delta_{\alpha'\beta'} + q_{\alpha'} q_{\beta'} \delta_{\alpha\beta})/q^2 \\ + C_T\,(\delta_{\alpha\alpha'}\delta_{\beta\beta'} + \delta_{\alpha\beta'}\delta_{\beta\alpha'}) + \big(C_\parallel + C_2 - 2C_\perp - 4C_T\big)\,q_\alpha q_\beta q_{\alpha'} q_{\beta'}/q^4, \end{aligned} \tag{2.133}$$

where $C_2 = C_2(q,s)$ is defined in eq. 2.132, and the functions $C_T = C_T(q,s)$, and $C_\parallel = C_\parallel(q,s)$ and $C_\perp = C_\perp(q,s)$ are defined in eqs. 2.122 – 2.124.

In particular, for the correlations of the shear-stress (σ_{xy}, where x, y are fixed-frame coordinates) we get the following general expression:

$$\begin{aligned} C_{xyxy}(\boldsymbol{q},s) = C_T + \big(C_\parallel + C_2 - 2C_\perp - 4C_T\big)\,q_x^2 q_y^2/q^4 \\ \simeq \frac{T\rho s G(s)}{\rho s + q^2 G(s)} + 4Tq^2 G^2(s)\Big(\frac{1}{\rho s + q^2 G(s)} - \frac{1}{\rho s + q^2 K(s)}\Big)\frac{q_x^2 q_y^2}{q^4}, \end{aligned} \tag{2.134}$$

which is valid for $\boldsymbol{q}\xi_s \ll 1$. The above equation is valid for compressible 2-dimensional (2d) systems, and in this respect it generalizes eq. 2 of ref. [12]. The latter equation formally agrees with eq. 2.134 if we suppress the term involving $K(s)$ there (thus assuming the incompressibility limit, $K \to \infty$) and take into account that $q^2 = q_x^2 + q_y^2$ in 2d. The correlation function defined in eq. 2.134 is analyzed in different time-distance regimes in the next section.

2.4 Stress correlations in real space

The spatial and temporal correlations of local shear stress in infinite 2d systems are analyzed in this section based on eq. 2.134. Formally the problem is to obtain the inverse Fourier/Laplace transform of the $C(\boldsymbol{q}, s)$ (we omit the subscripts $xyxy$ here and below for simplicity). The latter function as defined in eq. 2.134 consists of two terms: $C = C^{\mathrm{is}} + C^{\mathrm{s}}$. The first term C^{is} is isotropic; the second term C^{s} is anisotropic and singular at $q = 0, s = 0$ reflecting its long-range and long-time behavior (in the asymptotic sense as clarified below).

We first turn to the isotropic part:

$$C^{\mathrm{is}}(q, s) = T\frac{\rho s G(s)}{\rho s + q^2 G(s)} \tag{2.135}$$

The only unknown function involved here is $G(s) = \int_0^\infty G(t)\exp(-st)\,\mathrm{d}t$, where $G(t)$ is the shear relaxation modulus. Below we assume that $G(t)$ develops a plateau in the time-range between $\tau_{\min}$ and τ_{pl} (in the case of supercooled fluids $\tau_{\min}$ is the characteristic time of fast vibrational relaxation); by contrast, at longer times exceeding some $\tau_{\max} > \tau_{\mathrm{pl}}$ the relaxation modulus is assumed to decay significantly, either exponentially or, at least, faster than $1/t$. Such behavior is typical of entangled polymer systems and of supercooled liquids near T_g (note that $\tau_{\max}$ can become practically infinite below T_g). We thus focus on two main regimes of stress relaxation: (i) the plateau regime $\tau_{\min} \ll t \ll \tau_{\mathrm{pl}}$, where $G(t) \simeq G_{\mathrm{pl}}$ is nearly constant, and (ii) the long-time regime, $t \gg \tau_{\max}$, where $G(t)$ is small ($G(t) \ll G_{\mathrm{pl}}$). In the first regime $G(s) \simeq G_{\mathrm{pl}}/s$, hence:

$$C^{\mathrm{is}}(q, s) \simeq T\frac{sG_{\mathrm{pl}}}{s^2 + q^2 c_T^2},\ s \gg 1/\tau_{\mathrm{pl}} \tag{2.136}$$

where $c_T = (G_{\mathrm{pl}}/\rho)^{1/2}$ is the transverse (shear) sound velocity. The correlation function in real space-time reads (for $t \ll \tau_{\mathrm{pl}}$; here and below we have in mind but do not mention explicitly another condition $t \gg \tau_{\min}$):

$$C^{\mathrm{is}}(\boldsymbol{r}, t) \simeq TG_{\mathrm{pl}}\int \cos(qc_T t)\exp(\mathrm{i}\boldsymbol{q}\boldsymbol{r})\,\mathrm{d}^2 q/(2\pi)^2 \tag{2.137}$$

For $t = 0$ the r.h.s of the above equation formally gives $TG_{\mathrm{pl}}\delta(\boldsymbol{r})$ pointing to local stress correlations. Doing the integral for $t > 0$ we get:

$$C^{\mathrm{is}}(\boldsymbol{r}, t) \simeq T\frac{\rho}{2\pi t^2}\phi\left(\frac{r}{c_T t}\right),\ t \ll \tau_{\mathrm{pl}} \tag{2.138}$$

where:

$$\phi(x) = -\left(1 - x^2\right)_+^{-3/2} \tag{2.139}$$

Here the subscript "+" means truncation of the negative part: $(y)_+^v = y^v$ if $y > 0$, and $(y)_+^v = 0$ if $y < 0$; y is a real expression and the exponent v is a parameter. Thus C^{is} is negative (anticorrelation of shear stress) for $r < l_1 = c_T t$, and it vanishes at large distances: $C^{\text{is}} = 0$ at $r > l_1$. The "isotropic" stress correlations therefore decay in time as t^{-2}, while their range $l_1 = c_T t$ is defined by the transverse sound.

Eq. 2.135 implies that:

$$\int C^{\text{is}}(r,t)\,\mathrm{d}^2 r = TG(t)\,, \tag{2.140}$$

for any t, hence it must be nearly equal to TG_{pl} in the short-time regime we consider. On the other hand, using eq. 2.138 we find:

$$\int C^{\text{is}}(r,t)\,\mathrm{d}^2 r \simeq TG_{\text{pl}} I, \tag{2.141}$$

where

$$I = \int \phi(x)\,\mathrm{d}^2 x/(2\pi) \tag{2.142}$$

Therefore it must be expected that $I = 1$, which may seem to contradict the above definition of $\phi(x)$ implying that it is either negative or zero. Moreover, the integral I seems to be divergent. Fortunately, both this contradiction and the divergence are actually fictitious. In fact, the formally diverging integral, eq. 2.142, can be redefined in terms of the analytical continuation replacing the exponent $(-3/2)$ in eq. 2.139 by a parameter. Alternatively the whole function ϕ can be defined as:

$$\phi(x) = -\Re \lim_{\epsilon \to 0} \left(1 + i\epsilon - x^2\right)^{-3/2}, \tag{2.143}$$

with the idea that the limit must be taken after the integration. The latter equation agrees with eq. 2.139 and can be used to calculate any integral involving $\phi(x)$ by first taking the integral and then setting $\epsilon \to 0$. Both ways give $I = 1$ as it should be.

Let us turn to the long-time regime, $t \gg \tau_{\max}$, roughly corresponding to $s \ll 1/\tau_{\max}$. Here $G(s) = \int_0^\infty G(t) \exp(-st)\,\mathrm{d}t$ is nearly independent of s: $G(s) \simeq \eta$, where:

$$\eta = \int_0^\infty G(t)\,\mathrm{d}t \tag{2.144}$$

is the shear viscosity. So:

$$C^{\mathrm{is}}(q,s)/T \simeq \frac{s\eta}{s+q^2\eta/\rho} = \eta\left(1-\frac{q^2D}{s+q^2D}\right) \tag{2.145}$$

where $D=\eta/\rho$ is the vorticity (transverse momentum) diffusion constant (also known as the kinematic viscosity of the fluid [112]). The inverse Fourier-Laplace transforms of $C^{\mathrm{is}}(q,s)$ then give:

$$C^{\mathrm{is}}(r,t) \simeq T\frac{\rho}{4\pi t^2}\phi_2\left(\frac{r}{2l_2(t)}\right),\ t \gg \tau_{\max}, \tag{2.146}$$

where

$$l_2(t)=\sqrt{Dt},\ \phi_2(x)=\left(x^2-1\right)\exp\left(-x^2\right) \tag{2.147}$$

Thus in both time-regimes (short-time and long-time) $C^{\mathrm{is}}(r,t)$ behaves qualitatively in the same way: $C^{\mathrm{is}} \sim T\rho/t^2$ for $r \lesssim l(t)$, while the isotropic stress correlations are strongly suppressed, $C^{\mathrm{is}} \to 0$, for $r \gg l(t)$, where the propagation length $l(t)$ can be generally defined as [10]:

$$l(t) \sim \sqrt{\eta(t)\,t/\rho} \tag{2.148}$$

Here:

$$\eta = \int_0^t G(t)\,\mathrm{d}t \sim G(s=1/t) \tag{2.149}$$

is the effective time-dependent viscosity [10]. In the two-regimes considered above this length is:

$$l(t) \sim \begin{cases} l_1 = c_T t,\ t \lesssim \tau_{\mathrm{pl}} \\ l_2 = \sqrt{\eta t/\rho},\ t \gtrsim \tau_{\max} \end{cases} \tag{2.150}$$

Therefore, the propagation length $l(t)$ is elasto-inertial (acoustic) in nature in the short-time regime, and visco-inertial (diffusive momentum spreading) at long times.

Let us now turn to the singular part of stress correlations:

$$C^{\mathrm{s}}(\boldsymbol{q},s) = 4T\frac{q_x^2q_y^2}{q^2}G^2(s)\left(\frac{1}{\rho s+q^2G(s)}-\frac{1}{\rho s+q^2K(s)}\right) \tag{2.151}$$

At short times, $t \ll \tau_{\text{pl}}$, the relaxation moduli can be approximated as (the condition $\tau_{\min} \ll t$ is also assumed here and below):

$$G(s) \simeq G_{\text{pl}}/s,\ K(s) \simeq K_{\text{pl}}/s \tag{2.152}$$

Doing then the inverse Laplace transformation of eq. 2.151, we get:

$$C^{\text{s}}(\boldsymbol{q}, s) \simeq 4T\frac{G_{\text{pl}}^2}{\rho}\frac{q_x^2 q_y^2}{q^4}\left[\frac{1-\cos(qc_T t)}{c_T^2} - \frac{1-\cos(qc_L t)}{c_L^2}\right],\ t \ll \tau_{\text{pl}} \tag{2.153}$$

where $c_L = \sqrt{K_{\text{pl}}/\rho}$ is the longitudinal sound velocity. Transforming it to the real space correlation function yields:

$$C^{\text{s}}(\boldsymbol{r}, t) \simeq \frac{TG_{\text{pl}}^2}{2\pi\rho t^2}\left[c_T^{-4}\psi\left(\frac{r}{c_T t}, \theta\right) - c_L^{-4}\psi\left(\frac{r}{c_L t}, \theta\right)\right], \tag{2.154}$$

where θ is the polar angle between $\boldsymbol{r}$ and the x-axis, and the new nondimensional function ψ is:

$$\psi(x, \theta) = \sin^2(2\theta)\left[4\delta\left(x^2\right) + \left(1-x^2\right)_+^{-3/2}\right] + \frac{4\cos(4\theta)}{x^4}\left[-3 + \phi(x)\right] \tag{2.155}$$

Here x is the reduced radius, $\delta(y)$ is the symmetric (even) Dirac's delta-function: $\int_0^\infty \delta(y)\,\mathrm{d}y = 1/2$, and:

$$\phi(x) = \left(3-2x^2\right)\left(1-x^2\right)_+^{-1/2} \tag{2.156}$$

(the meaning of the "+" symbol is explained below eq. 2.139).

The full stress correlation function $C = C^{\text{is}} + C^{\text{s}}$ for $\tau_{\min} \ll t \ll \tau_{\text{pl}}$ is defined in eqs. 2.154 and 2.138. It is useful to write it in a more explicit way:

$$C(\boldsymbol{r}, t)/T \simeq \frac{G_{\text{pl}}}{2}\left(1 - \left(\frac{c_T}{c_L}\right)^2\right)\delta(\boldsymbol{r}) - \frac{\rho}{2\pi t^2}\left[\cos^2(2\theta)\left(1 - \left(\frac{r}{c_T t}\right)^2\right)_+^{-3/2} + \right.$$
$$\left. + \sin^2(2\theta)\left(\frac{c_T}{c_L}\right)^4\left(1 - \left(\frac{r}{c_L t}\right)^2\right)_+^{-3/2}\right] + \frac{2}{\pi}G_{\text{pl}}\frac{(c_T t)^2}{r^4}\cos(4\theta)\left[\phi\left(\frac{r}{c_T t}\right) - \phi\left(\frac{r}{c_L t}\right)\right] \tag{2.157}$$

Thus, there are 3 contributions to the correlation function here:

(i) The first $\delta(\boldsymbol{r})$-term reflects the local structural correlations; it is nearly constant for $\tau_{\min} \ll t \ll \tau_{\rm pl}$ due to little change of the memory function $G(t)$ in this regime.

(ii) The second term is due to acoustic waves; it decays rather fast as $1/t^2$, and its range is characterized by two finite length scales, $l \simeq c_T t$ and $l' \simeq c_L t$, which both increase in time. Note that this correlation contribution strongly decreases at $r \approx l$: it is typically much lower for $r > l$ than for $r < l$ since normally $(c_T/c_L)^4 \ll 1$. This term is anisotropic: it depends on the $\boldsymbol{r}$-direction given by θ and includes both isotropic and quadrupolar ($\cos(4\theta)$) parts. Further, being proportional to ρ/t^2 this contribution can be considered as "internal" in nature. Noteworthily, it is negative (corresponding to anti-correlation of the shear stress) for any θ and distances in the transverse wave-zone, $r < c_T t$ (that is, away from the wave fronts where the correlation function changes its sign).

(iii) The last term is of major interest: it is long-range (with correlation lengths $l \simeq c_T t$ and $l' \simeq c_L t$) and it does not decay in time in the regime $\tau_{\min} \ll t \ll \tau_{\rm pl}$ we consider. This term is not relevant for simple liquids well above the glass transition temperature T_g (due to short relaxation time $\tau_{\max}$), and it is not present in crystalline solids. The reason is that in crystals the correlation function $C(\boldsymbol{r}, t)$ decays rather fast with the characteristic time $\sim r/c_T$ (since the relevant stress fluctuations are due to thermal acoustic waves with wave-vector $k \sim 1/r$ and frequency $\sim kc_T$). For $t \gg r/c_T$ the decay of C due to destructive interference follows the $1/t^2$ power law (in 2d) which is actually given by the second term in eq. 2.157 in the case of isotropic crystals. However, the last term becomes dominant in viscoelastic liquids for $t \gg r/c_T$. It implies the existence of significant transient (but persistent) stress fluctuations in such liquids (in particular, in supercooled liquids close to the glass transition). In the most important regime $t \gg r/c_T$ (note that in supercooled liquids the latter condition is compatible with long $r \gg a_m$ since typically $c_T \tau_{\rm pl} \gg a_m$ in these systems near or below T_g) the dominant contribution to the stress correlation function, eq. 2.157, can be approximated as:

$$C(\boldsymbol{r}, t) \simeq -\frac{T}{\pi} G_{\rm pl} \cos(4\theta) \left(1 - \frac{G_{\rm pl}}{K_{\rm pl}}\right) r^{-2}, \; r \ll c_T t, \; \tau_{\min} \ll t \ll \tau_{\rm pl} \qquad (2.158)$$

In this regime the correlation function $C(\boldsymbol{r}, t)$ is thus nearly independent of time and is long-range (LR) in space showing an algebraic decay as $1/r^2$. It is noteworthy that the

magnitude of the long-range correlations depends on both elastic moduli, $G_{\rm pl}$ and $K_{\rm pl}$. Eq. 2.158 qualitatively agrees with MD simulation results of a 2d binary glass former [11].

So far we have considered the short-time regime $t \ll \tau_{\rm pl}$. The latter condition is rather restrictive for viscoelastic liquids which normally show a very broad spectrum of relaxation times with a large gap between $\tau_{\rm min}$ and $\tau_{\rm max}$. Nevertheless, the detailed analysis of the short-time regime given above is useful to show how the long-range character of stress correlations emerges and develops as illustrated in Figs. 2.3 – 2.6 and Fig. 2.9 (adopted from ref. [9]) ($\tilde{C}$ is calculated for $c_L/c_T = \sqrt{K_{\rm pl}/G_{\rm pl}} \approx 2.45$ corresponding to $K_{\rm pl}/G_{\rm pl} = 6$ using eq. 2.157 without the $\delta(\boldsymbol{r})$ term). The dotted vertical lines show the wave fronts ($r = l = c_T t$) and ($r = l' = c_L t$). Note that C for $\theta = \pi/4$ changes its sign at $\tilde{r} \approx 0.84$, $\tilde{r} = 1$ and $\tilde{r} \approx 2.26$.

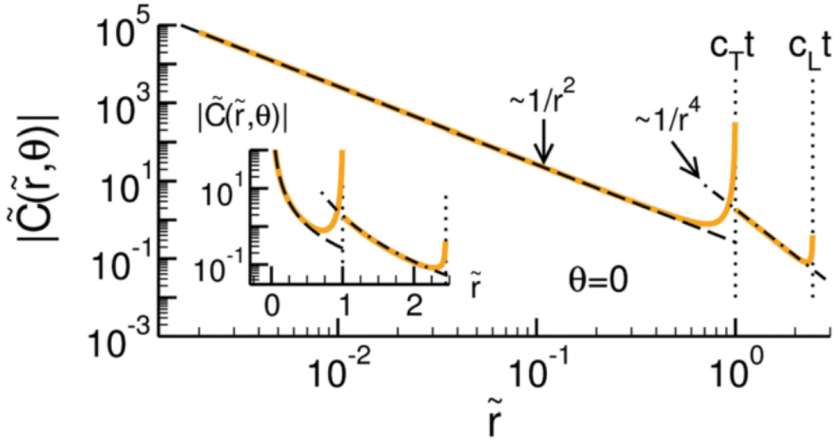

Figure 2.3: The reduced correlation function $|\tilde{C}|$, $\tilde{C} \equiv Ct^2/(T\rho)$ vs. $\tilde{r} = r/(c_T t)$ on a log-log scale for $\theta = 0$.

Below we lift the short-time restriction, leaving essentially the only condition $r \ll c_T t$, which is likely to be valid in viscoelastic liquids (generally due to rather high sound velocity and long relaxation times in these systems). The singular terms dominate in eq. 2.134 in this case, hence:

$$C(\boldsymbol{q}, s) \simeq 4T \frac{q_x^2 q_y^2}{q^4} \tilde{G}(s), \; \tilde{G}(s) \equiv G(s) - \frac{G^2(s)}{K(s)} \tag{2.159}$$

The inverse Laplace transform of $\tilde{G}(s)$ gives the effective relaxation modulus $\tilde{G}(t)$ which behaves similarly to the standard shear modulus $G(t)$: in the liquid state $\tilde{G} \to 0$ for $t \gg \tau_{\rm max}$, while in the glassy state it tends to a finite level $\tilde{G}_\infty = G_\infty - \frac{G_\infty^2}{K_\infty}$ for $t \sim t_{\rm lab}$, where $t_{\rm lab} = \Delta t$ is the sampling time.

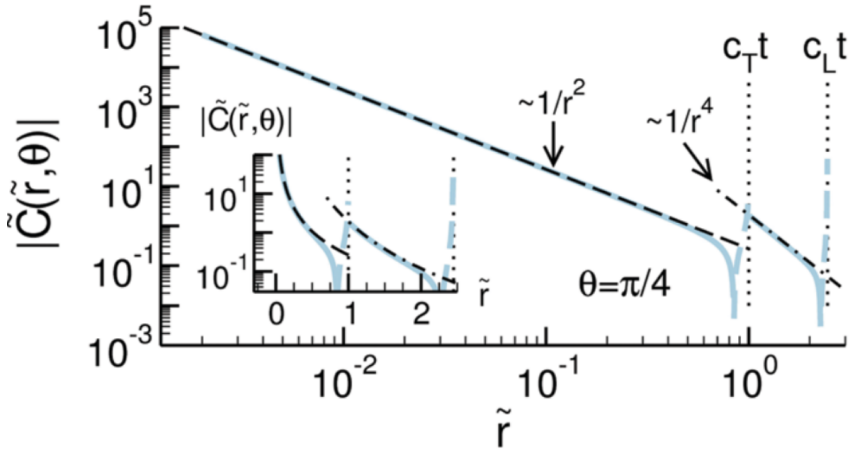

Figure 2.4: The reduced correlation function $|\tilde{C}|$, $\tilde{C} \equiv Ct^2/(T\rho)$ vs. $\tilde{r} = r/(c_T t)$ on a log-log scale for $\theta = \pi/4$.

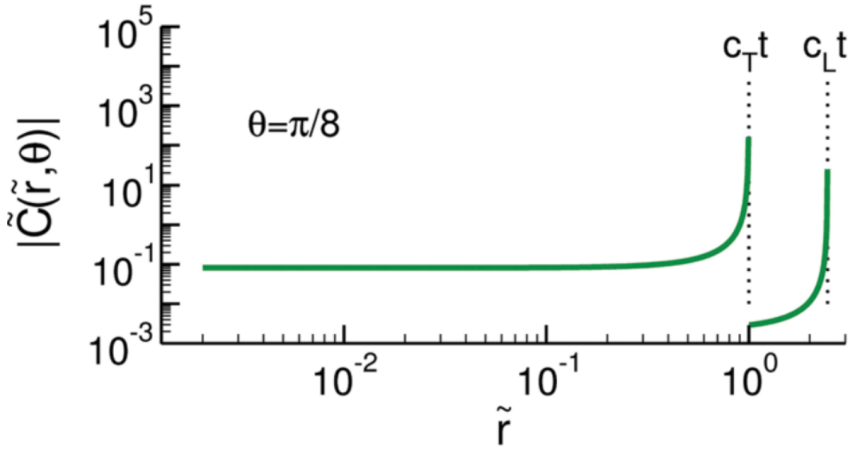

Figure 2.5: The reduced correlation function $|\tilde{C}|$, $\tilde{C} \equiv Ct^2/(T\rho)$ vs. $\tilde{r} = r/(c_T t)$ on a log-log scale for $\theta = \pi/8$.

Doing also the inverse Fourier transform of eq. 2.159 we get the stress correlation function in real space-time:

$$C(\boldsymbol{r}, t) \simeq -\frac{T}{\pi} \cos(4\theta)\, \tilde{G}(t)\, r^{-2},\ r \ll l(t) \tag{2.160}$$

where the propagation length $l(t)$ is defined in eq. 2.148. This result agrees with eq. 2.158 generalizing it. Thus, the LR stress correlations gradually decay in time and vanish for $t \gg \tau_{\max}$ in the liquid state, or tend to a plateau (proportional to $\tilde{G}_\infty$) for vitrified systems. The latter conclusion qualitatively agrees with theoretical results [12] obtained for 3-dimensional systems.

Note that while the results for $C(\boldsymbol{q}, t)$ obtained in this section are valid for 2d systems,

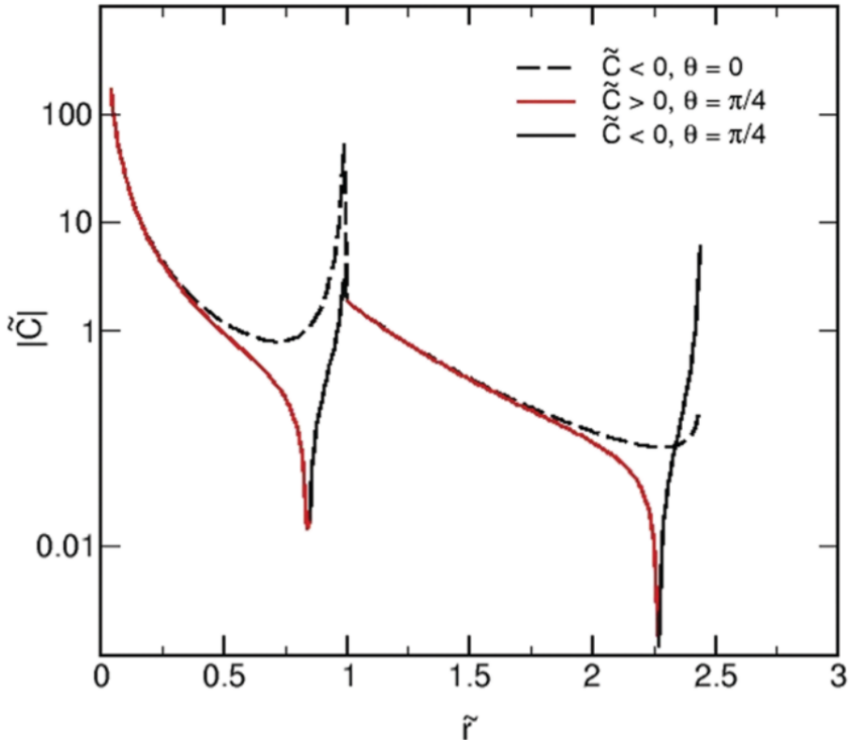

Figure 2.6: The reduced correlation function $|\tilde{C}|$, $\tilde{C} \equiv Ct^2/(T\rho)$ vs. $\tilde{r} = r/(c_T t)$ on a log-log scale for $\theta = 0, \pi/4$.

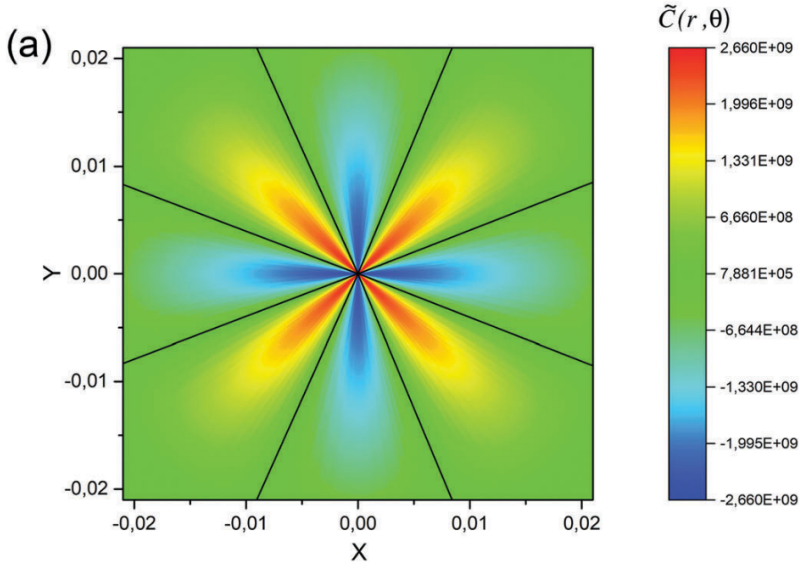

Figure 2.7: Two-dimensional plots $\tilde{C} = Ct^2/(T\rho)$ in polar coordinates $(\tilde{r}, \theta)$ using eq. 2.157 with the same c_L/c_T; $\tilde{x} = \tilde{r}\cos(\theta)$, $\tilde{y} = \tilde{r}\sin(\theta)$. $\tilde{C}$ for short $\tilde{r} \lesssim 0.02$ showing regions of negative (blue to green) and positive (red to green) correlations; black lines separating these regions correspond to $C = 0$.

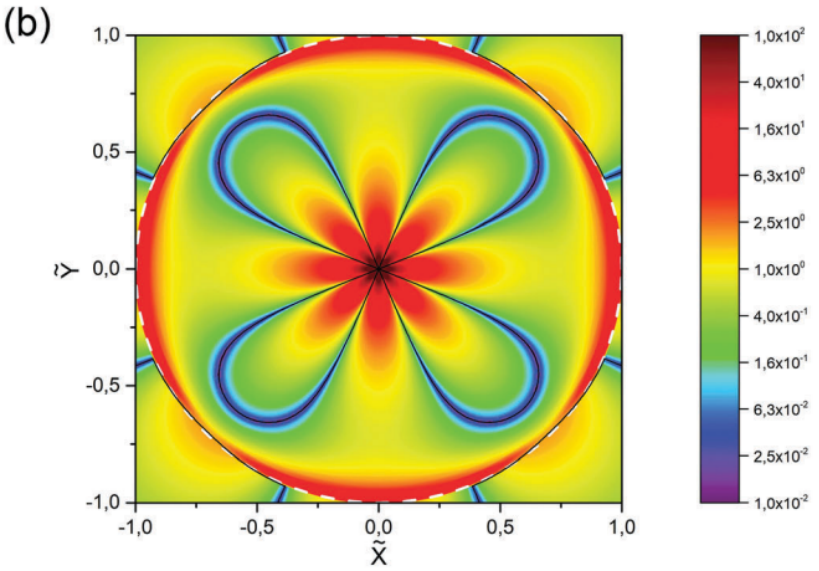

Figure 2.8: Two-dimensional plots $\tilde{C} = Ct^2/(T\rho)$ in polar coordinates $(\tilde{r}, \theta)$ using eq. 2.157 with the same c_L/c_T; $\tilde{x} = \tilde{r}\cos(\theta)$, $\tilde{y} = \tilde{r}\sin(\theta)$. $|\tilde{C}|$ for $\tilde{r} \lesssim 1$ showing the transverse wave front (the red/white dashed circle, $\tilde{r} = 1$). Black curves (separating the regions $C > 0$ and $C < 0$) include 4 "petals" with the central crossing and 4 arcs (belonging to the circle, $\tilde{r} = 1$).

they are also fully applicable in 3 (and higher) dimensions if $\boldsymbol{q}$ belongs to the xy plane. Note also that the stress correlations at exactly $t = 0$ (rather than for $t \gg \tau_{\min}$) can be deduced directly from the general eq. 2.134. The general result is:

$$C(\boldsymbol{r}, 0) = C^{\text{is}}(\boldsymbol{r}, 0) = TG(0)\,\delta(\boldsymbol{r}), \tag{2.161}$$

pointing to localized static (structural) stress correlations in agreement with our assumption of short ξ_s.

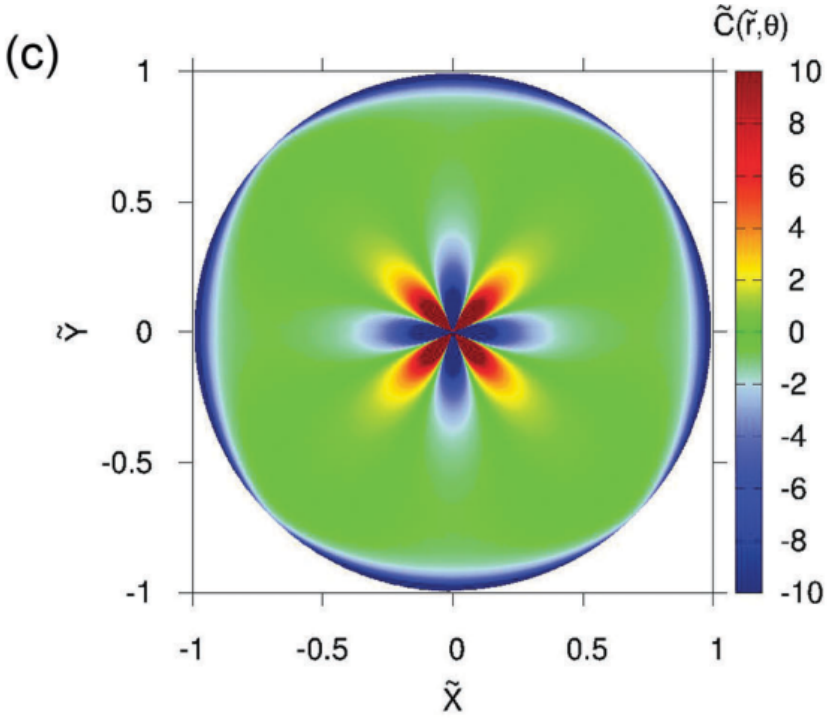

Figure 2.9: Two-dimensional plots $\tilde{C} = Ct^2/(T\rho)$ in polar coordinates $(\tilde{r}, \theta)$ using eq. 2.157 with the same c_L/c_T; $\tilde{x} = \tilde{r}\cos(\theta)$, $\tilde{y} = \tilde{r}\sin(\theta)$. $\tilde{C}$ for $\tilde{r} < 1$ using a color code highlighting the behavior in the region $\tilde{r} < 0.5$.

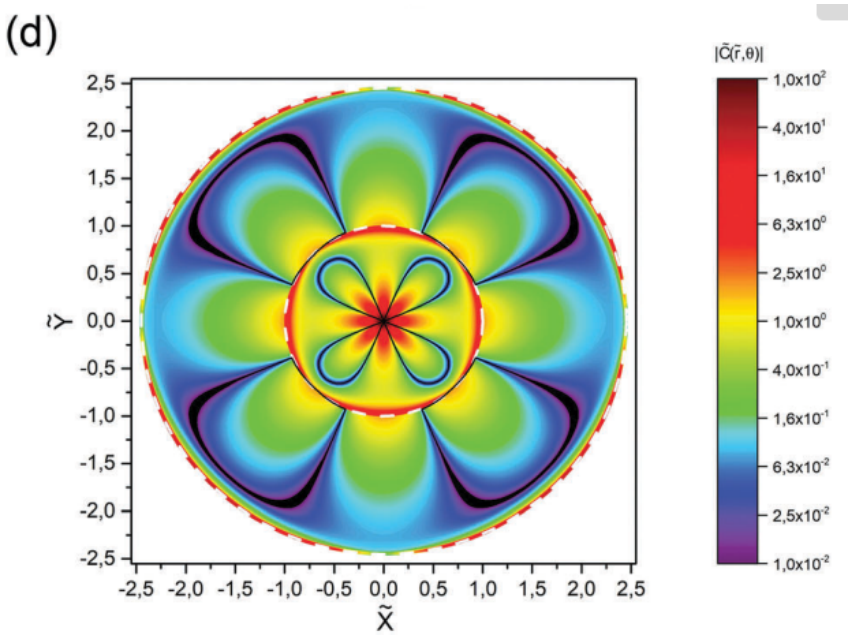

Figure 2.10: Two-dimensional plots $\tilde{C} = Ct^2/(T\rho)$ in polar coordinates $(\tilde{r}, \theta)$ using eq. 2.157 with the same c_L/c_T; $\tilde{x} = \tilde{r}\cos(\theta)$, $\tilde{y} = \tilde{r}\sin(\theta)$. The whole 2d plot for $|\tilde{C}|$ showing 2 wave fronts as red/white circles (for transverse, $\tilde{r} = 1$, and longitudinal $\tilde{r} = l'/l \approx 2.45$, sound waves). $C > 0$ inside 4 small petals (in region $\tilde{r} < 1$) and in 4 large petals (for $1 < \tilde{r} < l'/l$) shown with black contour lines; $C < 0$ outside the petal regions; and $C = 0$ for $\tilde{r} > l'/l$.

Chapter 3

Glass-forming 3-dimensional oligomer system

3.1 Polymer model

We studied a glass-forming polymer model in the 3 dimensional space [6, 113, 114]. The system contains $M = 768$ oligomer chains with $N = 4$ monomers connected by permanent bonds. Particles, which are connected by such bonds, interact with a harmonic (bond) potential:

$$u_{\mathrm{b}}(l_b) = \frac{1}{2} k_{\mathrm{b}} (l_b - l_0)^2 , \tag{3.1}$$

where l_b is the bond length, $k_{\mathrm{b}} = 1110$ is the spring constant, and $l_0 = 0.967$ is the equilibrium bond length. The constants k_{b} and l_0 are chosen so that the probability for bond crossing is virtually null (the bond length cannot exceed r_{cut} for the same reason).

All unconnected monomers interact with a Lennard-Jones (LJ) potential, which is truncated and shifted at $r = r_{\mathrm{cut}} = 2.3$ ($r_{\mathrm{cut}} \approx 2r_{\mathrm{min}}$ is roughly twice the distance of the distance where potential has a minimum [7]) so that $u_{\mathrm{LJ}}(r) = 0$ for $r \geqslant r_{\mathrm{cut}}$:

$$u_{\mathrm{LJ}}(r) = \begin{cases} 4\epsilon_{\mathrm{LJ}} \left[\left(\frac{\sigma_{\mathrm{LJ}}}{r}\right)^{12} - \left(\frac{\sigma_{\mathrm{LJ}}}{r}\right)^{6} \right] - 4\epsilon \left[\left(\frac{\sigma_{\mathrm{LJ}}}{r_{\mathrm{cut}}}\right)^{12} - \left(\frac{\sigma_{\mathrm{LJ}}}{r_{\mathrm{cut}}}\right)^{6} \right], & r < r_{\mathrm{cut}} \\ 0, & \text{else,} \end{cases} \tag{3.2}$$

where σ_{LJ} is the particle diameter and ϵ_{LJ} is the depth of the potential minimum. The constants ϵ_{LJ} and σ_{LJ} are set respectively as a scale for the energy and the length. The truncation of the potential at $r = r_{\mathrm{cut}}$ is needed to increase the numerical efficiency of calculation and its shifting resulted in $u_{\mathrm{LJ}}(r_{\mathrm{cut}}) = 0$ is needed to avoid its discontinuous behavior at $r = r_{\mathrm{cut}}$.

3.2 Simulation protocol

We performed Molecular Dynamics (MD) simulation using a velocity-Verlet scheme [79] with time step $\delta t = 0.005\tau_{\mathrm{LJ}}$ in a cubic box with periodic boundary conditions. The simulations are performed in the NPT and the NVT ensembles. The temperature T and the pressure $P = 0$ are imposed using the Nosé-Hoover-Andersen algorithm [90] (cf. Chapter 2).

As it can be seen from eqs. 2.27 – 2.31, choice of parameters P_{damp} and T_{damp} is an interesting task. The investigation of the applicable values of Q and W in ref. [83] (cf. Figs. 4.1 and 4.3) was shown. Our former students [74, 115] in their works continued to develop relevant values for Q and W in order to get good temperature and pressure control in the NVT and NPT simulations. Obviously, as can be seen from eqs. 2.27 – 2.31, the relevant values P_{damp} and T_{damp} are different and correlate with the system properties (volume, number of particles, etc.) and the dimension. In order to get reproducible results as in refs. [74, 115], we chose the same damping parameter for pressure, $P_{\mathrm{damp}} = 75$, and for the temperature, $T_{\mathrm{damp}} = 1$.

3.2.1 Sample preparation

We start a protocol with NPT equilibration (for $\Delta t = 2{\cdot}10^4\tau_{\mathrm{LJ}}$) at the initial temperature $T_i = 0.6$ which is well above the temperature of the glass transition T_g. In this liquid regime we perform a new NPT run (for $\Delta t = 10^5\tau_{\mathrm{LJ}}$) to generate $m = 100$ independent configurations (saving independent configurations every $10^3\tau_{\mathrm{LJ}}$ steps. The criteria to prove that independent configurations are really independent is the plot of the orientational correlation function of the end-to-end vector $\phi_e(t)$ vs. t at the initial temperature T_i. In the earlier works [74, 115] it was shown that even for much bigger systems [74] the $\phi_e(t)$ decorrelates during times less than $10^3\tau_{\mathrm{LJ}}$ [74, 115]). All the configurations are slowly cooled down to $T_f = 0.05$ with a cooling rate $\Gamma = -\partial T/\partial t = 10^{-5}$ (at $P = 0$). During cooling, we were keeping the initial configurations for $n_T = 19$ temperatures $T = 0.55, 0.5, ..., 0.05$.

For each T and for each system from the m-ensemble, we did:

1. NPT tempering run for time $\Delta t_{\mathrm{NPT}} = 10^5\tau_{\mathrm{LJ}}$, $P = 0$;

2. Determination of the time-, and ensemble-average volume $\langle\overline{V}\rangle$ and switching to the NVT ensemble, short run for time $\Delta t_{\langle\overline{V}\rangle} = 10^3\tau_{\mathrm{LJ}}$;

3. NVT relaxation run for time $\Delta t_{\mathrm{NVT}} = 10^5 \tau_{\mathrm{LJ}}$;

4. NVT production run for time $\Delta t_{\mathrm{NVT}} = 10^5 \tau_{\mathrm{LJ}}$;

The schematic representation of the simulation procedure is represented in Fig. 3.1. During the NPT tempering run, we recorded the values for instantaneous volume $\tilde{V}$ every $\delta t_{\tilde{V}} = 0.05\tau_{\mathrm{LJ}}$. Next, we found the time- (over the last second part of the run interval $\left[\frac{\Delta t_{\mathrm{NPT}}}{2}, \Delta t_{\mathrm{NPT}}\right]$) and the ensemble- (over m independent configuration) volume $V = \left\langle \overline{V} \right\rangle$ for a given T and performed a short deformation run to set the same volume for all the systems of the ensemble before switching to the NVT relaxation run. During the NVT production run, we were recording data for the instantaneous stress components such as σ_{xx}, σ_{yy}, σ_{zz}, σ_{xy}, σ_{yz}, and σ_{xz} every $\delta t_{\tilde{\sigma}} = 0.05\tau_{\mathrm{LJ}}$ and the positions of all particles every $\delta t_{\mathrm{pos}} = 500\tau_{\mathrm{LJ}}$.

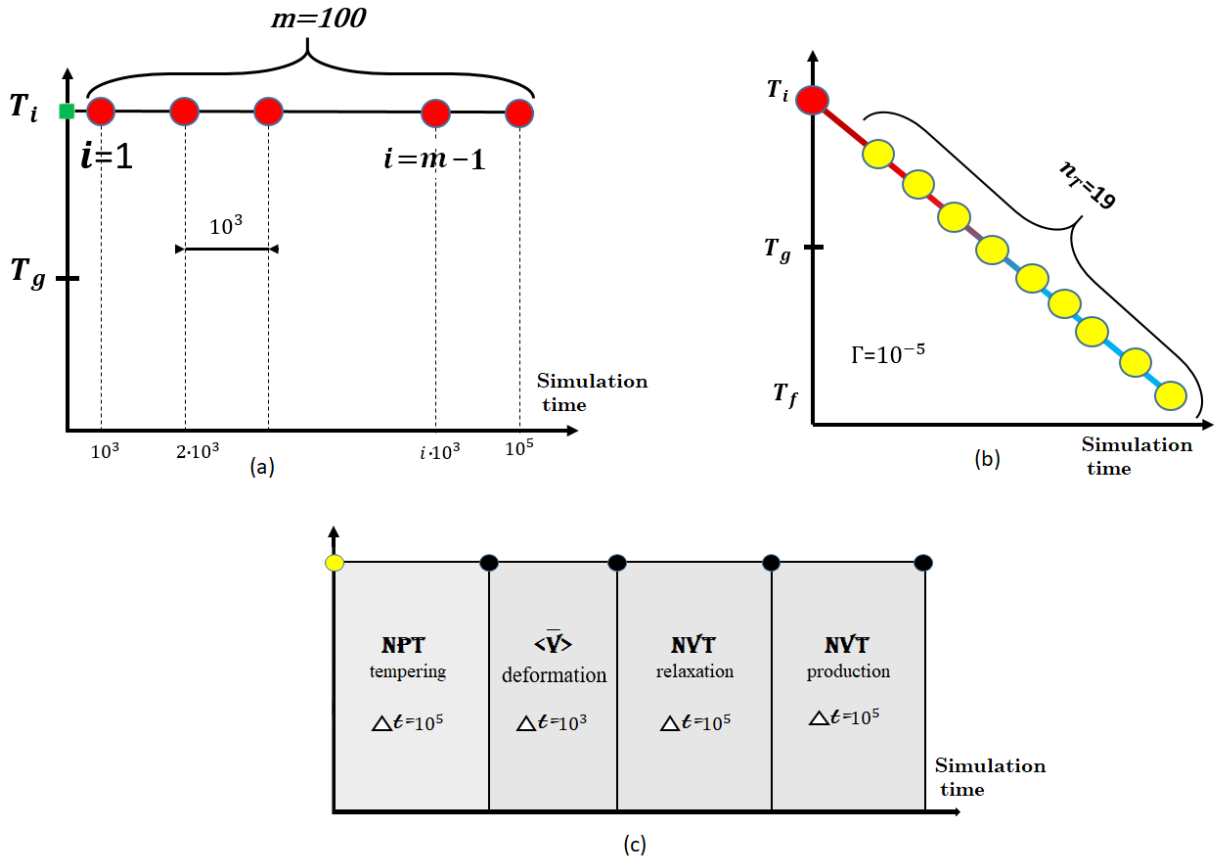

Figure 3.1: The schematic representation of the simulation protocol. (a) The green square corresponds to the already equilibrated (NPT ensemble, $\Delta t = 2 \cdot 10^4 \tau_{\mathrm{LJ}}$) initial configuration at $T_i = 0.6$ (liquid regime). Using the initial configuration we performed simulation in the NPT ensemble for $\Delta t = 10^5 \tau_{\mathrm{LJ}}$, saving independent configurations (on the sketch they are shown as red circles) every $10^3 \tau_{\mathrm{LJ}}$. The criteria to prove that independent configurations are really independent is the plot of the orientational correlation function of the end-to-end vector $\phi_e(t)$ vs. t at the initial temperature T_i. In the earlier works [74, 115] it was shown that even for much bigger systems [74] the $\phi_e(t)$ decorrelates during times less than $10^3 \tau_{\mathrm{LJ}}$ [74, 115]. T_g is the glass transition temperature, i is the configuration index in the set of $m = 100$ configurations. (b) The schematic representation of the cooling procedure which was applied to each independent configuration at $T_i = 0.60$. The red circle is the initial independent configuration. The gradient line from red to light blue represents the linear cooling procedure with speed $\Gamma = 10^{-5}$. During cooling we recorded the whole configuration for a number of working temperatures, $n_T = 19$. Such saved configurations are shown as yellow circles in the figure. $T_f = 0.05$ is the final temperature. (c) The schematic representation of the simulation protocol for each T and for each system from the m-ensemble. By deformation (2^{nd} stage) we mean the volume adjustment for each system.

3.3 Temperature dependence of volume and radial distribution function $g(r)$

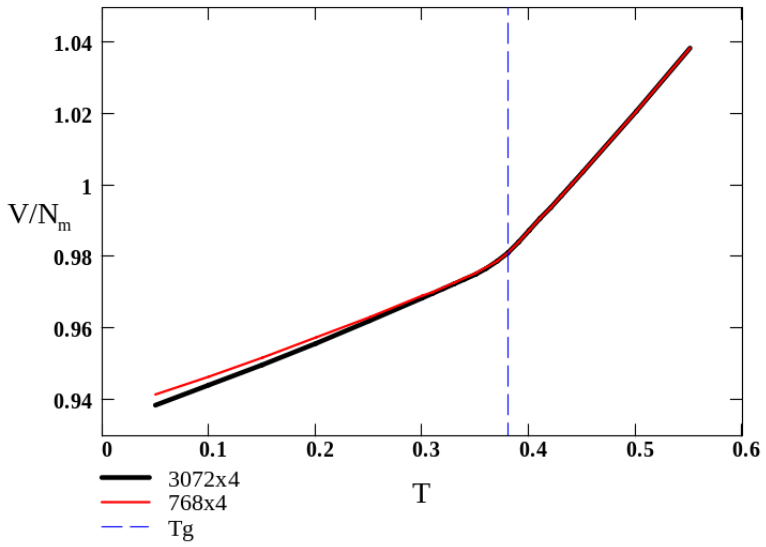

Figure 3.2: The volume per monomer at $P = 0$ vs. T for the two systems: $N_m = 3072 \times 4$ (black) and $N_m = 768 \times 4$ (red). Vertical line: $T_g = 0.38$.

The system of $M = 3072$ short linear chains of LJ beads, with $N = 4$ beads per chain, was studied in ref. [7]. We performed additional simulations of the same system along with a detailed study of a new oligomer system with $M = 768$ chains and systematically compared various properties of the two systems. The linear dimension of the simulation box, L, for the smaller system (768×4) varies from $L = 14.25$ to 14.72 LJ units in the T-range from $T = 0.05$ to 0.55. The size of the larger system (3072×4) is between $L =$ 22.60 to 23.40 LJ.

The T-dependence of the mean specific volume (per monomer) is shown in Fig. 3.2. The two systems have nearly the same density (the smaller system being a little bit less dense at low temperatures). The standard dilatometric criterion gives the glass transition at $T_g \approx 0.38$ for both systems (cf. ref. [7], note that the dilatometric T_g is a reference estimate: generally T_g depends on the cooling rate Γ, T_g is lower for a longer relaxation time scale).

The radial distribution function (RDF) $g_{\rm nb}(r)$ for *nonbonded* monomer pairs is shown in Fig. 3.3 for both systems at two temperatures (above and below T_g). One can observe that the RDFs for the two systems are almost identical (the difference is not visible). The

main peak just weakly depends on T: it is only slightly more pronounced well below T_g (at $T = 0.25$). In all the cases, the obtained RDFs show no sign of crystallization being typical of liquids and disordered amorphous systems.

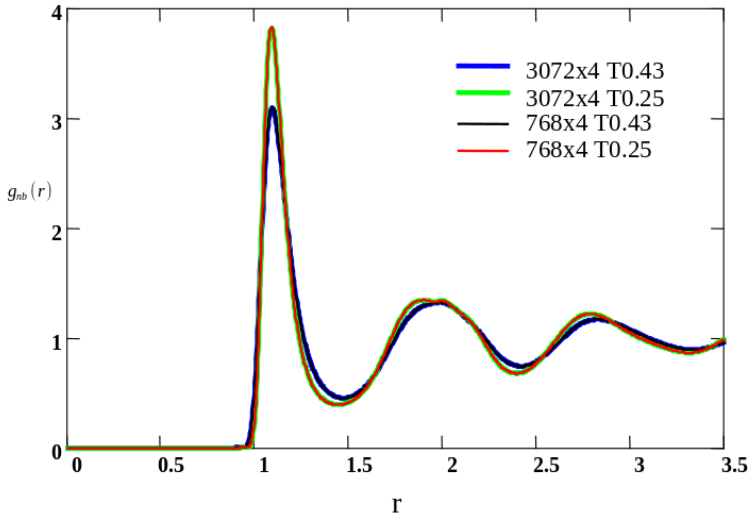

Figure 3.3: The radial distribution functions for nonbonded monomers, $g_{\mathrm{nb}}(r)$, for two systems, 3072×4 and 768×4 at $T = 0.43$ (blue and black curves) and at $T = 0.25$ (green and red curves). The curves for different systems superimpose perfectly on one another.

Thus, we established that both systems are characterized by virtually the same density and the same pair correlation functions (including $g_{\mathrm{nb}}(r)$ and the standard Kirkwood RDF, $g(r)$). This fact means that all related static properties such as energy, pressure, the affine shear modulus μ_A etc., must also be nearly identical for both systems. Below we verify this statement for μ_A.

3.4 Affine shear modulus μ_A

One of the main goals of this work was to investigate the dynamical and static behavior of glassy polymer systems based on an analysis of different physical quantities. The ensemble-averaged affine shear modulus μ_A [8] was described in section. 2.2 and can be calculated using eqs. 2.57 and 2.59.

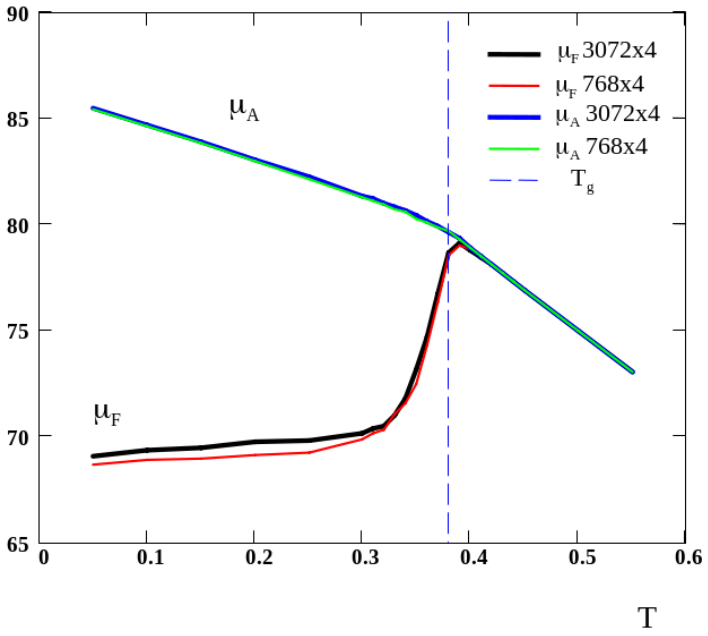

Figure 3.4: Temperature dependence of the affine shear modulus μ_A (blue and green curves) and fluctuation modulus μ_F (black and red curves) for $\Delta t = 10^5$ for the two systems (3072×4 and 768×4, respectively).

While the chosen LJ potential is continuous, its derivative is not, giving rise to a singular contribution to μ_A known as an impulsive correction (cf. subsection 2.2.2 and ref. [94]):

$$\Delta\mu_A = -\frac{2\pi}{15} c^2 u'_{LJ}\left(r_{\text{cut}}\right) r_{\text{cut}}^4 g_{nb}\left(r_{\text{cut}}\right) \tag{3.3}$$

where c is the monomer concentration $c = N/V$, g_{nb} is the RDF for nonbonded monomer pairs.

The obtained temperature dependencies of the time- and ensemble-averaged affine shear modulus for both system sizes are shown in Fig. 3.4. (If not specified otherwise, an ensemble-averaging is taken over $m = 100$ independent configurations and 3 shear planes, xy, yz, and xz). It is clear that μ_A is virtually the same for the two system sizes at all temperatures; it increases at low T reflecting an increase of the system density.

3.5 Relaxation modulus $G(t)$ and stress correlation function $C(t)$

This topic was discussed in section 2.2.1. The eqs. 2.43, 2.44 presented there were employed to find the relaxation modulus $G(t)$ for both systems at different temperatures. We obtained the correlation function $C(t)$ by averaging the r.h.s. of eq. 2.33 over t' (for the time interval $\approx \Delta t$), over the ensemble of $m = 100$ independent systems, and over the 3 shear planes. The results for $G(t)$ are shown in Fig. 3.5 (the data for the larger system have been presented in ref. [7]).

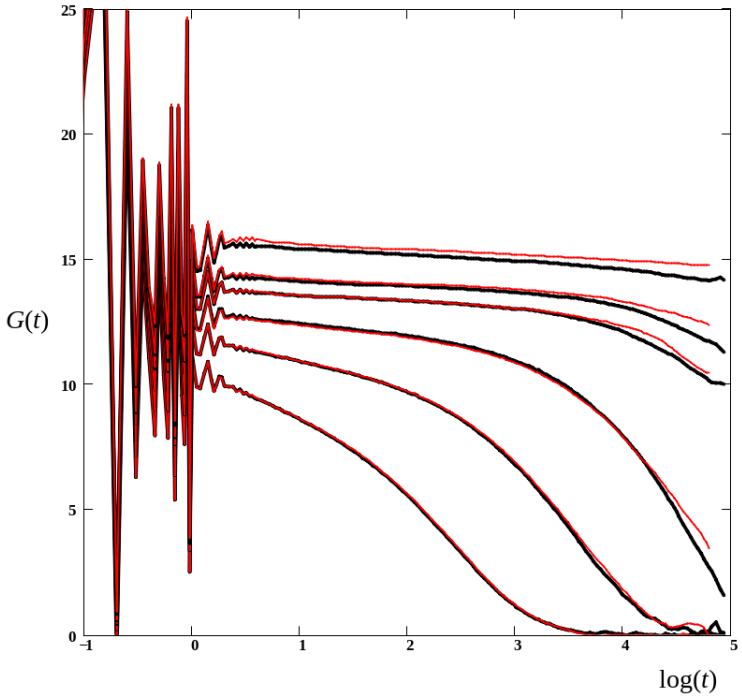

Figure 3.5: Comparison of the shear relaxation moduli $G(t)$ vs. $\log(t)$ for the systems 3072×4 (black curves) and 768×4 (red curves) at $T = 0.40$, 0.38, 0.36,0.30,0.25, and 0.15 (from bottom to top). Note that the dilatometric T_g is close to 0.38.

At short times, $t \lesssim 3$, $G(t)$ shows oscillations. These oscillations are not just a thermal noise, nor are they due to numerical errors: the oscillation pattern is reproducible and coincides for two systems. It reflects vibrations of the molecular chain bonds [116, 117]. It is, moreover, obvious that the whole $G(t)$ relaxation is independent of the system size in liquid regime ($T > T_g$). Below T_g, the relaxation modulus shows a shoulder at $t \gtrsim 3$ which gets larger and gradually transforms into a plateau as T is further decreased.

It is remarkable that the $G(t)$ relaxation function is identical for both systems at all temperatures $T > 0.25$ (both above and below T_g) not only at short times, but also for a wider time-range, $t \lesssim 10^3$, including most of the plateau regime. At longer times ($t \gtrsim 10^4$) in the glassy regime ($T \lesssim 0.36$), the relaxation of the smaller system (768×4) becomes retarded with respect to the larger one. For example, the apparent "terminal" relaxation time is about twice longer for the smaller system at $T = 0.25$. To define the apparent terminal relaxation time τ_α, we applied several procedures. First of all, we define a time, where we do not have oscillations $t_{\min}$. Next, we found the terminal relaxation time from the relation $G(\tau_\alpha)/G(t_{\min}) \approx 20\%$.

What is the meaning of these results? The $G(t)$ relaxation at short times must reflect the identical local structure of the two systems (in agreement with the RDF data). A slower long-time relaxation (longer τ_α) for smaller system below T_g may seem counter-intuitive (also in view of a slightly lower density of this system). Still, this feature agrees with the previous simulation results and theoretical views on the glassy dynamics [7, 118, 119] (in particular, it was shown [118, 119] that τ_α for binary LJ mixtures increases as the system size decreases at T below the onset of the glassy dynamics). This effect shows that the terminal α-relaxation is not a local property but rather is a collective process involving transformations of large parts of the system. The corresponding correlation length (the size of the optimal CRR) may thus exceed the size of the smaller system ($L \approx 14$) leading to its slower relaxation (as the optimal relaxation pathway gets prohibited due to the system size). Such reasoning is also similar in spirit to the Adam-Gibbs-DiMarzio theory [2] (cf. their argument based on the size dependence of the configurational entropy [119]). It is remarkable that at very low $T \lesssim 0.25$, the relaxation modulus $G(t)$ is a bit higher for the smaller system in the plateau regime. This effect is not due to a difference of the affine shear modulus $\mu_A = G(0)$, which is negligible between the two systems; rather, it must be due to long-range relaxation modes which are effective for the larger system, but not for the smaller one.

Noteworthily, there is actually no contradiction between a lower density and a longer relaxation in the 768×4 system. The latter feature means that the 768×4 system must be a bit farther from equilibrium than the larger system at low T in the glassy state. For the density, this means a stronger downward shift (cf. Fig. 3.2) from the equilibrium line, hence a lower density as compared with the 3072×4 system.

3.6 The quasi-static shear modulus and its $T-$ dependence

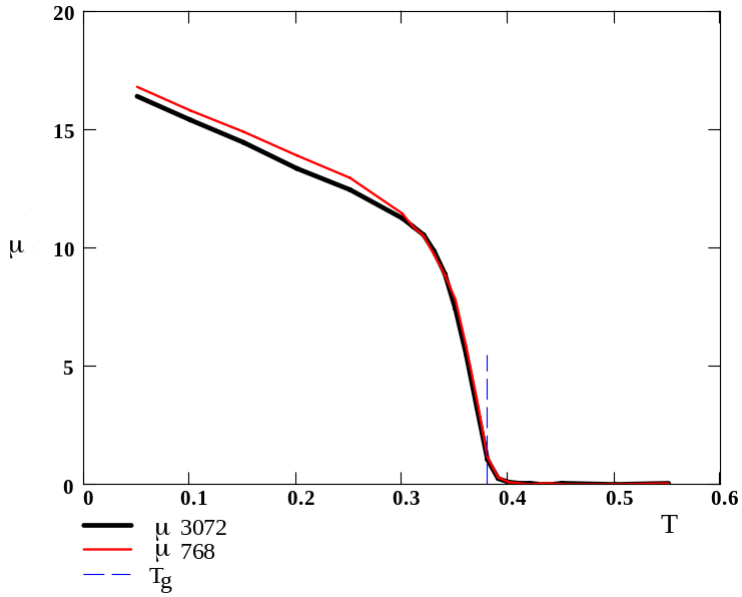

Figure 3.6: Temperature dependence of the quasistatic modulus μ for $\Delta t = 10^5$ for the 3072×4 (black curve) and 768×4 (red curve).

The long-time quasi-static modulus μ was obtained as a function of temperature using the FDT relation, eq. 2.45, for both systems, 768×4 and 3072×4. The temperature behavior of the moduli $\mu_F = \frac{V}{T}\left\langle \overline{\sigma^2} - \overline{\sigma}^2 \right\rangle$ and μ for the sampling time $\Delta t = 10^5$ in LJ units is shown in Fig. 3.4 and Fig. 3.6 (the data for the larger system have been obtained in ref. [7]). The LJ time unit is $\tau_{\mathrm{LJ}} = \sigma_{\mathrm{LJ}}\sqrt{m/\epsilon_{\mathrm{LJ}}}$ (eq. 2.8), where σ_{LJ} is the monomer diameter (the distance between monomer centers corresponding to the first knot of the original LJ potential), m is the monomer mass, and ϵ_{LJ} is the depth of the LJ potential well.

The glassy modulus μ nearly vanishes at high T's (in the liquid state), while it sharply increases (and $\mu_F = \mu_A - \mu$ decreases) as the temperature is lowered near T_g. Below T_g (in the glassy state), μ continues to grow, in a linear fashion. The moduli μ_F and μ are nearly the same for both systems at all temperatures apart from the low-T region ($T \lesssim 0.3$) where the smaller system shows a bit lower μ_F and therefore a bit higher μ. The latter low-T effect is consistent with two features of stress relaxations discussed in the previous section (recall that μ_F and μ are directly related to $G(t)$, cf. eq. 2.42 and 2.52):

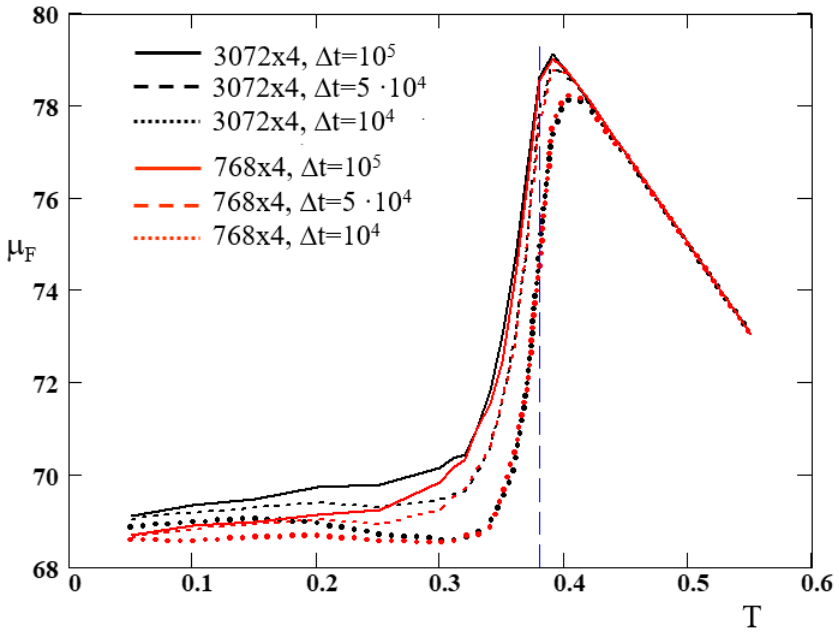

Figure 3.7: Temperature dependence of μ_F for different sampling times $\Delta t = 10^5$, 5×10^4, and 10^4 for the 2 systems: 3072×4 (black curves from top to bottom) and 768×4 (red curves).

(i) $G(t)$ in the "plateau" regime is a bit higher for the smaller system;

(ii) the stress relaxation time τ_α is longer for this system below T_g (note that a lower $\Delta t/\tau_\alpha$ always leads to a higher effective modulus μ).

Let us turn to the sampling time effect for the moduli. The T-dependence of μ and μ_F for both systems at different Δt is depicted in Figs. 3.7, 3.8 and 3.9.

It is obvious that μ decreases (μ_F increases) with increasing Δt at a given T as it should be (longer relaxation leads to a lower terminal modulus μ). It is also clear that, as expected, the glass transition shifts to lower temperatures as Δt is increased. However, the steepness of the transition (of the growth of μ near T_g) does not increase with Δt being apparently nearly constant (more precisely, the transition becomes sharper as Δt increases from 500 to 10^4 LJ units, but a further increase of Δt makes it a bit less sharp). An increase of the transition sharpness reported in ref. [7] for the larger 3072×4 system concerns short sampling times, $\Delta t \leqslant 10^4$.

This feature seems to be a curiosity of the system: at long Δt, we expect the glass transition to become progressively sharper (see section 3.9). Apparently, much longer sampling times are required to test this expectations.

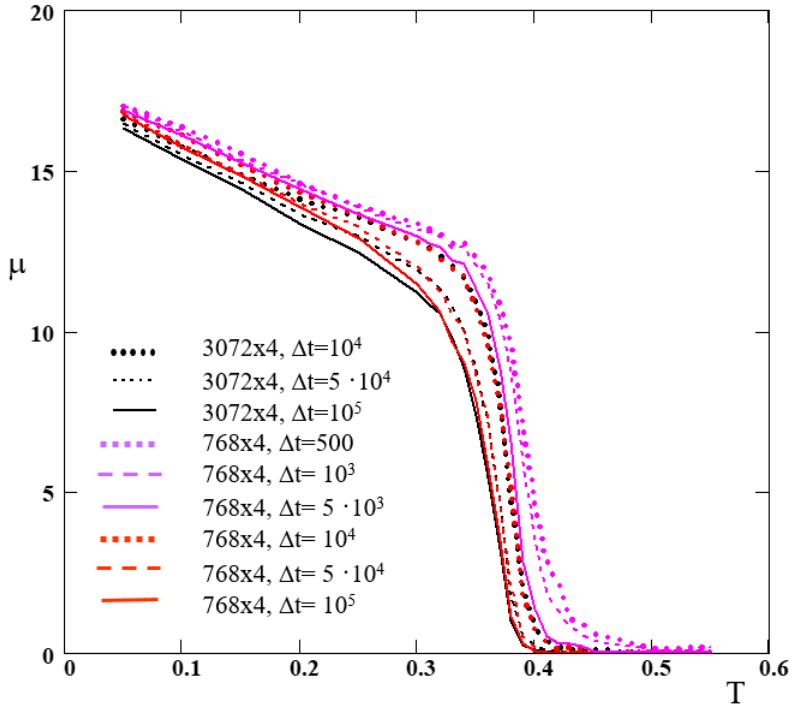

Figure 3.8: Temperature dependence of μ for different sampling times Δt for the 2 systems: 768×4 (3 red curves and 3 magenta curves, from bottom to top for $\Delta t = 10^5$, 5×10^4, 10^4, 5×10^3, 10^3, and 500) and 3072×4 (black from bottom to top for $\Delta t = 10^5$, 5×10^4, 10^4).

We attempted to perform the time-temperature superposition (TTS) to collapse the $\mu(T)$ curves for different Δt times. The natural idea is that the glass transition occurs when the sampling time Δt gets comparable to the characteristic time of stress relaxation $\tau_\alpha = \tau_\alpha(T)$. This concept implies that the relevant variable is $\tau_\alpha(T)/\Delta t$. Assuming an Arrhenius (activation) behavior for the relaxation time, $\tau_\alpha(T) = \text{CONST} \cdot \exp(E/T)$, where E is the activation energy, we arrive at the relevant time-temperature variable $x = \frac{1}{T} + \frac{1}{E} \ln\left(\frac{\Delta t_{\text{ref}}}{\Delta t}\right)$, where Δt_{ref} is an arbitrary reference time. A reasonable collapse of μ vs. x is achieved for $E \approx 18$ (see Fig. 3.9). The same activation energy can be deduced from the temperature behavior of the shear viscosity η near T_g (in the range of $0.37 \leqslant T \leqslant 0.41$) for the larger 3072×4 system (cf. Fig. 13 of ref. [7]). The validity of the TTS verified in Fig. 3.9 is important as it supports the smooth dependence of $G(t)$ on time upon cooling through the glass transition. In fact, a continuous dependence of T_g on Δt (which is implied in the TTS) is incompatible with a discontinuous dependence of shear modulus $\mu(T)$ as defined in eq. 2.42, at a finite Δt.

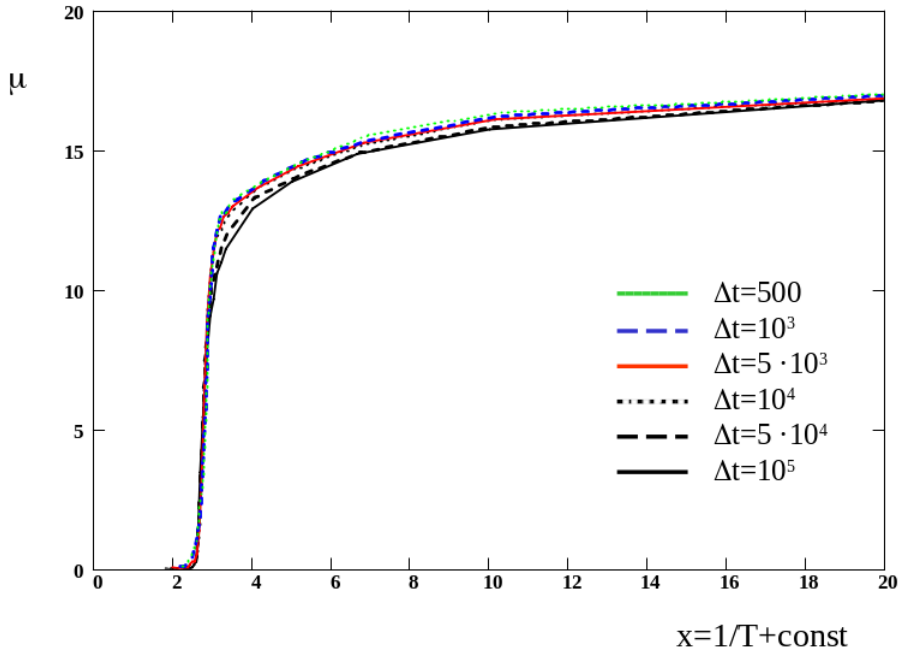

Figure 3.9: Time-temperature superposition for the effective shear modulus μ for the 768×4 system: μ is plotted vs. $x = \frac{1}{T} + \frac{1}{E} \ln\left(\frac{\Delta t_{\max}}{\Delta t}\right)$, where the activation energy $E = 18$ LJ units and $\Delta t_{\max} = 10^5$. The curves correspond to different sampling times: $\Delta t = 10^5$ (solid black), 5×10^4 (dashed black), 10^4 (dotted black), 5×10^3 (solid red), 10^3 (dashed blue), and 500 (green).

3.7 Fluctuations and correlations of μ_A

The modulus μ_A provides an instant response to a small instant shear. It is therefore a static, structural property of the system. The deviations of μ_A discussed in ref. [7] refer to the dispersion of the mean μ_A values time-averaged along a trajectory. More precisely, the instant affine moduli were calculated using eq. 2.57 at regular times separated by $\Delta t_A = 500$ LJ units, so the mean μ_A is based on $n_A = \Delta t / \Delta t_A = 200$ configurations for the time-window $\Delta t = 10^5$ LJ. Note, that the so-called impulsive correction to μ_A, which is proportional to $g_{\mathrm{nb}}(r_{\mathrm{cut}})$, cf. eq 2.59 was taken into account as described in ref. [94]. For better comparison, μ_A and its standard deviation, $\delta\mu_A$, were calculated in a similar way for 768×4 system:

$$(\delta\mu_A)^2 = \left\langle (\tilde{\mu}_A - \mu_A)^2 \right\rangle , \tag{3.4}$$

where $\tilde{\mu}_A$ is the mean affine modulus of a trajectory and $\mu_A = \langle \tilde{\mu}_A \rangle$ is the ensemble-averaged modulus.

The standard deviations of μ_A are shown for both system sizes in Fig. 3.10.

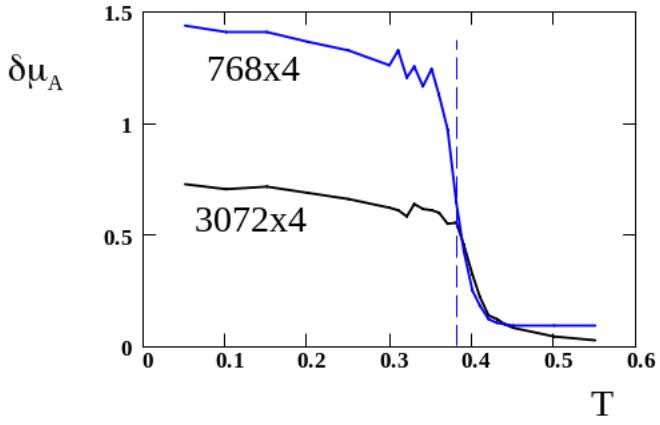

Figure 3.10: Comparison of the temperature dependence of $\delta\mu_A$ for the 3072×4 system (black curve) with $\delta\mu_A$ for the smaller system, 768×4 (blue curve). In both cases, $\delta\mu_A$ is based on the time-averaged μ_A obtained by MD simulations for the ensemble of $m = 100$ systems and 3 shear planes.

It is clear that $\delta\mu_A$ strongly increases as the system is cooled through the glass transition region. It is also obvious that $\delta\mu_A$ decreases with the system size. The ratio of standard deviations $\delta\mu_A\,(768)\,/\delta\mu_A\,(3072)$ is close to 2 at low $T \lessapprox 0.35$ (cf. Fig. 3.11).

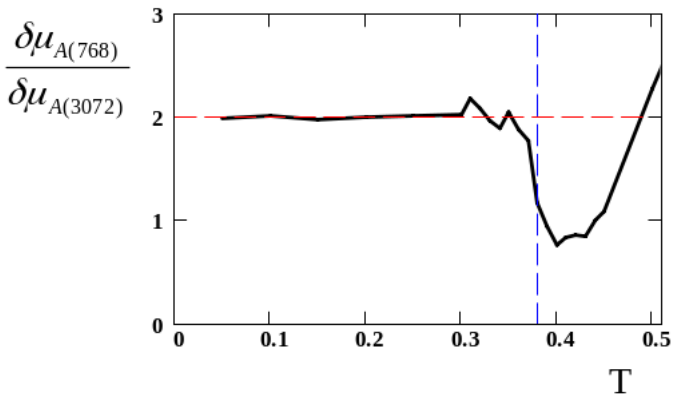

Figure 3.11: The T-dependencies of the ratio of $\delta\mu_A$ for 768×4 over that for 3072×4. The ratio is close to 2 for $T < 0.35$ (below T_g) indicating that $\delta\mu_A$ follows the classical $1/\sqrt{V}$ law (self-averaging of μ_A).

This fact points to the standard power-law dependence of $\delta\mu_A$ on the system volume, $\delta\mu_A \propto 1/\sqrt{V}$ (note that the system volume is proportional to the number of particles). The ratio $\delta\mu_A\,(768)\,/\delta\mu_A\,(3072)$ is close to 1 in the glass transition region, where $\delta\mu_A$

strongly depends on T. This feature may be due to a small difference in the effective glass transition temperature between the 2 systems.

Therefore, μ_A appears to be a self-averaging quantity whose variance decreases with the total volume as $1/V$. This conclusion is in line with simulation studies of self-assembling networks [120]. In view of this property, it may be tempering to relate the variance of μ_A with some microscopic correlation volume V_c, $(\delta\mu_A)^2 \simeq (V_c/V)\,\mu_A^2$. What is the nature of V_c? Does an increase of $\delta\mu_A$ at low T signify an increase of a structural correlation volume? These and other questions related to the statistics of μ_A are discussed below in this section.

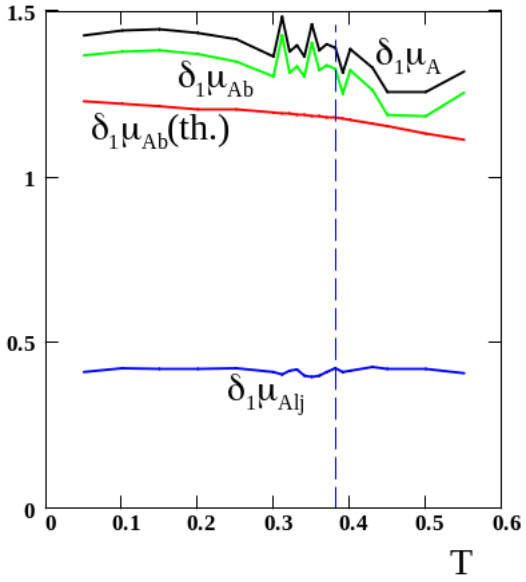

Figure 3.12: The affine modulus and its dispersion for the 768×4 system. The standard deviations of the instantaneous affine modulus, $\delta_1\mu_A$ (black curve), and of its parts: $\delta_1\mu_{Ab}$ due to bonds (green curve), theoretical $\delta_1\mu_{Ab}$ (red curve), and $\delta_1\mu_{Alj}$ due to LJ-interactions (blue curve). The bond and LJ contributions to μ_A are generally rather weakly correlated, so the following rule of additive variances works with good accuracy (relative error $\lesssim 1\%$: $\delta_1\mu_A = \sqrt{\delta_1\mu_{Ab}^2 + \delta_1\mu_{Alj}^2}$).

It is worth stressing that the statistics of the time-averaged μ_A involve time-correlations between instant μ_A along the trajectory. These correlations are dynamical (rather than solely structural) in nature and therefore are strongly dependent on the temperature. To avoid the dynamical aspect, one has to consider directly the statistics of the instant moduli $\tilde{\mu}_A$ ($n_A m$ values in total for $m = 100$ independent trajectories). The corresponding standard deviation is denoted here as $\delta_1\mu_A$; it was calculated based on 100 independent

trajectories for each T. We analysed separately the two nonideal (excess) contributions to μ_A, one due to interactions between bonded monomers (μ_{Ab}) and another due to LJ-interactions (μ_{Alj}).

They can be written as (cf. eq. 2.59):

$$\begin{aligned} \mu_{Ab} &= \frac{1}{V}\sum_l n_y^2 \left[r_l^2 u_{\mathrm{b}}''(r_l)\, n_x^2 + r_l u_{\mathrm{b}}'(r_l) \left(1 - n_x^2\right)\right], \\ \mu_{Alj} &= \frac{1}{V}\sum_l n_y^2 \left[r_l^2 u_{\mathrm{LJ}}''(r_l)\, n_x^2 + r_l u_{\mathrm{LJ}}'(r_l) \left(1 - n_x^2\right)\right], \end{aligned} \tag{3.5}$$

where u_{b} and u_{lj} are the bond and LJ interaction potentials. The overall μ_A is a sum of the above terms and the ideal-gas term ρT ($\rho = N_m/V$; the ideal term contributes only $\sim 1\%$ to μ_A; its fluctuations are totally negligible). The results for the 768×4 system are shown in Fig. 3.13. One can observe that the mean μ_A, μ_{Ab}, and μ_{Alj} all increase weakly as T is lowered (cf. Fig. 3.13). Being static properties, the instantaneous μ_A-moduli are expected to show a cusplike feature at the glass transition in analogy with the T-dependence of density (cf. Fig. 3.2). Such features (weak virtual cusp near T_g) are indeed visible in the T-dependencies of μ_A, μ_{Ab}, and μ_{Alj} (cf. Fig. 3.13).

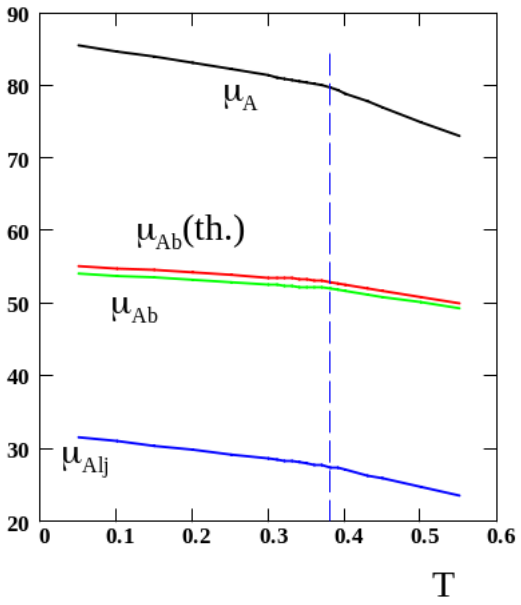

Figure 3.13: The affine modulus and its parts for the 768×4 system. The T-dependencies of the instantaneous affine modulus μ_A (black curve), its bond contribution μ_{Ab} (green curve), and the LJ-interaction term μ_{Alj} (blue curve). Vertical line corresponds to $T_g = 0.38$.

Remarkably, however, the standard deviations (across the mn_A ensemble) of the instant values of the μ_A-moduli are nearly independent of T (cf. Fig. 3.12) in drastic constant with a strong increase of $\delta\mu_A$ (deviations of the time-averaged μ_A) near and below T_g (cf. Fig. 3.14). Note that $\delta_1\mu_A \approx \delta\mu_A$ for $T \lesssim 0.36$, but $\delta_1\mu_{\rm a} \gg \delta\mu_A$ for $T \gtrsim 0.4$. It means that the amorphous structure stays largely frozen at low T (so, in particular, bond-orientational fluctuations are suppressed), and therefore the fluctuations of μ_A along the time-trajectory become negligible in this regime (as the system rests in a virtually single inherent structure within a metabasin). We also observe that generally μ_A is dominated by the bond contribution, μ_{Ab}. A similar statement is even more true for the standard deviations: the total deviation $\delta_1\mu_A$ is nearly equal to that for bonds, $\delta_1\mu_{Ab}$.

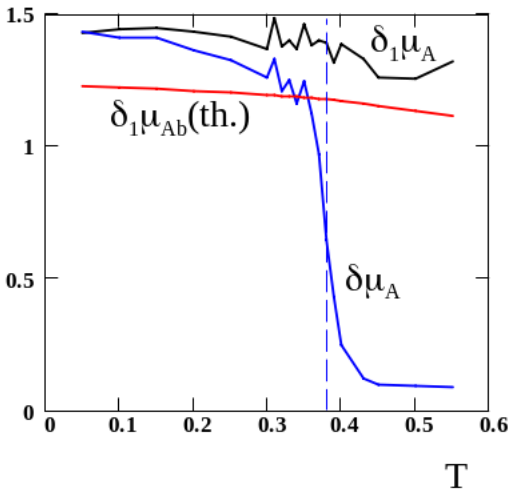

Figure 3.14: The affine modulus and its dispersion for the 768×4 system. Comparison of T-dependence of instant deviations [$\delta_1\mu_A$ for the total modulus (black curve), its theoretical bond contribution $\delta_1\mu_{Ab}$ (red curve)] and standard deviations of the total time-averaged modulus, $\delta\mu_A$ (blue curve). Note that $\delta_1\mu_A \approx \delta\mu_A$ for $T < 0.36$. This means that the inherent structure of the system is frozen in this regime: fluctuations of μ_A along the time-trajectory are negligible.

We obtained and compared contributions to the dispersion of the instant μ_A due to the thermal fluctuations along the trajectory, $\mathrm{var}_F(\mu_A)$, and due to permanent variations between independently cooled configurations (metabasins), $(\delta\mu_A)^2 = \mathrm{var}_{\rm MB}(\mu_A)$. As we already mentioned above, $\delta\mu_A$ is approximately the same as $\delta_1\mu_A$ for $T \lesssim 0.36$. The connection between $\mathrm{var}_F(\mu_A)$, $\mathrm{var}_{\rm MB}(\mu_A)$, and $\delta_1\mu_A$ can be written as $(\delta_1\mu_A)^2 = \mathrm{var}_{\rm MB}(\mu_A) + \mathrm{var}_{\rm F}(\mu_A)$. As expected, we found that the MB-contribution dominates well

below T_g (at $T \lesssim 0.3$), while both contributions are comparable near T_g (and, of course, the fluctuation contribution dominates above T_g).

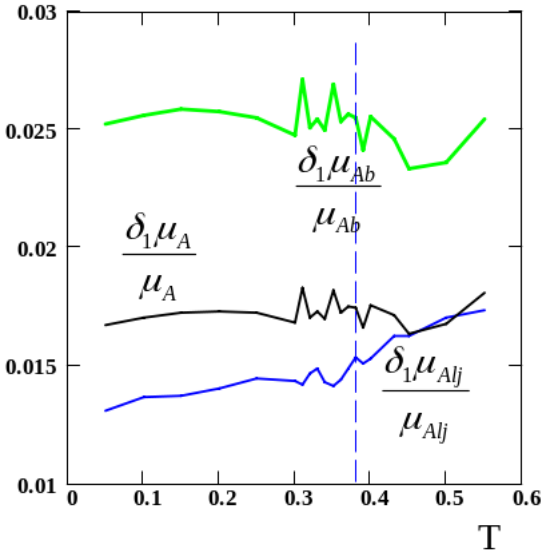

Figure 3.15: The affine modulus and its dispersion for the 768×4 system. The relative standard deviations of instantaneous moduli: $\delta_1\mu_A/\mu_A$ (black), $\delta_1\mu_{Ab}/\mu_{Ab}$ (green), $\delta_1\mu_{Alj}/\mu_{Alj}$ (blue).

One may wonder if a structural correlation length ξ_s can be estimated based on these results. Below we show that this is not really possible. The point is that both μ_{Ab} and $\delta_1\mu_{Ab}$ (providing dominant contributions to the affine modulus and its standard deviation) can be predicted assuming no correlation at all between the polymer bonds. This assumption is reasonable since bonding interactions are much stronger than LJ interactions in our simulation model with $k_b = 1110$ in LJ units. (A renormalization of k_b due to LJ interactions can be neglected for the same reason). It leads to the following results (small corrections of relative order $T/(k_b l_b^2)$ are neglected here):

$$\mu_{Ab} \approx \frac{1}{20}\rho k_b l_b^2,\ \delta_1\mu_{Ab} \approx \frac{1}{5}\sqrt{\frac{2}{21}}\rho k_b l_b^2/\sqrt{N_m},\ \frac{\delta_1\mu_{Ab}}{\mu_{Ab}} \approx 4\sqrt{\frac{2}{21N_m}} \tag{3.6}$$

These theoretical results are also shown in Figs. 3.13 – 3.14. The relative instant deviations of μ_{Ab} are thus predicted to be T-independent, $\delta_1\mu_{Ab}/\mu_{Ab} \approx 0.0223$ for $N_m = 768 \times 4$, while simulations point to ≈ 0.025 for this ratio (cf. Figs. 3.15 and 3.16).

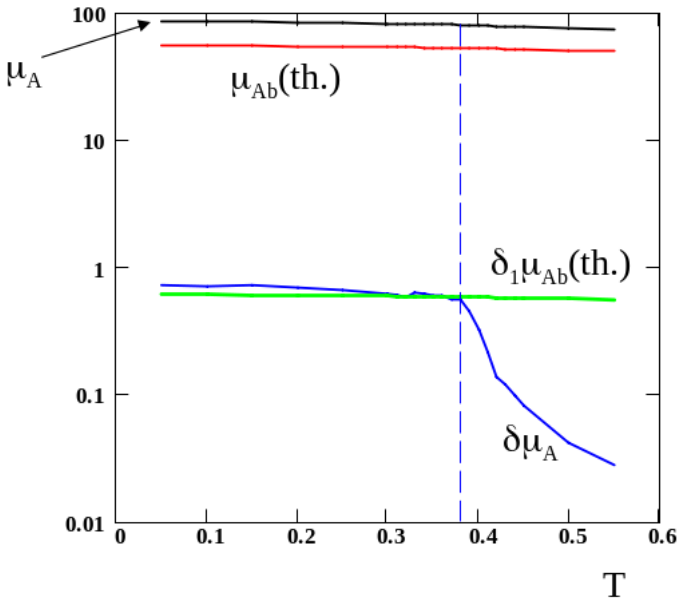

Figure 3.16: Temperature dependence of the affine modulus μ_A, its standard deviation $\delta\mu_A$, the theoretical prediction for its bond part μ_{Ab}, and the theoretical deviation of the instant bond contribution to the modulus, $\delta_1\mu_{Ab}$ (respectively black, blue, red, and green curves) for the 768×4 system. The vertical blue curve corresponds to the $T_g = 0.38$.

It is clear that the predictions are generally in good agreement with our simulation data: the theory just slightly overestimated μ_{Ab} and underestimates $\delta_1\mu_{Ab}$. Given that $\delta_1\mu_A \approx \delta_1\mu_{Ab}$ (cf. Fig. 3.12), we conclude that structural correlations cannot be resolved based on fluctuations of instant μ_A for the model we consider. In other words, μ_A does not seem to be an appropriate variable to probe the correlation length ξ_s. As for the effective correlation volume V_c, it always corresponds to about 1 particle (monomer) independent of temperature and the system size (cf. eq. 3.6).

The revealed T-independence of $\delta_1\mu_A$ invites the question: why the deviations $\delta\mu_A$ of the time-averaged μ_A depend on T so strongly (they increase by a factor of ~ 20 between $T = 0.55$ and 0.05)? The reason is that while μ_A is always averaged over $n_A = 200$ transient configurations along each trajectory, these instant states are independent at $T = 0.55$ (where relaxation time τ_α is much shorter than the time interval Δt_A between the configurations), but they are strongly correlated for $T = 0.05$ ($\tau_\alpha \gg \Delta t_A$). As a result, $\delta\mu_A$ is smaller than $\delta_1\mu_A$ by a factor of $1/\sqrt{n_A}$ at high T's, but this reduction is not applicable at low T, where $\delta\mu_A \sim \delta_1\mu_A$ (cf. Figs. 3.14 and 3.16).

So far, the instant (and time-averaged) μ_A were calculated for a given fixed shear plane (say, xy). The instant μ_A was thus calculated using the general eqs. 2.57 and 2.59

(cf. [7,94]). Recalling the macroscopic isotropy of the system, we tried a different approach to obtain instant μ_A using preaveraging over all possible shear planes. The resultant expression for the preaveraged instant μ_A does not involve bond orientations and can be conveniently written in terms of pair correlation functions like $g(r)$, the Kirkwood radial distribution function:

$$\mu_A = \mu_{Alj} + \mu_{Ab} + \rho T, \tag{3.7}$$

where

$$\mu_{Alj} = A_d \rho^2 \left[\int_0^{r_{\text{cut}}} \left(r u''_{\text{LJ}}(r) + (d+1)\, u'_{\text{LJ}}(r) \right) g_{nb}(r)\, r^d \mathrm{d}r - \left[r^{d+1} u'_{\text{LJ}}(r)\, g_{nb}(r) \right]_{r=r_{\text{cut}}} \right],$$

and

$$\mu_{Ab} = A_d \rho^2 \int_0^{r_{\text{cut}}} \left[r u''_{\text{b}}(r) + (d+1)\, u'_{\text{b}}(r) \right] g_b(r)\, r^d \mathrm{d}r \tag{3.8}$$

Here, $d = 3$ is the space dimension, $A_d = \frac{\pi^{d/2}}{4\Gamma(d/2+2)} \overset{\text{d=3}}{=} \frac{2\pi}{15}$, $u_{\text{b}}(r) = 0.5 k_b (r - l_0)^2$ is the interaction potential for bonded monomers, $u_{\text{LJ}}(r) = 4\left(r^{-12} - r^{-6}\right)$ is the LJ potential in LJ units, $g_b(r)$ is the pair correlation function for bonded monomers (analogous to the Kirkwood function), and $g_{nb} = g(r) - g_b(r)$. Note that:

$$\int g_b \mathrm{d}^d r = \frac{2(N-1)}{N\rho} = \frac{3}{2\rho}, \text{ with } N = 4 \tag{3.9}$$

In practice, the two integrals in eqs. 3.8 are replaced by sums according to the rule:

$$A_d \rho^2 \int_0^{r_{\text{cut}}} X(r)\, g_\alpha(r)\, r^d \mathrm{d}r \to \frac{1}{d(d+2)} \frac{1}{V} \sum_{l(\alpha)} r_l X(r_l), \tag{3.10}$$

where α is either "b" (polymer bond) or "nb" (LJ interaction), $l(\alpha)$ runs over all (disordered) monomer pairs of type α, and $X(r)$ is any function.

We found that the orientation-averaging dramatically reduces the variance of μ_A: both standard deviations $\delta\mu_A$ and $\delta_1\mu_A$ (of time-averaged and instant μ_A values, respectively) decrease as a result by a factor changing from ~ 6 to ~ 20 as T is lowered from 0.55 to 0.05 (see Figs. 3.17 and 3.18).

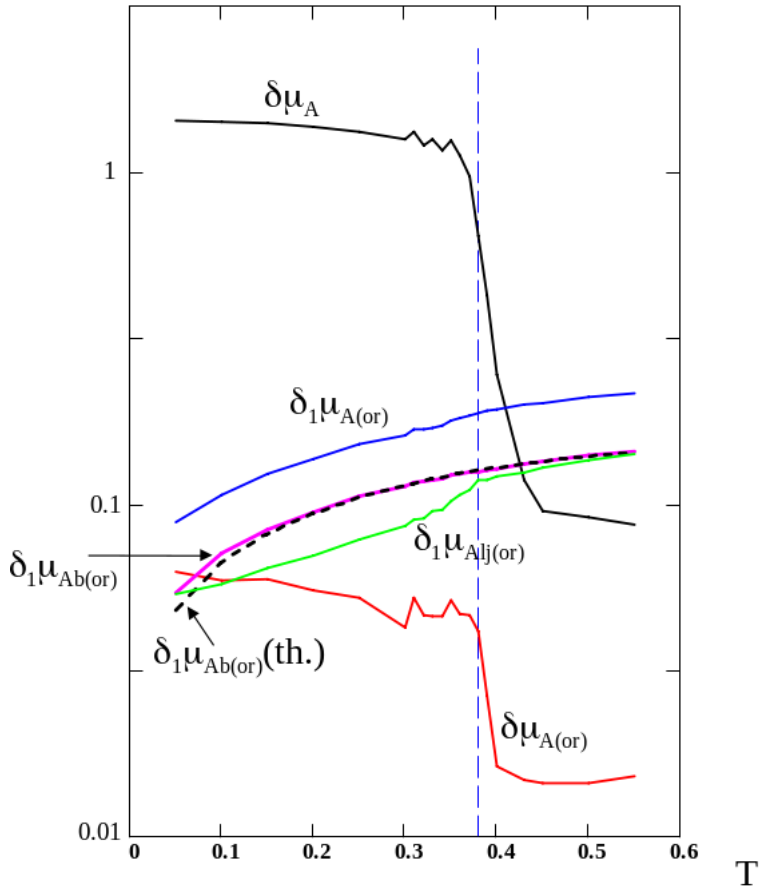

Figure 3.17: The affine modulus and its dispersion for the 768 × 4 system. The T-dependencies for standard deviations of the time-averaged μ_A: $\delta\mu_A$ for a fixed shear plane (black curve) and $\delta\mu_{A(\mathrm{or})}$ for the orientation-averaged modulus (red curve). Deviations of the instant but orientation-averaged affine modulus and its parts (due to bonds and LJ interactions): total $\delta_1\mu_{A(\mathrm{or})}$ (blue curve), bond contribution $\delta_1\mu_{Ab(\mathrm{or})}$ (magenta), theoretical deviation due to bonds (dashed black), and LJ contribution $\delta_1\mu_{Alj(\mathrm{or})}$ (green).

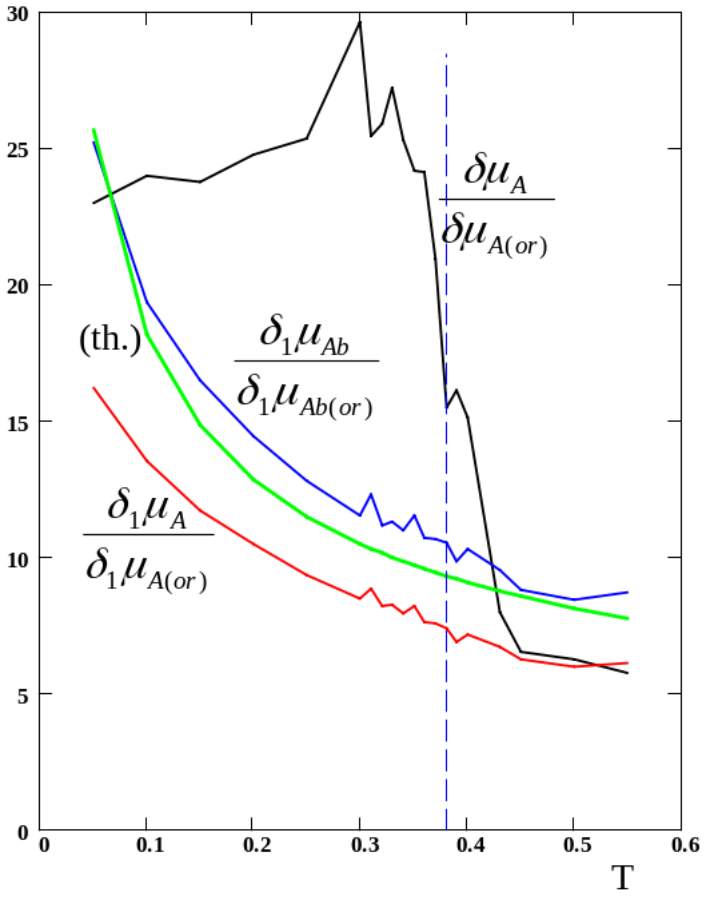

Figure 3.18: The affine modulus and its dispersion for the 768 × 4 system. The T-dependencies of the ratio $\delta\mu_A/\delta\mu_{A(\mathrm{or})}$ (black curve); $\delta_1\mu_A/\delta_1\mu_{A(\mathrm{or})}$ (red), $\delta_1\mu_{Ab}/\delta_1\mu_{Ab(\mathrm{or})}$ (blue), and theory for the latter (green).

This unexpectedly strong effect has a simple physical meaning: the variance of μ_A is dominated by bond-orientational fluctuations which are effectively eliminated in the new definition, eqs. 3.7 and 3.8. On more quantitative grounds, this effect can be analyzed for the dominant bond-related part of μ_A. Fluctuations of the preaveraged μ_{Ab} defined in eqs. 3.7 and 3.8 are due to bond-length fluctuations which are much weaker than orientational fluctuations. Assuming (as before) independent bonds, we found:

$$\delta_1\mu_{Ab(\mathrm{or})} \approx 0.2\rho l_b \sqrt{\frac{3Tk_b}{N_m}} \tag{3.11}$$

This standard deviation of instant but orientation-averaged μ_{Ab} is thus expected to decrease as $\sqrt{T}$ at low temperatures (following the amplitude of bond-length fluctuations). This prediction is in very good agreement with simulation results for $\delta_1\mu_{Ab(\mathrm{or})}$ in the whole studied T-range (cf. dashed black and magenta curves in Fig. 3.17).

Comparing eq. 3.11 and eq. 3.6, we observe that the standard deviation of μ_{Ab} is now significantly reduced by a large factor:

$$\frac{\delta_1\mu_{Ab}}{\delta_1\mu_{Ab(\mathrm{or})}} = \frac{l_b}{3}\sqrt{\frac{2k_b}{7T}} \approx \frac{5.74}{\sqrt{T}} \tag{3.12}$$

in quantitative agreement with simulation results and in qualitative agreement with a similar reduction of $\delta_1\mu_A$ and $\delta\mu_A$ (deviations of instant and time-averaged μ_A, cf. Fig. 3.18).

Note that a fast increase of the ratio of the time-averaged deviations, $\delta\mu_A/\delta\mu_{A(\mathrm{or})}$ near T_g (cf. Fig. 3.18), is due to an increase of the orientational relaxation time (leading to a poorer self-averaging of μ_A over the sampling time at $T < T_g$, hence to an increase of $\delta\mu_A$), while a decrease of the same ratio at lower $T < 0.3$ is due to a slowdown (partial freezing) of bond-length fluctuations leading to a poorer self-averaging of $\mu_{A(\mathrm{or})}$, hence an increase of the denominator, $\delta\mu_{A(\mathrm{or})}$, on further cooling.

To conclude, eqs. 3.7 and 3.8 are useful to obtain more precise instantaneous affine shear modulus μ_A. With the standard definition of μ_A (without orientational pre-averaging), the standard deviation $\delta\mu_A$ becomes comparable to $\delta\mu_F$ at low T (in particular, for the smaller 768×4 system, cf. Figs. 3.17 and 3.20), so the standard deviation of $\mu = \mu_A - \mu_F$ gets somewhat larger than $\delta\mu_F$. Using μ_A obtained with eqs. 3.7 and 3.8, we arrive at less fluctuating μ with $\delta\mu \approx \delta\mu_F$ at all T's since fluctuations of μ_A in this case are always totally negligible.

3.8 Dispersion of μ_F

The fluctuation modulus $\tilde{\mu}_F$ (cf. eq. 2.51) is a random variable changing across the m-ensemble; its standard deviation $\delta\mu_F$ (with a large ensemble, $m \gg 1$) is defined in analogy with $\delta\mu_A$:

$$(\delta\mu_F)^2 = \left\langle (\tilde{\mu}_F - \mu_F)^2 \right\rangle, \tag{3.13}$$

where μ_F is the mean value defined in eq. 2.49. The simulation results for the deviations $\delta\mu_F$ at different temperatures are shown for both systems (at $\Delta t = 10^5$) in Fig. 3.20. The data for the 3072×4 system have been discussed in ref. [7]. It was reported there that both $\delta\mu_F$ and $\delta\mu \approx \delta\mu_F$ (this equation comes from eq. 2.45 and the fact that the variance of μ_A can be neglected with respect to the variance of μ_F, cf. section 3.7 and ref. [7]) show

a peak near the apparent glass transition temperature T_g. This feature is confirmed here for the new 768×4 system. The peaks are located at the same temperature $T \approx 0.36$. It is interesting that the peak height is nearly independent of the system volume (the peak is just a bit higher for the smaller system) and that the deviations, $\delta\mu_F$, are identical for both systems in the liquid regime ($T > T_g$). On the other hand, at low-T, $\delta\mu_F$ is significantly larger for the smaller system (as compared to the large one).

The sampling time effect on $\delta\mu_F$ is illustrated in Fig. 3.19. In the liquid regime, $\delta\mu_F$ significantly increases as Δt is shortened (this behaviour is in accord with an increase of effective T_g for shorter Δt, cf. the end of section 3.6). A different conclusion was drawn in the previous work [7]. By contrast, $\delta\mu_F$ decreases (albeit rather moderately) for shorter Δt in the peak region and below the transition. This tendency (an increase of $\delta\mu_F$ with Δt) seems to weaken at low T and disappears at the lowest $T = 0.05$.

The discovered peak of $\delta\mu_F$ near T_g is a remarkable feature demanding an explanation. A qualitative argument elucidating this behavior is presented in section 3.9. Below, instead, we describe a quantitative approach predicting $\delta\mu_F$ based on the known relaxation modulus $G(t)$.

The fluctuation modulus for a given trajectory, $\tilde{\mu}_F$, is directly related to the stress function $\sigma(t)$, cf. eq. 2.51, which is stochastic process characterized by some stationary probability distribution enveloping all systems of the statistical ensemble we consider. The basic assumption adopted here is that this distribution in nearly Gaussian (i.e., $\sigma(t)$ is a Gaussian process). Its validity is discussed in section 3.9. It is instructive to consider a discrete version of the theory involving arrays $\sigma_i \equiv \sigma(t_i)$ of stress recorded at times $t_i = i\delta t$, where δt is the time interval between successive stress calculations ($\delta t = 0.05$ in our simulations) and i as an integer changing from 1 to $I = \Delta t/\delta t$. Then:

$$\tilde{\mu}_F = \frac{V}{T}\left(I^{-1}\sum_i \sigma_i^2 - I^{-2}\sum_{i,j}\sigma_i\sigma_j\right), \tag{3.14}$$

where j is also changing from 1 to I. The mean value of $\tilde{\mu}_F$ can be obtained nothing that:

$$\frac{V}{T}\langle\sigma_i\sigma_j\rangle = G_{i-j} + \text{const}, \tag{3.15}$$

with $G_{i-j} \equiv G(|t_i - t_j|)$,

$$\mu_F = G_0\left(1 - I^{-1}\right) - 2I^{-2}\sum_{s=1}^{I-1}(I-s)\,G_s \tag{3.16}$$

The latter equation can be considered as the discrete version of eq. 2.52. The variance of μ_F is:

$$(\delta\mu_F)^2 = \left\langle (\tilde{\mu}_F)^2 \right\rangle - \mu_F^2 \tag{3.17}$$

The r.h.s. of the above equation involves terms such as $\langle \sigma_i \sigma_j \sigma_{i'} \sigma_{j'} \rangle$ (emerging on recalling eq. 3.14). For a Gaussian $\sigma(t)$, such quartic correlations are reduced to pair correlators:

$$\langle \sigma_i \sigma_j \sigma_{i'} \sigma_{j'} \rangle = \langle \sigma_i \sigma_j \rangle \langle \sigma_{i'} \sigma_{j'} \rangle + ..., \tag{3.18}$$

which are related to $G(t)$ via eq. 3.15. As a result, we get:

$$\left(\delta\mu_F^{(\mathrm{G})}\right)^2 = \frac{2}{I^4}\left\{ \left[\sum_{i,j} G_{i-j}\right]^2 + I^2 \sum_{i,j} G_{i-j}^2 - 2I \sum_{i,j,s} G_{s-i} G_{s-j} \right\} \tag{3.19}$$

The superscript "G" here means that eq. 3.19 gives the variance of μ_F using the Gaussian approximation.

The "Gaussian" standard deviations, $\delta\mu_F^{(\mathrm{G})}$, were calculated for both systems and different T's and sampling times Δt. (In practice, all the multiple sums in eq. 3.19 were reduced to single sums using recursive relations between the sums for different I's[1].) The obtained results are compared with simulation data for $\delta\mu_F$ in Fig. 3.21.

Noteworthily, the T-dependence of the "Gaussian" deviations $\delta\mu_F^{(\mathrm{G})}$ are nearly the same for both systems. One can observe an excellent agreement between $\delta\mu_F^{(\mathrm{G})}$ and $\delta\mu_F$ in the liquid regime, $\delta\mu_F \approx \delta\mu_F^{(\mathrm{G})}$ at $T > T_g$ for both systems. Moreover, the Gaussian approximation correctly reproduces the simulation data also in the peak region (for $T \gtrsim 0.3$) for the larger system, while for 768×4 system, the peak height is somewhat underestimated by the theory. At low temperatures, $T < 0.3$, the predicted $\delta\mu_F^{(\mathrm{G})}$ strongly decreases, while $\delta\mu_F$ seems to saturate at a finite level.

The above conclusions are supported with Fig. 3.23 illustrating the T-dependence of $\delta\mu_F$ and $\delta\mu_F^{(\mathrm{G})}$ at different sampling times Δt. At low $T < T_g$, the effect of Δt is complicated: at $T \gtrsim 0.2$, the theoretical deviation $\delta\mu_F^{(\mathrm{G})}$ increases with Δt, while the opposite tendency works at lower temperatures ($T \lesssim 0.15$). (Note that $\delta\mu_F$ seems to exhibit a qualitatively similar behavior, albeit with a crossover at a lower $T \sim 0.05$, cf. Fig. 3.19). Where such behavior could originate from? It is relatively easy to clarify it

[1] **Submitted paper:** G. George, L. Klochko, A. N. Semenov J. Baschnagel, and J. P. Wittmer, "Ensemble fluctuations matter for variances of macroscopic variables", European Physical Journal E

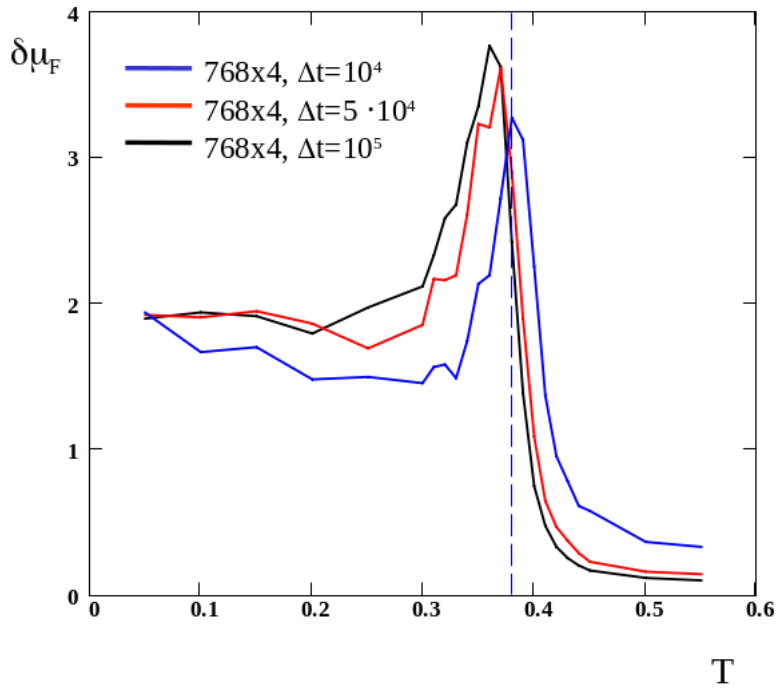

Figure 3.19: Standard deviations of the fluctuation modulus for 768×4 system: $\delta\mu_F$ vs. T for different time windows: $\Delta t = 10^5$ (black), 5×10^4 (red), and 10^4 (blue curve).

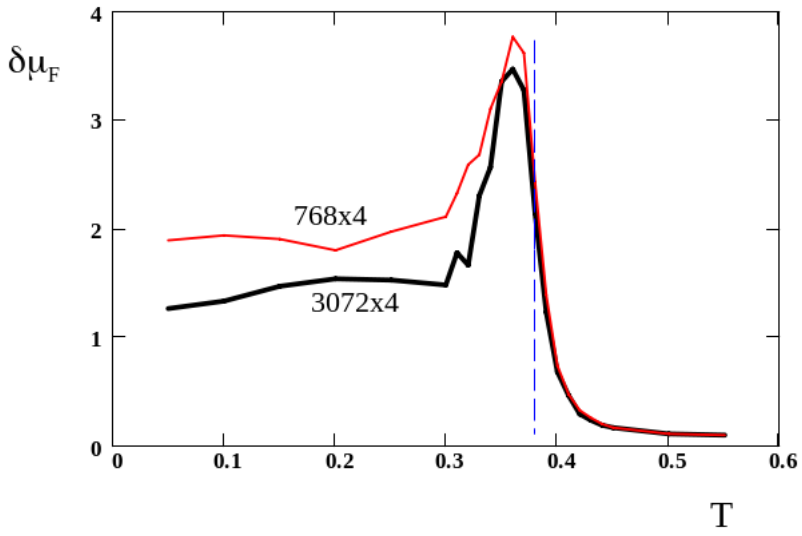

Figure 3.20: Standard deviations of the fluctuation modulus for $\Delta t = 10^5$: $\delta\mu_F$ vs. T for 768×4 (red curve) and 3072×4 (black curve). Vertical line is the reference for $T_g = 0.38$.

for $\delta\mu_F^{(\mathrm{G})}$. The analysis can be based on the following equation stemming directly from

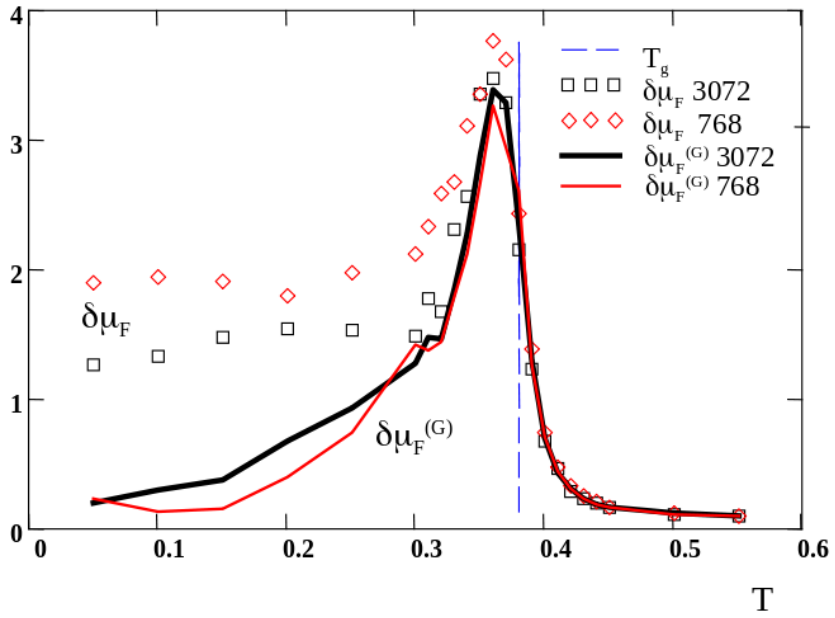

Figure 3.21: Standard deviations of the fluctuation modulus for $\Delta t = 10^5$: temperature dependence of $\delta\mu_F$ (red rhombuses and black boxes) and its Gaussian part, $\delta\mu_F^{(\mathrm{G})}$ (red and black curves) for 768×4 and 3072×4 systems, receptively.

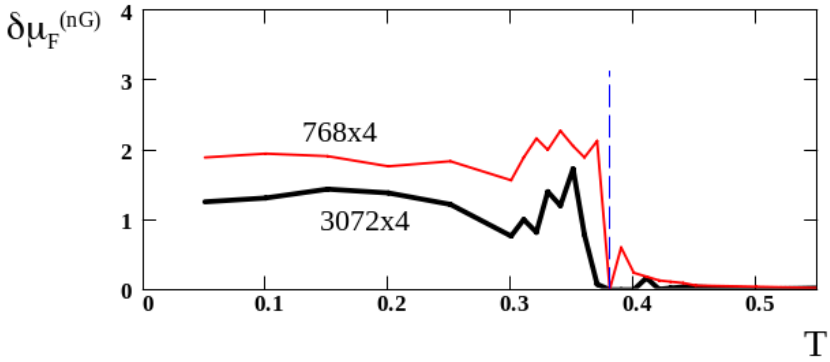

Figure 3.22: Standard deviations of the fluctuation modulus for $\Delta t = 10^5$: non-Gaussian deviation $\delta\mu_F^{(\mathrm{nG})}$ vs. T for 768×4 and 3072×4 systems (red and black curves).

eq. 3.19:

$$\left(\delta\mu_F^{(\mathrm{G})}\right)^2 = \frac{1}{2I^4}\sum_{iji'j'}\left(G_{i-j} + G_{i'-j'} - G_{i-j'} - G_{j-i'}\right)^2 \tag{3.20}$$

At low T's, the lion's share of time points falls into the plateau regime, where G is nearly constant (cf. Fig. 3.5), hence the summand is small: its typical value is $\left(G\left(\Delta t\right) - G\left(\Delta t/2\right)\right)^2 \sim g^2$, where $g = \left(\partial G/\partial \ln t\right)_{t\sim\Delta t}$. The long-time contribution to the variance, $\left(\delta\mu_F^{(\mathrm{G})}\right)^2$, is therefore $\sim g^2$ with small $g = g\left(T, \Delta t\right)$ ($g \lesssim 1$ for $T < 0.3$).

When 2 time points (say, i and j) get close to each other, the summand can take a much larger value ($\sim (\mu_A - \mu)^2 = \mu_F^2$), but the "probability" of such an event is low, $\sim \tau_{\min}/\Delta t$. Taking into account both contributions, we write:

$$\left(\delta\mu_F^{(\mathrm{G})}\right)^2 \sim g\,(T, \Delta t)^2 + \mu_F^2 \tau_0/\Delta t,\ \Delta t > \tau_0, \tag{3.21}$$

where $\tau_0 = \tau_{\min}$ is the time scale of initial fast stress relaxation (before the plateau regime). The g-factor here increases with Δt, but this increase becomes extremely weak at low T (cf. Fig. 3.5). By contrast, the second term decreases with Δt (for $\Delta t > \tau_0$) and is nearly independent of temperature. It wins at very low T's where the g-variation can be neglected thus leading to a decrease of the whole variance $\left(\delta\mu_F^{(\mathrm{G})}\right)^2$ with Δt.

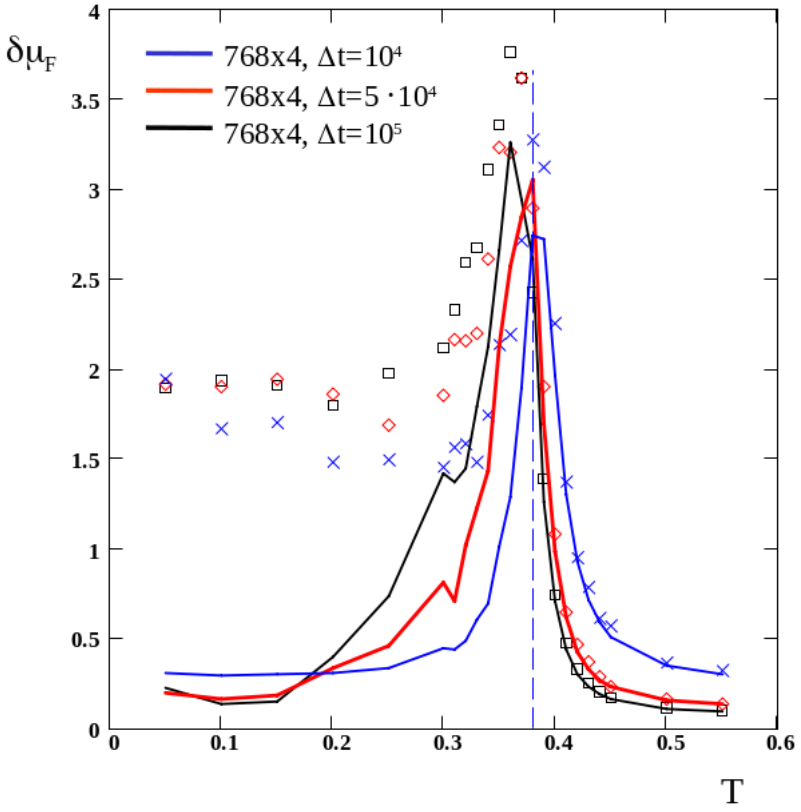

Figure 3.23: Standard deviations of the fluctuation modulus for 768×4 system: $\delta\mu_F$ (black boxes, red rhombuses, and blue crosses) and its Gaussian contribution $\delta\mu_F^{(\mathrm{G})}$ (black, red, and blue solid curves) for different $\Delta t = 10^5,\ 5\times10^4$, and 10^4.

It is interesting that the Δt-dependence of $\delta\mu_F^{(\mathrm{G})}$ for $\Delta t \gg \tau_0$ is qualitatively similar to its T-dependence (the main relevant parameter is $\Delta t/\tau_\alpha$ which increases either with Δt or with T). Both μ_F and $\delta\mu_F^{(\mathrm{G})}$ obviously vanish at $\Delta t = 0$. At high temperatures (above

T_g), the Gaussian deviation $\delta\mu_F^{(G)}$ first increases with Δt at the time scale $\Delta t \lesssim \tau_\alpha$ and then decreases at longer Δt. At low T ($T \lesssim T_g$), the stress relaxation proceeds in two steps with times $\sim \tau_0$ and $\sim \tau_\alpha$, and we predict 2 peaks of $\delta\mu_F^{(\mathrm{G})}$ vs. Δt: one is related to $\Delta t \sim \tau_0$ and the other one to much longer time, $\Delta t \sim \tau_\alpha$. This qualitative discussion is considered be explicit calculation for model function for $G(L)$[2]

To sum up, it appears that the Gaussian theory works well above T_g and in the transition (peak) region but fails at low T's. In section 3.9, we explain this behavior and deduce some important information stemming from it.

3.9 Discussion

3.9.1 Solidification transition

Our analysis shows (cf. section 3.6) that the transition from liquid to amorphous solid behavior (a nearly steplike increase of the static shear modulus μ) occurs in the T-region where the terminal relaxation time is comparable with the sampling time, $\tau_\alpha(T) \sim \Delta t$ (for long enough Δt, this regime involves a long-time plateau in the shear relaxation modulus $G(t)$). The latter condition defines the apparent glass transition temperature $T_g = T_g(\Delta t)$ which depends on the explored time-window Δt and corresponds to both the steepest increase of $\mu = \mu(T)$ (cf. Fig. 3.8) and the maximum of its standard deviation $\delta\mu \approx \delta\mu_F$ (cf. Fig. 3.19).

In terms of relaxation functions like $G(t)$, the vitrification can be considered as a transition from the glassy plateau regime to the liquid regime with vanishing $G(t)$. This transition occurs at $t \sim \tau_\alpha(T)$, more precisely, in the region where $G(t)/G(\tau_\alpha) \sim 1$. Assuming the KWW stretched exponential relaxation law [2] for $G(t)$, it leads to the time-region whose width in log-scale is defined by $\delta(\ln(t/\tau_\alpha(T))) \sim 1/\beta$, where β is the stretching exponent. Therefore, the temperature width, δT_g, of the glass transition region (for a given time-window Δt) can be roughly defined by the condition $\delta(\ln(\tau_\alpha(T)/\Delta t)) \sim 1/\beta$ leading to $\delta T_g |\partial \ln \tau_\alpha/\partial T|_{T=T_g} \sim 1/\beta$. The latter estimate can be rewritten as:

$$\delta T_g/T_g \sim 1/(\beta m_f), \tag{3.22}$$

where $m_f = -\partial \ln \tau_\alpha/\partial \ln T|_{T=T_g}$ is the fragility index (a similar dependence of δT_g on m_f was predicted in the review [121]). An Arrhenius increase of the relaxation time

[2]**Submitted paper:** G. George, L. Klochko, A. N. Semenov J. Baschnagel, and J. P. Wittmer, "Ensemble fluctuations matter for variances of macroscopic variables", European Physical Journal E

below T_g, $\tau_\alpha \sim \tau_0 \exp(E/T)$ (τ_0 is the time scale of particle collisions), leads to $m_f \sim \ln(\tau_\alpha/\tau_0) \sim \ln(\Delta t/\tau_0)$. Hence, the transition width $\delta T_g/T_g$ is expected to logarithmically decrease with the sampling time Δt:

$$\delta T_g/T_g \propto 1/\ln(\Delta t/\tau_0) \tag{3.23}$$

This decrease is very slow, and perhaps this is the reason why it is not apparent in the simulation data (cf. Fig. 3.8). Note that in the case of super-Arrhenius increase of τ_α, $\tau_\alpha \sim \tau_0 \exp(E/(T-T_0))$ (the VFT law), the fragility index shows a faster, but still logarithmic dependence on τ_α. Theoretically, there is no doubt that the transition width must vanish in the limit $\Delta t \to \infty$ as long as the glassy plateau [2] persists at however low temperatures (and we are not aware of any data pointing to the contrary). In this case, the glass transition becomes asymptotically discontinuous as $\Delta t \to \infty$, but the main question here is whether the amorphous state is possibly stable at the transition temperature $T_g(\Delta t)$ in this limit.

3.9.2 Dispersion of μ_A

In section 3.7, we analyzed separately the LJ and chemical bond contributions to the affine shear modulus μ_A. It was shown that orientational preaveraging leads to a strong decrease of $\delta\mu_A$, the standard deviation of μ_A. This effect elucidates an important role of bond orientational fluctuations for $\delta\mu_A$.

It is also remarkable that while the fluctuations of the total instant orientation-averaged μ_A get weaker at low T roughly in parallel with those for the chemical bond contribution (μ_{Ab}), the analogous fluctuations of the LJ-contribution, $\mu_{Alj(\mathrm{or})}$, show a stronger decay right below T_g (see Fig. 3.17: the green curve for $\delta_1\mu_{Alj(\mathrm{or})}$ shows a downward cusp at T_g). What is the physical meaning of this feature? The modulus $\mu_{Alj(\mathrm{or})}$ is sensitive to distances between the neighboring particles, so behavior of $\delta_1\mu_{Alj(\mathrm{or})}$ (note that this quantity is a static property) indicates that the amorphous glassy structures below T_g involve progressively weaker dispersion of interparticle distances as T is decreased (a similar structural effect for chemical bonds is much less pronounced due to their high rigidity k_b).

Another interesting feature concerns the behavior of $\delta\mu_A$ and $\delta\mu_{A(\mathrm{or})}$ shown in Fig. 3.17 (cf. black and red curves): both deviations show a sharp increase as T is lowered in the glass transition region; however, the increase of $\delta\mu_A$ (by a factor of 10) is much stronger

than that for $\delta\mu_{A(\mathrm{or})}$ (roughly by a factor of $\sqrt{10}$). This difference can be explained as follows: μ_A fluctuations are mainly due to rotations of chemical bonds, which get virtually frozen below T_g leading to a poorer self-averaging of μ_A (hence, to a significant increase of $\delta\mu_A$). By contrast, $\mu_{A(\mathrm{or})}$ is insensitive to bond orientations: rather its fluctuations are defined be the bond-length dynamics which become only partially constrained right below T_g (leading to a weaker increase of $\delta\mu_{A(\mathrm{or})}$). It is also likely that bond-length fluctuations get progressively more restricted at lower T leading to a further increase of $\delta\mu_{A(\mathrm{or})}$ (and, hence, to a decrease of the ratio $\delta\mu_A/\delta\mu_{A(\mathrm{or})}$, cf. Fig. 3.18). The same effect also results in finite levels of both $\delta\mu_{Ab(\mathrm{or})}$ and $\delta_1\mu_{Ab(\mathrm{or})}$ (and, of course, of $\delta\mu_{A(\mathrm{or})}$ and $\delta_1\mu_{A(\mathrm{or})}$) at $T \to 0$ since not only bond orientational heterogeneities but also bond-length fluctuations must be arrested in this limit.

3.9.3 Peaks of μ_F and $\delta\mu_F$

The fluctuation modulus μ_F shows a peak near T_g (cf. Figs. 3.4 and 3.7). This behavior can be clarified in a simple way. At high T (above T_g), the terminal shear modulus μ is close to zero, so $\mu_F \approx \mu_A$ by virtue of eq. 2.45. As T decreases at constant pressure, the instantaneous modulus μ_A increases due to a stronger interactions between particles: the density (monomer concentration ρ) of the system increases, hence the mean interparticle distance decreases leading to a higher interaction energy at lower T; this interaction contribution to μ_A typically overwhelms the momentum contribution which is equal to ρT. By contrast, at low $T \lesssim T_g$, the modulus μ starts to grow rapidly (the solidification transition). This increase is stronger than the moderate increase of μ_A, hence $\mu_F = \mu_A - \mu$ decreases as the system is cooled below T_g (this tendency also comes from a simple observation that the system's dynamics slow down at low T, hence the drop of $G(t)$ during the same time $t \sim \Delta t$ becomes weaker). As a result, μ_F as a function of T (at a constant sampling time Δt and pressure) develops a peak near T_g.

Let us turn to the variance of μ_F, defined in eq. 3.13, which is nearly equal to the variance of μ (cf. section 3.6) and shows a sharp peak near T_g (cf. Fig. 3.20). A qualitative explanation of this behavior is given below: at high temperatures ($T > T_g$), in the liquid regime, the fluctuation modulus $\tilde{\mu}_F$ is dominated by the term $\tilde{\mu}_0$ in eq. 2.50 (since $\tilde{\sigma}$ is strongly suppressed by self-averaging to 0):

$$\tilde{\mu}_F \approx \tilde{\mu}_0 = \mathrm{const} \int_0^{\Delta t} \sigma(t)^2 \, \mathrm{d}t \tag{3.24}$$

The stresses $\sigma(t_1)$ and $\sigma(t_2)$ are virtually uncorrelated if $|t_1 - t_2| \gtrsim \tau_\alpha$, where τ_α is the thermal (longest) stress relaxation time. Above T_g, the time τ_α is short, $\tau_\alpha \ll \Delta t$, hence the integral in eq. 3.24 can be considered as a sum of many (K) uncorrelated similar contributions, $K = \Delta t/\tau_\alpha \gg 1$. As a result, $\tilde{\mu}_F$ efficiently self-averages in this regime: its variance is small being inversely proportional to K:

$$(\delta\mu_F)^2 / \mu_F^2 \sim 1/K = \tau_\alpha/\Delta t \tag{3.25}$$

As a matter of fact, that sort of argument (to get eq. 3.25) is well-known in the simulation literature (cf. section 4.2.4 of ref. [122] showing that finite sampling time effects may lead to statistical and systematic errors of numerical results). Note that eq. 3.25 resembles eq. 3.21 where τ_0 is replaced by τ_α and the first term is omitted (being negligible) as there is no plateau in the liquid regime. Therefore, here $\delta\mu_F \propto \sqrt{\tau_\alpha}$, and so the standard deviation $\delta\mu_F$ increases significantly as the system is cooled towards T_g, following the behavior of the relaxation time $\tau_\alpha = \tau_\alpha(T)$. Quantitatively, $\delta\mu_F$ in the liquid regime (where $\tau_\alpha \ll \Delta t$) is accurately predicted with the Gaussian approximation (cf. eqs. 3.19 and 3.20) giving:

$$(\delta\mu_F)^2 \simeq 4\eta_2/\Delta t, \tag{3.26}$$

where

$$\eta_2 = \int_0^\infty G(t)^2 \, \mathrm{d}t \tag{3.27}$$

Turning in passing to the terminal modulus μ, recall that $\mu \simeq 2\eta/\Delta t$ for $\Delta t \gg \tau_\alpha$ (cf. eq. 2.42 and [7]), where $\eta = \int_0^\infty G(t)\, dt$ is the shear viscosity. Therefrom, we find the relative variance of μ (also recalling that $\delta\mu \simeq \delta\mu_F$):

$$(\delta\mu/\mu)^2 \simeq \left(\eta_2/\eta^2\right) \Delta t \sim \Delta t/\tau_\alpha, \tag{3.28}$$

which is increasing with the time-window Δt in the liquid regime.

At $T < T_g$, the system enters the glassy regime where the terminal relaxation time is very long, $\tau_\alpha \gg \Delta t$. As a result, the time τ_α becomes irrelevant for $\delta\mu_F$. Close to T_g (but below it), the standard deviation $\delta\mu_F$ is still well-described by the Gaussian approximation (cf. Figs. 3.21 and 3.23), so we can make use of eq. 3.21. The second term in this equation is nearly constant below T_g (for a given Δt and $\tau_0 \ll \Delta t$), while the first term involving

$g(T, \Delta t) = (\partial G / \partial \ln t)_{t \sim \Delta t}$ strongly decreases as the system is further cooled below T_g (cf. Fig. 3.5).

To sum up, the arguments presented above show that $\delta\mu_F$ must strongly diminish as T deviates from T_g getting either cooler or warmer, thus producing a sharp peak near T_g.

The dependencies of $\delta\mu \approx \delta\mu_F$ and μ on T are depicted in Fig. 3.24.

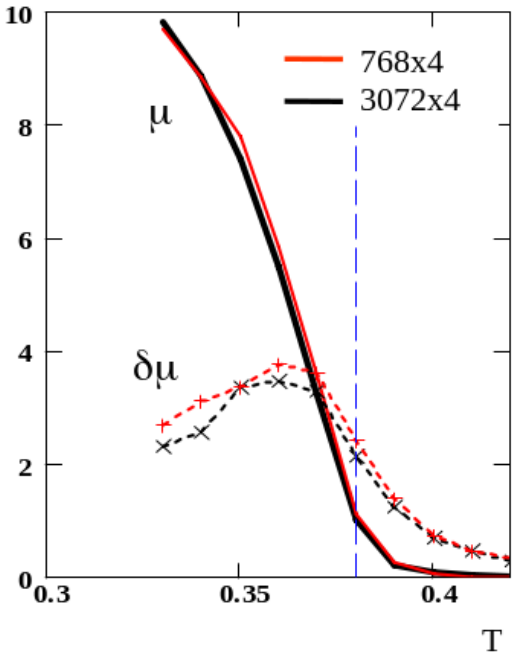

Figure 3.24: The dependence of μ (solid curves) and $\delta\mu$ (dotted curves) on T for $\Delta t = 10^5$ for the two systems (768×4 red, and 3072×4, black). The $\delta\mu$ data for the 2 systems (768×4 and 3072×4) are indicated with "red pluses" and "black crosses", respectively.

It is obvious that $\delta\mu \sim \mu$ near the peak of $\delta\mu(T)$: the fluctuations of the long-time shear modulus across the ensemble are of the same order as its average over all the independent configurations, so the mean μ is not necessarily a good reporter of the typical system behavior near the glass transition. This important finding was mentioned in the previous paper [7] for the 3072×4 system. It is now clear that this feature is general. It is also supported by the Gaussian theory: eq. 3.20 shows that $\delta\mu_F$ is roughly equal to the typical change of $G(t)$ in the region $t \sim \Delta t$ (say, between $t_1 \sim \Delta t/2$ and $t_2 \sim \Delta t$); this change is comparable to μ for $\Delta t \sim \tau_\alpha$ (that is, near the glass transition, at the peak). Noteworthily, the relation $\delta\mu \sim \mu$ also comes from eq. 3.28 with $\Delta t \sim \tau_\alpha$.

3.9.4 Gaussian approximation

We developed a theory of μ_F fluctuations assuming the Gaussian statistics for the instant stress $\sigma(t)$ (cf. section 3.8). This approach can be applied to analyze fluctuations of other properties. As an example, let us consider the mean-square of the time-averaged stress, $\mu_1 = \frac{V}{T}\langle\overline{\sigma}^2\rangle$, which is equal to μ for well equilibrated systems (at $T \geq 0.3$). The Gaussian theory predicts the following universal relation:

$$\delta\mu_1 = \sqrt{2}\mu_1 \tag{3.29}$$

This prediction is verified by our simulation data as presented in Fig. 3.25. It shows that in this case the Gaussian approximation works also at low T's: its failure to correctly predict $\delta\mu_F$ at $T \lesssim 0.3$ is related to the fact that the Gaussian variance of μ_F strongly decreases at low T's, while the normally subdominant correction stays finite.

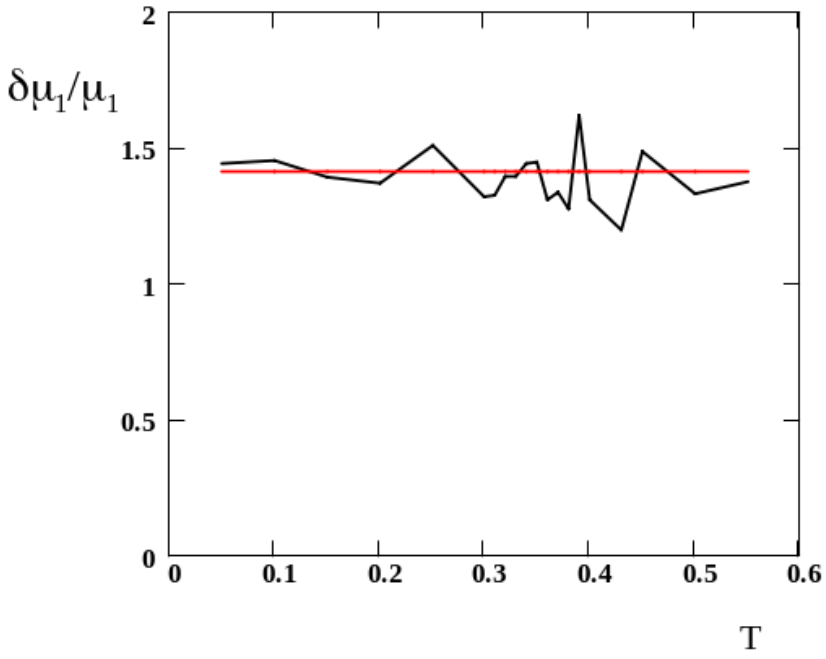

Figure 3.25: The dependence of the ratio $\delta\mu_1/\mu_1$ for 768×4 system (black curve) and the prediction, eq. 3.29 (red line).

3.9.5 Finite size effects and dispersion of μ_F and μ

The results shown in Fig. 3.21 indicate that (i) the dispersion of μ_F at $T \gtrsim T_g$ (in the liquid regime and near the glass transition) is well described by the Gaussian approximation and

(ii) $\delta\mu_F$ nearly does not depend on the system size in this regime. The first observation means that the statistics of stress fluctuations is likely to be nearly Gaussian at $T \gtrsim 0.35$, which is quite natural for the liquid regime. The second point simply follows from the first one (that $\delta\mu_F \approx \delta\mu_F^{(\mathrm{G})}$) and the fact that $\delta\mu_F^{(\mathrm{G})}$ does not explicitly depend on the system size (cf. eqs. 3.19 and 3.20): it is directly defined by the stress relaxation function $G(t)$ which is system-size independent for $T \gtrsim T_g$ (cf. Fig. 3.5).

By contrast, at low temperatures ($T \lesssim 0.3$), the Gaussian deviation is significantly lower than the total $\delta\mu_F$ (for both systems). To characterize this discrepancy, we introduce a non-Gaussian contribution to the variance of μ_F postulating that:

$$(\delta\mu_F)^2 = \left(\delta\mu_F^{(\mathrm{nG})}\right)^2 + \left(\delta\mu_F^{(\mathrm{G})}\right)^2 \tag{3.30}$$

The non-Gaussian term, $\delta\mu_F^{(\mathrm{nG})}$, is plotted against T in Figs. 3.22, 3.26, and 3.27 for both systems. It is obviously significant at temperatures well below T_g: $\delta\mu_F^{(\mathrm{nG})}$ is close to the total $\delta\mu_F$ at $T \lesssim 0.3$. On the other hand, $\delta\mu_F^{(\mathrm{nG})}$ rapidly decreases near T_g and becomes negligible at higher temperatures for both systems. It is furthermore apparent that $\delta\mu_F^{(\mathrm{nG})}$ at low T's is significantly higher for the smaller system (cf. Fig. 3.22).

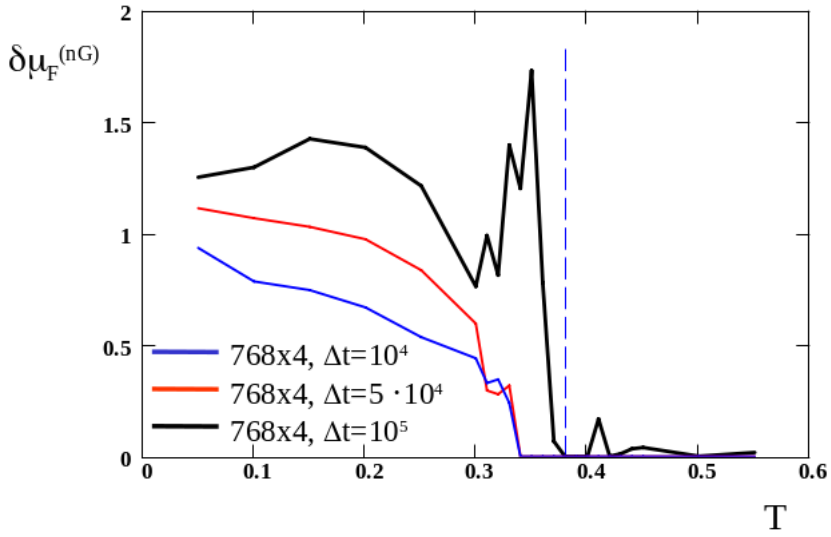

Figure 3.26: The dependence $\delta\mu_F^{(\mathrm{nG})}$ vs. T for different sampling times, $\Delta t = 10^5$, 5×10^4, and 10^4 (black, red, and blue curves, respectively) for the 3072×4 system.

What is the reason for such system size dependence of the standard deviations $\delta\mu_F$ and $\delta\mu$ at low T's (recall that $\delta\mu \approx \delta\mu_F$, cf. section 3.6)? Before turning to this question, let us further clarify why the stress fluctuations are nearly Gaussian above T_g. The general point is that $\sigma(t)$ is never exactly a Gaussian process. However, its statistics are close to

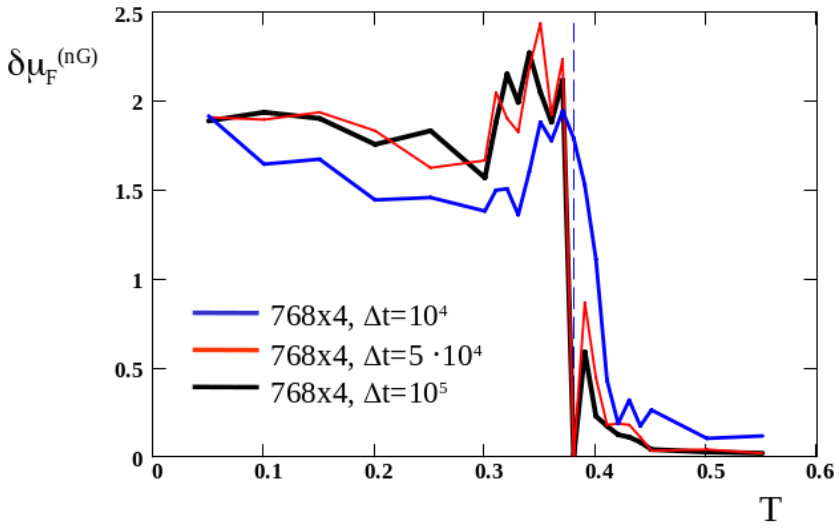

Figure 3.27: The dependence $\delta\mu_F^{(\mathrm{nG})}$ vs. T for different sampling times, $\Delta t = 10^5$, 5×10^4, and 10^4 (black, red, and blue curves, respectively) for the 768×4 system.

Gaussian for large volume V since $\sigma(t) = (1/V)\int_V \sigma(\boldsymbol{r},t)\,\mathrm{d}^d r$ can be considered as a sum of many quasi-independent contributions. Assuming that spatial correlations of $\sigma(\boldsymbol{r},t)$ are short-range, one can easily deduce that the non-Gaussian (nG) correction must scale as the inverse volume, $\mathrm{var}(\mu_F)_{nG} \equiv \left(\delta\mu_F^{(\mathrm{nG})}\right)^2 \propto 1/V$ [123]. This conclusion is based on the standard behavior of "finite-size" deviations from the central-limit theorem for random variables with symmetric distribution. Alternatively, it can be deduced from the cumulant theory [123] taking into account that $\mathrm{var}(\mu_F)$ involves only second- and 4th-order moments of σ and that $\langle\sigma\rangle = 0$. Above T_g, this is a small correction, $\mathrm{var}(\mu_F)_{nG}/(\delta\mu_F)^2 \sim V_c/V$, where V_c is the stress correlation volume, $V_c \ll V$. This estimate has emerged in analogy with the analysis of standard deviations, $\delta\mu_A$, of the affine modulus (cf. section 3.7). Below T_g, the situation is different: here the Gaussian contribution is small as $\mu_F^{(\mathrm{G})}$ strongly decreases for long Δt at low T (cf. the end of section 3.8). By contrast, the overall $\delta\mu_F$ does not vanish (remains finite) for however low T and long Δt due to quenched structural correlations (in particular stress correlations) characterizing the amorphous solidlike state of the system. As a result, for a finite V, low T, and long Δt, the variance of μ_F becomes dominated by the volume-dependent non-Gaussian term:

$$(\delta\mu_F)^2 \approx \mathrm{var}(\mu_F)_{\mathrm{nG}} \propto V_c/V, \text{ at } T \lesssim 0.3 \tag{3.31}$$

The ideas described above are qualitatively supported with the data shown in Figs. 3.22, 3.26, and 3.27 showing that $\delta\mu_F^{(nG)}$ is indeed almost T-independent for $T \lesssim 0.3$ (and, be-

sides, it weakly depends on the sampling time Δt). It is remarkable, however, that the system volume dependence of $\delta\mu_F^{(\mathrm{nG})}$ is significantly weaker than that implied by eq. 3.31. Based on our simulation data for the 3 lowest temperatures ($T = 0.05, 0.10, 0.15$) and different sampling times $\Delta t = 10^5, 10^4$, we find $\mathrm{var}(\mu_F)_{\mathrm{nG}} \approx 1.22 \pm 0.1$ for the 3072×4 system and $\mathrm{var}(\mu_F)_{\mathrm{nG}} \approx 3.34 \pm 0.3$ for the 768×4 system. These data are compatible with the power law $\mathrm{var}(\mu_F)_{\mathrm{nG}} \propto 1/V^\alpha$ with $\alpha \approx 0.7 \pm 0.1$.

As mentioned above, at low T's, the standard deviation of the terminal modulus $\delta\mu \approx \delta\mu_F$, and $\delta\mu_F$ is dominated by the non-Gaussian contribution, $\delta\mu_F^{(\mathrm{nG})}$, so the obtained V-dependence is applicable to $\delta\mu$ as well: in this regime $(\delta\mu)^2 \propto 1/V^\alpha$. A similar behavior for the variance of the elastic modulus with $\alpha \approx 0.68 \pm 0.08$ was obtained by studying more system sizes than we do in a simulation study of a 2D binary LJ mixture [124]. This and a related study [125] also report an anomalous behavior of nonlinear elastic coefficients for model glass-forming systems at $T < T_g$. The fact that $\alpha < 1$ means that the basic physical assumption of just local (short-range) structural stress correlations underlying eq. 3.31 is not valid. We are thus driven to conclude that spatial correlations of local stress and of local structure (including local rigidity) in the studied amorphous systems are likely to be long-ranged (in addition to being persistent in time). Two main possibilities can be anticipated (i) that the relevant structural correlation length ξ_s (characterizing the amorphous inherent structure) is finite, but is larger than (or comparable with) the system size, $\xi_s \gtrsim L \sim 20$, and (ii) that ξ_s is practically infinite and stress correlations follow a power-law decay with the distance r. The latter scenario is in harmony with recent theoretical results reveling long-range correlations of the shear-stress frozen in the inherent structure showing a universal decay law, $1/r^d$ (here d is the space dimension) [9, 13]. Interestingly, a large dynamical correlation length is also hinted at by a difference of the long-time behavior of the relaxation modulus $G(t)$ for the two systems (cf. section 3.5). We believe that further studies (perhaps, on larger systems) are required to clarify this issue.

3.10 Stress fluctuations in the 3-dimensional oligomer system

The glass transition region around T_g is characterized by a number of anomalies including a jump of the heat capacity, or an emergence of elasticity (of a finite shear modulus μ) in a nearly discontinuous manner. However, the solidification is not accompanied by a

significant change of the static structure which remains disordered. In particular, the static structure factor $S(\boldsymbol{q})$ changes very little near T_g [2, 52].

This common view implies that structural correlations in glass-forming systems must remain short-ranged near and below T_g. There is however a growing opinion that (at least for fragile glass-formers) the glassy structure is characterized by some (perhaps hidden and subtle) long-range correlations that are not visible in $S(\boldsymbol{q})$. We showed that investigations of stress fluctuations provide a powerful tool to study both the emergence of shear rigidity μ at the glass transition and the long-range structural correlations in supercooled liquids [6, 9].

Using the relation 2.43, $G(t)$ was obtained in the range $0 \leq t \leq 10^5$, and the quasi-equilibrium shear modulus μ was calculated as a time-average of $G(t)$ (cf. ref. [6, 7]):

$$\mu = \langle G(t_i - t_j) \rangle , \tag{3.32}$$

where $\langle ... \rangle$ here means the simple arithmetic average over i and j (cf. eq. 2.33). The modulus μ defined above is close to $G(t)$ for $t \sim \Delta t$ both above and below T_g.

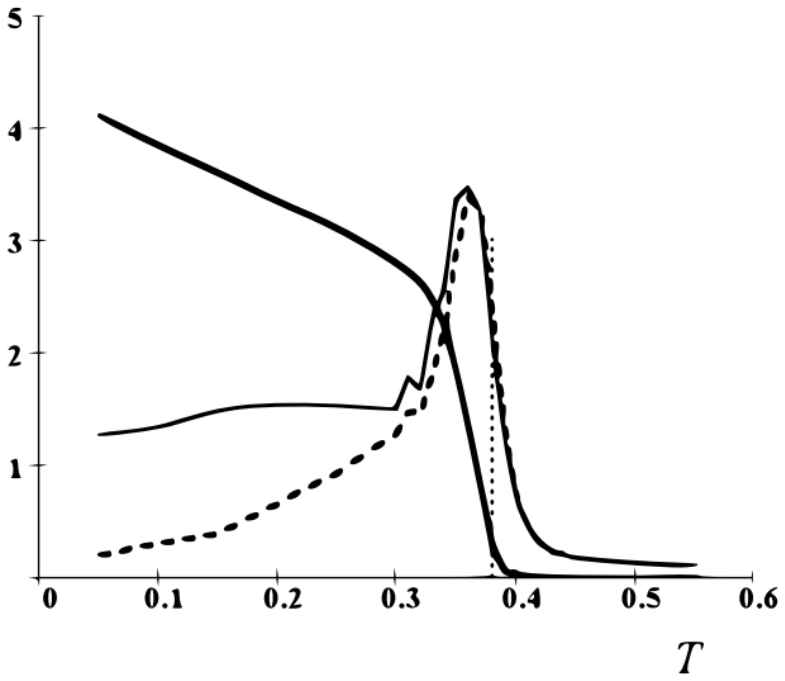

Figure 3.28: (a) Temperature dependence of the quasi-equilibrium shear modulus μ (thick solid line shows $\mu/4$), its standard deviation $\delta\mu$ (thin solid line), and $\delta\mu^{(G)}$, the theoretical Gaussian approximation of $\delta\mu$ (dashed curve) for the 3D 4-mer system with 12288 beads, with dilatometric $T_g = 0.38$.

The obtained T-dependencies of $\mu = \mu(T)$ are shown in Fig. 3.28 (thick solid curves); the dotted vertical lines in Fig. 3.28 indicate T_g in energy units. It is clear that μ is very small at high T, but starts to grow sharply right below T_g. The standard deviation $\delta\mu$ of the modulus (across the ensemble of m-independent configurations) is also shown in Fig. 3.28 (thin curves). The peak of $\delta\mu$ near T_g can be explained by the rigorous theory based on the assumption that the stress fluctuations are Gaussian [6] (more details are provided in section 3.8). The theoretical results are shown as dashed curve in Fig. 3.28. While the agreement is good around T_g and above it, it is obvious that well below T_g the simulated $\delta\mu$ is much higher than the theoretically predicted $\delta\mu^{(G)}$. This discrepancy indicates that stress fluctuations must be strongly non-Gaussian at low T's. Recalling that the Gaussian character of random variables averaged over a large system volume V naturally comes from their short-range correlations, the latter result also means that correlations of stress fluctuations must become long-ranged well below T_g. This conclusion is also supported by the revealed system size dependence of the non-Gaussian part ($\delta\mu^{(nG)}$) of $\delta\mu$: our data show that at low temperatures $\delta\mu^{(nG)}$ decreases with V slower than $1/V$ suggesting that the 4-point correlations of local stress decay with distance r more slowly than $1/r^d$, where $d = 3$ is the dimension of our system [6, 9].

3.11 Summary of Chapter 3

In this chapter we have investigated an LJ oligomeric glass-former system with 768×4 particles. We presented results and comparisons with data obtained by a former PhD student [7] from our group, including new ways and approaches for analysis of well known quantities [6] such as μ, μ_A, $G(t)$. Let us briefly summarize the main achievements of the work, ref. [6], below:

1. Analyzing a model LJ oligomeric glassformer using MD simulations, we established its static and dynamical parameters as a function of temperature and system size (two systems with 3072×4 and 768×4 particles have been studied). The shear relaxation modulus $G(t)$, obtained using the fluctuation-dissipation relation, eq. 2.43, generically shows a fast vibrational relaxation with time scale τ_0 (or $\tau_{\min}$), the terminal relaxation with much longer time scale τ_α, and (on cooling from liquid to the glass state) also an intermediate transient (slowly decaying) quasiplateau (cf. Fig. 3.5). The $G(t)$ relaxation for the smaller system compares well with the results

for the larger one (reported in ref. [7]). The main difference is that the 768×4 system shows a somewhat longer τ_α in the low-temperature regime ($T \lesssim T_g$).

2. The effective shear modulus of the system, μ (obtained using the stress-fluctuation relations, eqs. 2.45 and 2.46: $\mu = \mu_A - \mu_F$, where the fluctuation modulus μ_F, eq. 2.47, depends on the sampling time Δt) shows a strong increase as the system is cooled below the glass transition temperature T_g. The steplike function $\mu(T)$ is almost independent of the system size, but it gets shifted to lower temperatures as the sampling time Δt is increased. The rise of μ near T_g is always sharp but continuous. The transition is narrow, its relative width, $\delta T/T_g \sim 0.15$, is the same for both systems, and it does not show a visible tendency to decrease as Δt gets longer for $\Delta t > 10^4$ (cf. section 3.6).

   There might be 2 reasons for such behavior: (i) the statistics somewhat deteriorate in the time averages as the sampling time reaches the upper limit $\Delta t = \Delta t_{\max} = 10^5$ and (ii) during a long production run, $\Delta t \sim \Delta t_{\max}$, the system gets slightly more equilibrated, which may lead to a weak drift of its glass transition temperature (in the course of simulation), resulting in some widening of the transition.

   Here, we define: $\delta T = -\mu/\max(\partial\mu/\partial T)$, where μ is taken right below the transition. Theoretically, we anticipate a logarithmic increase of the transition steepness at longer Δt, $T_g/\delta T_g \propto \ln(\Delta t)$ (as argued in subsection 3.9.1). Curiously, at low temperatures below the transition zone, the shear modulus μ is a bit higher for the smaller system despite its slightly lower density.

3. Analyzing the instantaneous affine shear modulus μ_A, we revealed that it is dominated by the contribution of bonds connecting the monomers in chains. A moderate increase of μ_A at low T's is mainly due to an enhancement of LJ interactions as the density gets slightly higher. The affine modulus does not depend on the system size. By contrast, $\mathrm{var}(\mu_A)$ depends on the system volume as V_c/V, where V_c is the effective correlation volume corresponding to just one particle ($V_c \sim 1$) suggesting that local contributions to the modulus are virtually independent. Noteworwhily, the volume V_c does not increase as the temperature is lowered (cf. eq. 3.6).

   Moreover, we found that the standard deviation of instantaneous μ_A, $\delta_1(\mu_A)$, is roughly independent of temperature. Therefore, the observed strong increase of the variance of the time averaged μ_A at low T's is solely due to an increase of the relevant relaxation time worsening the statistics of μ_A.

Remarkably, we also found that orientational preaveraging of μ_A (by rotations of the coordinate frame) leads to a drastic improvement of its statistics: the variance of μ_A decreases by a factor between 40 and 600 as a result (with the most dramatic increase at the lowest temperature). By contrast, averaging over just 3 fixed shear planes (xy, yz and xz) leads to a reduction factor of ~ 3. The effect of full preaveraging has a simple meaning: fluctuations of μ_A are generally due to variations of bond orientation and bond length. As shown is section 3.7, the bond orientation fluctuations are dominant but are completely wiped out by the orientational averaging.

4. To characterize the heterogeneous nature of the glass-forming systems, we obtained the standard deviations of μ and μ_F among different independent configurations and found that they are always nearly equal, $\delta\mu \approx \delta\mu_F$. For both systems, these deviations show a pronounced peak near T_g in agreement with results of ref. [7] for the larger system. For the smaller system, the peak gets a bit higher and broader. Its height also slightly increases for longer sampling time Δt. The peak of $\delta\mu$ reflects a sharp transition from liquidlike to solidlike behavior; its emergence is correlated with a strong variation of μ near T_g (a high slope $-\partial\mu/\partial T$).

5. We developed a quantitative theory predicting $\delta\mu_F$ in terms of the relaxation modulus $G(t)$. The theory is in excellent agreement with the simulation results in the liquid regime (cf. Figs. 3.21 and 3.23). In this regime, $\delta\mu_F$ can be predicted based on the function $\mu_F(\Delta t)$ which is directly related to the relaxation modulus (cf. eqs. 2.52 and 2.54). The peak region is also quantitatively reproduced by the theory (which works better for the larger system). The theoretical approach is based on the Gaussian approximation for stress fluctuations, which is asymptotically exact for large systems, $V \to \infty$ (note, however, that the convergence is not uniform: the finite "Gaussian" limit is approached for $L \gg l(T)$, where the length-scale $l(T)$ strongly increases at low T). In this limit, it is valid both in the equilibrium (liquid) state and in the glassy state falling out of the equilibrium. The theory thus generally proves that fluctuations of μ_F and μ do not vanish for large V, rather they tend to a T-dependent finite level.

6. The theoretical Gaussian deviations $\delta\mu_F^{(\mathrm{G})}$ strongly decrease at low temperatures, in contrast to simulation data pointing to saturation of $\delta\mu_F$ at a significant level at low T for the studied systems. Moreover, the low-T plateau of $\delta\mu_F$ strongly decreases

as the system gets larger. This effect is attributed to a highly heterogeneous amorphous structure of the super-cooled glassy liquids leading to markedly non-Gaussian stress fluctuations coupled to the quenched structural disorder. Our analysis shows that the non-Gaussian part of the variance of shear moduli, $\mathrm{var}(\mu_F)_{nG} \approx \mathrm{var}\,(\mu)_{nG}$, decreases with the system size as $1/V^{\alpha}$ with $\alpha < 1\,(\alpha \approx 0.7 \pm 0.1)$. This result indicates that the local elastic (structural) properties in the studied amorphous systems must show long-range spatial correlations (since a structure with uncorrelated elements would lead to a $1/V$ dependence of the variance). Such behavior is reminiscent of the so-called Gardner transition [72] possibly associated with a diverging length-scale of static heterogeneity below T_g [73]. A long dynamical length-scale comparable with the system size is also suggested by the revealed size-dependence (at low temperatures) of the terminal decay rate of the shear relaxation modulus which is slower for the smaller system (cf. sec 3.5).

Chapter 4

Glass-forming 2-dimensional simple liquid system

4.1 Polydisperse Lennard-Jones (pLJ) model

We studied a glass-forming system of $N = 10^4$ polydisperse Lennard-Jones (pLJ) particles with equal mass ($m_i = 1$) but different sizes [93, 95] in the 2-dimensional (2d) space. Similar models, including Kob-Andersen binary mixtures [126, 127], are widely used in simulations of (2d and 3d) glass-forming liquids [128]. Following ref. [93, 95], each pair of particles (of diameters σ_i and σ_j) interact with energy $u_{\mathrm{LJ}}\left(r/\sigma_{ij}\right)$, where $\sigma_{ij} = \left(\sigma_i + \sigma_j\right)/2$. To simplify equations, r/σ_{ij} can be replaced by a reduced dimensionless distance s, such as $s = r/\sigma_{ij}$. Now, eq. 2.58 can be written in following way:

$$u_{\mathrm{LJ}}\left(s\right) = \begin{cases} 4\epsilon_{\mathrm{LJ}}\left[\left(s\right)^{-12} - \left(s\right)^{-6}\right] - 4\epsilon_{\mathrm{LJ}}\left[\left(s_{\mathrm{cut}}\right)^{-12} - \left(s_{\mathrm{cut}}\right)^{-6}\right], & \text{if } s < s_{\mathrm{cut}} \\ 0, & \text{otherwise} \end{cases} \tag{4.1}$$

where s_{cut} is the reduced cutoff radius which is the same for all interaction pairs , $s_{\mathrm{cut}} = r_{\mathrm{cut}}/\sigma_{ij} = 2^{7/6}$. The diameter σ_i of a particle i ($i = 1..N$) is uniformly distributed between $\left(1-\Delta\right)\overline{\sigma}$ and $\left(1+\Delta\right)\overline{\sigma}$ with $\Delta = 0.2$. The mean-square particle size can be calculated as follows:

$$\overline{\sigma^2} = \left(1 + \Delta^2/3\right)\overline{\sigma}^2, \tag{4.2}$$

leading to the polydispersity index of particle sizes (PDI), $\delta_p = \overline{\sigma^2}/\overline{\sigma}^2 - 1 = \Delta^2/3 \approx 0.013$. In what follows, all quantities are given in LJ units, i.e., ϵ_{LJ}, particle mass m, the

mean particle diameter $\overline{\sigma}$ and Boltzmann constant k_{B} are set to unity.

4.2 Simulation protocol

The same way as for the 3-dimensional oligomer model (Chapter 3), we performed Molecular Dynamics (MD) simulation using a velocity-Verlet scheme [79] with time step $\delta t = 0.005\tau_{\mathrm{LJ}}$ in a cubic box with periodic boundary conditions. The simulations are performed in the NPT and the NVT ensembles. The temperature T and the pressure $P = 2.0$ are imposed using the Nosé-Hoover-Andersen algorithm. The damping parameter for pressure, $P_{\mathrm{damp}} = 100$ and for the temperature, $T_{\mathrm{damp}} = 0.01291$ (see section 2.1.2 for their definition). The relations between these parameters and mass parameter for the volume changes W, and the thermal inertia coefficient, Q, are given in eq. 2.27. The new values for Q are defined by the relation $Q = (10/3)T$, imposed to get T-independent frequency ω_T (see eq. 2.18).

The main task of this part of the thesis was the implementation of the calculation of $\sigma(q)$ using eq. 2.102 [11] in LAMMPS [76]. The technical details of the implementation are shown on our group code source storage[1].

4.2.1 Sample preparation

The system was kept at constant external pressure $P = 2.0$ and equlibrated by the swap Monte Carlo (MC) technique [128] by Dr. Joachim Wittmer. The resulting configurations m_T (different temperatures had different sets of configurations) for $n_T = 26$ temperatures ($T = 0.100, 0.120, ..., 0.500$) served as starting points for MD simulations in the NPT ensemble to equilibrate the particle velocities. Production runs were done in the canonical (NVT) ensemble where the volume V was fixed at the average volume corresponding to $P = 2.0$.

To summarize the statements above, for each T and for each system from the m_T-ensemble, we did:

1. NPT tempering run for time $\Delta t_{\mathrm{NPT}} = 2 \cdot 10^5 \tau_{\mathrm{LJ}}$, $P = 2.0$;
2. NVT relaxation run for time $\Delta t_{\mathrm{NVT}} = 2 \cdot 10^5 \tau_{\mathrm{LJ}}$;
3. NVT production run for time $\Delta t_{\mathrm{NVT}} = 11 \cdot 10^4 \tau_{\mathrm{LJ}}$;

[1] https://git.unistra.fr/tsp-ics/lammps.git

During the NPT tempering run, we recorded values for an instantaneous volume $\tilde{V}$ every $\delta\tau_{\tilde{V}} = 0.1\tau_{\mathrm{LJ}}$.

During the whole NVT production run ($\Delta t = 11 \cdot 10^4 \tau_{\mathrm{LJ}}$), we recorded data for the instantaneous stress components such as σ_{xx}, σ_{yy}, σ_{xy} every $\delta\tau_{\tilde{\sigma}} = 0.05\tau_{\mathrm{LJ}}$, the positions of all particles every $\delta\tau_{\mathrm{pos}} = 100\tau_{\mathrm{LJ}}$, and recorded the instant total energy E every $\delta\tau_{\tilde{E}} = 0.05\tau_{\mathrm{LJ}}$.

To obtain the stress correlations in the $\boldsymbol{q}$-space (section 2.2.4), we performed simulations for different values of wave-vector $\boldsymbol{q}$:

$$q_x = \frac{2\pi}{L} n_x,\ n_x = 0, \pm 1, .., \pm n_q, \tag{4.3}$$

and similarly for q_y, where q_x, q_y are Cartesian components of vector $\boldsymbol{q}$, L is the size of the simulation box (for our 2d system $L_x = L_y = L$). The number n_q defines the maximum magnitude of $\boldsymbol{q}$, $q_{\max} = \sqrt{2}\frac{2\pi}{L} n_q$.

Turning back to the NVT production run ($\Delta t = 11 \cdot 10^4 \tau_{\mathrm{LJ}}$), for different values of n_q we used:

1. $n_q = 2$, for simulation length $\Delta t = 10^5 \tau_{\mathrm{LJ}}$, recording:
   (a) $\sigma_{xx}(\boldsymbol{q})$, $\sigma_{yy}(\boldsymbol{q})$, $\sigma_{xy}(\boldsymbol{q})$ using eq. 2.102 (both real and imaginary parts) every $\delta\tau_{\tilde{\sigma}(q)} = 0.2\tau_{\mathrm{LJ}}$
   (b) $c(\boldsymbol{q}) = \sum_{j=1}^{N} \exp(\mathrm{i}\boldsymbol{q} \cdot \boldsymbol{r}_j)$, where N is the total number of particles, $\boldsymbol{r}_j$ is the position of j particle;
   (c) $c_{\mathrm{h}}(\boldsymbol{q}) = \sum_{j=1}^{N} \left(mv_j^2/2 - T\right) \exp(\mathrm{i}\boldsymbol{q} \cdot \boldsymbol{r}_j)$, T is the prescribed temperature, v_j is the velocity of j particle;
2. $n_q = 30$:
   (a) $\sigma_{xx}(\boldsymbol{q})$, $\sigma_{yy}(\boldsymbol{q})$, $\sigma_{xy}(\boldsymbol{q})$ (both real and imaginary parts) every $\delta\tau_{\tilde{\sigma}(q)} = 20\tau_{\mathrm{LJ}}$ for simulation length $\Delta t = 10^5 \tau_{\mathrm{LJ}}$;
   (b) $\sigma_{xx}(\boldsymbol{q})$, $\sigma_{yy}(\boldsymbol{q})$, $\sigma_{xy}(\boldsymbol{q})$ (both real and imaginary parts) every $\delta\tau_{\tilde{\sigma}(q)} = 0.2\tau_{\mathrm{LJ}}$ for the rest simulation time (from $\Delta t = 10^5 \tau_{\mathrm{LJ}}$ to $\Delta t = 11 \cdot 10^4 \tau_{\mathrm{LJ}}$).
3. $n_q = 120$:
   Here the difference with the previous step concerns the period of the grid of all wave-vectors $\boldsymbol{q}$. In order to have the same time for the calculation with a larger value of $q_{\max}$, we performed a new run, computing the quantities for n_x,n_y $= 0, \pm 4, \pm 8, ..., \pm 120$:

(a) $\sigma_{xx}(\boldsymbol{q})$, $\sigma_{yy}(\boldsymbol{q})$, $\sigma_{xy}(\boldsymbol{q})$ (both real and imaginary parts) every $\delta\tau_{\tilde{\sigma}(q)} = 20\tau_{\mathrm{LJ}}$ for simulation length $\Delta t = 10^5\tau_{\mathrm{LJ}}$;

(b) $\sigma_{xx}(\boldsymbol{q})$, $\sigma_{yy}(\boldsymbol{q})$, $\sigma_{xy}(\boldsymbol{q})$ (both real and imaginary parts) every $\delta\tau_{\tilde{\sigma}(q)} = 0.2\tau_{\mathrm{LJ}}$ for the rest simulation time (from $\Delta t = 10^5\tau_{\mathrm{LJ}}$ to $\Delta t = 11 \cdot 10^4\tau_{\mathrm{LJ}}$).

4.2.2 Determination of the glass transition temperature T_g

Let us remind the definition of the glass transition temperature T_g from section 1.1.2. Some liquids can be easily supercooled avoiding crystallization. Such supercooled liquids show dramatic slowdown of their dynamics (reflected in a strong increase of the α-relaxation time τ_α) as temperature T is cooled towards the vitrification point T_g where the system becomes kinetically arrested and forms an amorphous solid. Below T_g the relaxation time τ_α exceeds the time-scale Δt accessible experimentally (or in a computer simulation). The glass transition region around T_g is characterized by a number of anomalies including an emergence of elasticity with a finite quasi-static shear modulus (see Fig. 4.10) whose standard deviations (see Fig. 4.11) change in a nearly discontinuous manner. However, this solidification is not accompanied by a significant change of the liquid structure which remains disordered. In particular, the static structure factor $S(q)$ changes very little near T_g. The latter feature can be seen from Fig. 4.1 where the temperature dependence of the static structure factor $S(q)$ is shown. Its Fourier transform, the radial distribution function $g(r)$, is represented in Fig. 4.2 at different T.

To define the glass transition temperature T_g for our system, doing it in parallel to the main protocol (cf. subsection 4.2.1), we performed cooling runs using MD only. The cooling runs consisted of two steps: continuous cooling from the initial temperature $T = 1$ with rate $\Gamma = 10^{-5}$ followed by NPT and NVT tempering as described above. These cooling runs allowed us to determine the glass transition temperature T_g. T_g depends on the total time spent during cooling and tempering. For the times in the order of $\Delta t = 10^5\tau_{\mathrm{LJ}}$ used in this study we obtained $T_g \approx 0.26$ defining T_g as the onset of a quasi-static elasticity (when the long-time shear modulus μ exceeds 1% of the instantaneous affine shear modulus μ_A). Nearly the same T_g was obtained previously from MC simulations using a similar continuous cooling protocol and a dilatometric criterion [93][2].

Looking at Figs. 4.1 — 4.2 one can see that the system is liquid-like above T_g and

[2]**Submitted paper:** G. George, L. Klochko, A. N. Semenov J. Baschnagel, and J. P. Wittmer, "Ensemble fluctuations matter for variances of macroscopic variables", European Physical Journal E

amorphous for $T_g \gtrsim T > T_c$, while crystallization is suspected at $T < T_c \approx 0.15$ [93].

4.3 Violation of the relation between the compressibility and the structure factor

One of the most interesting features of the glass transition is the emergence of nonequilibrium effects for $T \leq T_g$. One example is the drop of the specific heat (c_p or c_v) on cooling through T_g (cf. subsection 1.1.2). In the liquid phase, this effect is supplemented by a significant frequency dependence of the dynamic heat capacity implying its slow increase towards the equilibrium value on the long-time scales [129]. Another example is the violation of the relation between the compressibility and the static structure factor $S(0) \equiv S(\boldsymbol{q} \to 0)$ for vanishing wave vector $\boldsymbol{q}$ in the glass. The latter relation — the so-called compressibility equation (CE) — is given by ref. [62, 130]:

$$S(0) = \frac{c_0 T}{K_T}, \tag{4.4}$$

where K_T is the static isothermal bulk compression modulus and $c_0 = N/V$ is the mean concentration of particles (note that $S(0)$ is related to fluctuations of the total number N of particles in the grand-canonical ensemble: $S(0) = (\delta N)^2 / \langle N \rangle$, where $(\delta N)^2 \equiv \langle N^2 \rangle - \langle N \rangle^2$ is the variance of N. This relation remains valid also for polydisperse systems). This fluctuation-dissipation relation is valid in the equilibrium liquid, but is not satisfied below T_g [131–133], where the concept of an effective "compressibility temperature" T_χ defined via eq. 4.4 was introduced (T_χ is higher than the actual temperature T for $T < T_g$) [133].

Many glass-forming systems have multiple components to suppress the tendency for structural ordering [128, 134, 135]. For systems with n components it is known since the work by Kirkwood and Buff that the CE must be modified even under equilibrium conditions [62, 136, 137]. The Kirkwood-Buff theory expresses the compressibility in terms of the inverse matrix of partial structure factors $S_{ij}(\boldsymbol{q} \to 0)$ where $i, j = 1, ..., n$. For binary systems, the resulting expression for $S(0)$ takes a compact form: $S(0)$ is given as a sum of $c_0 T/K_T$ and a term related to composition fluctuations and their coupling to number fluctuations [138], $S(0) = c_0 T/K_T + \delta^2 c_l c_s/\Phi$, where $\delta = c_0 (v_l - v_s)$ is the dilatation factor, $v_{l,s}$ are the partial molecular volumes (where the partial molecular volume is the change in solution volume after adding one molecule of a substance at constant pressure), $c_{l,s}$ are the number fractions of the l and s components ($c_l + c_s = 1$), and Φ is

the thermodynamic factor [138]. This expression can be utilized to analyze experimental data [138]. However, if n is large, the matrix inversion becomes "conceptually and computationally difficult" [139], in particular in the limit of continuous distributions of particle sizes. To cope with this problem, a systematic expansion of the Kirkwood-Buff theory in terms of the size deviation from the mean particle diameter was suggested [139]. This method is powerful if structural information about partial pair correlations is available, as demonstrated by applications to jammed packings of size-disperse spheres [139] and random-close packed colloidal dispersions [140].

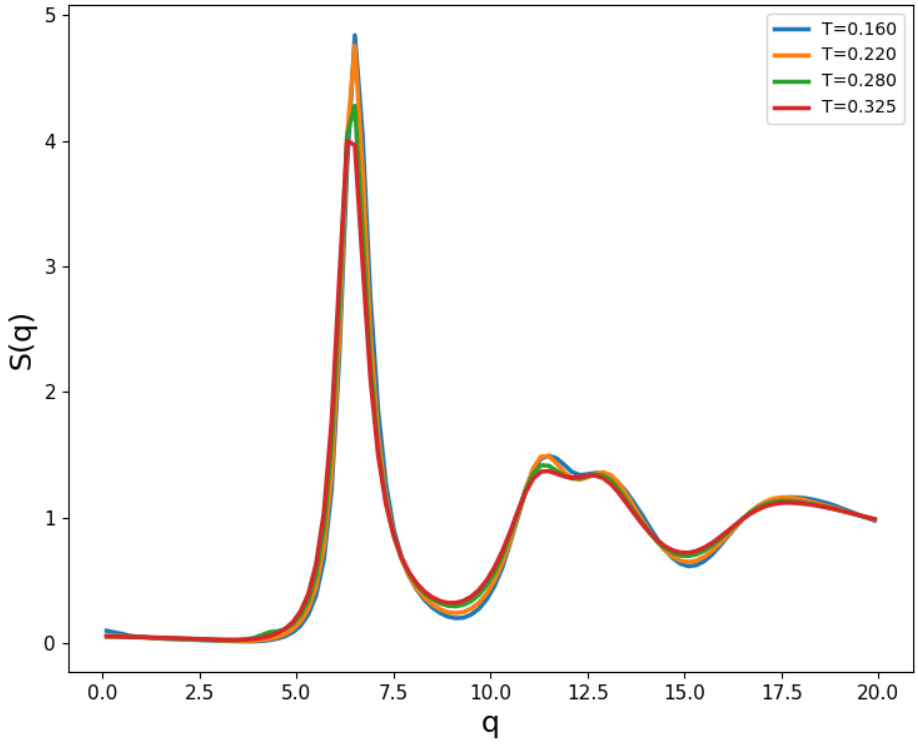

Figure 4.1: The temperature dependence of the static structure factor $S(q)$ for 2-dimensional pLJ system. The values for $S(q)$ were determined from the equilibrated configurations (see protocol in section 4.2).

We proposed another approach that does not require partial pair correlations, but combines thermodynamic (K_T) and simple compositional information (like polydispersity index of particle sizes (PDI) δ_p) to predict the polydispersity contribution (S_{pl}) to static, $S(\boldsymbol{q})$, and dynamical, $S(\boldsymbol{q}, t)$, structure factors for low $\boldsymbol{q}$. Our approach is valid in any spacial dimension (d) and explains why the monodisperse CE (eq. 4.4) can be violated

strongly even for systems with very low PDI ($\delta_p \sim 1\%$).

We compare our theory to results from MD simulations of a 2d system of polydisperse particles and show that polydispersity gives rise to glass-like effects already for T well above T_g: $S(\boldsymbol{q}, t)$ at low $\boldsymbol{q}$ decays in 2 steps with an intermediate plateau (at $S \approx S_{\rm pl}$), and the time-dependent specific heat increases slowly (as a power-law) towards its static equilibrium value. There relaxation features persist upon cooling towards T_g and are expected to interplay with the glassy dynamics [141–143].

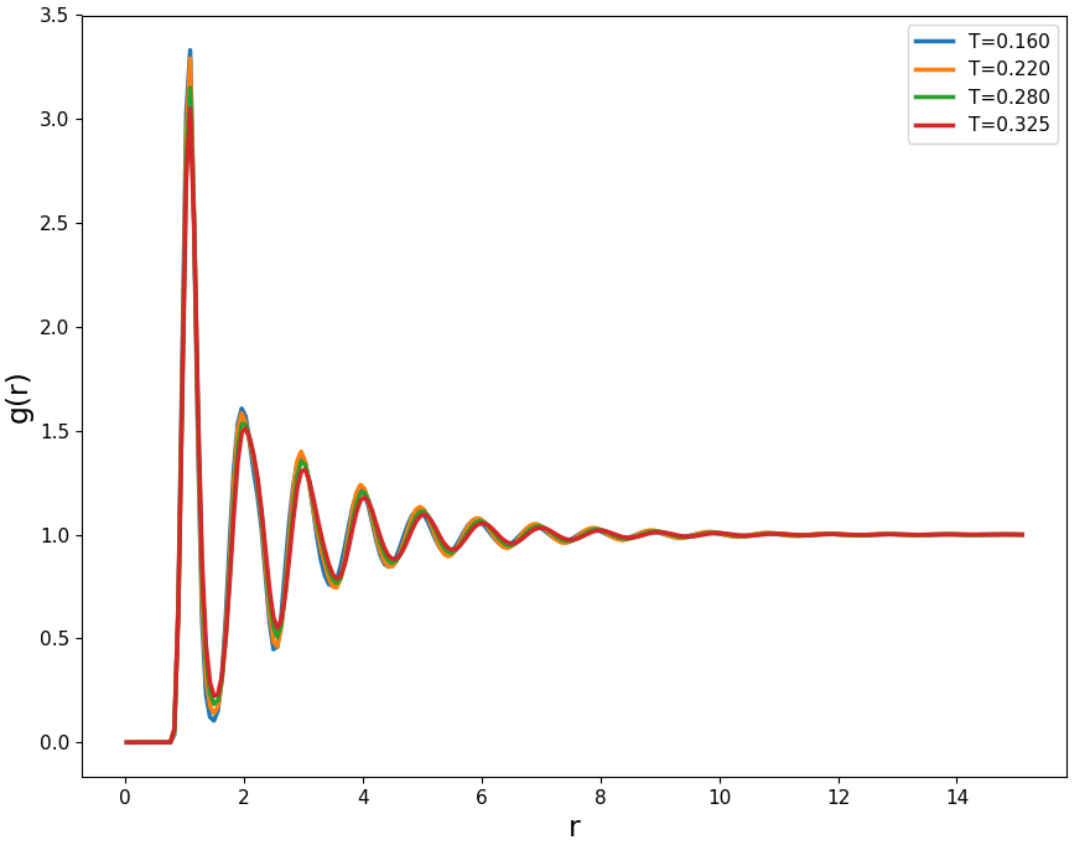

Figure 4.2: The temperature dependence of the radial distribution function $g(r)$ for 2-dimensional pLJ system. The values for $g(r)$ were determined from the equilibrated configurations (see protocol in section 4.2).

Fig. 4.4 represents $\phi_q(t) = S(q,t)/S(q)$ for the lowest $\boldsymbol{q} = \boldsymbol{q}_{\rm min}$ at different $T > T_g$. A pronounced long-time shoulder is visible at $T = 0.5$; it develops into a quasi-plateau persisting for $t \gtrsim 10^3 \tau_\alpha$ in the T-range between $T = 0.4$ and 0.3. Finally, Fig. 4.5 shows the relative deviation from the CE, eq. 4.4, defined as $\delta = 1 - S_K/S_0$, where $S_K \equiv c_0 T/K_T$ (the compression modulus K_T was determined by two methods: (i) by volume fluctuations in the NPT ensemble, $K_T = TV/\left\langle (\Delta V)^2 \right\rangle$), and (ii) by the stress-fluctuation formalism in

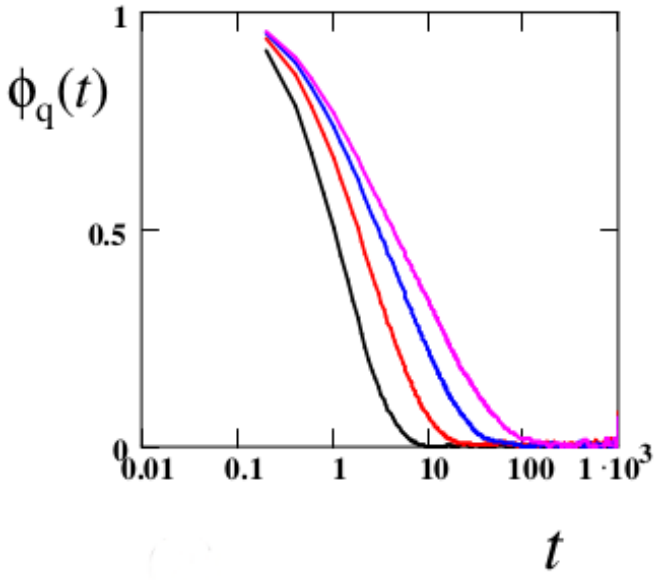

Figure 4.3: Coherent intermediate scattering function $\phi_q(t)$ at different temperatures $T = 0.5, 0.4, 0.35, 0.325$ (solid curves from bottom to top) at $q \approx q_{\max} \approx 6.35$ corresponding to the maximum of $S(q)$.

the NVT ensemble [93]; both methods gave the same results). Note that $S_0 = S(q_{\min}, 0)$ is nearly equal to $S(0)$ obtained by extrapolation of $S(q)$ to $q = 0$.

One can observe that δ always exceeds 70% meaning that eq. 4.4 is not satisfied. A significant difference between $S(0)/(c_0 T)$ and the compressibility $1/K_T$ was also discussed for jammed packings of size-dispersed hard disks and spheres [139], and in dynamic light scattering of colloidal dispersions [144]. In both cases the difference was shown to originate from polydispersity effects. These findings support the idea that the anomalous behavior reported in Figs. 4.4 and 4.5 is also related to polydipersity.

We pursue this idea below and discuss a theoretical approach to explain our simulation results. We start with the dynamical structure factor:

$$S(q,t) = \frac{V}{c_0} \left\langle c_{\boldsymbol{q}}(t)\, c^*_{\boldsymbol{q}}(0) \right\rangle, \tag{4.5}$$

where averaging is taken over the equilibrium ensemble, V is d-dimensional system volume, $d = 2$, $c_{\boldsymbol{q}}(t) = \int c(\boldsymbol{r}, t) \exp(-\mathrm{i}\boldsymbol{q}\boldsymbol{r})\, \mathrm{d}^d r / V$, and $c(\boldsymbol{r}, t)$ is the local concentration. According to the standard FDT [145] the dynamical factor:

$$S(q,t) = c_0^{-1} \left[R(q,\infty) - R(q,t) \right], \tag{4.6}$$

is related to the response function $R(q,t)$ defining the concentration wave $c_{\boldsymbol{q}}(t)$ in-

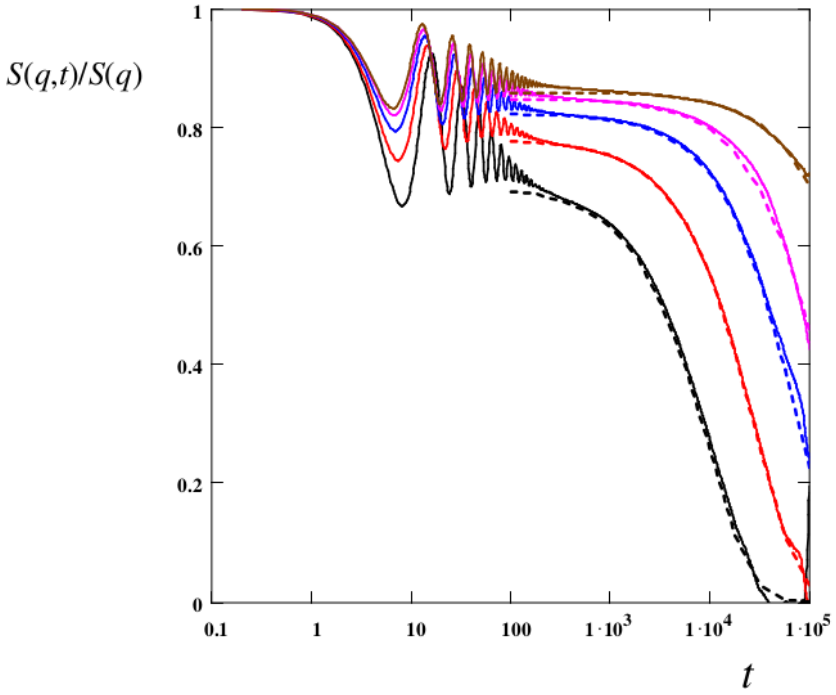

Figure 4.4: Coherent intermediate scattering function $\phi_q(t)$ at $q \approx q_{\min} = 2\pi/L$ (L is the linear dimension of the simulation box). Dashed lines show theoretical prediction, eq. 4.14, for the slow stage. $T = 0.5, 0.4, 0.35, 0.325, 0.3$ (solid curves from bottom to top).

duced by a weak external potential field $U(\boldsymbol{r}, t) = U_0 \exp(\mathrm{i}\boldsymbol{qr})$ applied to the system at $t > 0$:

$$\langle c_{\boldsymbol{q}}(t) \rangle = -R(q,t)\, U_0/T \tag{4.7}$$

Obviously $R(q,0) = 0$. We now focus on the low-q regime ($q\overline{\sigma} \ll 1$). The field U produces the volume force $-c\nabla U$ which generates a hydrodynamic flow leading to the pressure (δp) and concentration waves. The mechanical balance for $t \gg \tau_\alpha$ then demands $\delta p \simeq -cU$ with $\delta p \simeq K_T \delta c/c_0$, hence $R(q,t) \simeq \frac{Tc_0^2}{K_T}$ leading to the classical result for monodisperse systems, $S_0 \equiv S(q,0) \simeq Tc_0/K_T$ (for $q\overline{\sigma} \ll 1$). In the general (polydisperse) case the considered mechanism implies that the colloidal composition stays unchanged for each element of the system. This is valid for the first (fast) stage of concentration relaxation which serves to establish the local mechanical balance ($\nabla p + c\nabla U = 0$). However, later on the concentration wave amplitude (and $R(q,t)$) can still increase due to an exchange between small and large particles by their slow mutual diffusion ("slow" stage). The amplitude of this increase can be deduced from a simple model assuming that

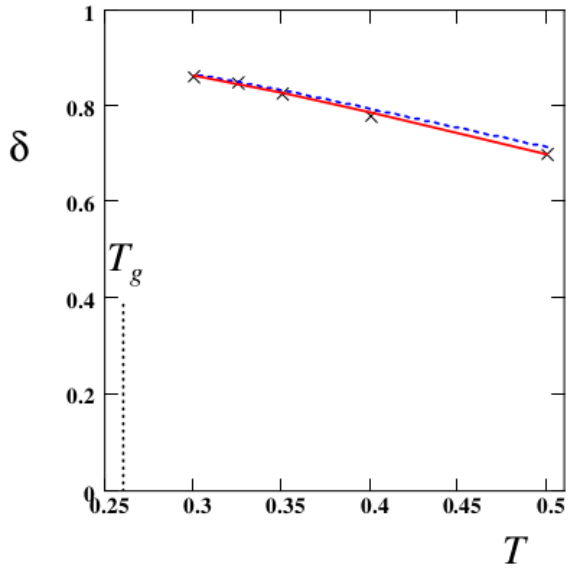

Figure 4.5: T-dependence of $\delta = S_{\rm pl}/S_0$ with (i) simulation data for S_0 and $S_{\rm pl} = S_0 - S_K$ (black crosses "x"), (ii) theory with $S_0 = S_{K*} = cT/K*$ and $S_{\rm pl}$ defined in eq. 4.13 (dashed blue curve). In all the cases $S_K = c_0 T/K_T$ with K_T obtained by simulations. The vertical dotted line indicates $T_g = 0.26$.

the free energy of interactions between the particles depends primarily on the local volume concentration, $\phi(r) = \sum_i v_i c_i(r)$, where $v_i = \sigma_i^d$. Here all the particles are separated in groups according to their size σ: particles with $\sigma \simeq \sigma_i$ belong to group i, $i = 1, 2, .., n$. The number of components n is such that $n \gg 1$, but $n \ll N$. Thus, the number of particles in each group, N_i, is large.

Then, the total free energy density is (position r is omitted for $\phi(r)$ and $c_i(r)$, $\overline{v} = \overline{\sigma^d}$):

$$f = \frac{1}{\overline{v}} f^*(\phi, T) + T \sum_{i=1}^{n} c_i \ln(c_i), \tag{4.8}$$

where the second term in the r.h.s. accounts for the entropy of mixing. The assumption to express the excess part f^* in terms of ϕ is backed by the success of similar approximate expressions employed to explore phase equilibria in polydisperse systems [146]. The crucial role of the local volume fraction for jammed polydisperse systems was also highlighted in ref. [139]. As we focus here on the linear response, we may expand f for small deviations $\delta c_i = c_i - c_i^{(0)}$ from the equilibrium state, and keep only the quadratic term (the linear

term is irrelevant as its volume integral is const = 0):

$$\delta f/T \simeq v^*\delta\phi^2/\left(2\overline{v}^2\right) + \sum_i \left(\delta c_i\right)^2/\left(2c_i\right), \tag{4.9}$$

where $\delta\phi = \sum_i v_i\delta c_i$ and the volume v^* is defined by $Tv^*/\overline{v} = \partial^2 f^*/\partial\phi^2$ at $\phi = \phi_0 = \sum_i v_i c_i^0$.

During the fast mechanical stage a fluid element deforms as a whole, keeping the same composition: $\delta c_i/c_i = \delta c/c_0$. Using eq. 4.9 with this condition leads to:

$$\delta f/T \simeq K_T\left(\delta c\right)^2/\left(2c_0^2\right),\ K_T = Tc_0\left(c_0v^* + 1\right), \tag{4.10}$$

so the plateau response (for $t \gg \tau_\alpha$ right after the fast mechanical relaxation stage) is $R_{\rm pl} = R\left(q \to 0, t\right) \simeq \frac{Tc_0^2}{K_T}$. To get the terminal amplitude $R_\infty = \lim_{q\to 0}\lim_{t\to\infty} R\left(q,t\right) = c_0 S\left(0\right)$ (recall that $R\left(q,0\right) = 0$) we have to allow for composition variations and hence minimize f, eq. 4.9, with respect to δc_i with the only side condition $\sum_i \delta c_i = \delta c$. The result is $\delta f = K^*\left(\delta c\right)^2/\left(2c_0^2\right)$, so the terminal response is given by $R_\infty = Tc_0^2/K^*$:

$$K^* = Tc_0\left[Z\left(1 - S_K\right) + 1\right]/\left[Z\left(1 - S_K\right) + S_K\right], \tag{4.11}$$

where $S_K = c_0T/K_T$ and

$$Z = \sum_i \frac{N_i}{N}\left(1 - v_i/\overline{v}\right)^2 = \overline{v^2}/\overline{v}^2 - 1 \overset{d=2}{=} 4\delta_p\left(1 + \delta_p/5\right)/\left(1 + \delta_p\right)^2 \tag{4.12}$$

eq. 4.11 remains valid in any dimension d with $v_i = \sigma_i^d$. So $S\left(0\right) = R_\infty/c_0 = S_{K*}$, where $S_{K*} \equiv c_0T/K^*$. It is thus predicted that $S\left(q,t\right)$ relaxes from the initial value (which is close to the static structure factor $S\left(0\right)$) $S_0 \simeq S_{K*}$ to the intermediate plateau at $S_{\rm pl} = \left(R_\infty - R_{\rm pl}\right)/c_0$:

$$S_{\rm pl} = S_{K*} - S_K = \frac{Z\left(1 - S_K\right)^2}{1 + Z\left(1 - S_K\right)} \tag{4.13}$$

This result resonates with the Kirkwood-Buff theory [138, 139]: For a polydisperse system $S\left(0\right)$ can be expressed as a sum of a compressibility contribution S_K and a term related to composition fluctuations $S_{\rm pl}$. Here, however, $S_{\rm pl}$ is defined as a dynamic quantity (rather than a combination of partial structure factors). Our approach is akin to the analysis of DLS (dynamical light scattering) of polydisperse colloidal suspensions in ref. [144].

The theoretical function $\delta = S_{\rm pl}/S_{K*}$ is compared with the simulation data in Fig. 4.5. A very good agreement is obvious. The proposed simple model thus fully accounts for the composition fluctuation effects. It shows that the "polydispersity" contribution to S_0 tends to $S_{\rm pl} \simeq \frac{Z}{Z+1}$ in the "incompressible" limit $K_T \to \infty$, so $S_{\rm pl}$ (which is roughly proportional to the size PDI, δ_p) can strongly exceed the compressibility term S_K for however low δ_p.

Furthermore, we find that the terminal relaxation of $S(q,t)$ from $S_{\rm pl}$ to 0 can be described by a single diffusion constant equal to the mean self-diffusion coefficient D_s deduced from the mean-square displacements averaged over all particles [147]:

$$S(q,t) \simeq (S_0 - S_K) \exp\left(-q^2 D_s t\right), \; t \gg \tau_\alpha, \tag{4.14}$$

where $S_0 = S(q,0)$ and $q\overline{\sigma} \ll 1$, as noted before. The theoretical curves (dashed) are shown in Fig. 4.4 for $t > 10^2$. A very good agreement with MD data is obvious. Thus, for $t \gg \tau_\alpha$ the collective interdiffusion coefficient governing the relaxation is close to the average self-diffusion coefficient, which means that the so-called Vineyard approximation [62] works very well here. The importance of interdiffusion processes for glass-forming systems with size polydispersity was discussed qualitatively in refs. [141, 144] and for binary mixtures in the framework of mode-coupling theory in ref. [142]. The theory for binary mixtures yields an expression analogous to eq. 4.14 with an amplitude given by the Kirkwood-Buff result for $S_0 - S_K$ [138] and a relaxation rate determined by the interdiffusion coefficient (cf. eq. 10b of ref. [142]).

4.4 Anomalous behavior of time-dependent heat capacity well above the T_g in polydisperse liquids

Turning to the simulation results, we first consider the specific heat per particle, $c_v = \frac{1}{N}\frac{\partial E}{\partial T}|_{V,N}$. Its time-dependent generalization can be defined via the energy (E) response to a small instant T-jump (from $T - \delta T$ to T at $t = 0$):

$$c_v(t) = \frac{\langle E(t) - E(0)\rangle}{N\delta T}, \tag{4.15}$$

where the static (equilibrium) c_v equals to $c_v(\infty)$. By virtue of the fluctuation-dissipation theorem (FDT, section 2.2) the response function $c_v(t)$ is related to the energy

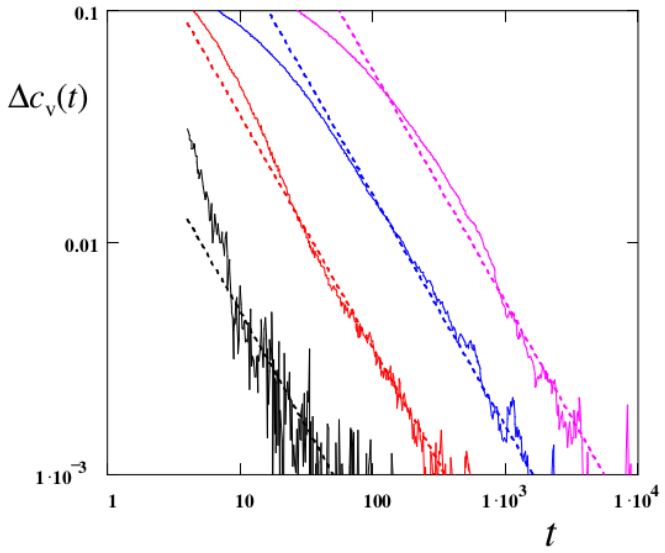

Figure 4.6: Heat capacity increment $\Delta c_v(t) = c_v(\infty) - c_v(t)$ vs. time in LJ units at different temperatures $T = 0.5, 0.4, 0.35, 0.325$ (solid curves from bottom to top). Dashed lines: fits with theoretical $1/t$ dependence [147].

correlation function $C_E(t) = \langle \Delta E(t+t')\,\Delta E(t') \rangle$, where $\Delta E = E - \langle E \rangle$, and $\langle \ldots \rangle$ denotes the canonical equilibrium average:

$$c_v(t) = \frac{1}{NT^2}\left[C_E(0) - C_E(t)\right] \tag{4.16}$$

At $t \to \infty$ the function $C_E(t) \to 0$, so eq. 4.16 turns into the classical relation $c_v(\infty) = \left\langle (\Delta E)^2 \right\rangle / (NT^2)$. The time-dependent heat capacity $c_v(t)$ is thus defined by $C_E(t)$ (for the total energy E) which was recorded at different T's for $m_T = 50 - 100$ independent trajectories. The results for $\Delta c_v(t) = c_v(\infty) - c_v(t)$ at $T > T_g$ are shown in Figs. 4.6, 4.7.

At short times, $t \lesssim \tau_\alpha$ the behavior for $\Delta c_v(t)$ is qualitatively consistent with the frequency dependence of c_v above T_g revealed in a simulation study of viscous silica [129]. The temperature dependence of heat capacity $c_V(t)$ at short time $t \lesssim 2$ is represented in Fig. 4.7. One can observe however a new feature: a weak long-time tail already at $T = 0.5$ (Fig. 4.6). It appears that the tail follows a power-law scaling as $\sim 1/t$ (cf. the dashed lines in Fig. 4.6). The power-law tail gets much stronger as T decreases down to $T = 0.325$ (which is significantly above $T_g \approx 0.26$ [93]).

Remarkably, the terminal time-scale of the tail is much longer (by a factor ~ 100) than the structural relaxation time τ_α defined as the relaxation time of the shear stress (cf. Fig. 4.8) or of $\phi_q(t) = S(q,t)/S(q)$ at the peak of $S(q)$ (cf. Fig. 4.3). The heat

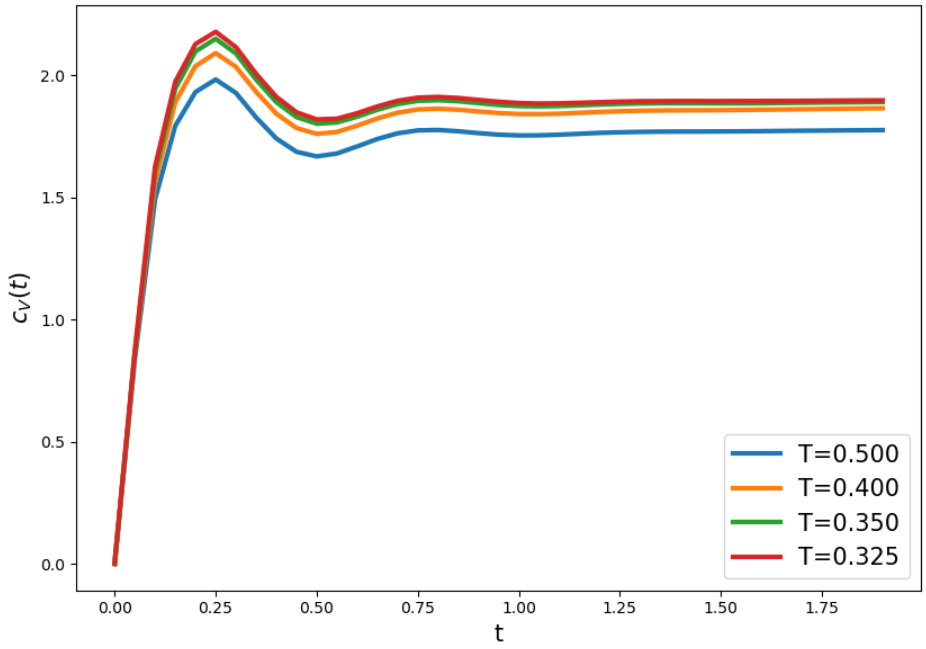

Figure 4.7: Heat capacity $c_v(t)$ at short time $t \lesssim 2$ at different temperatures $T = 0.5, 0.4, 0.35, 0.325$.

capacity $c_v(t)$ thus still increases in time for $t \gg \tau_\alpha$.

4.5 Elastic response and the long-range correlations

Viscoelastic properties of a liquid can be characterized by shear relaxation modulus $G(t)$ which is a central rheological function of a material. To obtain $G(t)$ in the range $0 \leq t \leq 10^5$ we used the generalized relation coming from FDT (eq. 2.43) and the quasi-equilibrium shear modulus μ was calculated as a time-average of $G(t)$ (cf. ref. [6, 7]):

$$\mu = \langle G(t_i - t_j) \rangle , \tag{4.17}$$

where $\langle ... \rangle$ here means the simple arithmetic average over i and j (cf. eq. 2.42):

$$\mu = \frac{1}{\Delta t^2} \int_0^{\Delta t} G(|t - t'|)\, dt dt'$$

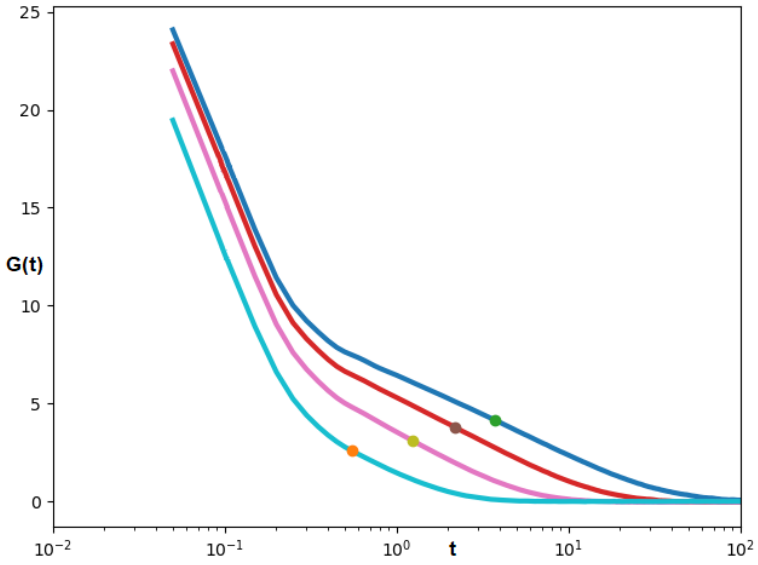

Figure 4.8: The shear relaxation modulus $G(t)$ at different temperatures $T = 0.5$, 0.4, 0.35, 0.325 (solid curves from bottom to top). Dots on the curves correspond to the different values of the structural relaxation time τ_α for each temperature T (from 0.5 to 0.325): 0.55, 1.25, 2.2, and 3.75 respectively. To obtain the values for τ_α one can use the criteria $G(\tau_\alpha)/G(0) \approx 10\%$ (cf. Chapter 2).

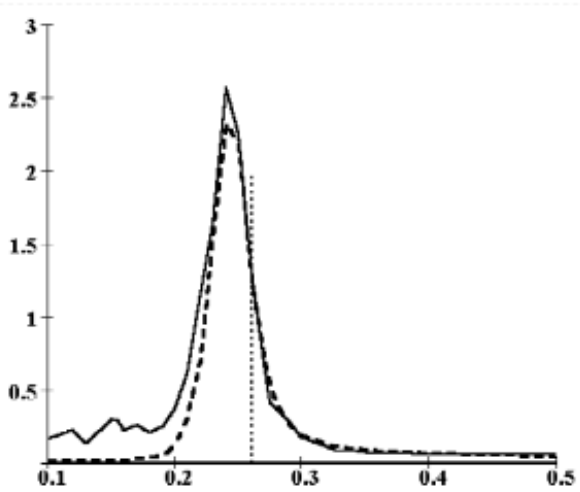

Figure 4.9: Temperature dependence of the quasi-equilibrium shear modulus standard deviation $\delta\mu$ (thin solid line), and $\delta\mu_F^{(G)}$, the theoretical Gaussian approximation of $\delta\mu_F \approx \delta\mu$ (dashed curve) for the 2d pLJ system with $N = 10^4$ particles, with dilatometric $T_g = 0.26$ (dotted vertical line). The sampling time is $\Delta t = 10^5 \tau_{\mathrm{LJ}}$.

The modulus μ defined above is close to $G(t)$ for $t \sim \Delta t$ both above and below T_g. For the same sampling time ($\Delta t = 10^5 \tau_{\mathrm{LJ}}$) we obtained the temperature dependencies of

the fluctuation modulus $\mu_F(T)$, the shear modulus $\mu(T)$, and their standard deviations $\delta\mu_F(T)$, and $\delta\mu(T)$. The obtained T-dependencies are shown in Figs. 4.9, 4.10, 4.11. One can see that those moduli exhibit similar behavior as the oligomer system (Chapter 3). It is clear that the difference between $\delta\mu_F$ and $\delta\mu$ is negligible for all T's (cf. Fig. 4.11).

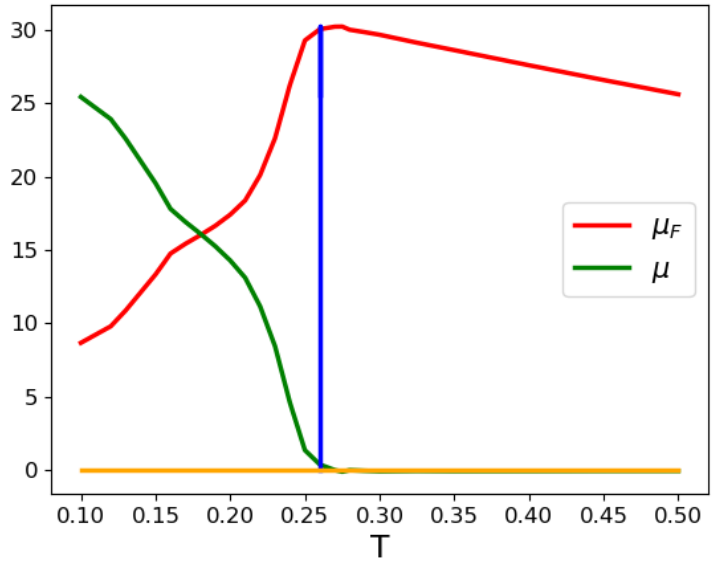

Figure 4.10: Temperature dependence of the quasi-equilibrium shear modulus μ and the fluctuation modulus μ_F for 2-dimensional pLJ system with $N = 10^4$ particles. The blue line corresponds to $T_g = 0.26$ and the orange line corresponds to 0. The sampling time is $\Delta t = 10^5 \tau_{\mathrm{LJ}}$.

To study the stress correlation range for the 2-dimensional system more directly we analyzed the correlation function of the stress tensor $\sigma_{\alpha\beta}$ at different wave-vectors $\boldsymbol{q}$ (in addition to the space-averaged stress corresponding to $\boldsymbol{q} = 0$). For each $\boldsymbol{q}$ we define the natural coordinate system with axis 1 along the wave-vector and axis 2 perpendicular to it.

Let us remind from section 2.2.4 the definition of the generalized correlation functions:

$$C_{\alpha\beta\gamma\delta}(\boldsymbol{q}, t) = \frac{1}{V} \left\langle \sigma_{\alpha\beta}(\boldsymbol{q}, t + t') \, \sigma^*_{\gamma\delta}(\boldsymbol{q}, t') \right\rangle, \tag{4.18}$$

where $\alpha, \beta, \gamma, \delta = 1$ or 2.

In sections 2.2.4 - 2.3 we obtained theoretical relations defining the correlation functions C_2 (eq. 2.132), C_T, $C_\parallel$, and $C_\perp$ in terms of material functions (eqs. 2.122 – 2.124).

From simulation results they can be obtained based on eq. 4.18 as:

$$\begin{aligned}
C_2(q,t) &= C_{2222}(q,t) = \frac{1}{V}\left\langle \sigma_{22}(\boldsymbol{q},t+t')\,\sigma^*_{22}(\boldsymbol{q},t')\right\rangle = \\
&= \frac{1}{V}\left\langle \sigma^{\mathrm{R}}_{22}(\boldsymbol{q},t+t')\,\sigma^{\mathrm{R}}_{22}(\boldsymbol{q},t') + \sigma^{\mathrm{I}}_{22}(\boldsymbol{q},t+t')\,\sigma^{\mathrm{I}}_{22}(\boldsymbol{q},t')\right\rangle + \\
&+ i\frac{1}{V}\left\langle \sigma^{\mathrm{I}}_{22}(\boldsymbol{q},t+t')\,\sigma^{\mathrm{R}}_{22}(\boldsymbol{q},t') - \sigma^{\mathrm{R}}_{22}(\boldsymbol{q},t+t')\,\sigma^{\mathrm{I}}_{22}(\boldsymbol{q},t')\right\rangle, \\
C_T(q,t) &= C_{1212}(q,t) = \frac{1}{V}\left\langle \sigma_{12}(\boldsymbol{q},t+t')\,\sigma^*_{12}(\boldsymbol{q},t')\right\rangle = \\
&= \frac{1}{V}\left\langle \sigma^{\mathrm{R}}_{12}(\boldsymbol{q},t+t')\,\sigma^{\mathrm{R}}_{12}(\boldsymbol{q},t') + \sigma^{\mathrm{I}}_{12}(\boldsymbol{q},t+t')\,\sigma^{\mathrm{I}}_{12}(\boldsymbol{q},t')\right\rangle + \\
&+ i\frac{1}{V}\left\langle \sigma^{\mathrm{I}}_{12}(\boldsymbol{q},t+t')\,\sigma^{\mathrm{R}}_{12}(\boldsymbol{q},t') - \sigma^{\mathrm{R}}_{12}(\boldsymbol{q},t+t')\,\sigma^{\mathrm{I}}_{12}(\boldsymbol{q},t')\right\rangle,
\end{aligned} \tag{4.19}$$

$$\begin{aligned}
C_{\parallel}(q,t) &= C_{1111}(q,t) = \frac{1}{V}\left\langle \sigma_{11}(\boldsymbol{q},t+t')\,\sigma^*_{11}(\boldsymbol{q},t')\right\rangle = \\
&= \frac{1}{V}\left\langle \sigma^{\mathrm{R}}_{11}(\boldsymbol{q},t+t')\,\sigma^{\mathrm{R}}_{11}(\boldsymbol{q},t') + \sigma^{\mathrm{I}}_{11}(\boldsymbol{q},t+t')\,\sigma^{\mathrm{I}}_{11}(\boldsymbol{q},t')\right\rangle + \\
&+ i\frac{1}{V}\left\langle \sigma^{\mathrm{I}}_{11}(\boldsymbol{q},t+t')\,\sigma^{\mathrm{R}}_{11}(\boldsymbol{q},t') - \sigma^{\mathrm{R}}_{11}(\boldsymbol{q},t+t')\,\sigma^{\mathrm{I}}_{11}(\boldsymbol{q},t')\right\rangle, \\
C_{\perp}(q,t) &= C_{2211}(q,t) = \frac{1}{V}\left\langle \sigma_{22}(\boldsymbol{q},t+t')\,\sigma^*_{11}(\boldsymbol{q},t')\right\rangle = \\
&= \frac{1}{V}\left\langle \sigma^{\mathrm{R}}_{22}(\boldsymbol{q},t+t')\,\sigma^{\mathrm{R}}_{11}(\boldsymbol{q},t') + \sigma^{\mathrm{I}}_{22}(\boldsymbol{q},t+t')\,\sigma^{\mathrm{I}}_{11}(\boldsymbol{q},t')\right\rangle + \\
&+ i\frac{1}{V}\left\langle \sigma^{\mathrm{I}}_{22}(\boldsymbol{q},t+t')\,\sigma^{\mathrm{R}}_{11}(\boldsymbol{q},t') - \sigma^{\mathrm{R}}_{22}(\boldsymbol{q},t+t')\,\sigma^{\mathrm{I}}_{11}(\boldsymbol{q},t')\right\rangle,
\end{aligned} \tag{4.20}$$

and:

$$\begin{aligned}
\sigma^{\mathrm{R}}_{11}(\boldsymbol{q}) &= \sum_{\alpha=x}^{y}\sum_{\beta=x}^{y}\sigma^{\mathrm{R}}_{\alpha\beta}(\boldsymbol{q})\cdot n_\alpha\cdot n_\beta, \\
\sigma^{\mathrm{I}}_{11}(\boldsymbol{q}) &= \sum_{\alpha=x}^{y}\sum_{\beta=x}^{y}\sigma^{\mathrm{I}}_{\alpha\beta}(\boldsymbol{q})\cdot n_\alpha\cdot n_\beta, \\
\sigma^{\mathrm{R}}_{12}(\boldsymbol{q}) &= \sum_{\alpha=x}^{y}\sum_{\beta=x}^{y}\sigma^{\mathrm{R}}_{\alpha\beta}(\boldsymbol{q})\cdot n_\alpha\cdot m_\beta, \\
\sigma^{\mathrm{I}}_{12}(\boldsymbol{q}) &= \sum_{\alpha=x}^{y}\sum_{\beta=x}^{y}\sigma^{\mathrm{I}}_{\alpha\beta}(\boldsymbol{q})\cdot n_\alpha\cdot m_\beta, \\
\sigma^{\mathrm{R}}_{22}(\boldsymbol{q}) &= \sum_{\alpha=x}^{y}\sum_{\beta=x}^{y}\sigma^{\mathrm{R}}_{\alpha\beta}(\boldsymbol{q})\cdot m_\alpha\cdot m_\beta, \\
\sigma^{\mathrm{I}}_{22}(\boldsymbol{q}) &= \sum_{\alpha=x}^{y}\sum_{\beta=x}^{y}\sigma^{\mathrm{I}}_{\alpha\beta}(\boldsymbol{q})\cdot m_\alpha\cdot m_\beta,
\end{aligned} \tag{4.21}$$

where $\sigma^{\mathrm{R}}_{\alpha\beta}(\boldsymbol{q})$, $\sigma^{\mathrm{I}}_{\alpha\beta}(\boldsymbol{q})$ are real and imaginary parts of the stress tensor, $n_x = \frac{q_x}{|q|}$, $n_y = \frac{q_y}{|q|}$, $m_x = n_y$, and $m_y = -n_x$.

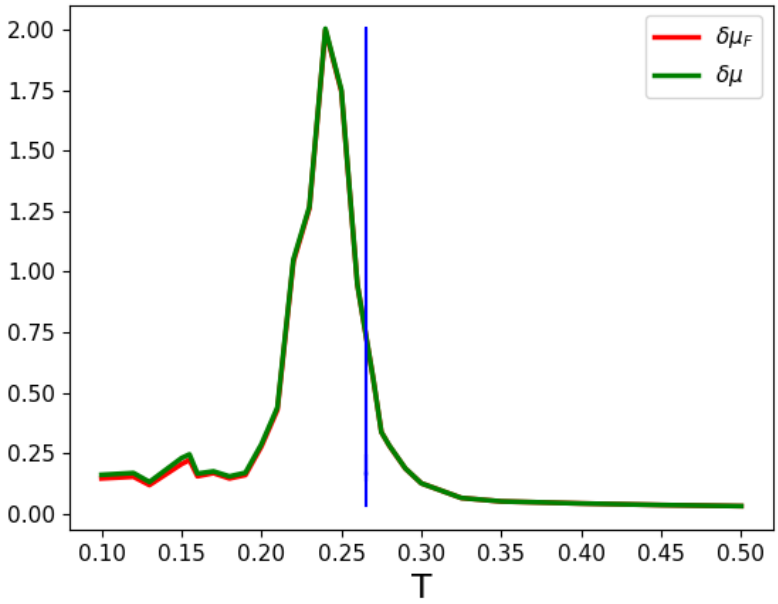

Figure 4.11: Temperature dependence of the standard deviations of the fluctuation modulus $\delta\mu_F$ and the quasi-equilibrium shear modulus $\delta\mu$ for 2-dimensional pLJ system with $N = 10^4$ particles. The blue line corresponds to $T_g = 0.26$. The sampling time is $\Delta t = 10^5 \tau_{\mathrm{LJ}}$.

To study the stress correlation range for the glass forming 2-dimensional polydisperse simple liquid system more directly we analyzed the correlation functions $C_T(t)$, $C_2(t)$, $C_{\parallel}(t)$, $C_{\perp}(t)$ based on the MD simulation data obtained by following the protocol from section 4.2 at different wave-vectors $\boldsymbol{q}$. Those correlation functions for the minimum wave-vector $q_{\min} = 2\pi/L$ (where $L \approx 100$ is the system size) at different temperatures (both above and below $T_g \approx 0.26$) are shown in Figs. 4.12 — 4.16 as solid curves. For each correlation function we obtained the theoretical predictions based on ref. [9], which are shown in the Figs. 4.13 — 4.16 as red dashed lines.

To get the numerical data for the theoretical curves one has to use eqs. 2.122 – 2.124, and 2.132. First of all, the Laplace transform of the shear-stress relaxation modulus $G(t)$, $G(s)$, should be applied. The longitudinal modulus $K(q,s)$ can be obtained from $K(q,t)$ in a similar way. Note that $K(q,t)$ is different from $K(t)$ (cf. eq. 2.73) due to finite heat conductivity (see end of ref. [9]) and composition fluctuations (cf. ref. [147]).

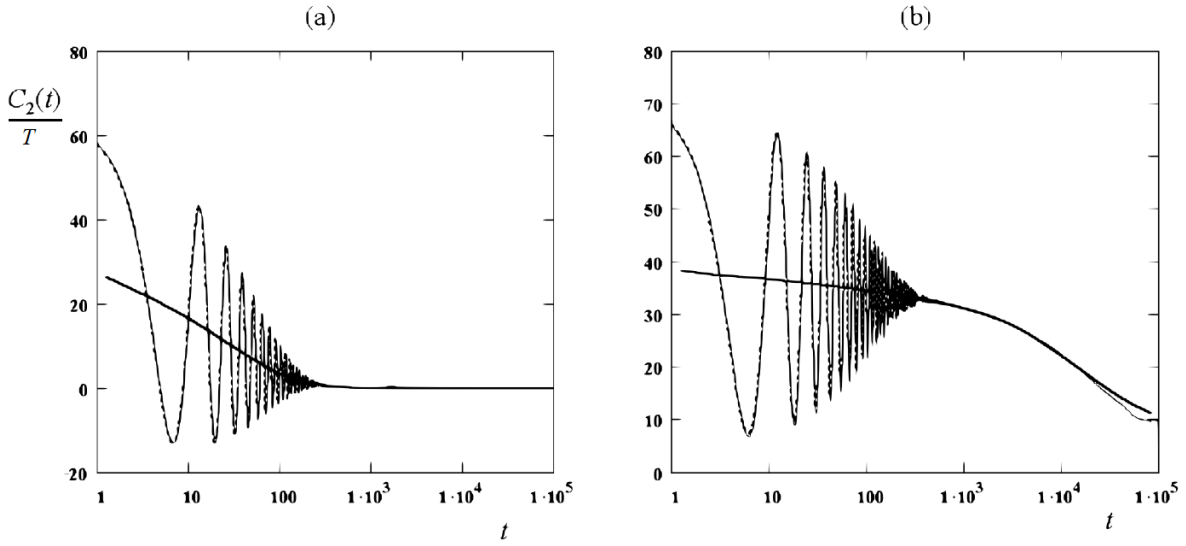

Figure 4.12: (a) Time-dependence of the stress correlation function $C_2(t)/T$ at wave-vector $q = 2\pi/L$ for the 2d pLJ system at $T = 0.3$ (above T_g): direct simulation data (thin solid curve), theoretical predictions (thick dashed curve). Note that the two curves superimpose almost exactly. Thick solid curve corresponds to the smoothed correlation function $C_{2\sim}(t)/T$ with no oscillations; t is the time in LJ units, $0 < t < 10^5$. (b) Similar data for $T = 0.24$ (below T_g).

Then, it is possible to obtain the $C_T(s)$, $C_2(s)$, $C_{\parallel}(s)$, $C_{\perp}(s)$. Note, that the notations are simplified by replacing $C_{\perp}(q,s) = C_{\perp}(s)$, $C_T(q,s) = C_T(s)$, $C_2(q,s) = C_2(s)$, and $C_{\parallel}(q,s) = C_{\parallel}(s)$. The last stage is to apply the inverse Laplace transform to get the time-dependent functions $C_T(t)$, $C_2(t)$, $C_{\parallel}(t)$, $C_{\perp}(t)$ which will be compared with the correlation functions calculated based on the MD simulation data.

As it can be seen from Figs. 4.12 – 4.16, the direct simulation data analyzed by using eqs. 4.19 – 4.21 show an excellent agreement (with no adjustable parameters) with the observed theoretical predictions [9].

The materials functions involved in eqs. 2.122 – 2.124, 2.132 are introduced in Chapter 2, section 2.2.4. In particular $G(t)$ defines the shear stress response to a shear strain, $K(t)$ and $M(t)$ define, respectively, the longitudinal and transverse stress generated by a longitudinal strain (by transverse strain we mean the normal stress in a direction perpendicular to $\boldsymbol{q}$). The transverse modulus, $M(t)$, can be found from the equation:

$$M(t) = K_b(t) - \frac{2}{d}G(t) = K(t) - 2G(t), \tag{4.22}$$

where $K_b(t)$ was obtained using eq. 2.68. A similar equation is valid for small q,

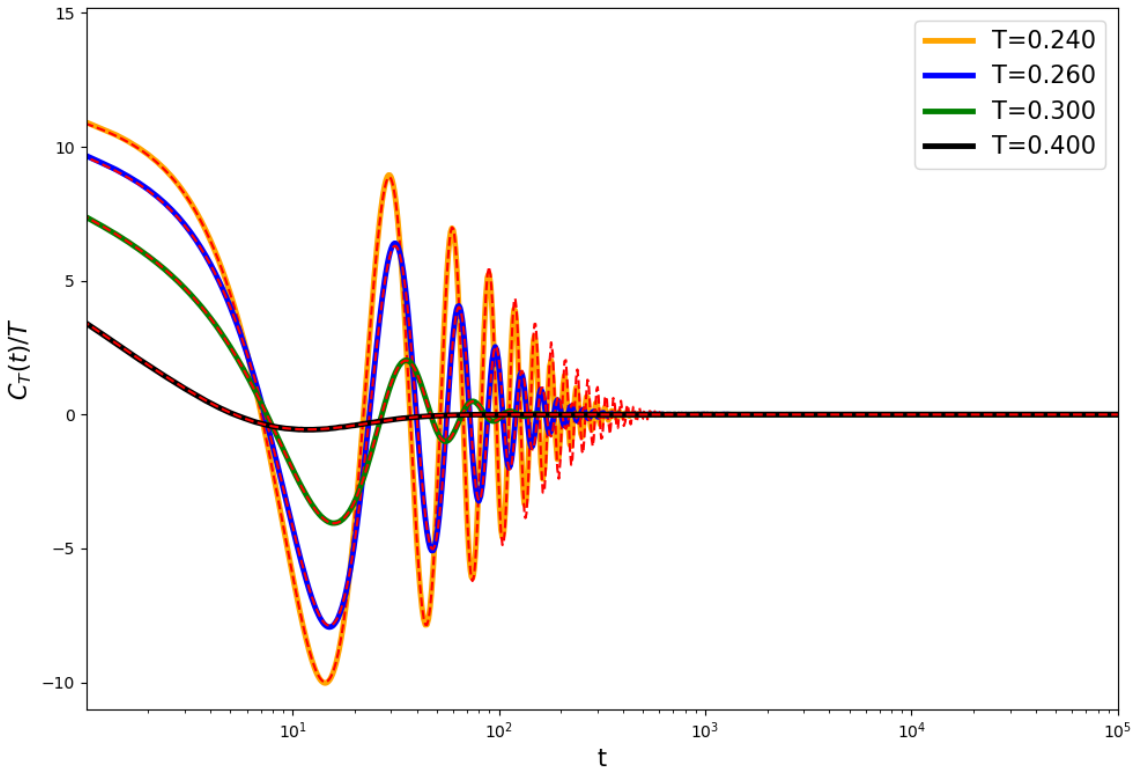

Figure 4.13: Time-dependencies of the stress correlation function $C_T(t)/T$ at wave-vector $q = 2\pi/L$ for the 2d pLJ system at different T, t is time in LJ units, $0 < t < 10^5$. The dashed red lines define the theoretical prediction obtained by the inverse Laplace transform of eq. 2.122.

$q\overline{\sigma} \ll 1$: $M(q,t) \simeq K(q,t) - 2G(q,t)$. The time and temperature dependence of those material functions are shown in Figs. 4.18 – 4.20. Based on the elasticity theory [148], in the limit of low q, one can find the Poisson's ratio ν which characterizes the elastic properties of an isotropic material as:

$$\nu = \frac{M^*}{(d-2)\cdot M^* + K^*}, \tag{4.23}$$

where the moduli K^*, M^* are the long-time levels of the time-dependent moduli $K(t)$

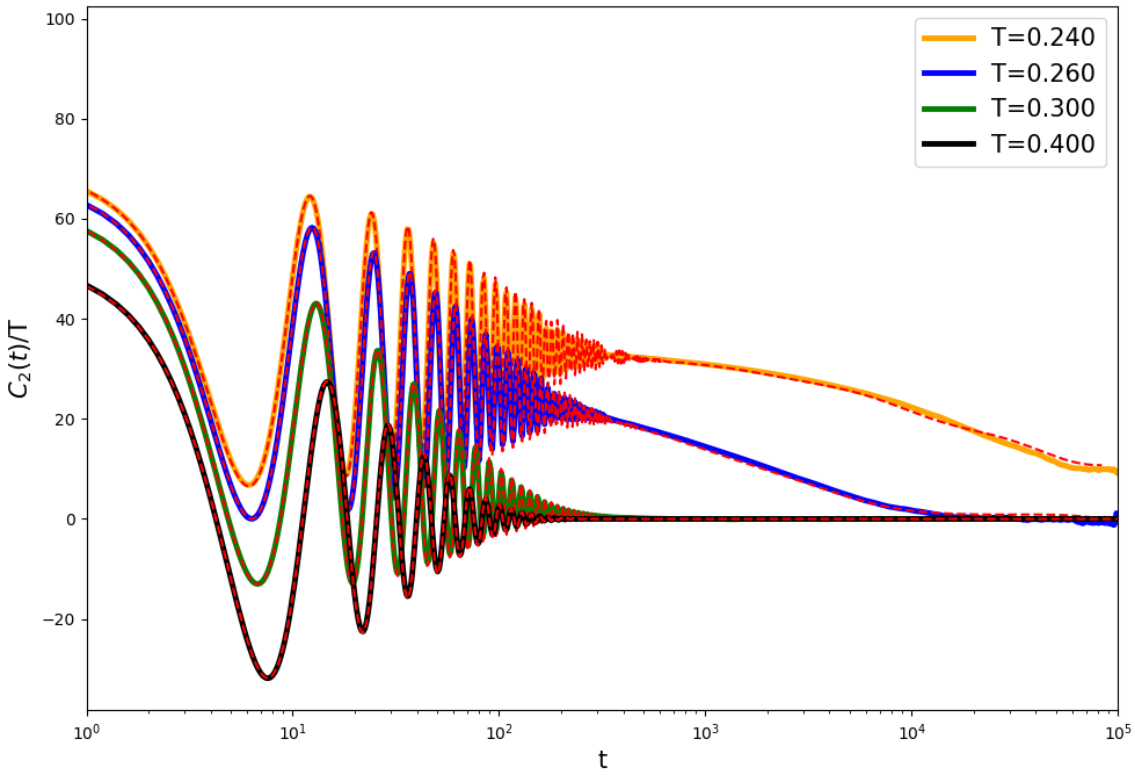

Figure 4.14: Time-dependencies of the stress correlation function $C_2(t)/T$ at wave-vector $q = 2\pi/L$ for the 2d pLJ system at different T, t is time in LJ units, $0 < t < 10^5$. The dashed red lines define the theoretical prediction obtained by the inverse Laplace transform of eq. 2.132.

and $M(t)$, which can be obtained taking into account eqs. 2.67, 2.73, and 4.22:

$$\begin{aligned} K^* &= K(t \sim \Delta t) = \eta + \left(2 - \frac{2}{d}\right)\mu, \\ M^* &= M(t \sim \Delta t) = \eta - \left(\frac{2}{d}\right)\mu, \end{aligned} \tag{4.24}$$

Note, that $G^* = G(t \sim \Delta t) = \mu$ [6, 7, 93] (cf. Chapters 2 and 3). The range for ν in d-dimensional case is $-1 < \nu \leq 1/(d-1)$. The temperature dependence of ν vs. T is shown in Fig. 4.17.

It is instructive to coarse-grain the time-dependence of $C_{\alpha\beta\gamma\delta}$ to remove the short-time oscillations with the period $\sim 2\pi/(qc_L) \sim 10\tau_{\mathrm{LJ}}$, where c_L is the longitudinal sound velocity defined in ref. [9] and below eq. 2.153. Such smoothed correlation functions

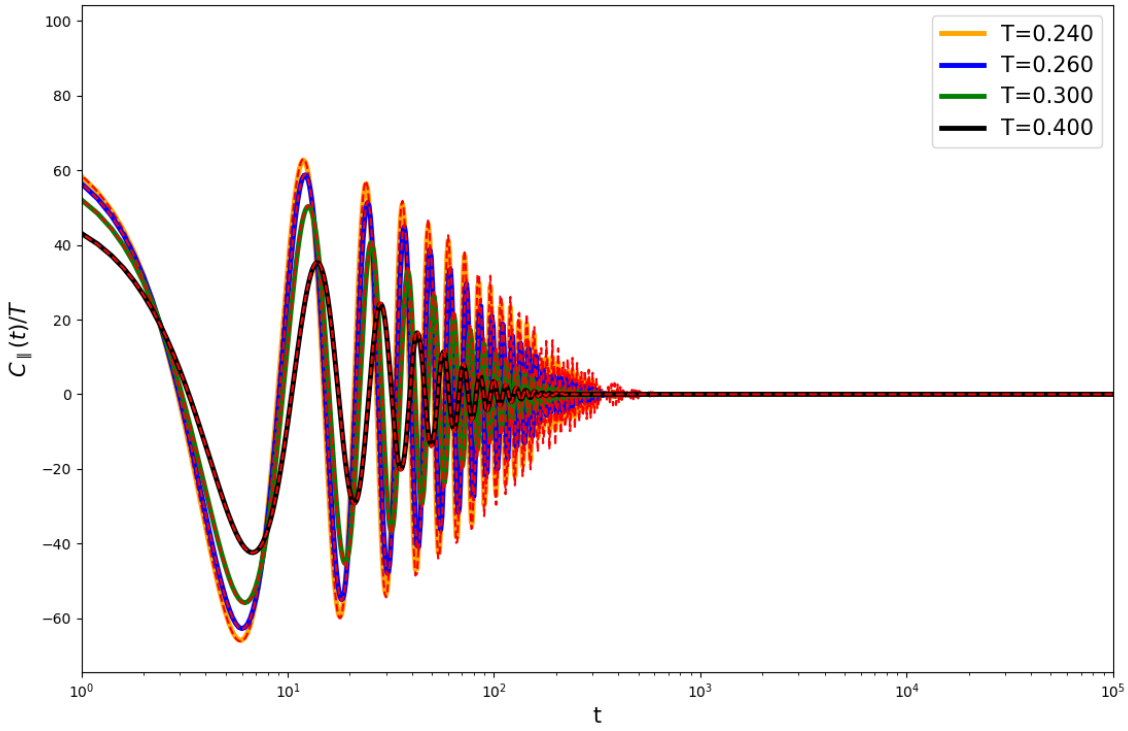

Figure 4.15: Time-dependencies of the stress correlation function $C_{\parallel}(t)/T$ at wave-vector $q = 2\pi/L$ for the 2d pLJ system at different T, t is time in LJ units, $0 < t < 10^5$. The dashed red lines define the theoretical prediction obtained by the inverse Laplace transform of eq. 2.123.

$C_{2\sim}(t)$ (with coarsening time-scale $t_c \sim 20\tau_{\rm LJ} \sim \frac{4\pi}{(qc_L)}$) are also shown in Fig. 4.12. The ensemble of simulation data supports the theoretical prediction [9] that the only correlation function surviving coarse-graining at $t \gtrsim t_c$ is C_{2222}. The smoothed version of this function $C_{2\sim}(t)$, just weakly depends on q for $q \ll q_{\rm peak} \sim 5$. This leads to the following distance dependence of the time-smoothed correlation function of the local shear stress $\sigma_{xy}(\boldsymbol{r}, t)$:

$$\langle \sigma_{xy}(\boldsymbol{r}+\boldsymbol{r}', t+t')\,\sigma_{xy}(\boldsymbol{r}', t')\rangle \simeq \frac{1}{\pi} C_{2\sim}(t)\left(\frac{1}{r^2} - \frac{8x^2y^2}{r^6}\right), \tag{4.25}$$

where $\boldsymbol{r} = (x, y)$. The above equation is valid for $t \gg t_c$ and $\overline{\sigma} \ll r \ll L$. It means that the stress correlation decay as $1/r^2$ in agreement with the previous simulation results [11] and theoretical predictions [9] (Chapter 2).

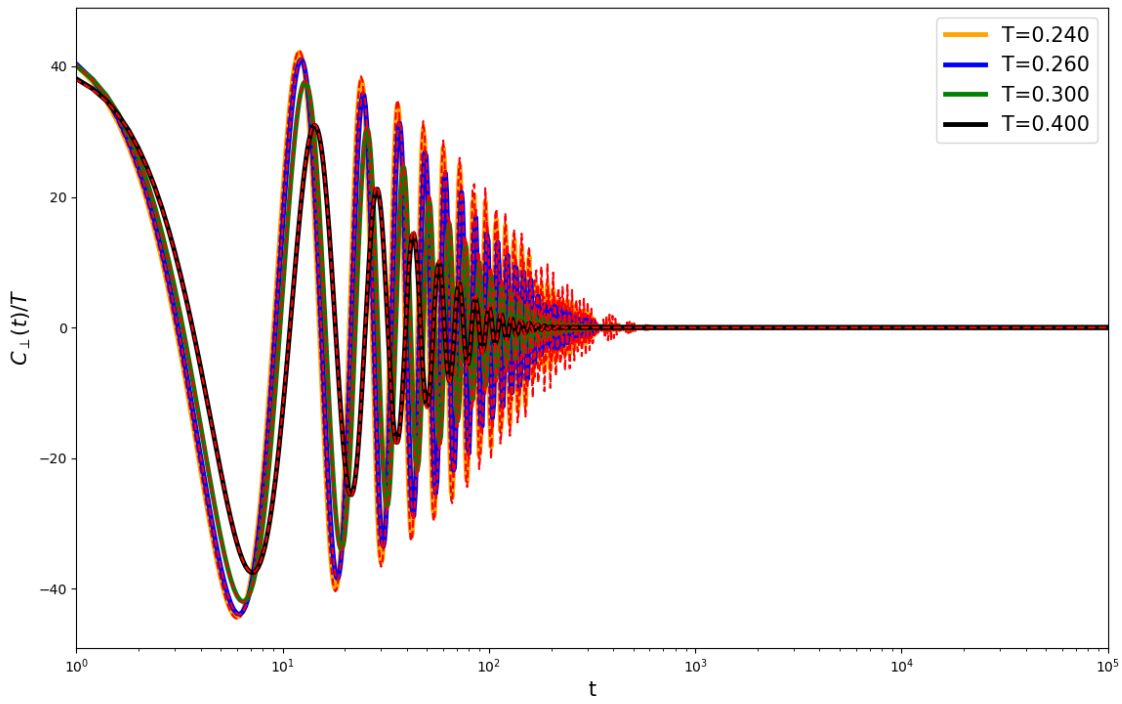

Figure 4.16: Time-dependencies of the stress correlation function $C_\perp(t)/T$ at wave-vector $q = 2\pi/L$ for the 2d pLJ system at different T, t is time in LJ units, $0 < t < 10^5$. The dashed red lines define the theoretical prediction obtained by the inverse Laplace transform of eq. 2.124.

4.6 Mean-square displacement (MSD) and the diffusion coefficient

The cooperative dynamical properties of the system are closely related to the mean-square displacement (MSD) of particles (cf. eq. 1.2). The temperature dependence of the MSD for 2-dimensional pLJ system is represented in Fig. 4.21.

At short time scale, the MSD is expected to have an early regime where $\mathrm{MSD}(t) \propto t^2$, when particles move ballistically without many collisions [2]. At longer time scales one can observe the slowing down of the dynamics with decreasing the temperature T, leading to emergence of an intermediate plateau regime. The "plateau" of MSD separates the ballistic and diffusive regime. Its length increases at low T's. For the time region where the plateau is observable the MSD increases very little. This fact can be explained by

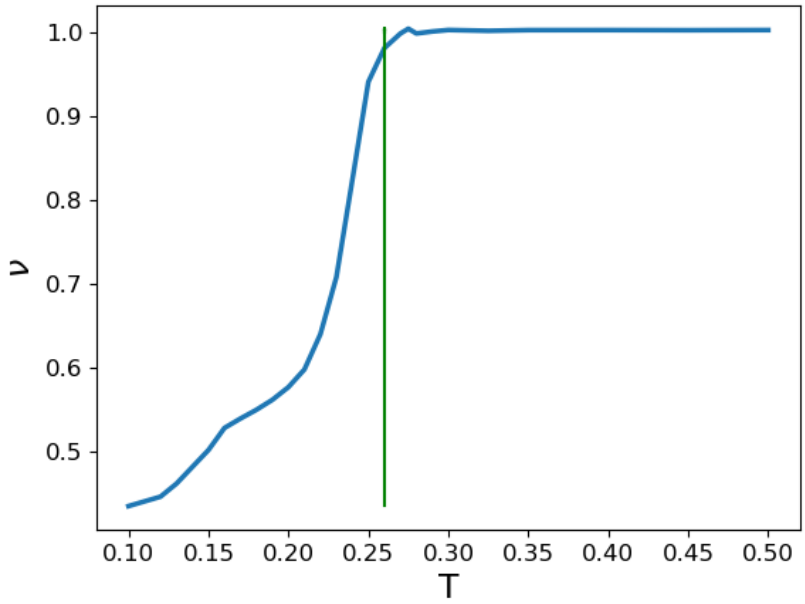

Figure 4.17: Temperature dependence of the Poisson's ratio ν for the 2d pLJ system. The green line corresponds to the glass transition temperature $T_g = 0.260$. As you can see, the upper bound is expected in the liquid regime where $\mu = 0$.

hypothesizing that the particles cannot exit the "cage" formed by their neighbors [2]. Therefore, the plateau corresponds to vibrations of the tagged particle i within the cage. Such vibrations within the local cage should not be mixed with the β-relaxation process. The time which a tagged particle i needs to get out from the cage corresponds to the α-relaxation time [2]. At long times, the diffusive motion is dominated: for times t longer compared to the relaxation time τ_α, MSD increases linearly with time as for a liquid, MSD $\propto t$.

Noteworthily, at longer times, the slope of MSD is proportional to the diffusion coefficient D as was shown in eq. 1.3. The temperature dependence of the diffusion coefficient is shown in Fig. 4.22.

4.7 Discussion

4.7.1 Local stress tensor correlations in the studied system

In Chapter 2 we analyzed the local stress tensor correlations in complex and supercooled liquids focusing on the time and distance dependencies of the shear stress correlation

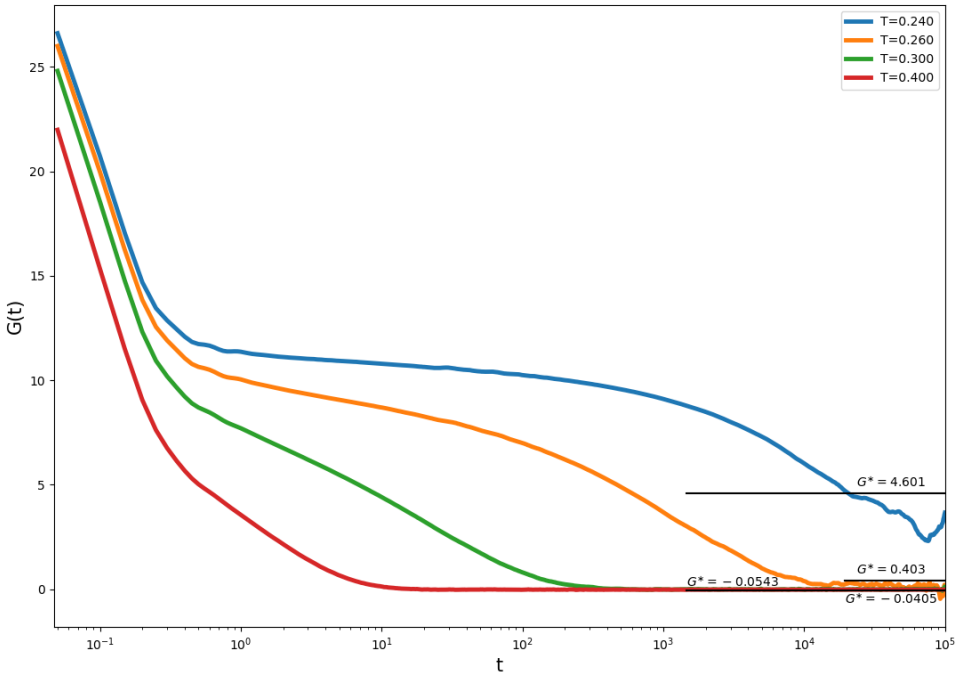

Figure 4.18: Time-dependencies of the relaxation modulus $G(t)$ for the 2d pLJ system for different T (t is the time in LJ units, $0 < t < 10^5$). The black solid lines highlight the values of the long-time limit of G^* (text below eqs. 4.24).

function $C(\boldsymbol{r}, t)$. It is important to summarized theoretical work done in Chapter 2 and ref. [9] due to the reason that in the current Chapter 4 we have analyzed the Fourier transform of the stress correlation function $C_{2222}(q, t)$ above and below T_g.

Let us start by reminding that our approach is based upon the fluctuation-dissipation theorem (FDT) and the concept of random forces due to local structural and momentum thermal fluctuations. It is similar in spirit to the classic theory of hydrodynamic fluctuations [105] and can be traced back to the theorems on regression of fluctuations and reciprocal relations in irreversible processes proposed long ago by Onsager [149–152].

The fluids we consider are characterized by slowly fading memory and long structural relaxations including the stress relaxation with the long terminal time $\tau_{\max}$ (or τ_α). Such fluids are viscoelastic by definition: for $t \ll \tau_{\max}$ they show quasi-elastic behavior (with considerable transient elastic moduli), while for $t \gg \tau_{\max}$ they behave as highly viscous media. This property is equally applicable to macromolecular solutions or melts and to glass-forming simple liquids, the major difference being that polymer systems are normally

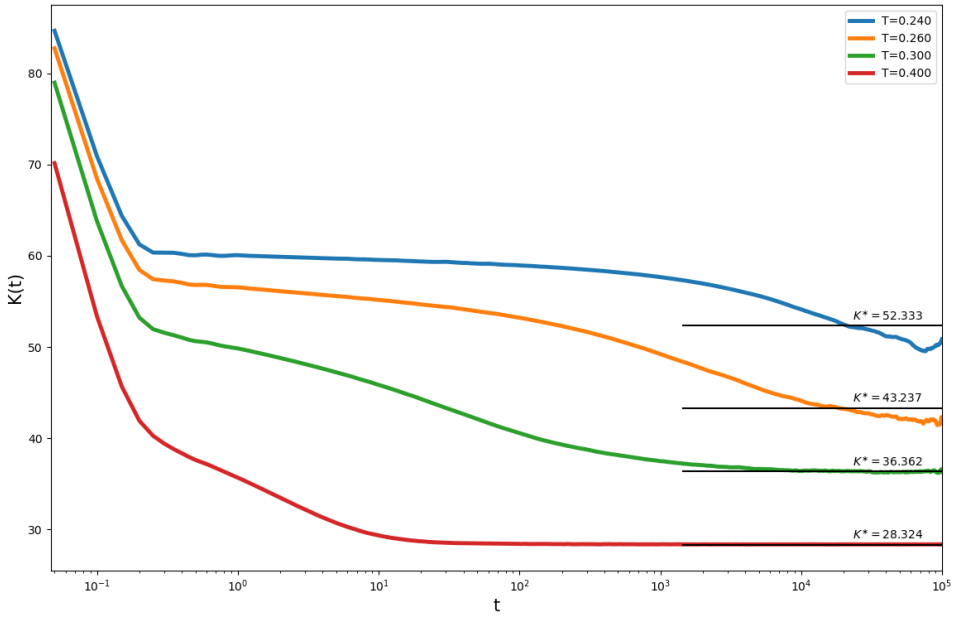

Figure 4.19: Time-dependencies of the longitudinal modulus $K(t)$ for the 2d pLJ system for different T (t is the time in LJ units, $0 < t < 10^5$). The black solid lines highlight the values of the long-time limit of K^* (eqs. 4.24).

highly elastic, while glasses are typically brittle. This difference however is not important for the present analysis since we consider weak fluctuations near the equilibrium state rather than non-linear flow effects.

The present theory assumes that structural correlations (due to irregularities of molecular packing) are local (short-range) in liquid systems we consider. This is true for all equilibrium viscoelastic liquids known so far (including glass-forming systems): the static structural correlation length ξ_s can increase as the system is cooled down close to the vitrification temperature [65, 72, 73, 153, 154], but this increase is typically limited by a few (at most $\sim$ 10) molecular sizes [2, 67, 68, 111, 155–157]. It is for this reason that we can neglect the q-dependence of the generalized relaxation moduli G, K and M in isothermal and isocompositional conditions as such dependence is essentially of structural origin. However, in the general case eq. 2.132 must be amended by replacing $K(s)$ and $M(s)$ with $K(q, s)$ and $M(q, s)$, respectively.

Note that the $q = 0$ approximation for material functions (cf. eq. 2.131) is equivalent to stating that these functions (relaxation moduli) reflect a localized in space response.

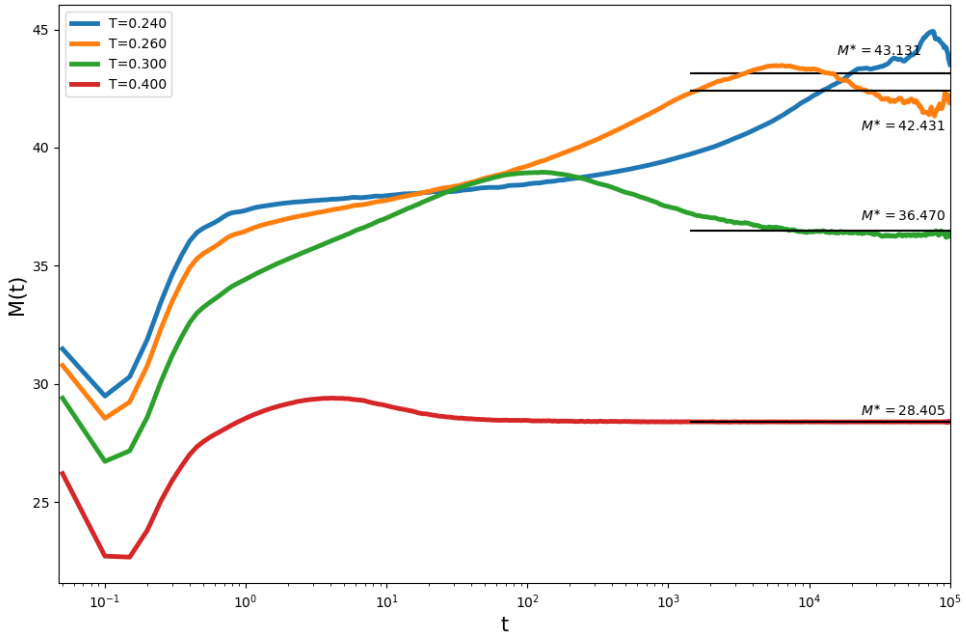

Figure 4.20: Time-dependencies of the transverse modulus $M(t)$ for the 2d pLJ system for different T (t is the time in LJ units, $0 < t < 10^5$). The black solid lines highlight the values of the long-time limit of M^* (eqs. 4.24).

The argument concerning their locality (around eq. 2.131) is based on the assumption that the local stress is defined by the local momentum and the local deformation history of a fluid element (by "local" we mean short-range in terms of the structural length ξ_s). Now, it is the deformation history (and, therefore, the momentum field) that is controlled by the definition of the material functions (cf. the constitutive relation in eq. 2.118 providing the stress response to a prescribed deformation field). The locality of the relaxation moduli then comes merely from the fact that a small deformation of a fluid element 1 (of size somewhat exceeding ξ_s) does not affect much the local stress in a distant fluid element 2 if the latter is kept undeformed.

By contrast, the deformation and momentum field are not prescribed in eq. 2.112 (which is equivalent to eq. 2.113) apart from the instant initial deformation at $t = 0$: at any later time, $t > 0$, the liquid is being deformed further due to the generated internal stresses. This effect gives rise to a fast momentum propagation and, as a result, to significant non-locality of the stress response. So, the distinction of eq. 2.113 (implying a non-local response) from the constitutive relation, eq. 2.118, (reflecting the local response)

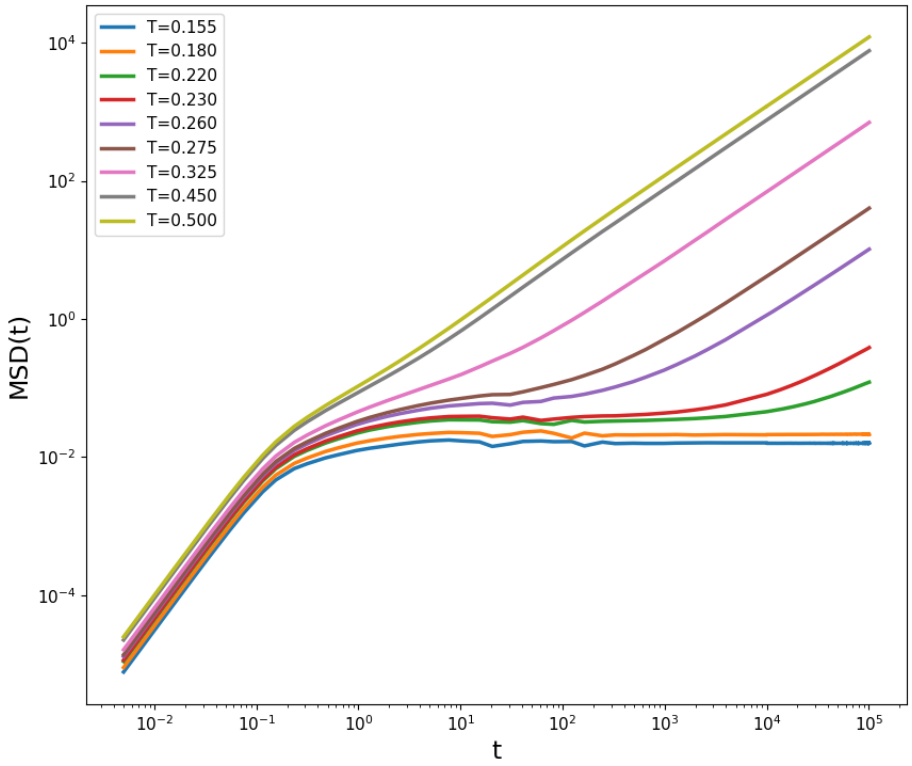

Figure 4.21: Temperature dependence of the mean-square displacement for 2-dimensional pLJ system with $N = 10^4$ particles. The sampling time is $\Delta t = 10^5 \tau_{\mathrm{LJ}}$.

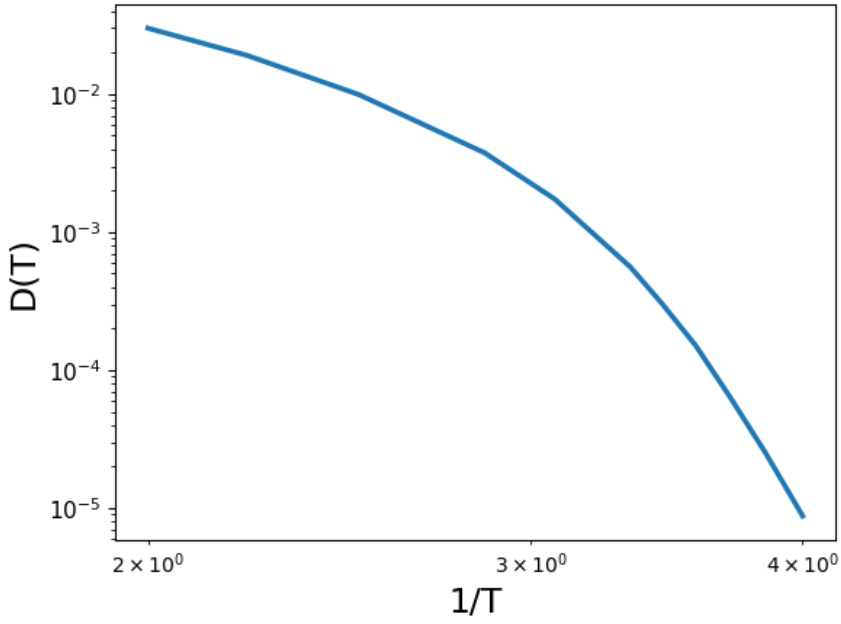

Figure 4.22: The diffusion coefficient D vs. the inverse temperature $1/T$ in double logarithmic scale for 2-dimensional pLJ system with $N = 10^4$ particles. The sampling time is $\Delta t = 10^5 \tau_{\mathrm{LJ}}$.

is that the former corresponds to the process in which neither the deformation history, nor the momentum field are prescribed.

To summarize, eq. 2.113 allows for internal flow (momentum field) as a consequence of the external perturbation, whereas the constitutive relation, eq. 2.118, defines the material functions solely in response to the prescribed external deformation (no "internal" flow on top of it). With no extra flow due to internal forces the information about a perturbation at one point cannot be transmitted to a distant point, so the response is local.

The effects we consider in this paper correspond to length-scales $\gg \xi_s$. It is demonstrated here that non-simultaneous stress correlations (with finite time-shift t) are long-range (LR) in viscoelastic liquids in agreement with the results of ref. [11–13]. As a major result we show that the stress correlations decay algebraically (rather than exponentially) with distance r, as r^{-2} for $r < l(t)$ in 2d systems, and that they decay in time only slowly for $t \lesssim \tau_{\max}$. Such behavior is of course very different from what is known about classical simple liquids [105]. Moreover, in the glassy state the shear-stress correlation function is predicted to show a finite plateau level in the long-time regime where the liquid is characterized by a nearly constant shear modulus, $G(t) = G_\infty$. Similar conclusions have been drawn in ref. [12, 13] based on a different theoretical approach. The relevant correlation length $l(t)$ (defining the region of validity of the $1/r^2$ correlation law) turns out to be the time-dependent momentum propagation length given in eq. 2.148 and 2.150. Thus, the correlation length $l(t)$ corresponds to sound propagation at short times and to vorticity diffusion at long times. Both processes are fast in highly viscous (viscoelastic or glass-forming) liquids leading to a long length-scale $l(t)$ for the characteristic time range coming from the relaxation spectrum of the liquid.

Note that transverse sound waves (with wavelength $\lambda \lesssim l(t)$) are not significantly damped in the time regime $\tau_{\min} \ll t \ll \tau_{\rm pl}$ corresponding to the plateau of the shear relaxation modulus $G(t)$: the liquid shows an elastic response in this time range, so the propagation length here is proportional to the sound velocity, $l(t) \simeq c_T t$. By contrast, the sound waves get damped for $t \gtrsim \tau_{\rm pl}$: the liquid response then becomes viscoelastic with the propagation length defined by the generalized time-dependent viscosity $\eta(t)$: $l(t) \sim \sqrt{\eta(t)\, t/\rho}$ (cf. eq. 2.148). In this regime l increases with t in a sublinear fashion.

Thus, we show that very long-range and anisotropic correlations of stress must develop in the transient regime $t \lesssim \tau_{\max}$ with the characteristic correlation range (for $t \sim \tau_{\max}$) being $l_{\max} \sim (\eta\tau_{\max}/\rho)^{1/2}$, where η is the zero-shear viscosity of the liquid. In viscoelastic (glass-forming) liquids η is high (it is roughly proportional to the relaxation time $\tau_{\max}$),

so the vorticity diffusion is fast giving rise to long $l_{\max}$ strongly exceeding the molecular size a_m.

Noteworthily, the stress correlations do not decay exponentially for $r > l$: in the distal region $l < r < l' \approx c_L t$ they still follow a power law, but with a significantly faster decrease with r, $C(\boldsymbol{r}, t) \propto r^{-4}$ (cf. Figs. 2.3 – 2.6). Here l' is the longest correlation length defined by the longitudinal sound velocity c_L. Interestingly, in the plateau time-regime ($\tau_{\min} < t < \tau_{\rm pl}$) the correlation function increases with time in the distal region $l < r < l'$: it is proportional there to $t^2 G_{\rm pl}^2 r^{-4}$(cf. the second part of the last term in eq. 2.157).

Thus, the developed theory allows us to see how the long-range stress correlations gradually emerge as a function of time-shift (t) starting from purely local simultaneous stress correlations (see eq. 2.157). We also predict how the magnitude of the long-range stress correlations gradually decreases in time according to the relaxation law reflecting both shear and longitudinal memory functions, $G(t)$ and $K(t)$ (cf. eqs. 2.159 – 2.160).

To further clarify the main results obtained here let us first recall what is known about the stress correlations in ordered (crystalline) solids. The fluctuations of stress there are essentially due to thermally excited acoustic waves. The correlation function of simultaneous fluctuations (with time-shift $t = 0$) is long-range (more precisely, infinite range) and anisotropic as follows from the classical elasticity theory [145]. However, the stress fluctuations in solids decay rather fast with characteristic time $t \sim r/c$ corresponding to the frequency of acoustic waves with wave-length $\sim r$ (c is the sound velocity). Thus, the stress fluctuations become uncorrelated at $t \gg r/c$. Similar high-frequency stress fluctuations ($\sigma^{\rm f}$) are also present in viscoelastic (glass-forming) fluids which behave as solids at short times, but this fluctuation field is superimposed with a quasi-permanent (virtually frozen) heterogeneous random stress pattern. The "frozen" (inherent) stress $\sigma^{\rm i}$ does not cause directly any fluid motion; being compatible with mechanical equilibrium it does not generate any internal force, $\sigma^{\rm i}_{\alpha\beta,\beta} = 0$. However, it is important to emphasize that the inherent (transiently frozen) stress is necessarily present in viscoelastic fluids; it serves to restore the short-range character of the total stress correlations at $t = 0$ (recall that these correlations are structural in nature).

Thus, the correlation function of the total stress, $\sigma = \sigma^{\rm f} + \sigma^{\rm i}$, is $C(\boldsymbol{r}, 0) = C^{\rm f}(\boldsymbol{r}, 0) + C^{\rm i}(\boldsymbol{r}, 0) \simeq 0$ for $r \gg \xi_s$. Hence, the correlation function of the inherent stress, $C^{\rm i}$, must be nearly opposite to the function $C^{\rm f}$ due to acoustic stress fluctuations. Therefore, $C^{\rm i}$ must also show infinite-range and anisotropic correlations. As the fluctuation part decays rather fast, the stress correlations at longer times ($t \gg r/c$) must be mostly due to the inherent

(frozen) stress, hence they must be also long-range and stay for a long time $\sim \tau_{\max}$. Some evidence for such a distinction between the inherent structure dynamics and the overall liquid dynamics can be found in simulation studies (see Fig. 5,6 in ref. [158] and Fig.1 in SM of ref. [11]).

Such long-range (and nearly frozen) "elastic" stress fields have be considered in the framework of elasto-plastic models [159–161]. It is worth mentioning that the anisotropic character of the frozen stress correlations directly follows from the condition of mechanical equilibrium ($\sigma^{\mathrm{i}}_{\alpha\beta,\beta} = 0$) which demands that shear stress must vanish for certain directions of the wave-vector $\boldsymbol{q}$. For example, $\sigma^{\mathrm{i}}_{xy} = 0$ if $\boldsymbol{q} \neq 0$ is parallel to either the x or the y axis. The latter example also explains why the second ("singular") term in the stress correlation function (cf. eq. 2.134) shows knots for $q_x = 0$ or $q_y = 0$.

It is worth emphasizing again that the predicted long-range spatial and temporal stress correlations are essentially viscoelastic in nature. The long-range character of $C(\boldsymbol{r}, t)$ is not exactly an inertial effect (in contrast to fast fluctuations due to acoustic waves): in fact, the correlation function is independent of the fluid density ρ for $r \ll l(t)$ (in this regime C is defined in eq. 2.160). Moreover, C is well-defined in the formal limit $\rho \to 0$ where the infinite range character of stress correlations emerges instantly.

As explained above, the revealed LR stress correlations are dynamical in nature and are not directly related to the static correlation length ξ_s. However, this does not imply that the LR stress correlations are completely unrelated to the static glass correlation length ξ_s. Since $l(t) \sim \sqrt{\eta t/\rho}$ (cf. eq. 2.148) at long times, l and ξ_s would be related if ξ_s indeed determines the increase of the viscosity at low T as $\eta/\eta_0 \sim \exp(E_A(T)/T)$ with the putative equation $E_A(T) \propto \xi_s(T)^{\psi}$ [106] and $\psi \leq d$ (d being the spatial dimension).

Let us recall that supercooled liquids are often characterized by a dynamical correlation length ξ_d which depends—as $l(t)$—on the time scale [2, 70, 107, 119]. Can we associate the stress correlation range with ξ_d? The point is that ξ_d depends on the nature of variables whose correlations are studied, so many dynamical lengths ξ_d can be defined at the same time scale [69, 162]. Typically, ξ_d is associated with the emergence of dynamical heterogeneities in glass-forming fluids and refers to the cluster size of an increasing number of particles with correlated motion at low T (e.g. the span of one-dimensional string-like motion or the length scale associated with dynamic fluctuations as measured by dynamic susceptibilities [2, 66, 69, 70] or a length-scale characterizing the distance between localized excitations of high mobility [163]). While stress fluctuations certainly affect the cooperative motion of fluid particles, the usually defined ξ_d is expected to be much shorter

than l, l' [107].

It is remarkable that the r, θ dependencies of the LR part of the stress correlation function, eq. 2.160, completely agree with the far field stress response to a localized plastic strain event [164,165] which, in turn, was shown to be equivalent to the stress field generated by a pair of "force dipoles" [164]. The corresponding characteristic quadrupolar (eight-lobe) LR stress pattern was also observed in simulation and experimental studies of the local rearrangement effects in 2d foams [166] 2d glass systems [167] and quasi-2d emulsions [168].

Long-range dynamical correlation effects have been reported in several other recent studies [11, 69, 70, 169]. Computer simulations of ref. [11] reveal LR correlations between plastic events in deeply supercooled 2d liquids, which have been attributed to $1/r^2$ correlations of the local inherent stresses a distance r apart, in agreement with our result given in eq. 2.160. The simulation studies [11] also revealed that the amplitude of power-law stress correlations first grows, then shows a transient plateau and finally decays. That sort of behavior is in harmony with our results (cf. eq. 2.157 and eq. 2.160) showing the early time increase of the correlation amplitude (due to the factor t^2 in the last term of eq. 2.157) and then its gradual decrease defined by the $\tilde{G}\,(t)$ factor in eq. 2.160 (the slow decrease is also visible in Figs. 4.12b, 4.14). The LR dynamical correlations between particle displacements and related functions have been demonstrated in refs. [11, 69, 70]. Remarkably, the studies [69,70] show that the corresponding dynamical correlation length ξ_4 grows linearly in time in glasses, while $\xi_4 \propto \sqrt{\eta t}$ in the long-time regime in liquids, in obvious agreement with the momentum propagation length $l(t)$ defining the range of stress correlations considered in the present paper (cf. eq. 2.150). Similar results are also found in ref. [169]. It is worth noting that generally the length $l(t)$ (cf. eq. 2.148 and 2.150) can be also considered as the range of viscoelastic hydrodynamic interactions in the liquid [10].

It is worth noting that all the results obtained in this paper are valid for equilibrium systems, either ergodic liquids or equilibrium ensembles of amorphous solids (glasses). In practice the glassy systems are normally out of equilibrium; the effect of their nonergodicity on stress correlations will be considered separately.

It is stress fluctuations in an infinite system that are considered in this paper. Simulation studies concern finite box systems, normally with periodic boundary conditions (PBC). The results obtained below for an infinite space are still applicable in the PBC case with box-size L if $l(t) \ll L$. In the general case $C\,(\boldsymbol{r}, t)$ with PBC is defined (in 2d)

as:

$$C(\boldsymbol{r},t,L) = L^{-2}\sum_{\boldsymbol{q}} C(\boldsymbol{q},t)\cdot\exp\left(\mathrm{i}\boldsymbol{q}\cdot\boldsymbol{r}\right), \tag{4.26}$$

where $\boldsymbol{q} = (2\pi/L)\boldsymbol{n}$, $\boldsymbol{n}$ is the vector whose components take independently all integer values between $-\infty$ and ∞. In the opposite regime $L \ll l(t)$ only one term above (with $q = 0$) matters for the isotropic part of the stress correlation function, C^{is}, thus giving:

$$C^{\mathrm{is}}(\boldsymbol{r},t,L) \simeq T\left[G\left(t\right) - G_e\right]/L^2,\ l\left(t\right) \gg L \tag{4.27}$$

Therefore, C^{is} turns out to be nearly independent of r in the regime $l(t) \gg L$ relevant in most simulation studies due to relatively small box-size L. Note that strictly speaking the above equation provides the correlation function $C^{\mathrm{is}}(\boldsymbol{r},t)$ which is coarse-grained over a time-interval $\Delta t \gg tL/l(t)$. This interval is relatively short, $\Delta t/t \ll 1$ at long times; the coarse-graining is necessary due to a singular behavior of $C^{\mathrm{is}}(\boldsymbol{r},t)$ at the wave front (cf. eq. 2.138). Note also that G_e in eq. 4.27 is the equilibrium shear modulus (cf. eq. 2.125), and that $G_e = 0$ for the systems we consider (ergodic liquids or glassy systems which are fully equilibrated thermodynamically). Turning to the singular part of the correlation function, C^s , and the full function $C = C^{\mathrm{is}} + C^{\mathrm{s}}$ in the regime $l(t) \gg L$, the infinite space results (cf. eqs. 2.154, 2.157 and 2.160) remain applicable provided that $r \ll L$.

4.8 Summary of Chapter 4

In this chapter we have investigated the 2-dimensional polydisperse LJ model with $N = 10^4$ particles in it. We found that:

(i) Temperature dependence of the static shear modulus is represented in Fig. 4.10. It was found that for the liquid regime $\mu = 0$, and on cooling the shear modulus $\mu > 0$ increases in a sharp way. Moreover, we have analyzed the standard deviations of μ, $\delta\mu$ (see Figs. 4.9 and 4.11), over the sampling time $\Delta t = 10^5\tau_{\mathrm{LJ}}$. In addition, the temperature dependence of the moduli μ_A, μ_F, their fluctuations and the dynamical quantities such as $G\left(t\right)$, $C\left(t\right)$ were studied as well. It was shown that they exhibit a rather similar behavior as for the 3-dimensional glass-forming olygomer system. Moreover, $\delta\mu(T)$ for both systems exhibit the similar behavior and has a peak near the glass transition region. Based on the obtained temperature dependencies for the

2-dimensional polydisperse LJ model we estimated the glass-transition temperature T_g for studied system (cf. sections 1.1.2 and 4.2.2), which is roughly $T_g = 0.26$.

(ii) The monodisperse CE, eq. 4.4, is strongly violated.

(iii) The dynamical structure factor $S(q,t)$ shows a two-step relaxation at low q, from S_0 to $S_{\rm pl}$ on the time scale τ_α and then from $S_{\rm pl}$ to 0 with a much longer relaxation time (cf. Fig. 4.4).

(iv) The time-dependent heat capacity $c_v(t)$ and the related energy correlation function $C_E(t)$ show long-time power-law tails. All these effects are reproduced with a simple model assuming the excess free energy density to depend only on local volume concentration. The model attributes the effects to slowly relaxing composition fluctuations. The polydispersity contribution ($S_{\rm pl}$) to S_0 is obtained in quantitative agreement with our data (cf. Fig. 4.5) and exceeds 70% of S_0. Such a large deviation from eq. 4.4, even for very low PDI ($\delta_p \sim 1\%$), comes as a result of a competition between polydispersity and compressibility. The monodisperse CE can still be used once S_0 is replaced with $S_0 - S_{\rm pl} = cT/K_T$, a result that resonates with the Kirkwood-Buff theory [139]. However, instead of determining $S_{\rm pl}$ from the matrix of static partial structure factors [139], we show that $S_{\rm pl}$ can be obtained from the relaxation of collective density fluctuations. Moreover, we established that the terminal decay of $S(q,t)$ (for $t \gg \tau_\alpha$ and $q\overline{\sigma} \ll 1$) is exponential for weak polydispersity, with a rate defined by the self-diffusion constant D_s averaged over all particles. All effects discussed above can be measured experimentally and are quite generic. They must be present in all polydisperse systems, including binary mixtures. Therefore, our work raises intriguing questions on the impact of composition fluctuations (which are important also because of growing awareness that they may trigger instability to crystallization [134]) and their interplay with the glassy dynamics [141–143].

(v) The MD results for tensorial stress correlations in the 2-dimenional pLJ system we studied show an excellent quantitative agreement with the theory developed in ref. [9] (Chaper 2) both above and below T_g.

(vi) Based on the MD results for tensorial stress correlations in the 2-dimenional pLJ system it was indicated that below T_g the time-smoothed local stress exhibits long-range spatial correlations decaying as $1/r^2$ with distance r. In other words, the

inherent structures of this system are characterized by pronounced correlations of the anisotropic stress [9] with almost infinite range, in agreement with the behavior reported for 2d and 3d Kob-Andersen (binary LJ) models [11, 170].

Chapter 5

Conclusion

5.1 Glass-forming 3-dimensional oligomer system

(i) It was found that static shear modulus μ is roughly independent of the system size [6] but its standard deviation shows significant system size dependence below T_g. For liquid regime $T \gg T_g$ the shear modulus $\mu = 0$ (Fig. 3.6). Vitrifying liquids cooled below the T_g form amorphous solids, whose shear modulus $\mu > 0$ increases in a sharp way on cooling near T_g. One can see in Fig. 3.6 that for our new system ($M = 768$ oligomer chains, $N = 4$ monomers) and a similar larger system studied earlier [7] ($M = 3072$, $N = 4$), $\mu(T)$ indeed strongly increases as the system is cooled near T_g. Moreover, based on Figs. 3.5 – 3.6, it can be seen that such quantities as the shear-relaxation modulus $G(t)$ and $\mu(T)$ exhibit similar behavior for both systems [7]. The main difference between the two systems is that the $M = 768$ system shows somewhat longer structural relaxation time τ_α in the low-T regime $T < \frac{2}{3}T_g$ [6].

(ii) We developed a technique [6] which allows to decrease fluctuations of the affine shear modulus μ_A by averaging over all possible orientations (assuming that our system is isotropic we can do averaging over rotations of the system coordinates frame). The strong effect of full pre-averaging (cf. Fig. 3.16) has a simple meaning: fluctuations of μ_A are mainly due to variations of bond orientations.

(iii) Moreover, we found that the statistics of the time-averaged μ_A involve time-correlations between instant μ_A along the trajectory, which are dynamical in nature [6], and therefore strongly depend on temperature T. To avoid this correlation aspect one has

to calculate the instant moduli $\tilde{\mu}_A$ ($n_A m_T$ values in total, where m_T is the number of independent trajectories and $n_A = \Delta t/\Delta t_A$, where Δt_A is the frequency of saving the positions of all particles). The corresponding standard deviation is denoted as $\delta_1\mu_A$, and it is roughly independent of temperature. The temperature behaviors of μ_A, $\delta\mu_A$, and $\delta_1\mu_A$ are shown in Fig. 3.4 and Fig. 3.16. The T-independence of $\delta_1\mu_A$ invites the question about the much stronger dependence of $\delta\mu_A$ on T. This can be explained as follows: while μ_A is always averaged over some transient configurations n_A along each trajectory, these instant states are independent at temperatures where the relaxation time τ_α is much shorter than the time-interval $\Delta t_{\rm A}$ between the configurations (for instance, at $T = 0.55$), but they are strongly correlated for lower temperatures where $\tau_\alpha \gg \Delta t_{\rm A}$. As a result, $\delta\mu_A$ is smaller than $\delta_1\mu_A$ by a factor of $1/\sqrt{n_A}$ at high T's, but this reduction is not applicable at low T's, where $\delta\mu_A \sim \delta_1\mu_A$.

(iv) We developed a quantitative theory [6] predicting the standard deviation $\delta\mu_F$ of the fluctuation modulus μ_F (which is approximately equal to the deviation of the static shear modulus $\delta\mu$) in terms of the relaxation modulus $G(t)$ which is in excellent agreement with the simulation results in the liquid regime. The theoretical approach is based on the Gaussian approximation for stress fluctuations, which is asymptotically exact for large systems, $V \to \infty$. It was shown that strong decrease of $\delta\mu_F$ at low T comes as a natural behavior of $\delta\mu_F^{(\rm G)}$.

(v) Moreover, we showed that the low-T plateau of $\delta\mu_F$ strongly decreases as the system gets larger (see Figs. 3.20 — 3.21). This effect is attributed to a highly heterogeneous amorphous structure of the super-cooled glassy liquids leading to markedly non-Gaussian stress fluctuations coupled to the quenched structural disorder. Our analysis shows that the non-Gaussian part of the variance of shear moduli (which is defined above eq. 3.30), $\mathrm{var}(\mu_F)_{nG} \approx \mathrm{var}\,(\mu)_{nG}$, decreases with the system size as $1/V^\alpha$ with $\alpha < 1$ ($\alpha \approx 0.7 \pm 0.1$). This result indicates that the local elastic (structural) properties in the studied amorphous systems must show long-range spatial correlations (since a structure with uncorrelated elements would lead to a $1/V$ dependence of the variance).

5.2 Glass-forming 2-dimensional simple liquid system

(i) The moduli μ, μ_A, their fluctuations $\delta\mu$, $\delta\mu_A$, and the response function $G(t)$ were obtained, analyzed, and summarized. It was shown that they exhibit a qualitatively similar behavior as for the 3-dimensional glass-forming oligomer system. Based on the Figs. 4.9 and 3.28 one can detect similar behavior of deviation of the quasi-equilibrium shear modulus μ, $\delta\mu$, for 2 different systems. The peak region of those standard deviations can be considered as a good signature to define the glass transition temperature T_g.

Based on the Figs. 3.28 and 4.9 one can see that for 2-dimensional simple liquid system the peak region for $\delta\mu(T)$ (Fig. 4.9) is much sharper than the one for the 3-dimensional oligomer system (Fig. 3.28) which is broader. The obtained temperature dependence of $\delta\mu$ for both systems exhibit similar behaviors at different T regimes: sharp transition from a liquidlike to a solidlike behavior, and weak T-dependence at low T's. The peak of $\delta\mu$ near T_g can be explained by the assumption that the stress fluctuations are Gaussian [6]. The theoretical results are shown as dashed curve in Figs. 3.28 and 4.9. The agreement is good around T_g and above it. At low T's, $\delta\mu \approx \delta\mu_F$ (cf. Fig. 4.11 and ref. [6]) and well below T_g the simulated $\delta\mu$ is much higher than the theoretically predicted $\delta\mu^{(G)}$. This discrepancy indicates that stress fluctuations must be strongly non-Gaussian at low T's. Recalling that the Gaussian character of random variables averaged over a large system volume V naturally comes from their short-range correlations, the latter result also means that correlations of stress fluctuations must become long-range well below T_g (for more detailed explanation see section 3.8).

(ii) We performed MD simulations of a 2d polydisperse LJ system well above T_g and found that (i) the monodisperse compressibility equation (CE), eq. 4.4, is strongly violated; (ii) the dynamical structure factor $S(q,t)$ shows a two-step relaxation at low q, from S_0 to $S_{\rm pl}$ on the time scale ~ 100 (LJ units) and then from $S_{\rm pl}$ to 0 with a relaxation time much longer than τ_α (cf. Fig. 4.4); (iii) the time-dependent heat capacity $c_v(t)$ and the related energy correlation function $C_E(t)$ show long-time power-law tails.

(iii) The long-time effects for $S(q,t)$ are quantitatively explained with a general theory developed for a low polydispersity degree. The theory attributes the effects to slowly relaxing composition fluctuations. The polydispersity contribution $S_{\rm pl}$ to S_0 is obtained in quantitative agreement with our simulation data (cf. Fig. 4.5) and exceeds 70% of S_0. Such a large deviation from eq. 4.4, even for very low PDI ($\delta_p \sim 1\%$), comes as a result of a competition between polydispersity and compressibility.

(iv) Moreover, we established that the terminal decay of $S(q,t)$ (for $t \gg \tau_\alpha$ and $q\overline{\sigma} \ll 1$) is exponential for weak polydispersity, with a rate defined by the self-diffusion constant D_s averaged over all particles. We therefore established that the long-time plateau of the coherent scattering function is due to a coupling between concentration and the slowly-relaxing composition fluctuations. Our idea is that the long-time tails in $\Delta c_v(t)$ and the energy correlation function $C_E(t)$ result from a similar coupling between the total energy and composition fluctuations. Both effects are therefore generally due to the polydispersity.

(v) To study the stress correlation range more directly we analyzed the correlation function $C_{\alpha\beta\gamma\delta}(\boldsymbol{q},t)$ of the stress tensor at different wave-vectors $\boldsymbol{q}$ using MD simulations. The MD simulations data show excellent quantitative agreement with the theoretical results derived before [9] both above and below T_g. The results for $C_2(t) = C_{2222}(\boldsymbol{q},t)$ (from eq. 4.18) for $q = \frac{2\pi}{L}$ (where $L \approx 100$ is the system box size) are represented in Figs. 4.12, 4.14 and superimpose almost exactly in both temperature regimes. Besides we established that the long time shoulder of $C_2(t)$ is nearly independent of $\boldsymbol{q}$ for small $\boldsymbol{q} \ll 1$. Our data thus indicate that the stress correlations decay as $\frac{1}{r^2}$ with distance r in agreement with the previous simulation results [11] and theoretical predictions [9].

5.3 Simulation improvements

(i) We have done LAMMPS implementation for calculation of the affine shear modulus for 2-dimensional simple liquid system, μ_A and $\mu_{A(\rm or)}$, based on eq. 2.63. With this improvement the data analysis is easier and the corresponding result does not need to be corrected with the "impulsive correction" term. Also, we have integrated in LAMMPS the program for calculation of the static structure factor, which decreases

the calculation time for the user.

(ii) In order to reduce unphysical oscillations (related to temperature oscillations inherent in the Nosé-Hoover thermostat) in the longitudinal modulus $K(t)$ and the energy correlation functions $C_E(t)$, the value of thermal inertia coefficient Q was decreased for the pLJ system by a factor ~ 6000 vs. Q for the polymer model.

(iii) We developed and implemented in LAMMPS a new algorithm, which allows to efficiently calculate anisotropic stress tensor $\sigma(q)$ for different sets of wave-vectors $\boldsymbol{q}$. Moreover, at $q = 0$, the user will receive the values for the mean stress σ rather than an error notice. The new LAMMPS method is suitable for the MPI (Message Passing Interface) parallel computing. This means that our program can be used with different amounts of computer cores. The average time of calculation of one trajectory for 24 cores machine takes roughly 90 min (including the calculation of $\sigma_{xx}(\boldsymbol{q})$, $\sigma_{yy}(\boldsymbol{q})$, $\sigma_{xy}(\boldsymbol{q})$ for $n_q = 30$, every $\delta\tau_{\tilde{\sigma}(q)} = 20\tau_{\mathrm{LJ}}$ for simulation length $\Delta t = 10^5\tau_{\mathrm{LJ}}$).

(iv) We developed a computing method in LAMMPS, which allows to calculate dynamical structure factor $S(q,t)$ on the fly during the production run.

(v) We developed post-simulation analysis tools, which allow to calculate different types of correlations (for instance, shear-stress correlation function $C(t)$, normal pressure correlation function $C_b(t)$) and tools to obtain the correlation functions such as $C_T(q,t)$, $C_2(q,t)$, $C_{\parallel}(q,t)$, and $C_{\perp}(q,t)$ (see Chapter 4). Those tools include unique block-averaging methods and the methods in C++ to read input files, which makes the calculation more efficient and faster.

Bibliography

[1] P. G. Debenedetti and F. H. Stillinger, "Supercooled liquids and the glass transition," *Nature*, vol. 410, no. 6825, pp. 259–267, 2001.

[2] A. Cavagna, "Supercooled liquids for pedestrians," *Phys. Rep.*, vol. 476, pp. 51–124, 2009.

[3] D. Li, H. Xu, and J. Wittmer, "Glass transition of two-dimensional 80-20 Kob-Andersen model at constant pressure," *Journal of Physics: Condensed Matter*, vol. 28, p. 045101, 2016.

[4] J. Wittmer, I. Kriuchevskyi, J. Baschnagel, and H. Xu, "Shear-strain and shear-stress fluctuations in generalized gaussian ensemble simulations of isotropic elastic networks," *Eur. Phys. J. B*, vol. 88, 2015.

[5] J.-L. Barrat, J.-N. Roux, J.-P. Hansen, and M. L. Klein, "Elastic response of a simple amorphous binary alloy near the glass transition," *Europhysics Letters (EPL)*, vol. 7, p. 707, 1988.

[6] L. Klochko, J. Baschnagel, J. P. Wittmer, and A. N. Semenov, "Relaxation dynamics in supercooled oligomer liquids: From shear-stress fluctuations to shear modulus and structural correlations," *J. Chem. Phys*, vol. 151, no. 5, p. 054504, 2019.

[7] I. Kriuchevskyi, J. Wittmer, H. Meyer, O. Benzerara, and J. Baschnagel, "Shear-stress fluctuations and relaxation in polymer glasses," *Phys. Rev. E*, vol. 97, 2018.

[8] J. Wittmer, H. Xu, O. Benzerara, and J. Baschnagel, "Fluctuation-dissipation relation between shear stress relaxation modulus and shear stress autocorrelation function revisited," *Molecular Physics*, vol. 113, no. 17-18, pp. 2881–2893, 2015.

[9] L. Klochko, J. Baschnagel, J. P. Wittmer, and A. N. Semenov, "Long-range stress correlations in viscoelastic and glass-forming fluids," *Soft Matter*, vol. 14, pp. 6835–6848, 2018.

[10] A. N. Semenov, J. Farago, and H. Meyer, "Length-scale dependent relaxation shear modulus and viscoelastic hydrodynamic interactions in polymer liquids," *J. Chem. Phys.*, vol. 136, p. 244905, 2012.

[11] A. Lemaître, "Structural relaxation is a scale-free process," *Phys. Rev. Lett.*, vol. 113, p. 245702, 2014.

[12] M. Maier, A. Zippelius, and M. Fuchs, "Emergence of long-ranged stress correlations at the liquid to glass transition," *Phys. Rev. Lett.*, vol. 119, p. 265701, 2017.

[13] M. Maier, A. Zippelius, and M. Fuchs, "Stress auto-correlation tensor in glass-forming isothermal fluids: From viscous to elastic response," *J. Chem. Phys*, vol. 149, no. 8, p. 084502, 2018.

[14] B. Bensaude-Vincent, "Book Review: The Substance of Civilization: Materials and Human History from the Stone Age to the Age of Silicon Stephen L. Sass," *Isis*, vol. 90, 1999.

[15] A. Macfarlane and G.Martin, "Glass: A world history," *University of Chicago Press*, 2002.

[16] H. Aben, J. Anton, M. Õis, K. Viswanathan, S. Chandrasekar, and M. M. Chaudhri, "On the extraordinary strength of Prince Rupert's drops," *Applied Physics Letters*, vol. 109, no. 23, p. 231903, 2016.

[17] A. Guillemin, N. Lockyer, and W. J. Lockyer, *The forces of nature: a popular introduction to the study of physical phenomena.* London: Macmillan and co., 1873.

[18] J. Baschnagel, I. Kriuchevskyi, J. Helfferich, C. Ruscher, H. Meyer, O. Benzerara, J. Farago, and J. P. Wittmer, ch. Glass Transition and Relaxation Behavior of Supercooled Polymer Melts: An Introduction to Modeling Approaches by Molecular Dynamics Simulations., pp. 55–106. Taylor & Francis Group: CRC Press, 2016.

[19] W. Kob, "Computer simulations of supercooled liquids and structural glasses," in *Annual Reviews of Computational Physics* (D. Stauffer, ed.), vol. 3, p. 1, Singapore: World Scientific, 1995.

[20] K. Vollmayr, W. Kob, and K. Binder, "How do the properties of a glass depend on the cooling rate? A computer simulation study of a Lennard-Jones system," *J. Chem. Phys*, vol. 105, p. 4714, 1996.

[21] J. Buchholz, W. Paul, F. Varnik, and K. Binder, "Cooling rate dependence of the glass transition temperature of polymer melts: Molecular dynamics study," *J. Chem. Phys*, vol. 117, no. 15, pp. 7364–7372, 2002.

[22] W. Bragg, "Chapter 2 - the glassy state," in *Structural Chemistry of Glasses* (K. Rao, ed.), pp. 13 – 76, Oxford: Elsevier Science Ltd, 2002.

[23] W. Klement, R. H. Willens, and P. Duwez, "Non-crystalline structure in solidified gold-silicon alloys," *Nature*, vol. 187, no. 4740, pp. 869–870, 1960.

[24] M. I. Ojovan, "Glass formation in amorphous SiO_2 as a percolation phase transition in a system of network defects," *Journal of Experimental and Theoretical Physics Letters*, vol. 79, no. 12, pp. 632–634, 2004.

[25] W. N. Sharpe, J. Pulskamp, D. S. Gianola, C. Eberl, R. G. Polcawich, and R. J. Thompson, "Strain measurements of silicon dioxide microspecimens by digital imaging processing," *Experimental Mechanics*, vol. 47, no. 5, pp. 649–658, 2007.

[26] M. D. Ediger, C. A. Angell, and S. R. Nagel, "Supercooled liquids and glasses," *J. Phys. Chem.*, vol. 100, no. 31, pp. 13200–13212, 1996.

[27] W. Kauzmann *Chem. Rev.*, vol. 43, p. 219, 1948.

[28] J. M. Hutchinson, "Determination of the glass transition temperature," *Journal of Thermal Analysis and Calorimetry*, vol. 98, no. 3, p. 579, 2009.

[29] D. H. Napper, "Polymeric stabilization of colloidal dispersions," *Academic Press, London*, 1983.

[30] H. Lekkerkerker and R. Tuiner, "Colloids and the depletion interaction," *Springer*, 2011.

[31] F. Sciortino and P. Tartaglia, "Glassy colloidal systems," *Advances in Physics*, vol. 54, no. 6-7, pp. 471–524, 2005.

[32] A. A. Shvets and A. N. Semenov, "Effective interactions between solid particles mediated by free polymer in solution," *J. Chem. Phys*, vol. 139, no. 5, p. 054905, 2013.

[33] A. N. Semenov and A. A. Shvets, "Theory of colloid depletion stabilization by unattached and adsorbed polymers," *Soft Matter*, vol. 11, pp. 8863–8878, 2015.

[34] A. Semenov, "Theory of long-range interactions in polymer systems," *J. Phys. II France, 6 12*, 1996.

[35] A. N. Semenov, "Theory of colloid stabilization in semidilute polymer solutions," *Macromolecules*, vol. 41, no. 6, pp. 2243–2249, 2008.

[36] J. Goodwin, *Colloids and Interfaces with Surfactants and Polymers, 2nd Ed.* Wiley, 2009.

[37] R. Larson, "The structure and rheology of complex fluids," *Oxford Univ. Press*, 1999.

[38] V. Mansard and A. Colin, "Local and non local rheology of concentrated particles," *Soft Matter*, vol. 8, pp. 4025–4043, 2012.

[39] M. Siebenbürger, M. Fuchs, and M. Ballauff, "Core-shell microgels as model colloids for rheological studies," *Soft Matter*, vol. 8, p. 4014, 2012.

[40] N. Koumakis, A. Pamvouxoglou, A. Poulos, and G. Petekidis, "Direct comparison of the rheology of hard and soft particle glasses," *Soft Matter*, vol. 8, p. 4271, 2012.

[41] T. Voigtmann, J. M. Brader, M. Fuchs, and M. E. Cates, "Schematic mode coupling theory of glass rheology: single and double step strains," *Soft Matter*, vol. 8, pp. 4244–4253, 2012.

[42] G. Hunter and E. Weeks, "The physics of the colloidal glass transition," *Reports on progress in physics. Physical Society (Great Britain)*, vol. 75, 2012.

[43] W. C. Poon, "Colloidal glasses," *MRS Bulletin*, vol. 29, no. 2, p. 96–99, 2004.

[44] L. Berthier, G. Biroli, J.-P. Bouchaud, L. Cipelletti, and W. van Saarloos, *Dynamical Heterogeneities in Glasses, Colloids and Granular Media*. Oxford: Oxford University Press, 2011.

[45] E. Bartsch, V. Frenz, J. Baschnagel, W. Schärtl, and H. Sillescu, "The glass transition dynamics of polymer micronetwork colloids. A mode coupling analysis," *J. Chem. Phys.*, vol. 106, p. 3743, 1997.

[46] M. Fuchs, "Nonlinear rheological properties of dense colloidal dispersions close to a glass transition under steady shear," *Adv. Polym. Sci.*, vol. 36, pp. 55–115, 2010.

[47] R. Courtland and E. Weeks, "Direct visualization of aging in colloidal glasses," *Journal of Physics: Condensed Matter*, vol. 15, 2002.

[48] T. Gleim, W. Kob, and K. Binder, "How does the relaxation of a supercooled liquid depend on its microscopic dynamics?," *Phys. Rev. Lett.*, vol. 81, no. 20, pp. 4404–4407, 1998.

[49] E. Donth, *The Glass Transition*. Berlin–Heidelberg: Springer, 2001.

[50] L. Berthier and G. Biroli, "Theoretical perspective on the glass transition and amorphous materials," *Rev. Mod. Phys.*, vol. 83, pp. 587–645, 2011.

[51] C. Angell, "Formation of glasses from liquids and biopolymers," *Science (New York, N.Y.)*, vol. 267, pp. 1924–35, 1995.

[52] C. A. Angell, K. L. Ngai, G. B. McKenna, P. F. McMillan, and S. W. Martin, "Relaxation in glassforming liquids and amorphous solids," *J. Appl. Phys.*, vol. 88, p. 3113, 2000.

[53] D. Huang and G. McKenna, "New insights into the fragility dilemma in liquids," *J. Chem. Phys*, vol. 114, pp. 5621–5630, 2001.

[54] K. Vollmayr, W. Kob, and K. Binder, "Cooling-rate effects in amorphous silica: A computer-simulation study," *Phys. Rev. B*, vol. 54, pp. 15808–15827, 1996.

[55] D. S. Sanditov, M. V. Darmaev, and V. V. Mantatov, "The Bartenev and Williams-Landel-Ferry equations in the relaxation theory of the glass transition and the model of delocalized atoms," *Polymer Science Series A*, vol. 57, no. 1, pp. 86–93, 2015.

[56] D. S. Sanditov, "On the nature of the liquid-to-glass transition equation," *Journal of Experimental and Theoretical Physics*, vol. 123, no. 3, pp. 429–442, 2016.

[57] G. M. Bartenev, I. V. Razumovskaya, D. S. Sanditov, and I. A. Lukyanov, "A contribution to the theory of the structural glass transition," *Journal of Polymer Science Part A-1: Polymer Chemistry*, vol. 7, no. 8, pp. 2147–2157, 1969.

[58] S. Sastry, P. G. Debenedetti, and F. H. Stillinger, "Signatures of distinct dynamical regimes in the energy landscape of a glass-forming liquid," *Nature*, vol. 393, no. 6685, pp. 554–557, 1998.

[59] F. H. Stillinger, "A topographic view of supercooled liquids and glass formation," *Science*, vol. 267, p. 1935, 1995.

[60] L. Landau and E. Lifshitz, *Statistical Physics (Third Edition)*. Butterworth-Heinemann, 1980.

[61] J. H. Gibbs and E. A. DiMarzio, "Nature of the glass transition and the glassy state," *J. Chem. Phys*, vol. 28, no. 3, pp. 373–383, 1958.

[62] J. P. Hansen and I. R. McDonald, *Theory of Simple Liquids*. London: Academic Press, 1986.

[63] F. H. Stillinger, P. G. Debenedetti, and T. M. Truskett, "The Kauzmann paradox revisited," *J. Phys. Chem. B*, vol. 105, p. 11809, 2001.

[64] L. Berthier, M. Ozawa, and C. Scalliet, "Configurational entropy of glass-forming liquids," *J. Chem. Phys*, vol. 150, no. 16, p. 160902, 2019.

[65] G. Adam and J. H. Gibbs *J. Chem. Phys.*, vol. 43, p. 139, 1965.

[66] C. Bennemann, C. Donati, J. Baschnagel, and S. C. Glotzer, "Growing range of correlated motion in a polymer melt on cooling towards the glass transition," *Nature*, vol. 399, no. 6733, pp. 246–249, 1999.

[67] H. Tanaka, T. Kawasaki, H. Shintani, and K. Watanabe, "Critical-like behaviour of glass-forming liquids," *Nature Materials*, vol. 9, no. 4, pp. 324–331, 2010.

[68] A. N. Semenov, "Thermodynamic nature of vitrification in a 1d model of a structural glass former," *J. Chem. Phys*, vol. 143, no. 4, p. 044510, 2015.

[69] E. Flenner and G. Szamel, "Long-range correlations in glasses and glassy fluids," *Journal of Physics: Condensed Matter*, vol. 27, no. 19, p. 194125, 2015.

[70] E. Flenner and G. Szamel, "Long-range spatial correlations of particle displacements and the emergence of elasticity," *Phys. Rev. Lett.*, vol. 114, p. 025501, 2015.

[71] L. Berthier, P. Charbonneau, Y. Jin, G. Parisi, B. Seoane, and F. Zamponi, "Growing timescales and lengthscales characterizing vibrations of amorphous solids," *Proceedings of the National Academy of Sciences*, vol. 113, no. 30, pp. 8397–8401, 2016.

[72] P. Charbonneau, J. Kurchan, G. Parisi, P. Urbani, and F. Zamponi, "Fractal free energy landscapes in structural glasses," *Nature Communications*, vol. 5, no. 1, p. 3725, 2014.

[73] P. Charbonneau, Y. Jin, G. Parisi, C. Rainone, B. Seoane, and F. Zamponi, "Numerical detection of the gardner transition in a mean-field glass former," *Phys. Rev. E*, vol. 92, p. 012316, 2015.

[74] S. Frey, *Viscoelastic Properties of Glass-Forming Polymer Melts*. PhD thesis, Université de Strasbourg, Strasbourg, 2012. (available from `http://www.sudoc.fr/165862653`).

[75] J. Baschnagel and F. Varnik, "Computer simulation of supercooled polymer melts in the bulk and in confined geometry," *J. Phys.: Condens. Matter*, vol. 17, p. R851, 2005.

[76] Large-scale Atomic/Molecular Massively Parallel Simulator (LAMMPS), http://lammps.sandia.gov.

[77] N. Metropolis, "Equation of state calculations by fast computing machines," *J. Chem. Phys.*, vol. 21, p. 1087, 1953.

[78] M. P. Allen and D. J. Tildesley, *Computer Simulation of Liquids*. Oxford: Clarendon Press, 1987.

[79] L. Verlet, "Computer "experiments" on classical fluids. ii. equilibrium correlation functions," *Phys. Rev.*, vol. 165, pp. 201–214, 1968.

[80] E. B. Tadmor and R. E. Miller, *Modeling Materials: Continuum, Atomistic and Multiscale Techniques*. Cambridge University Press, 2011.

[81] M. Tuckerman, B. J. Berne, and G. J. Martyna, "Reversible multiple time scale molecular dynamics," *J. Chem. Phys*, vol. 97, no. 3, pp. 1990–2001, 1992.

[82] J. E. Jones and S. Chapman, "On the determination of molecular fields: From the variation of the viscosity of a gas with temperature," *Proceedings of the Royal Society of London. Series A, Containing Papers of a Mathematical and Physical Character*, vol. 106, no. 738, pp. 441–462, 1924.

[83] F. Varnik, *Molecular Dynamics Simulations on the Glass Transition in Macromolecular Films*. PhD thesis, Johannes Gutenberg University Mainz, Mainz, 2001. (available from http://varnik.free.fr/PhDThesis.html).

[84] D. Frenkel and B. Smit, *Understanding Molecular Simulation*. London: Academic Press, 2nd ed., 2002.

[85] H. C. Andersen, "Molecular dynamics simulations at constant pressure and/or temperature," *J. Chem. Phys*, vol. 72, no. 4, pp. 2384–2393, 1980.

[86] S. Nosé, "A unified formulation of the constant temperature molecular dynamics methods," *J. Chem. Phys.*, vol. 81, pp. 511–519, 1984.

[87] W. G. Hoover, "Canonical dynamics: Equilibrium phase-space distributions," *Phys. Rev. A*, vol. 31, pp. 1695–1697, 1985.

[88] S. Nosé, "Constant Temperature Molecular Dynamics Methods," *Progress of Theoretical Physics Supplement*, vol. 103, pp. 1–46, 1991.

[89] R. C. Tolman., "A general theory of energy partition with applications to quantum theory," *Phys. Rev.*, vol. 11, pp. 261–275, 1918.

[90] W. G. Hoover, "Constant-pressure equations of motion," *Phys. Rev. A*, vol. 34, pp. 2499–2500, 1986.

[91] J. P. Wittmer, H. Xu, and J. Baschnagel, "Shear-stress relaxation and ensemble transformation of shear-stress autocorrelation functions," *Phys. Rev. E*, vol. 91, p. 022107, 2015.

[92] P. G. Debenedetti and F. H. Stillinger, "Supercooled liquids and the glass transition," *Nature*, vol. 410, p. 259, 2001.

[93] J. P. Wittmer, H. Xu, P. Polińska, F. Weysser, and J. Baschnagel, "Shear modulus of simulated glass-forming model systems: Effects of boundary conditions, temperature, and sampling time," *J. Chem. Phys.*, vol. 138, p. 12A533, 2013.

[94] H. Xu, J. P. Wittmer, P. Polińska, and J. Baschnagel, "Impulsive correction to the elastic moduli obtained using the stress-fluctuation formalism in systems with truncated pair potential," *Phys. Rev. E*, vol. 86, p. 046705, 2012.

[95] A. Tanguy, J. P. Wittmer, F. Léonforte, and J.-L. Barrat, "Continuum limit of amorphous elastic bodies: A finite-size study of low-frequency harmonic vibrations," *Phys. Rev. B*, vol. 66, p. 174205, 2002.

[96] J. S. Rowlinson, *Liquids and Liquid Mixtures*. London: Butterworths, 1959.

[97] C. Ruscher, A. N. Semenov, J. Baschnagel, and J. Farago, "Anomalous sound attenuation in voronoi liquid," *J. Chem. Phys*, vol. 146, no. 14, p. 144502, 2017.

[98] U. Balucani and M. Zoppi, *Dynamics of the Liquid State*. Oxford: Oxford University Press, 2003.

[99] F. Varnik, J. Baschnagel, and K. Binder, "Molecular dynamics results on the pressure tensor of polymer films," *J. Chem. Phys*, vol. 113, no. 10, pp. 4444–4453, 2000.

[100] I. Goldhirsch and C. Goldenberg, "On the microscopic foundations of elasticity," *Eur. Phys. J. E*, vol. 9, p. 245, 2002.

[101] D. J. Evans and G. Morriss, *Statistical Mechanics of Nonequilibrium Liquids*. Cambridge University Press, 2 ed., 2008.

[102] P. Chaudhuri and J. Horbach, "Onset of flow in a confined colloidal glass under an imposed shear stress," *Phys. Rev. E*, vol. 88, p. 040301(R), 2013.

[103] J.-L. Barrat and A. Lemaître, "Heterogeneities in amorphous systems under shear," in *Dynamical Heterogeneities in Glasses, Colloids and Granular Media* (L. Berthier, G. Biroli, J.-P. Bouchaud, L. Cipelletti, and W. van Saarloos, eds.), pp. 264–297, Oxford: Oxford University Press, 2011.

[104] H. Yoshino, "Replica theory of the rigidity of structural glasses," *J. Chem. Phys*, vol. 136, no. 21, p. 214108, 2012.

[105] L. Landau and E. Lifshitz, *Fluid Mechanics: Volume 6*. Elsevier Science, 2013.

[106] S. Yaida, L. Berthier, P. Charbonneau, and G. Tarjus, "Point-to-set lengths, local structure, and glassiness," *Phys. Rev. E*, vol. 94, p. 032605, 2016.

[107] S. Karmakar, C. Dasgupta, and S. Sastry, "Length scales in glass-forming liquids and related systems: A review," *Reports on progress in physics. Physical Society (Great Britain)*, vol. 79, p. 016601, 2016.

[108] H. Huth, M. Beiner, and E. Donth, "Temperature dependence of glass-transition cooperativity from heat-capacity spectroscopy: Two post-adam-gibbs variants," *Phys. Rev. B*, vol. 61, pp. 15092–15101, 2000.

[109] M. Mosayebi, E. Del Gado, P. Ilg, and H. C. Öttinger, "Probing a critical length scale at the glass transition," *Phys. Rev. Lett.*, vol. 104, p. 205704, 2010.

[110] A. Furukawa and H. Tanaka, "Nonlocal nature of the viscous transport in supercooled liquids: Complex fluid approach to supercooled liquids," *Phys. Rev. Lett.*, vol. 103, p. 135703, 2009.

[111] G. Biroli, J.-P. Bouchaud, A. Cavagna, T. S. Grigera, and P. Verrocchio, "Thermodynamic signature of growing amorphous order in glass-forming liquids," *Nature Physics*, vol. 4, no. 10, pp. 771–775, 2008.

[112] R. Bird, R. Bird, R. Armstrong, and O. Hassager, *Dynamics of Polymeric Liquids, Volume 1: Fluid Mechanics*. Dynamics of Polymeric Liquids, Wiley, 1987.

[113] B. Schnell, H. Meyer, C. Fond, J. Wittmer, and J. Baschnagel, "Simulated glass-forming polymer melts: Glass transition temperature and elastic constants of the glassy state," *Eur. Phys. J. E*, vol. 34, p. 97, 2011.

[114] S. Peter, S. Napolitano, H. Meyer, M. Wübbenhorst, and J. Baschnagel, "Modeling dielectric relaxation in polymer glass simulations: Dynamics in the bulk and in supported polymer films," *Macromolecules*, vol. 41, p. 7729, 2008.

[115] I. Kriuchevskyi, *Propriétés mécaniques et viscolélastiques des polymères vitrifiables en volume et en films minces : études par dynamique moléculaire de systemes modeles*. PhD thesis, Université de Strasbourg, Strasbourg, 2017.

[116] M. Vladkov and J.-L. Barrat, "Linear and nonlinear viscoelasticity of a model unentangled polymer melt: Molecular dynamics and rouse modes analysis," *Macromolecular Theory and Simulations*, vol. 15, no. 3, pp. 252–262, 2006.

[117] A. E. Likhtman, S. K. Sukumaran, and J. Ramirez, "Linear viscoelasticity from molecular dynamics simulation of entangled polymers," *Macromolecules*, vol. 40, p. 6748, 2007.

[118] L. Berthier, G. Biroli, D. Coslovich, W. Kob, and C. Toninelli, "Finite-size effects in the dynamics of glass-forming liquids," *Phys. Rev. E*, vol. 86, p. 031502, 2012.

[119] S. Karmakar, C. Dasgupta, and S. Sastry, "Growing length and time scales in glass-forming liquids," *Proceedings of the National Academy of Sciences*, vol. 106, no. 10, pp. 3675–3679, 2009.

[120] J. P. Wittmer, I. Kriuchevskyi, A. Cavallo, H. Xu, and J. Baschnagel, "Shear-stress fluctuations in self-assembled transient elastic networks," *Phys. Rev. E*, vol. 93, p. 062611, 2016.

[121] W. Götze and L. Sjögren, "Relaxation processes in supercooled liquids," *Rep. Prog. Phys.*, vol. 55, p. 241, 1992.

[122] D. P. Landau and K. Binder, *A Guide to Monte Carlo Simulations in Statistical Physics*. Cambridge: Cambridge University Press, 2013.

[123] E. Lukacs, "Characteristic functions," 1970.

[124] I. Procaccia, C. Rainone, C. A. B. Z. Shor, and M. Singh, "Breakdown of nonlinear elasticity in amorphous solids at finite temperatures," *Phys. Rev. E*, vol. 93, p. 063003, 2016.

[125] H. G. E. Hentschel, S. Karmakar, E. Lerner, and I. Procaccia, "Do athermal amorphous solids exist?," *Phys. Rev. E*, vol. 83, p. 061101, 2011.

[126] W. Kob and H. C. Andersen, "Testing mode-coupling theory for a supercooled binary Lennard-Jones mixture: The van Hove correlation function," *Phys. Rev. E*, vol. 51, no. 5, pp. 4626–4641, 1995.

[127] W. Kob and H. C. Andersen, "Testing mode-coupling theory for a supercooled binary Lennard-Jones mixture: Intermediate scattering function and dynamic susceptibility," *Phys. Rev. E*, vol. 52, no. 4, pp. 4134–4153, 1995.

[128] A. Ninarello, L. Berthier, and D. Coslovich, "Models and algorithms for the next generation of glass transition studies," *Phys. Rev. X*, vol. 7, p. 021039, 2017.

[129] P. Scheidler, W. Kob, A. Latz, J. Horbach, and K. Binder, "Frequency-dependent specific heat of viscous silica," *Phys. Rev. B*, vol. 63, p. 104204, 2001.

[130] L. S. Ornstein and Z. F. *Physik. Z*, vol. 19, p. 134, 1918.

[131] E. Donth, *The Glass Transition: Relaxation Dynamics in Liquids and Disordered Materials*. Springer Series in Materials Science, Springer Berlin Heidelberg, 2013.

[132] F. H. Stillinger, P. G. Debenedetti, and S. Sastry, "Resolving vibrational and structural contributions to isothermal compressibility," *J. Chem. Phys*, vol. 109, no. 10, pp. 3983–3988, 1998.

[133] T. K. Haxton, "Ratio of effective temperature to pressure controls the mobility of sheared hard spheres," *Phys. Rev. E*, vol. 85, p. 011503, 2012.

[134] T. S. Ingebrigtsen, J. C. Dyre, T. B. Schrøder, and C. P. Royall, "Crystallization instability in glass-forming mixtures," *Phys. Rev. X*, vol. 9, p. 031016, 2019.

[135] W. van Megen, T. C. Mortensen, S. R. Williams, and J. Müller, "Measurement of the self-intermediate scattering function of suspensions of hard spherical particles near the glass transition," *Phys. Rev. E*, vol. 58, pp. 6073–6085, 1998.

[136] J. C. Rasaiah, "Molecular theory of solutions by arieh ben-naim (the hebrew university, jerusalem, israel)," *Journal of the American Chemical Society*, vol. 129, no. 28, pp. 8922–8922, 2007.

[137] J. G. Kirkwood and F. P. Buff, "The statistical mechanical theory of solutions. i," *J. Chem. Phys*, vol. 19, no. 6, pp. 774–777, 1951.

[138] A. L. Thorneywork, S. K. Schnyder, D. Aarts, J. Horbach, R. Roth, and R. P. A. Dullens, "Structure factors in a two-dimensional binary colloidal hard sphere system," *Molecular Physics*, vol. 116, no. 21-22, pp. 3245–3257, 2018.

[139] L. Berthier, P. Chaudhuri, C. Coulais, O. Dauchot, and P. Sollich, "Suppressed compressibility at large scale in jammed packings of size-disperse spheres," *Phys. Rev. Lett.*, vol. 106, p. 120601, 2011.

[140] R. Kurita and E. R. Weeks, "Incompressibility of polydisperse random-close-packed colloidal particles," *Phys. Rev. E*, vol. 84, p. 030401, 2011.

[141] F. Weysser, A. M. Puertas, M. Fuchs, and T. Voigtmann, "Structural relaxation of polydisperse hard spheres: Comparison of the mode-coupling theory to a langevin dynamics simulation," *Phys. Rev. E*, vol. 82, p. 011504, 2010.

[142] M. Fuchs and A. Latz, "α-relaxation in a supercooled binary mixture," *Physica A: Statistical Mechanics and its Applications*, vol. 201, no. 1, pp. 1 – 13, 1993.

[143] P. Kuhn, J. Horbach, F. Kargl, A. Meyer, and T. Voigtmann, "Diffusion and interdiffusion in binary metallic melts," *Phys. Rev. B*, vol. 90, p. 024309, 2014.

[144] P. N. Pusey, H. M. Fijnaut, and A. Vrij, "Mode amplitudes in dynamic light scattering by concentrated liquid suspensions of polydisperse hard spheres," *J. Chem. Phys*, vol. 77, no. 9, pp. 4270–4281, 1982.

[145] L. Landau and E. Lifshitz, *Statistical Physics*. Pergamon Press, Oxford, 1998.

[146] P. Sollich, "Predicting phase equilibria in polydisperse systems," *Journal of Physics: Condensed Matter*, vol. 14, no. 3, pp. R79–R117, 2001.

[147] L. Klochko, J. Baschnagel, J. P. Wittmer, O. Benzerara, C. Ruscher, and A. N. Semenov, "Composition fluctuations in polydisperse liquids: Glasslike effects well above the glass transition," *Phys. Rev. E*, vol. 102, p. 042611, 2020.

[148] L. D. Landau and E. M. Lifshitz, *Theory of Elasticity*, vol. 7. Amsterdam: Elsevier, 1986.

[149] L. Onsager, "Reciprocal relations in irreversible processes. i.," *Phys. Rev.*, vol. 37, pp. 405–426, 1931.

[150] L. Onsager, "Reciprocal relations in irreversible processes. ii.," *Phys. Rev.*, vol. 38, pp. 2265–2279, 1931.

[151] L. Onsager and S. Machlup, "Fluctuations and irreversible processes," *Phys. Rev.*, vol. 91, pp. 1505–1512, 1953.

[152] S. Machlup and L. Onsager, "Fluctuations and irreversible process. ii. systems with kinetic energy," *Phys. Rev.*, vol. 91, pp. 1512–1515, 1953.

[153] T. R. Kirkpatrick, D. Thirumalai, and P. G. Wolynes, "Scaling concepts for the dynamics of viscous liquids near an ideal glassy state," *Phys. Rev. A*, vol. 40, pp. 1045–1054, 1989.

[154] L. Berthier, P. Charbonneau, Y. Jin, G. Parisi, B. Seoane, and F. Zamponi, "Growing timescales and lengthscales characterizing vibrations of amorphous solids," *Proceedings of the National Academy of Sciences*, vol. 113, no. 30, pp. 8397–8401, 2016.

[155] E. Donth, H. Huth, and M. Beiner, "Characteristic length of the glass transition," *Journal of Physics: Condensed Matter*, vol. 13, no. 22, pp. L451–L462, 2001.

[156] K. Binder, C. Bennemann, J. Baschnagel, and W. Paul, "Anomalous diffusion of polymers in supercooled melts near the glass transition," in *Anomalous Diffusion From Basics to Applications* (A. Pekalski and K. Sznajd-Weron, eds.), (Berlin, Heidelberg), pp. 124–139, Springer Berlin Heidelberg, 1999.

[157] M. Mosayebi, E. Del Gado, P. Ilg, and H. C. Öttinger, "Probing a critical length scale at the glass transition," *Phys. Rev. Lett.*, vol. 104, p. 205704, 2010.

[158] S. Abraham and P. Harrowell, "The origin of persistent shear stress in supercooled liquids," *J. Chem. Phys.*, vol. 137, p. 014506, 2012.

[159] G. Picard, A. Ajdari, F. Lequeux, and L. Bocquet, "Elastic consequences of a single plastic event: A step towards the microscopic modeling of the flow of yield stress fluids," *Eur. Phys. J. E*, vol. 15, p. 371, 2004.

[160] E. E. Ferrero, K. Martens, and J.-L. Barrat, "Relaxation in yield systems through elastically interacting activated events," *Phys. Rev. Lett.*, vol. 113, p. 248301, 2014.

[161] A. Nicolas, J. Rottler, and J.-L. Barrat, "Spatiotemporal correlations between plastic events in the shear flow of athermal amorphous solids," *Eur. Phys. J. E*, vol. 37, p. 50, 2014.

[162] L. Berthier, G. Biroli, J.-P. Bouchaud, and R. L. Jack, "Overview of different characterizations of dynamic heterogeneity," in *Dynamical Heterogeneities in Glasses, Colloids and Granular Media* (L. Berthier, G. Biroli, J.-P. Bouchaud, L. Cipelletti, and W. van Saarloos, eds.), pp. 69–109, Oxford: Oxford University Press, 2011.

[163] A. S. Keys, L. O. Hedges, J. P. Garrahan, S. C. Glotzer, and D. Chandler, "Excitations are localized and relaxation is hierachical in glass-forming liquids," *Phys. Rev. X*, vol. 1, p. 021013, 2011.

[164] G. Picard, A. Ajdari, F. Lequeux, and L. Bocquet, "Elastic consequences of a single plastic event: A step towards the microscopic modeling of the flow of yield stress fluids," *Eur. Phys. J. E*, vol. 15, no. 4, pp. 371–381, 2004.

[165] J. D. Eshelby and R. E. Peierls, "The elastic field outside an ellipsoidal inclusion," *Proceedings of the Royal Society of London. Series A. Mathematical and Physical Sciences*, vol. 252, no. 1271, pp. 561–569, 1959.

[166] A. Kabla and G. Debrégeas, "Local stress relaxation and shear banding in a dry foam under shear," *Phys. Rev. Lett.*, vol. 90, p. 258303, 2003.

[167] A. Tanguy, F. Léonforte, and J.-L. Barrat, "Plastic response of a 2D Lennard-Jones amorphous solid: Detailed analysis of the local arrangements at very low strain rate," *Eur. Phys. J. E*, vol. 20, p. 355, 2006.

[168] K. W. Desmond and E. R. Weeks, "Measurement of stress redistribution in flowing emulsions," *Phys. Rev. Lett.*, vol. 115, p. 098302, 2015.

[169] B. Illing, S. Fritschi, D. Hajnal, C. Klix, P. Keim, and M. Fuchs, "Strain pattern in supercooled liquids," *Phys. Rev. Lett.*, vol. 117, p. 208002, 2016.

[170] A. Lemaître, "Tensorial analysis of eshelby stresses in 3d supercooled liquids," *J. Chem. Phys*, vol. 143, no. 16, p. 164515, 2015.

List of Figures

List of Tables